Modelling foam flow through vein-like geometries

Tirion Gruffudd Roberts

Supervisor: Prof. S. J. Cox

A thesis presented for the degree of
Doctor of Philosophy

Department of Mathematics
Aberystwyth University
Wales
2020

Mor browd ydwyf heddiw o'm tylwyth
Mae gymaint i'm cadw yn fyw
Cael gwylied y tyfiant a'r llwyddiant
Fel capten a'i law ar y llyw.

BRIAN CHARLES MORRIS (TAID), 1943-2020

Abstract

We explore the effectiveness of using foam in its application within a minimally invasive treatment for varicose veins called foam sclerotherapy. The foam is injected into a varicose vein where it aims to displace the blood and deliver the surfactant to the veins' endothelial cells. This leads to the collapse of the vessel. Foam is used in the treatment due to its yield stress, which allows an effective displacement of blood.

The value of the yield-stress of the foam can be empirically estimated in terms of its surface tension, liquid fraction and bubble radius [Princen and Kiss, 1989]. Further investigation is carried out on the average bubble radius R_{32} thus the value of the yield stress τ_0, allowing us to estimate the yield stress for both the Varethina® and Physician-compounded foams using the data from Carugo et al. [2016].

In order to analyse the effectiveness of the treatment, we conduct finite element simulations of yield-stress fluid through two dimensional channels of various geometries. Due to the nature of the microfluidic flows, we solve the Stokes equations in unison with the Papanastasiou model [Papanastasiou, 1987], treating the foam as a generalised Newtonian fluid with a shear rate dependent viscosity.

The algorithms are validated by comparing the numerical velocities with the respective analytical velocity profile. This is done through both straight and curved channel geometries. In order to validate the latter geometry, we produce an analytical velocity profile for a pressure-driven Bingham fluid. The effect of curvature on the channel flow provides added complexity as the yield surfaces are derived as functions of yield-stress, pressure gradient and additionally channel curvature.

Once the simulation has been validated, we consider more complex geometries such as a sinusoidal channel. This allows us to explore the effect of deviating from the straight channel case and increasing the channel amplitude has on the size of the rigid plug regions, which is the essential region of the foam in displacing blood.

Declaration

Word Count of thesis: DECLARATION	77,716
This work has not previously been accepted in substance for any degree and is not being concurrently submitted in candidature for any degree.	
Candidate name	Tirion Gruffudd Roberts
Signature:	
Date	06 November 2020

STATEMENT 1

This thesis is the result of my own investigations, except where otherwise stated. Where ***correction services** have been used, the extent and nature of the correction is clearly marked in a footnote(s).

Other sources are acknowledged by footnotes giving explicit references. A bibliography is appended.

Signature:	
Date	06 November 2020

[*this refers to the extent to which the text has been corrected by others]

STATEMENT 2

I hereby give consent for my thesis, if accepted, to be available for photocopying and for inter-library loan, and for the title and summary to be made available to outside organisations.

Signature:	
Date	06 November 2020

Acknowledgements

I would like to start off by thanking my supervisor, Prof. Simon Cox, for all his guidance, time and effort throughout my PhD. I will be eternally thankful for the encouragement and faith that I received from him, particularly towards the end of my research, reading through several drafts of my thesis during the summer months. His diligence and connections allowed him to secure my PhD funding from BTG, which allowed me to spend three wonderful years at Aberystwyth.

I would also like to acknowledge the support of Dr. Tudur Davies, my second supervisor and my supervisor for the postgraduate teaching course at Aberystwyth. He was always available to commit time to help me with my teaching and research.

None of this research would of been possible had it not been for BTG and their financial support for my PhD stipend. I had the opportunity to collaborate with both Dr. Andrew Lewis and Dr. Stephen Jones, who they kindly took their time to review my research papers and to comment on our results. Chapter 6 summarises the results of the paper [Roberts et al., 2020], which was a completed in collaboration with both Andrew and Stephen. I would extend a special mention to my office mate Alex, who was always available to help me out with anything and for his friendship throughout my time at the University.

Lastly, I would like to thank for all the support and patience from Miriam throughout my three years at Aberystwyth, in particular the writing up period. I could not have been able to complete my PhD and education without the continued support from my close knit family. My parents, Richard and Sioned, my siblings, Grisial, Begw and Brython (all of which have studied at Aberystwyth) and my Grandfather, Brian. I was extremely close to my grandfather and wish to dedicate my work to him in particular. Their unconditional faith and support has had a great influence on the man I have become.

Contents

List of Figures

1 Introduction

The work presented in this thesis aims to investigate the effectiveness of foam in varicose vein sclerotherapy. Foam sclerotherapy is a minimally-invasive treatment for varicose veins and consists of the injection of a surfactant-laden foam into the affected vein. The foam front displaces the stationary (or slow moving) blood within the vein and delivers surfactant to the vein walls. We consider the flow of foam through vein-like geometries to investigate the effect of vein geometry and foam properties on the effectiveness of foam in sclerotherapy.

A detailed discussion of the treatment, as well as alternative non-foam based treatments for varicose veins occurs in chap. 1.3. Before going into the details of the existing available treatments for these dysfunctional veins, a greater knowledge of veins is beneficial (chap. 1.1), as well as knowledge concerning the formation of varicose veins, outlined in chap. 1.2.

The well-known concepts of foam structure and the rheology of foams as well as the applications of foams are discussed in chap. 1.4. The properties of foam are complex and comply with mathematical laws (chaps. 1.4.1 and 1.4.2), such as the Laplace-Young and Plateau's laws. Liquid and solid foams have many useful characteristics and appear in many real-life applications (chap. 1.4.3). It is in many applications a cost effective method of displacing fluids (such as blood [Carugo et al., 2016; Nastasa et al., 2015]) or collecting material (such as oil [Farajzadeh et al., 2012; Li et al., 2010]) in both industrial and medical applications, as it is formed of over 80% gas in some instances.

Depending on the liquid fraction of the foam ϕ_l (chap. 1.4.1.2), there may exist a yield stress τ_0 (chap. 1.4.2.3), that depends on the foams properties such as bubble size R, liquid fraction ϕ_l and surface tension γ (chap. 1.4.2.3). Providing that the yield-stress is non-zero, it allows us to characterise the foam as a yield-stress fluid (chap. 2.1.4). Yield-stress fluids are a category of non-Newtonian fluids, characterised by having a yield-stress [Frigaard, 2019] and are fluids that don't comply to the same mathematical laws as Newtonian fluids.

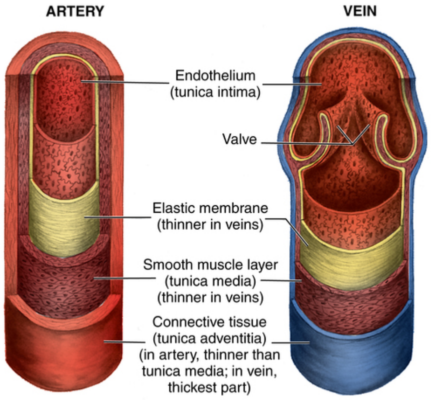

Figure 1.1: A diagram showing the different components of the arterial walls for both the arteries and veins (credit basicmedicalkey.com).

Channel flows of yield-stress fluids have regions at small strain rates moving as a rigid solid material at constant speed towards the channel centerline, while regions experiencing larger stresses (and strains) closer to the channel walls flow like Newtonian fluids. Individual bubbles in contact at the wall become stationary (or move at a smaller velocity), which breaks up the plug structure of the foam near the walls allowing bubbles to freely pass each other. Bubbles can either stick to the wall of the channel and become stationary i.e. no-slip boundary condition or slip along the walls i.e. Navier [1823] slip condition.

1.1 Veins

Veins are blood vessels that return blood from all the organs in the body toward the heart. When organs use oxygen from the blood to perform their functions, they release the used blood containing waste products (such as carbon dioxide) into the veins. The deoxygenated blood is then transported to the heart through the veins and returned to the lungs, where the waste carbon dioxide is released and more oxygen is loaded by the blood and taken back to the rest of the body by the arteries [Vlachopoulos et al., 2011].

Veins also have the additional purpose of storing blood, keeping it inactive, when only a proportion of blood is used in circulation i.e. when the body is at rest and the stored blood enters circulation once additional oxygen is required. The veins can do this because of the elasticity of their walls, allowing the vein to expand in order to facilitate the storage of additional blood [Vlachopoulos et al., 2011]. The elasticity of the vein wall (or the endothelial layer of cells) has been modelled extensively in numerical simulations [Deng et al., 2012; Pontrelli et al., 2011; Sumetc, 2017] when considering flow of blood through veins. The different layers that form the vein (and arterial) walls are shown in fig. 1.1:

- **Tunica adventitia** - It is the tough outer layer of the vein, which contains collagen and acts as a supportive element for the vein [Gray, 1918]. As indicated in the figure, this layer relatively thin for arteries and is the thickest layer for veins.
- **Tunica media** - By its name, it is the middle layer of the vein or artery and is comprised of smooth muscle cells and elastic tissues [Gray, 1918], which gives the vein its elasticity.
- **Tuncia intima** - Made up of multiple layers, the tuncima intima consists of a layer of endothelial cells and a supporting elastic membrane. The size of these layers differ depending on the type of blood vessel [Gray, 1918].

For the purpose of our investigation into sclerotherapy, most relevant is the "Tuncia intima", in particular, the inner layer of endothelial cells, which is the only layer which is in contact with the foam.

Veins also have a series of one way valves, which consist of two flap-like structures (see fig. 1.1) made of elastic tissue [Caggiati, 2013], positioned within the endothelial lining. These valves are positioned approximately an inch (roughly 2.5cm) apart [Moore et al., 2011], while arteries have none. The role of the valves is to prevent the backward flow of blood away from the heart [Gottlob et al., 1986; Zervides et al., 2008]. Unlike veins, arteries have no valves as the pressure within them is much higher than the pressure within a vein thus preventing the backward motion of blood. The pressure within healthy veins is usually less than 15 mmHg, whereas in healthy arteries, the pressure can be between $70 - 110$ mmHg [Klabunde, 2013]. See [Gottlob et al., 1986] for further information. For simplicity, we acknowledge their primary function of providing one way flow towards the heart and only consider lengths of vein between the valves.

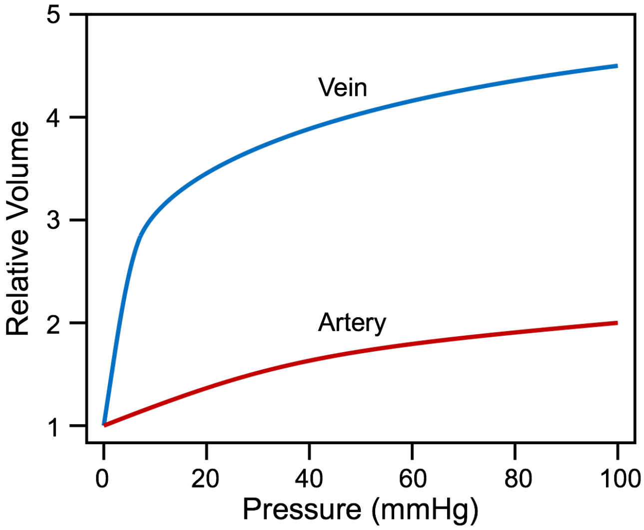

Figure 1.2: The relationship between the relative volume of the vein and the pressure [Klabunde, 2013].

The vein walls can expand and contract passively, depending on the pressure within the vein, due to the elasticity of the tuncia media. Figure 1.2, taken from Klabunde [2013], shows mean experimental values for the relative volume of a vein for a range of pressures, where the relative volume is defined by the volume of the vein (or artery) divided by the volume for the case where the pressure is zero. The vein (and artery) volumes are determined by the respective vein/artery diameter and lengths. Superficial veins, which are the most common veins that become varicose, have a typical diameter of $2.3 - 4.4$mm [Spivack et al., 2012], where arteries can have a diameter from anything in the range of 1mm to $2 - 3$cm [BostonScientific.com, 2020a], depending on their location in the human body. We see that the relative volume of veins increases much more than arteries, where a sharp increase in relative volume is achieved by increasing pressure from 0 to 5 mmHg. The walls of the vein allow a greater relative expansion due to the elastic properties of the walls [Molnár et al., 2010] compared to arteries. In the process of developing to a varicose veins (chap. 1.2), the vein walls lose their elasticity as they become stretched [Clarke et al., 1989; Vvali and Ra, 2002], allowing us to neglect any elastic wall effects in this thesis.

There is a great amount of literature discussing experimental work on blood flow through arteries and veins. Pelc et al. [1992] quantified measurements of the flow of blood through arteries and veins using MR imaging. Walsh et al. [1987] considered the obstruction of valves in saphenous veins on the mean flow. Gabe et al. [1969] and Wexler et al. [1968] focused on tracing the velocity of blood through a human body in veins, measuring the velocities using a catheter tip velocity probe. Huo and Kassab [2006] produced experimental data using pumps to produce an estimated pulsatile flow of blood through an arterial tree, concentrating on the value of pressures and mean flow rates within the tubes. Baker and Wayland [1974] consider experimental measurements of the velocity profiles of blood in microvessels, showing a parabolic velocity profile implying that the yield-stress is small.

There have been many efforts to simulate flow in arteries, such as the work of Taylor et al. [1998], who validated the accuracy of their finite element model using experimental flow data. Johnston et al. [2004] used finite volume method (which is a method for solving partial differential equations like the Navier-Stokes equations in the form of algebraic equations [Sharifahmadian, 2015]) produce steady state simulations of non-Newtonian blood flow in arteries, tracing the effects/relationship between arterial curvature and the wall shear stress within tortuous channel geometries. Ku [1997] modelled blood flow in arteries, noting that the results suggest that diseased arteries can create “turbulent and choked-flow conditions in which tubes can collapse”. There is also interest in modelling blood flow within veins, such as Petkova et al. [2003], who examined a model of a vein in 3D with and without obstructions, suggesting that blockages in veins lead to regions of small velocity and large pressures, which can lead to further shrinking of the vein and eventually a stoppage in circulation (i.e. leading to varicose veins). Hajati et al. [2020] considered the interaction of blood with vein valves using a (Galerkin) finite element method, as well as a Doppler ultrasound image to design the computational geometry. The results suggest that the bloods velocity increases while it passes the valve and vortices are formed in trapped regions behind the valve, which are conclusions supported by Noda et al. [2006].

For the purpose of modelling, blood is considered as either a Newtonian fluid or a yield-stress fluid with a small yield stress [Merrill et al., 1969; Picart et al., 1998; Thurston, 1972] (with the yield-stress τ_0 measured by a Couette viscometer). The flow of blood through either veins or arteries can be modelled a number of different non-Newtonian viscosity models such as the Bingham [Bingham, 1922], Herschel-Bulkley model [Herschel and Bulkley, 1926] and the Casson model [Casson, 1959], all discussed in chap. 2.1.4. Several authors [Johnston et al., 2004; Quanyu et al., 2017; Stoltz and Lucius, 1981] prefer the Bird-Carreau model [Bird and Carreau, 1968] as an accurate representation of blood. The Bird-Carreau model suggests that blood behaves as a Newtonian fluid at low and high shear rates and a power law fluid at intermediate shear rates.

1.2 Veins becoming varicose

The first mention of varicose veins in history was circa 1550 BCE, from the papyrus of Ebers, according to van den Bremer and Moll [2010]. The veins are described as "tortuous, solid with many knots, as if blown up by air" and the text advised against surgery. In the 21st century, varicose veins are well-known and are commonly treated, either by surgery or a minimally invasive treatment using laser or foam, to prevent further medical complications. Here, we discuss the process of a healthy vein developing into a varicose vein.

Veins become varicose when the valves within the vein become less effective over a period of time or if the body is under additional strains, allowing blood to seep backwards. Once these valves become warped or damaged over time, it prevents them from closing effectively, restricting a healthy flow of blood through the vein and leading to the pooling of blood. Over time, the dysfunctional valves reduce the flow rate of blood, which increases the pressure inside the vein, causing it to expand (fig. 1.2). For example, in a study by Sandri et al. [1999], the average diameter of a healthy vein located in the calf was equal to 2.2 ± 0.8mm, compared to 3.7 ± 1.0mm for varicose veins i.e. as a healthy vein becomes varicose, the average diameter of the vein increases by nearly 70%. This expansion in vein diameter causes the vein walls to lose their elasticity [Clarke et al., 1989; Vvali and Ra, 2002], as mentioned previously. Varicose veins usually develop from superficial veins (veins that are close to the surface of the body). These veins can be replaced by the body if damaged and they are used to carry de-oxygenated blood towards the heart as well as to cool the body by transferring heat to the surrounding environment.

Varicose veins are extremely common throughout the human population, with up to 35% of Americans being affected by varicose veins [Hager, 2020]. Galanopoulos and Lambidis [2012] suggest that 25% of women and 15% of men develop dysfunctional veins. In some families, varicose veins are more common as they can be genetically inherited [NHS, 2020]. Additional risk factors in developing varicose veins list as age, gender, being pregnant, weight and lack of movement [Lee et al., 2003]. Many who develop varicose veins do not have any physical symptoms [NHS, 2020], but for more extreme cases the individual can feel aching and throbbing, known as phlebitis, caused by inflammation of the vein and the formation of blood clots [Homans, 1928]. Other extreme cases of varicose veins can lead to deep vein thrombosis and leg ulcers [NHS, 2020], which require urgent medical attention. The majority of varicose veins appear in the legs but it is possible for them to form in most parts of the body. They can be separated into two different categories:

- **Large Varicose veins** - these veins are visible, bulging, long, dilated (greater than 2mm in diameter [Sandri et al., 1999]) and can be felt by touching. They are also more susceptible to cause pain and aching to the individual [Sampson, 2020].
- **Small spider veins** - may look like short, fine lines, “starburst” clusters, or a web-like maze. These veins typically cannot be felt by touching, and are commonly treated cosmetically due to their appearance [Bottaro et al., 2019] but are harmless [NHS, 2020].

In the following, we will consider large varicose veins as these are most likely to cause further medical complications [NHS, 2020]. We consider veins with diameter of at least 4mm. Smaller spider veins can be effectively treated with conventional sclerotherapy, injecting pure surfactant into the vein, so called “Microsclerotherapy” [Guex, 1993], due to their small diameter.

1.3 Varicose vein treatment

The aim of treating varicose veins is to destroy or remove the vein. The body will replace the vein by growing new ones in its place. In fact, there are suggestions that the body can grow new veins if a pathway is blocked, called collateral circulation [Faber et al., 2014]. There are three main treatment options available for varicose veins:

- Surgical stripping (chap. 1.3.1)
- Laser ablation (chap. 1.3.2)
- Foam sclerotherapy[1] (chap. 1.3.3)

We include some background information on on all three treatments, with a particular focus on foam sclerotherapy, the treatment at the nucleus of our research. In chap. 1.3.4, we consider the literature related to the effectiveness of all three treatment options.

1.3.1 Surgical stripping

Surgical stripping is the most well-known of the three treatments and has been developed since the start of the 20th century [Perrin, 2011]. The patient undergoes surgery in order to strip the vein from the leg. As explained by Myers [1957], the surgeon will make several small incision or cuts near the top and bottom of the affected vein. One incision will be made in the groin while the other will be made lower in the leg, as seen in fig. 1.3. Once the incisions are made, the surgeon will thread a thin flexible plastic wire into the groin incisions. The wire is then tied to the vein and both will be pulled out through the incision

---

[1] Sclerotherapy is a treatment where a practitioner injects medicine into blood vessels which causes them to shrink.

Figure 1.3: An image of the surgical stripping process, with an incision made at the groin as well as the lower leg (credit varicoseveinremovals.com).

made at the lower leg before closing the cuts.

This treatment is typically the most painful option and has a long patient recovery timescale, with the suggested recovery time being between 3-7 days [Bartholomew et al., 2005] (although Nael and Rathbun [2009] suggests that the time required for a full recovery is between two and three weeks). The method can also introduce some medical complications due to the invasive nature of the treatment [Critchley et al., 1997]; abscesses can be seen in 2.8% of patients and $2 - 15\%$ develop wound infections [Beale and Gough, 2005] after undergoing surgical stripping. The performance of surgical stripping in clinical trials is competitive with the non-invasive treatments [Nesbitt et al., 2014; Rasmussen et al., 2007, 2011], but the outdated invasive features of the treatment has disadvantages in recovery time and cosmetic outcomes [Rass et al., 2012]. The National Institute for Health and Care Excellence (NICE) recommended that both laser ablation and foam sclerotherapy should be considered before surgical stripping [Nesbitt et al., 2014].

1.3.2 Laser ablation

Laser ablation, developed in the early 21st century [Min and Khilnani, 2005], uses laser energy to burn the endothelial lining of the vein, with the first appearance of the treatment in the literature from Bone [1999] in the late 20th century. Ablation means progressive destruction of a material (a vein in this case), by a physical agent, which is the electromagnetic energy produced by a laser [Galanopoulos and Lambidis, 2012]. Laser ablation is acknowl-

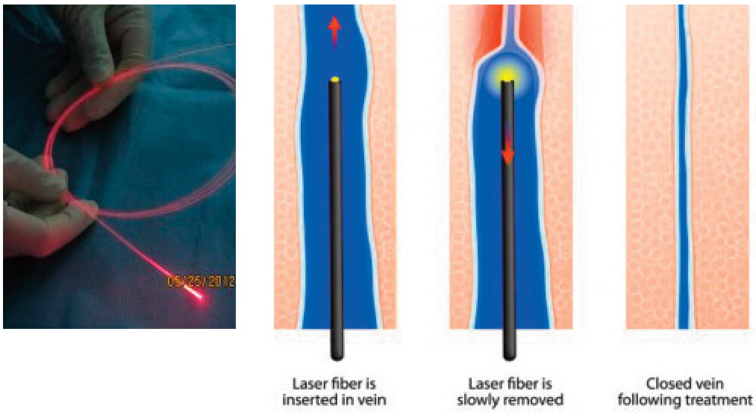

Figure 1.4: An image of the laser ablation process, split into three steps (credit indyveins.com).

edged in the field as an "*image-guided, minimally invasive treatment to burn and close the abnormal veins that lead to varicose veins*" [Radiological Society of North America (RSNA), 2020].

First of all, the area of the incision into the vein is numbed using local anaesthetic and the doctor uses ultrasound to visualize the vein and its path. Using ultrasound as a guide, the doctor inserts a catheter into the affected vein. A laser fibre, as shown in fig. 1.4, is inserted through the catheter and its tip is exposed by pulling the catheter back. Local anaesthetic is injected into the tissues around the vein to collapse the vein around the electrode and act as insulation for the heat energy produced by the laser [Almeida and Raines, 2008]. Once inserted, the laser fiber is slowly removed with the vein closing behind it, shown in fig. 1.4, collapsing due to the destruction of the vein's integral endothelial lining. In order to cause the sealing of the vein, the vein wall must absorb enough energy to generate sufficient heat to damage all vein layers. If not enough energy is absorbed, the vein could fail to collapse, and too much energy can lead to the energy dissipating the surrounding tissue, causing damage [Almeida and Raines, 2008].

Post-procedure pain is a common side effect following treatment, so cooling agents and some form of anaesthesia are used to decrease the pain [Bartholomew et al., 2005]. The recovery time for patients is usually much less than surgical stripping and similar (although slightly longer) to foam sclerotherapy (about a day, compared to $3 - 7$ days for surgical stripping). The treatment can also be undertaken using radio frequency instead of laser energy, with laser showing to be slightly more effective [Almeida and Raines, 2006]. Data collected from nearly 700 patients showed that laser ablation closed 92% of primary veins, where as only 85% of radio frequency ablations were successful. Laser ablation is an effective treatment of removing varicose veins, with the results from clinical trials suggesting that the performance of laser ablation is superior to both surgical stripping and foam sclerotherapy treatments [Rasmussen et al., 2011; Van der Velden et al., 2015].

1.3.3 Sclerotherapy

The origins of sclerotherapy can be traced back to the mid-20th century, as early as 1939 and its effectiveness has continuously improved over time [Wollmann, 2004]. Foam sclerotherapy is the process of using an aqueous foam to deliver surfactant (the sclerosant) to a varicose vein to damage vein wall endothelial cells, causing the vein to spasm, collapse and ultimately be re-absorbed into the body [Coleridge Smith, 2009]. Once collapsed, the vein becomes a fibrous cord [Rabe et al., 2004], in a process called sclerosis [Munavalli and Weiss, 2007], and is then dissolved by the body over time. The treatment is a minimally invasive process that involves an injection (usually a single injection but sometimes multiple injections are required [BostonScientific.com, 2020c]) of a surfactant-laden microfoam (a foam with average bubble size of order $R \approx 100\mu$m) into the affected vein. This treatment, like laser ablation, causes collapse of the vein by targeting the vein's endothelial lining, allowing patients to experience minimal pain and small recovery times.

Foams with a broad range of properties are used in this treatment, with various methods of production, generally using the surfactants polidocanol or sodium tetradecyl sulphate. The physician administering the treatment may control the choice of gas (which controls solubility of the foam in the bloodstream), the bubble size (and its in-sample variation, which we refer to as polydispersity) and the liquid fraction of the foam, that is the proportion of liquid sclerosant present in a given volume of foam. Prior to injection, the site of the injection is usually numbed by anaesthesia, meaning only 4% of individuals experience pain at the injection site [BostonScientific.com, 2020c].

The process of foam sclerotherapy can be split into three steps, illustrated in fig. 1.5:

- **Injection** - The microfoam is injected into the varicose vein through a syringe. The foam has a half-life (the time taken for the foam to drain to half its original solution [Pu et al., 2017]) between 80-110s [Carugo et al., 2016; Rao and Goldman, 2005], so the physician has only one or two minutes to successfully dispense the foam into the vein. For Varithena, the physician has 75s to use the foam once dispensed from the canister [BostonScientific.com, 2020c]. The foam can be guided by ultrasound during the treatment [Barrett et al., 2004; Carugo et al., 2016], allowing the physician to trace the real-time foam progress in veins.
- **Displacement** - The foam fills the vein and the foam front displaces the stagnant blood within as well as delivering the sclerocent to the vein walls, ensuring that it comes into contact with the endothelial cells.
- **Collapse** - The sclerosent destroys the endothelial lining of the vein, causing it to collapse. The vein then becomes a fibrous cord that is dissipated by the body over time. The foam is deactivated once it encounters healthy blood and the gas is absorbed into the bloodstream. The sclerosant solution within the foam is metabolised by the liver within a few hours [British Vein Institute, 2021; Eckmann, 2009]. Common side effects include bruising near the injection site or discomfort in the region of the collapsed vein.

The process is completed in under quarter an hour [Min and Navarro, 2000] and most only require a single treatment [BostonScientific.com, 2020c], although compression stockings are recommended for two weeks following injection.

Foam is used due to its effectiveness in displacing blood, in comparison to the pure sclerocent used in conventional sclerotherapy. One of the reasons that a foam is used for this

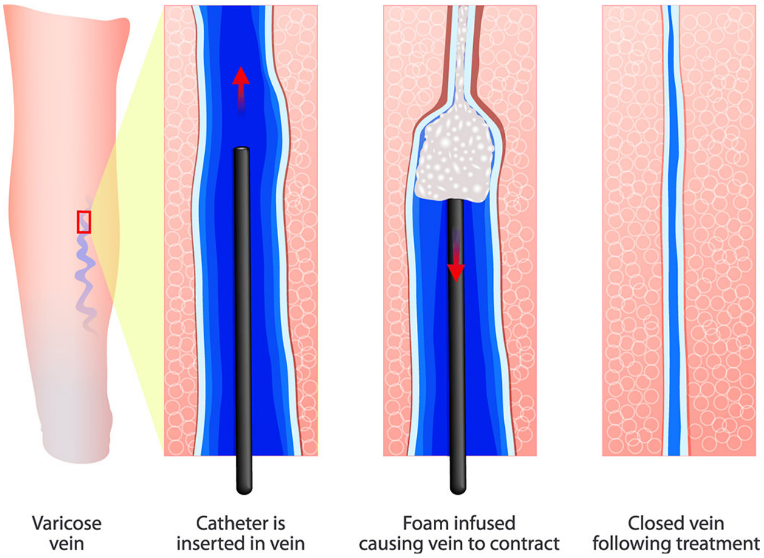

Figure 1.5: A diagram of the foam sclerotherapy treatment progress, showing each of the steps involved (credit drricardoruz.com).

process is that the bubble microstructure endows it with beneficial flow properties. In particular, assuming complete vessel filling and no gravitational effects, these properties enable it to efficiently displace the blood in the vein, rather than to mix with it, which would lead to deactivation of the sclerosant. In the language of non-Newtonian fluid dynamics, aqueous foams have a *yield stress*: when the foam is subjected to a large stress, it flows in the familiar manner of more common fluids such as water, but below a certain “yield” stress τ_0 flow is arrested, and the foam is either stationary or moves as a plug. This manifestation of the yield stress is what drives the process of sclerotherapy: the plug region in the centre of the vein displaces the blood in the vein, with little mixing between blood and foam, while to the sides the foam coats the vein wall with surfactant but due to the shearing the bubbles are moving relative to one another and so there is a greater likelihood of mixing.

The yield stress τ_0, reduces the effects of gravity override (seen in oil recovery [Rossen and Van Duijn, 2004]) and viscous fingering (criterion for stable displacements suggested by Pascal [1986]) between the foam and blood, allowing efficient displacements. The bubbles in the foam are packed closely together, and this induces an effective viscosity higher than that of the (continuous) liquid phase. The importance and characterisation of this yield stress will be discussed in chap. 6. Friction acts to slow down the foam close to the walls of the vein, and this induces a stress, which effectively liquifies the foam and allows it to flow (see figure 1.10). The stress acting on a foam within a vein varies widely, depending for example on the distance from the vein wall, and hence the size of the vein, and also the flow rate. Towards the centre of the vein, the effect of the walls is weaker, the stresses reduce, and a plug of rigid foam results.

Optimising the process of sclerotherapy requires a fairly high value of the yield stress. Too high, and the force required to push the foam out of a syringe and along a vein will be too great; too low, and the plug region will be too small, leading to excessive mixing of blood and foam close to the vein wall, which hinders effective delivery of the sclerosant.

Much of the literature on foam sclerotherapy concentrates on the properties of the foam before it enters the vein. The choice of gas affects foam stability: a foam created with carbon dioxide is much less stable than foam created with air [Beckitt et al., 2011; Peterson and Goldman, 2001], although it avoids the risks associated with introducing nitrogen into the cardiovascular system [Carugo et al., 2016]. The properties of the sclerosant influence the rate at which liquid drains from the foam (again reducing its lifetime) [Carugo et al., 2016; Wollmann, 2010], and choice of sclerosant is more significant than foam temperature and delivery rate [Bai et al., 2018]. A foam with small bubbles and a narrow bubble size distribution offered high stability and cohesion in a biomimetic vein model, with consistent performance [Carugo et al., 2015; Roberts et al., 2020].

In this study, we compare the properties of physician compounded foams (PCFs) and the commercial product Varithena® (polidocanol injectable foam 1%, also referred to as polidocanol endovenous microfoam, or PEM). PEM is generated by a proprietary device that produces consistent, pharmaceutical-grade low nitrogen ($< 0.8\%$) with O_2:CO_2 $(65 : 35)$ foam [Carugo et al., 2016], with a liquid fraction of $\phi_l \approx 0.125$. Using gases rather than room air allows the formation of more stable foam [Star et al., 2018], with a more predictable bubble size [Gibson and Kabnick, 2017]. Also as oxygen and carbon dioxide are more soluble in the blood in comparison to nitrogen, there is less chance of small bubbles of nitrogen forming, leading to gas embolisms [Bush et al., 2008] which cause strokes in extreme cases [Eckmann and Kobayashi, 2006].

PCFs on the other hand are made with room air (78% Nitrogen, 21% Oxygen etc.). Using syringes connected by a valve, the physician passes sclerosent and gas back and fourth until a foam is produced. Two examples of PCFs are the Tessari and DSS foam, produced using a three-way and two-way valve respectively usually resulting in a liquid fraction $\phi_l = 0.2 - 0.25$ [Carugo et al., 2016]. Making a foam with room air is directly associated with producing foams with larger bubbles (compared to PEM) and causes the greatest obstruction of blood flow.

For a Tessari foam, the treatment effectiveness rate reported by Frullini and Cavezzi [2002] over a three-year period was 93.3%, with minor complications in 7.1% of patients. The results suggest that sclerotherapy is an effective treatment method for varicose veins with high success and low complication rate. It also has the benefit of being a low cost treatment Rasmussen et al. [2011]. For the DSS foam, the results suggest a success rate of 84% was achieved in patients (compared to 40% in conventional sclerotherapy) [Hamel-Desnos et al., 2003]. Other authors report greater (although similar) success rates for both Tessari (94.4% [Alos et al., 2006]) and DSS foam (85% [Ouvry et al., 2008]). For PEM, only 3.4% of patients required re-treatment of the same vein after the initial treatment [BostonScientific.com, 2020b].

1.3.4 Comparison of treatments

In the last few decades, minimally-invasive treatments for varicose veins like foam sclerotherapy and laser ablation have become more popular [Thomasset et al., 2010]. Consequently there have been many comparisons of the effectiveness of the different treatments discussed in chaps. 1.3.1 (surgical stripping), 1.3.2 (laser ablation) and 1.3.3 (sclerotherapy).

Rasmussen et al. [2011] consider the data produced by a randomized clinical trial of all three treatments using 500 patients. The main result is a comparison in the failure rates between the treatments, where failure was defined as when a treated vein refluxes, or if the vein was not stripped successfully. The results show that both minimally invasive methods of foam sclerotherapy and laser ablation have smaller failure rates a month after treatment in comparison to surgical stripping, the most invasive painful method. For longer timescales (1 year), there is a growth in the failure rates in foam sclerotherapy as some of the veins recanalise after 1 year where 16.3% of patients were affected, compared to 6% and 5% for laser ablation and surgical stripping. These results suggest that the minimally-invasive treatments develop larger failure rates over long periods of time. One should note that the foam in this study was produced using the Tessari method, which contains larger bubbles and has the associated risks of using room air in comparison to PEM, discussed in more detail in chap. 6.

The conclusion above was supported by Van der Velden et al. [2015], where 5 years after treatment their data showed that absence or obliteration of the vein had occurred in a larger proportion of patients that underwent surgical stripping in comparison to laser ablation and foam sclerotherapy. The probability that patients require further treatment is similar for all three treatments, increasing to around 30% over a 5 year period, with surgical stripping providing the smallest value out of the three. Other work by Van Der Vleuten et al. [2014] suggest that the effectiveness of foam sclerotherapy is around 90% as is surgical stripping, where laser ablation is slightly more effective (93%).

For Tessari and DSS foams, the effectiveness of the foam sclerotherapy declines significantly over the length of time after treatment. This is echoed by Lawaetz et al. [2017], who noted that foam sclerotherapy doesn't have the "long term efficacy" of other treatments. This finding is also supported by Biemans et al. [2013], who found that foam sclerotherapy has a success rate (72.7%) which falls considerably below laser ablation (85.5%) and surgical stripping (88.2%).

Contrary to this, Frullini and Cavezzi [2002] suggest that the success rate for sclerosing foams is significantly higher, closer to 93.3%. In addition, Kakkos et al. [2006] suggest that only between $3 - 8\%$ of patients experience recurrence of canalisation of the vein two years after treatment. For Varithena®, only 3% of patients require re-treatment of a treated area [BostonScientific.com, 2020c; Todd III et al., 2014], implying that the success rate for PEM is high. We attribute the poor results of sclerotherapy from the data of Biemans et al. [2013] and Lawaetz et al. [2017] to the quality of the foam used during the treatment, produced using the Tessari method and room air. The PEM foam at the heart of our research is designed to be more effective than Tessari foam, as it consists of monodisperse small bubbles produced with mainly oxygen and carbon dioxide ($\approx 0.5\%$ of nitrogen). To date, there is no available literature concerning the success rate of PEM in clinical trials, but there is research supporting the superior foam properties of PEM in comparison to PCFs [Carugo et al., 2016; Star et al., 2018].

Min and Navarro [2000] reported that following the treatment of 50 patients' varicose veins using foam sclerotherapy, all of the veins treated remained closed following initial treatment and no patients needed any re-treatment after 1 year, with 100% patient satisfaction. Van der Velden et al. [2015] suggests that the performance of sclerotherapy improves for veins of smaller diameters and it is an excellent alternative for older patients, due to its minimally invasive nature.

Foam sclerotherapy takes the smallest amount of time to complete in comparison to stripping and ablation, and takes on average 19 minutes to administer, 13 less than surgical stripping, which is expected to be the most time consuming treatment [Min and Navarro, 2000]. Laser ablation had an average time of 26 minutes to administer. Nael and Rathbun [2009] suggest that the patient recovery time for foam sclerotherapy is much smaller in comparison to laser ablation and surgical stripping.

A secondary result in Min and Navarro [2000] is a measure of amount of pain that patients experience post-treatment as a function of time. Patients were asked to report a score of pain out of 10 for ten days following the treatment and the mean (and standard deviation) was considered. The results show that initially the surgical stripping was the most painful treatment, which remains true for the first three days. For days four onwards, the patients who experience most pain are the ones that underwent laser ablation, also supported by Rasmussen et al. [2007]. Foam sclerotherapy was reported to be the least painful of three treatments. Venermo et al. [2016] reported a general trend of patients experiencing less pain following foam sclerotherapy compared to laser ablation or surgical stripping, both at the time of hospital discharge and a week following surgery.

The factor of cost effectiveness also requires discussion. Rasmussen et al. [2011] suggests that the total cost of each treatment for the patient, including recovery time is around €2200 for each patient for both surgical stripping and laser ablation. The high cost for laser ablation came due to the cost of the catheter. The cheapest treatment was foam sclerotherapy, at a total of €1554 per patient, assuming that the physician produces the foam using the Tessari or DSS method. Lattimer et al. [2012] suggests that foam sclerotherapy is over three times more cost effective in comparison to laser ablation, with Marsden et al. [2015] also supporting that foam sclerotherapy is the most cost effective. It is also suggested that both foam sclerotherapy and laser ablation are cost effective alternatives to surgical stripping.

To conclude, the results from clinical trials show mixed results for the long term effectiveness of foam sclerotherapy [Min and Navarro, 2000; Rasmussen et al., 2011; Van der Velden et al., 2015; Van Der Vleuten et al., 2014], with laser ablation and surgical stripping often out performing the treatment, but in some instances it can be a highly effective treatment [Min and Navarro, 2000; Van der Velden et al., 2015; Van Der Vleuten et al., 2014]. The clinical trials used a Tessari foam (PCF) and we suggest that PEM would yield better results due to its' superior foam properties [BostonScientific.com, 2020b; Carugo et al., 2016]. Sclerotherapy is a more cost-effective [Lattimer et al., 2012] and less painful [Min and Navarro, 2000; Rasmussen et al., 2007] treatment and has the shortest recovery and treatment time for patients [Min and Navarro, 2000].

1.4 Foam

There are examples of foam which appear in everyday life, whether you are washing the dishes with a bubbly liquid, shaving using a dense thick shaving foam or even sleeping on a comfortable memory foam mattress, encounters with foam are a regular occurrence. We briefly outline the structure of foam (chap. 1.4.1), its treatment as a yield stress fluid (chap. 1.4.2) and the applications of foam (chap. 1.4.3). Although some of these topics are not essential for understanding the aims of the project, they give the reader some additional background information into foam rheology.

Foam behaves as a solid under low shear rates and like a viscous fluid under high shear rates, when the structure of the foam has been "broken". This behaviour is seen in yield stress fluids and the relationship between the stress and strain, shown in a schematic representation of bulk foam in fig. 1.6, is discussed further in chap. 1.4.2. These yield stress properties make the foam desirable in numerous applications in both industrial [Farajzadeh et al., 2012; Rossen, 1996] and medical fields [Carugo et al., 2016; Roberts et al., 2020].

One should note other possible variations to the stress-strain relationship of foam in fig. 1.6. In the Hershel-Bulkley [Herschel and Bulkley, 1926] description of systems with a yield-stress, the excess stress is resisted by " dissipative term proportional to some power of the strain rate" [Weaire et al., 2002] and one could calculate the exponent value in order to over-simplifying the relationship. Additionally, in experimental observations of shearing two-dimensional foam, bubble rearrangement is highly dependent on the experimental method [Hutzler et al., 1995; Weaire et al., 2002].

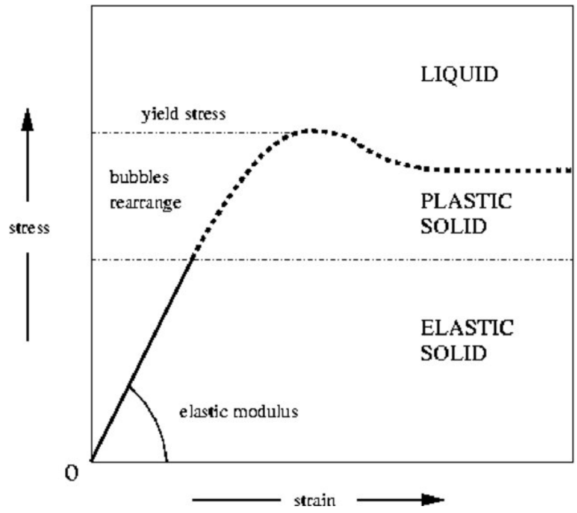

Figure 1.6: A schematic sketch of the stress-strain relationship in a foam undergoing start-up strain, which shows the variation of the yield stress and elastic modulus, taken from Drenckhan et al. [2005].

1.4.1 Foam structure

Foam can be defined as a two-phase system which consists of gas bubbles separated by thin films of liquid [Weaire and Hutzler, 2001]. The shape of the liquid films are determined by the Laplace-Young law (chap. 1.4.1.1), with film curvature proportional to the difference in pressure between neighbouring bubbles.

These films of liquid all join at Plateau borders, which contain most of the foams' liquid. The Plateau borders are liquid-filled channels which allow the transport of surfactant [Weaire and Hutzler, 2001; Weaire et al., 2002; Zaccagnino et al., 2018] and liquid. The Plateau borders comply with the aptly-named Plateau laws, equilibrium laws that the local foam structure complies with [Weaire and Hutzler, 2001]. The total volume of liquid that is contained in the Plateau borders compared to the total foam volume is defined as the liquid fraction of the foam ϕ_l (chap. 1.4.1.2). The value of the liquid fraction ϕ_l is important in determining the value of the yield-stress τ_0 of the foam (chap. 1.4.2.3).

1.4.1.1 Laplace-Young law

The Laplace-Young law governs the shape of the liquid films that separate the bubbles, determined by the respective bubble pressures p and surface tension γ. The difference in pressure between the bubbles across the interface, is balanced by the surface tension along the film multiplied by the mean local curvature of the film. This is the Laplace-Young law. It was formulated by Thomas Young and Pierre-Simon Laplace in the early 19th century. The (nonlinear) partial differential equation associates the difference in (capillary) pressure across the interface of two fluids to the surface tension and curvature [Weaire and Hutzler, 2001].

The pressure within each bubbles can depend on the properties of the gas contained within. The smaller the bubble the larger the pressure. Surface tension pushes in on the bubble, and the smaller the bubble, the higher the air pressure inside the bubble must be to keep it from collapsing [Wofsey, 2007]. Over time, there is a transfer of gas between interfaces from small bubbles to large bubbles caused by the difference in pressures across the bubble interface. This sets the foams' half life.

1.4.1.2 Liquid fraction

The liquid fraction of a foam ϕ_l, is the volume of liquid in the foam divided by the total volume of the foam. The gas fraction of the foam, is equal to $\phi_g = 1 - \phi_l$. The influence of the value of ϕ_l on the structure of the foam can be seen in fig. 1.7. For small liquid fraction $\phi_l \to 0$ (i.e. the dry limit [Weaire and Hutzler, 2001]) or in practice, if ϕ_l much less than 0.01 [Weaire et al., 2005], there is a tight packing of bubbles, which require large shear stresses to deform the structure of the foam. In this dry limit, the cross section of a Plateau border is a concave triangle with curvature $1/r$ [Cohen-Addad et al., 2013].

By increasing the liquid fraction, we see regions of liquid within the Plateau borders between bubbles. The critical liquid fraction of the foam, denoted by ϕ_c, is equal to 0.36

and is derived from random close packing of spheres in three dimensions, where spheres fill 64% of the space [Jaeger and Nagel, 1992]. For random close packing of 0.64, all spheres are in contact with neighbouring spheres meaning that the maximum volume taken by the spheres is around 64% of the total volume. Relating this to foam would mean that the critical gas fraction of the foam ϕ_g is equal to 0.64. At $\phi_l = 0.36$, the foam is at the wet limit, (or the jamming transition according to fig. 1.7), this is a fraction where the bubbles start to come apart, lose contact with each other and bubbles are allowed to move freely [Langevin, 2017]. Any foam with a liquid fraction greater than ϕ_c, is called a bubbly liquid (or liquid when $\phi_l = 1$). Throughout this thesis, we will be discussing foams with a liquid fraction which is less than ϕ_c, where the neighbouring bubbles are in contact with each other.

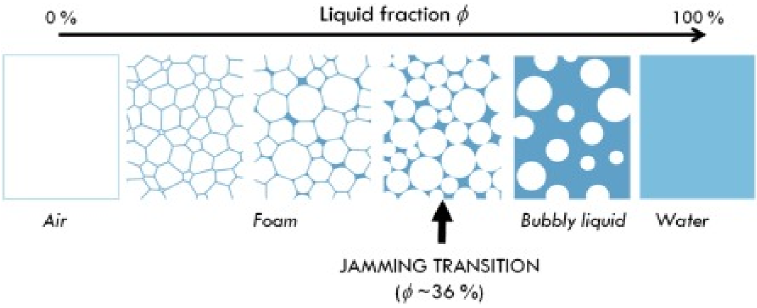

Figure 1.7: A diagram showing the different aspects of foam with varying liquid fraction (credit [Langevin, 2017]).

1.4.2 Foam rheology

Interest in foam rheology has been increasing over the last few decades [Cox et al., 2004; Kraynik and Hansen, 1987; Weaire and Hutzler, 2001], due to foams' use in applications and its association with many industrial and geophysical phenomena, outlined in chap. 1.4.3. The term *Rheology* is defined as the study of flowing matter and deformation of non-Newtonian and viscoplastic fluid, which are families of fluids that foam are related to due to the plastic behaviour of foam at low shear rates (fig. 1.6).

Under low applied stresses, foam will behave as a solid, such as a shaving foam adheres to a shavers face as the gravitational force is too weak to cause it to flow [Weaire and Hutzler, 2001]. For larger applied stress, greater in magnitude than the yield stress τ_0, the foam flows and behaves as a liquid. In this regime of large stress, past the elastic limit (fig. 1.6) leads to T1 events occurring, where bubbles switch neighbours. A foams yield stress is defined and discussed in chap. 1.4.2.3 and has a quadratic dependence on the value of liquid fraction as suggested by fig. 1.8.

1.4.2.1 Drainage

Drainage is the study of the flow of liquid through foam. It is an important factor for foam stability and is of great interest to the detergent industry [Hutzler et al., 2005]. The liquid within a foam is able to flow which can consequently lead to differences in the local liquid fraction, in response to the local capillary pressure [Weaire et al., 2002]. This suggests that drainage leads to local differences in yield stress within the foam, meaning that the yield stress is particularly hard to determine experimentally as the foam evolves with time [Gardiner et al., 1998]. Avoiding these complications has been the focus of experimental work on concentrated emulsions [Princen and Kiss, 1986; Yoshimura et al., 1987]. In addition to the local liquid fraction, foam drainage plays an important role in the foam stability. When the foam dries, its structure becomes more fragile leading to thinner films and they can break, causing the foam to collapse [Kruglyakov et al., 2008].

The assumptions made in this thesis is that the vein diameter is small (allowing us to neglect gravitational flow of fluid through films [Kraynik, 1983]) and the viscosity of the scloresent is large enough to stabilize the foam and to prevent the transport of liquid [Kraynik, 1983], which allows us to neglect the effects of drainage [Verbist et al., 1996] and the differences in local liquid fraction. For a Poiseuille flow of foam, a criterion for neglecting drainage was constructed by Kraynik [1983], suggesting that the phenomenon is neglected providing that the sclerocent viscosity μ_s is greater than $5\phi_l^{1/2}R$, where R denotes the average bubble radius of the foam. Assuming that this is the case, this allows us to treat a foam as having a fixed liquid fraction ϕ_l, everywhere.

1.4.2.2 Shear modulus

The shear modulus of the foam (or modulus of rigidity), denoted by G_0 and measured in Pa, describes a material's elastic response to shear stress [Barnes et al., 1989] at low strains ε. For a pressure driven yield-stress fluid in a straight channel, the shear modulus takes the form [Cox and Whittick, 2006]:

$$G_0 = \left. \frac{\partial \tau_{xy}}{\partial \varepsilon} \right|_{\varepsilon=0} \tag{1.1}$$

A large value of the shear modulus indicates high rigidity such that it takes a large amount of stress to be applied in order to deform the foam. Princen and Kiss [1986] suggest an empirical approximation for the (static) shear modulus of a foam with surface tension γ, liquid fraction ϕ_l and average bubble radius R is

$$G_0 \approx 1.8 \frac{\gamma}{R} \left(\phi_c - \phi_l\right) \left(1 - \phi_l\right)^{1/3}. \tag{1.2}$$

If the foam has a larger average bubble radius, the shear modulus decreases and the foam gets softer [Cohen-Addad et al., 1998]. From fig. 1.8, for a fixed surface tension γ and avg. bubble size R, we see the relationship between the liquid fraction of the foam and the shear modulus; for small ϕ_l it is large (as is τ_0) and for larger ϕ_l, G_0 becomes smaller as $\phi_l \to \phi_c$.

1.4.2.3 Yield stress

A yield stress, sometimes called a yield point in engineering applications, is a scalar representation of the stress tensor at the yielding point [Thompson et al., 2018], i.e. the stress required for the material to deform and flow. Foam can be characterized as a yield stress fluid due to the plastic effects caused by topological rearrangements, labelled as T1 transformations [Weaire and Hutzler, 2001] and is only one example of a yield-stress fluid found in every day life. One could encounter yield stress fluids in food such as syrup and chocolate. Examples from nature include magma [McBirney and Murase, 1984] and mud [Hemphill

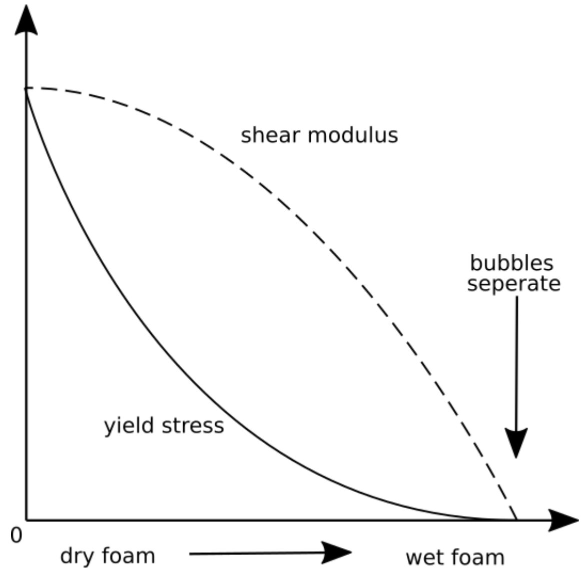

Figure 1.8: A sketch of the relationship between the shear modulus (as well as yield stress) and a (bulk) foam's liquid fraction in the two-dimensional case.

et al., 1993].

Much like the shear modulus G_0, the yield stress τ_0 of a foam can be empirically estimated in terms of the surface tension γ, average bubble radius R and liquid fraction ϕ_l, although Rouyer et al. [2005] suggested that this is a very rough approximation.

Providing $\phi_l \leq \phi_c$, we can empirically estimate a value for the yield stress of a foam, which is positive (fig. 1.8). In dry foam (small ϕ_l), the bubbles within the foam cannot move freely and are in contact with neighbouring bubbles. The structure of the foam remains rigid unless a large enough shear stress is exerted on the foam in order to deform the foam structure [Dlugogorski et al., 2002]. In this limit, the yield stress is at its largest [Roberts et al., 2020].

Increasing the liquid fraction ϕ_l of the foam causes the bubbles to move apart and decreases the value of τ_0 significantly by allowing the bubbles to have room to manoeuvrer, decreasing the rigidity of the foam. At $\phi_c \approx 0.36$, they are no longer deformed by any contact with their neighbours and are therefore spherical, indicating that the yield stress is zero. Above this value, the foam is effectively a bubbly liquid, or a dilute suspension of bubbles, with zero yield stress. Wet foams, with a liquid fraction close to the critical value ϕ_c ($\phi_l \approx 0.2 - 0.25$ is typical of physician-compounded foams, or PCFs [Star et al., 2018]) and will have a small yield stress and are likely to be inefficient in sclerotherapy.

The yield stress should therefore be described by some function $\tau_0(\phi_l)$ that is positive for $\phi_l < \phi_c$ and reaches zero at $\phi_l = \phi_c$. For vanishingly-small liquid fractions ("dry" foams), the yield stress is highest, recognising the difficulty of deforming a foam consisting of a tight packing of polyhedral bubbles. The consensus points now to a dependence of the form [Mason et al., 1996; Saint-Jalmes and Durian, 1999]:

$$\tau_0 \sim (\phi_c - \phi_l)^2 . \tag{1.3}$$

The squared dependence on the liquid fraction means that small differences in liquid fraction may have a disproportionately large effect, as we will illustrate in figures 1.8 and 6.3.

Bubble size also plays a role in determining the yield stress. At fixed liquid fraction, an appropriate scale for the stress in a foam is given by the Laplace pressure [Cantat et al., 2013; Cohen-Addad et al., 2013], the ratio of surface tension γ to bubble size R. That is, for a given volume of foam, there are more interfaces when the bubbles are smaller, so the yield stress will increase. Supplementing eq. (1.3) with this scale suggests

$$\tau_0 \approx 0.5\frac{\gamma}{R}(\phi_c - \phi_l)^2 , \tag{1.4}$$

where the pre-factor of 0.5 brings this expression into close agreement with experimental data on foams and compressed emulsions [Mason et al., 1996; Princen and Kiss, 1989].

In chapter 6, we will consider the affect of the choice of averaging the bubble radii on the value of the yield stress. Princen and Kiss [1986] suggest that choosing a volume weighted Sauter mean is an appropriate choice, which allows us to consider the role of polydispersity on the value of the yield stress τ_0.

The gravitational effects and transfer of gas from small to large bubbles due to Laplace pressure results in changes to the local liquid fraction within the foam over time, thus affecting the value of the yield stress [Gardiner et al., 1998]. Transient experimental techniques are used due to the time dependence of the yield stress. Some experimental investigation into foam rheology has been done on concentrated emulsions [Calvert and Nezhati, 1987; Princen and Kiss, 1986; Yoshimura et al., 1987] to try to overcome this complication of foam evolution. We consider veins of narrow geometries and that the viscosity of the sclerosent is large enough such that it allows us to neglect the effects of drainage in varicose vein treatment [Kraynik, 1983] (chap. 1.4.2.1).

1.4.3 Foam applications

Foam has many industrial, medical and every day applications. We encounter foam when washing dishes or enjoy a thick layer of dense foam on the top of a pint of Guinness, but it also has useful properties that make it useful for a large range of applications such as fire suppression and oil recovery. In this chapter, we briefly discuss several applications of foam.

1.4.3.1 Fire fighting

Foam is used for fire suppression. Coating the fire with the foam cools down the fire while also preventing the fuel to have contact with oxygen, which sustains the fire. Fire fighting foam was invented in the early 20th century by chemist and engineer Aleksandr Loran, who discovered the method of distinguishing flammable liquid fire by blanketing it with foam [Patel et al., 2014].

The desirable properties for fire fighting foam are low shear viscosity and a large yield stress [Dlugogorski et al., 2002]. Additional properties include high heat resistance and slow drainage and coarsening. To measure the yield stress of fire fighting foam, Gardiner et al. [1998] used the experimental measurements of the very dry firefighting foam to suggest an estimate for τ_0. Thus, the yield stress of the firefighting foam can be empirically estimated as a function of liquid fraction ϕ_l (albeit, for only very dry foam ($\phi_l \leq 0.015$)), average bubble size R and surface tension γ [Gardiner et al., 1998]:

$$\tau_0 = 0.0036\frac{\gamma}{R}\left[\frac{(1-\phi_l)^{1/3}}{\left(1-0.99999\,(1-\phi_l)^{1/4}\right)} - 1.1125\right]. \tag{1.5}$$

Here the average bubble size R is the sum of the bubble radii divided by the number of bubbles. As the liquid fraction is much smaller in this case, the expressions for the yield stress τ_0 suggested by both Princen and Kiss [1989] in eq. (1.4) and Gardiner et al. [1998] in eq. (1.5) are not comparable. The direct investigation of Gardiner et al. [1998] was on aqueous foam ($\phi_l \leq 0.05$), with the majority of foam samples between $\phi_l = 0.005$ and 0.015. Both the surface tension and average bubble radius were larger ($\gamma = 20 \times 10^{-3} M/m$, $R = 135 - 700 \mu m$) than for the values used by Princen and Kiss [1989] ($\gamma = 6.4 \times 10^{-3} N/m$, $R = 8.75 \mu m$). The estimates of the yield-stresses from eq. (1.5) fall below the estimates of others (for the yield stress of concentrated emulsions [Khan et al., 1988; Princen and Kiss, 1989; Yoshimura et al., 1987]), suggesting that eq. (1.5) slightly underestimates the true value of τ_0.

The yield-stress of the firefighting foam is an investigated parameter as it determines how quickly the foam flows away from the point of application on a horizontal surface of burning liquid or fuel [Gardiner et al., 1998], with a larger yield-stress yielding a slower flow away from the application point.

1.4.3.2 Food and Drink

Foam can be seen in many types of food and drink. These examples can range from the pockets of air that appear in bread to a very dense head of nitrogen foam sitting on the top of a pint of Guinness. The quality of the foam on a pint of beer or Guinness is determined by its stability, adherence to glass and texture [Evans and Sheehan, 2002]. Food foams, emulsions, and suspensions are a sizeable part of the foods and beverages produced and sold on the market today [Green et al., 2013].

Other than foam, spreadable food such as butter and margarine are viscoplastic and have a yield stress. The fluid mechanics of such materials suggested that there exists a correlation between the spreadability of the material (i.e. how easy it is to spread) and the shear stress on a knives surface [Kokini and Dickie, 1982]. Daubert et al. [1998] suggested that the spreadability Sp of a material is inversely proportional to the yield stress τ_0:

$$Sp \approx \frac{1}{\tau_0}$$

i.e. increasing the yield-stress decreases spreadability. In addition to this, there is an agreement in the literature that the yield-stress is a better measure of spreadability of a viscoplastic material than the apparent viscosity [Ak and Gunasekaran, 2000; Sun and Gunasekaran, 2009]. This shows that identifying the yield stress of viscoplastic material such as butter would be beneficial for the producers.

1.4.3.3 Enhanced Oil recovery

A common practice in the petroleum industry is to inject water or gases underground in order to recover as much oil as possible. Common gases which are used are Carbon dioxide, Nitrogen, air and Hydrocarbon. But injecting water, for example, into the geological formation will only recover around half of the oil, dispersed as droplets in the pores of the rock. The residual oil can be collected by adding appropriate chemicals which alter the interfacial tension forces between the oil and fluid [Weaire and Hutzler, 2001].

Foam is also used in industrial application of recovering oil and has the advantage of being a cost effective alternative of delivering the chemicals to the residual droplets in the pores. By pumping foam into porous rocks, it is desirable to attain a good understanding of foam flow through such materials and therefore useful to know some of the basics of foam rheology (chap. 1.4.1).

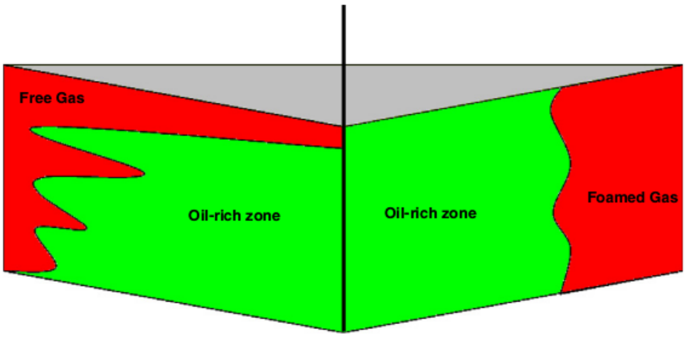

Figure 1.9: An illustration of a comparison between gas flooding (left) and foam flooding (right) in oil recovery, from Farajzadeh et al. [2012].

Viscous fingering, which is an instability on the interface of the two fluids, occurs between both gas and oil due to the difference in viscosity, thus reducing the recovery of oil [Farajzadeh et al., 2012]. The gases used are much less dense and viscous than the oil causing the gas to finger through the oil to the surface of the reservoir. The use of foam dampens the effect of the viscous fingering, allowing for a more efficient recovery of oil [Rossen, 1996], as seen in fig. 1.9. Gravity override, in which a less dense fluid flows over the top of a more dense fluid, hampers the collection of oil [Faisal et al., 2009]. Like in sclerotherapy, foam is used to reduce the effects of this phenomenon and to result in a more effective displacement of oil [Hussain et al., 2017].

1.4.4 Modelling sclerotherapy

In order to model the scelotherapy process, we simplify the problem by making several assumptions. The effects of gravity can be neglected in a closed vascular system, particularly in narrow veins [Badeer, 2001]. Therefore in this study, we neglect the effects of gravitational forces within the vein and the elasticity of the vein walls, which would allow the walls to expand and contract in response to the flow rate of foam. The problem reduces to a displacement of blood, which can be modelled as either a Newtonian fluid or a yield-stress fluid with a small τ_0 [Merrill et al., 1969; Picart et al., 1998; Thurston, 1972], by a sclorecent-laden foam, characterised as a yield-stress fluid as illustrated in fig. 1.10.

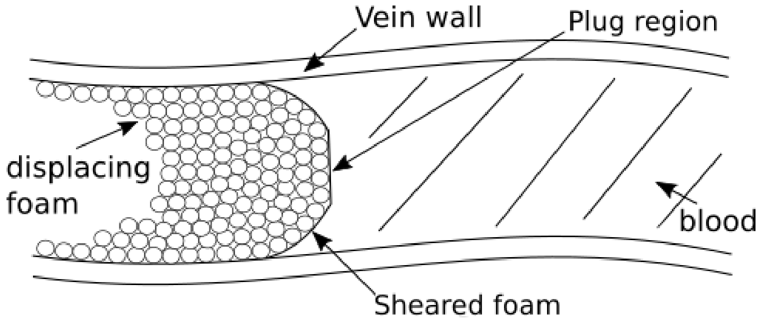

Figure 1.10: The goal of the process of sclerotherapy is to entirely displace blood from a vein and then collapse the vein permanently. The shape of the front where the foam meets the blood is important in determining the degree of mixing and hence the efficacy of the process.

From the related research of the displacement of Newtonian fluid (i.e. blood) by yield-stress fluid (foam), we obtain relatively flat and stable interfaces when the apparent viscosity of the yield-stress fluid is much larger than the viscosity of the Newtonian fluid [Bakhtiyarov and Siginer, 1996; Obernauer et al., 2000], allowing for an "efficient sweep" [Wu et al., 1991] of fluid. The efficiency of the sweep of blood is independent of the flow rate providing the interface is stable [Yortsos et al., 1986]. The efficiency of the displacement of blood increases as the apparent viscosity of the non-Newtonian fluid increases [Wu, 1990]. Throughout this thesis, we assume that the apparent viscosity of the foam (see [Khan et al., 1988; Nastasa et al., 2015]) is much larger than the blood viscosity (around 3mPa s [Rosenson et al., 1996]), neglecting any possibility of instability at the fluid-fluid interface. Martinsson and Sichen [2016] suggests that the apparent viscosity of the foam is at least 5 times the viscosity of the origin fluid. This allows us to simplify the problem and consider flows of a single foam and conclude that the efficiency of the displacement is determined by the size of the rigid plug region of highly viscous material. We label efficient displacement of blood by foam as the "piston effect" in chap. 6, with the rigid core plug region acting as the piston driving the blood from the vein.

In applications where the width of the bubbles are much smaller than the width of the channel, the foam can be treated as a "complex but homogeneous fluid" [Balan et al., 2011] i.e. a bulk foam. A typical width of a varicose vein is 4mm [Sandri et al., 1999], therefore approximately 20 bubbles (of average radius $100\mu m$) are positioned across the cross-sections. Both Debrégeas et al. [2001] and Dollet et al. [2005] used continuum models for yield-stress fluids to compare against experimental results of foam with approx 20-25 bubbles positioned along a cross-section, thus in this thesis we find it appropriate to simulate the foam used within sclerotherapy as a continuous yield-stress fluid. As the foam exhibits non-Newtonian responses to strain [Yue et al., 2015], we can use the continuum model for yield-stress fluids in order to derive approximations of foam flow fronts through vein-like geometries. We focus on flows of a single yield-stress fluid through various vein-like geometries, quantifying the size of the plug area relative to the area of the vein, as a measure of displacement effectiveness.

We have introduced background information concerning varicose veins and their possible treatments, as well as foam rheology in this chapter. We move on to explain the continuum models and numerical methods behind modelling foam as a yield-stress fluid in chapter 2, characterising the foam as a Bingham fluid. These numerical methods are used to produce the data shown in latter chapters. Chapter 3 considers the flow of foam through straight veins, the simplest geometry considered in this thesis. The work here allows us to predict what the most effective foam for sclerotherapy through straight veins. The aim of chapter 4 is to consider the flow of foam through curved veins and how vein curvature affects the sclerotherapy process. We expect to learn the extent of the degradation of the foams plug region with increasing vein curvature, in particular the situation where a foam flows from a straight section to a curved section of a vein. In both chapters 3 and 4, we derive analytical velocity profiles of flows of Bingham in straight and curved channels, respectively. The flow of a pressure-driven Bingham fluid in a sinusoidal channel is considered in chapter 5. This chapter provides us with a prediction of foam behaviour in a more typical vein geometry. Here we consider the effect of increasing the channel amplitude on the flow of foam, in particular, to the size of the plug region for each geometry. Chapter 6 characterises the foam used in sclerotherapy and allows us to draw on conclusions from chaps. 3-5 and relate the numerical results to implications for the effectiveness of foam in sclerotherapy in vein-like geometries. We use the numerical data to predict the velocity profiles of different foams used in sclerotherapy through a straight cylindrical vein. The conclusions and aims for future work are discussed in chap. 7.

2 Continuum models and numerical methods of simulating yield-stress fluids

2.1 Introduction

From this point forward, we use an idealization of continuum mechanics under which fluids can be treated as continuous, even though, on a microscopic scale, they are composed by molecules [Batchelor, 2000] or for foam, individual bubbles. As foam also exhibits a yield stress, we consider flows of yield stress fluids through vein like geometries. In order to investigate these flows both analytically and numerically, we need to consider the governing equations for fluid flow, discussed in chaps. 2.1.1 and chap. 2.1.2.

We model a foam as a Bingham fluid [Bingham, 1922] using the continuum models for a yield-stress fluid, treating the foam as a continuum, not as a collection of bubbles. We consider the Navier slip boundary condition [Navier, 1823] on the channel walls, discussed in chap. 2.1.5. The no-slip boundary condition as a special case where the slip length is zero and the foam becomes stationary at the channel walls, which allow us to examine the effect of wall-slip on the performance of foam in sclerotherapy.

The simulation method, explained in chap. 2.2.2, uses the finite element method (FEM) to solve the governing Stokes equations, which are written in weak form[2], and combined with the "regularised" Papanastasiou viscosity model [Papanastasiou, 1987]. The regularised model smooths over singularities that occur at yield surfaces due to the vanishing strain-rate i.e. overcomes the difficulties of modelling the discontinuous behaviour of the continuum models. Other alternative simulation methods for Bingham fluids, as well as other regularised viscosity models, are also discussed to justify this choice.

The continuum models of yield-stress fluid are outlined in chap. 2.1.4. We present several

---

[2] The weak formulation turns a differential equation into an integral equation - see §2.2.2.2

continuum models of yield-stress fluids [Bingham, 1922; Casson, 1959; Herschel and Bulkley, 1926]. The simplest model, a Bingham fluid is used, to derive analytical profiles and produce finite element simulations of foam in vein-like geometries. The methods used in our finite element simulations are outlined in chap. 2.2.

2.1.1 Navier-Stokes equations

The governing Navier-Stokes equations are partial differential equations in fluid mechanics that describe the flow of incompressible fluids. The equations are credited to Claude-Louis Navier and George Gabriel Stokes, were derived during the 19th century and arise from Newton's second law. The Navier-Stokes equations can be used to model many different examples of flows, such as large scale turbulent flow of the flow of air over an airfoil, or small scale laminar flow such as the flow of blood in veins. The Navier-Stokes equations mathematically express the conservation of momentum and mass in a system [Batchelor, 2000].

The (absolute) viscosity is a measure of the fluid's resistance to deformation at a given rate (Pa s) and the density of the liquid is the mass per unit volume of the fluid (kg/m^3). The material derivative is defined as:

$$\frac{D}{Dt} = \frac{\partial}{\partial t} + (\underline{u}.\underline{\nabla})\,. \tag{2.1}$$

Throughout this thesis, we neglect any gravitational effects ($\underline{g} = \underline{0}$) in the governing equations, as in a closed vascular system the importance of gravity is "deemphasized" [Badeer, 2001], although foam sclerotherapy patients are suggested to raise their legs above hip height (more importantly, the height of the heart) post treatment so that the foam within the veins don't have to work against gravity [De Gorter, 2020].

For an incompressible fluid with density ρ, viscosity μ, pressure p and velocity $\underline{u}$, the momentum and continuity equations take the following form:

$$\rho\frac{D\underline{u}}{Dt} = -\underline{\nabla}p + \underline{\nabla}.\underline{\underline{\tau}}, \tag{2.2a}$$

$$\underline{\nabla}.\underline{u} = 0. \tag{2.2b}$$

Eqs. (2.2a) and (2.2b) represent the conservation of momentum and mass, respectively. The stress $\underline{\underline{\tau}}$, measured in Pa, is a measure of internal forces that neighbouring particles of a continuous material exert on each other. The constitutive model for the stress of a non-Newtonian fluid is discussed in detail in chap. 2.1.4, which predict the values of stress experienced by the fluid. For a Newtonian fluid, the stress model is written in terms of the strain rate $\underline{\underline{\dot{\gamma}}}$ and fluid viscosity μ and is fully defined everywhere. For the non-Newtonian case, the constitutive model for the stress takes a more complex form (seen in the constitutive equations in chaps. 2.1.4.2-2.1.4.3) due to the existence of a yield stress τ_0 in the fluid.

Due to the tensorial nature of equations (2.2a) and (2.2b), we can write out the Navier-Stokes equations in eq. (2.2) in both the Cartesian and Cylindrical polar co-ordinates, used in both chaps. 3 and 4, to solve the governing equations.

2.1.2 Stokes equations

For the purpose of this thesis, we will consider a laminar flow of fluid that is both slow (with a mean velocity around 3mm/s) and steady. These assumptions on the flow allow us to simplify the governing Navier-Stokes equations significantly. As we consider steady flow of fluid, we can neglect any dependence on time t, which means that any derivative with respect to t can be neglected (i.e. $\frac{\partial}{\partial t} = 0$ in the material derivative in eq. (2.1)).

The Reynolds number is a well-known non-dimensional number in fluid dynamics, named after Osbourne Reynolds, and is an important quantity to determine and is equal to the ratio of inertial to viscous effects. For a vein of width h, and a foam with density ρ and (apparent) viscosity μ, flowing with mean velocity U, Re is defined as:

$$Re = \frac{\rho U h}{\mu}. \tag{2.3}$$

By investigating the flow of foam through veins, the slow nature of the flow will allow us to neglect any inertial effects, as the Reynolds number will be small $Re \ll 1$. For flows that have a Reynolds number $Re \gg 1$, inertial effects are dominant over viscous effects and are turbulent, fast or large scale flows such as flow of air over an airplane wing or studying the current flow in oceans. For the purpose of this thesis, we will investigate flows with only a small Reynolds number, which indicate viscous dominant flows.

We non-dimensionalise the Navier-Stokes equations (eqs. (2.2)) relative to the channel width h and velocity scale U. The velocity scale can be written in terms of the pressure-gradient which drives the flow $U = Gh^2/\mu$.

$$\underline{u}^* = \frac{u\mu}{Gh^2}, \quad \underline{x}^* = \frac{x}{h}, \quad \underline{\nabla}^* = h\underline{\nabla}, \quad \underline{\underline{\tau}}^* = \frac{\underline{\underline{\tau}}}{Gh}, \quad t^* = \frac{t\mu}{Gh}. \tag{2.4}$$

Applying the non-dimensionalisation quantities in eq. (2.4) to the Navier-Stokes equations, shown in eqs. (2.2), gives the Navier-Stokes equations (and the continuity equation) in their non-dimensional form:

$$Re\frac{D\underline{u}^*}{Dt^*} = -\underline{\nabla}^* p^* + \underline{\nabla}^*.\underline{\underline{\tau}}^*, \tag{2.5a}$$

$$\underline{\nabla}^*.\underline{u}^* = 0. \tag{2.5b}$$

By assuming that the value of the Reynolds number is small ($Re \ll 1$) and a steady flow of fluid ($\frac{\partial}{\partial t} \to 0$), the inertial term on the left hand side is neglected, which gives us the Stokes equations:

$$0 = -\underline{\nabla}^* p^* + \underline{\nabla}^*.\underline{\underline{\tau}}^*, \tag{2.6a}$$

$$\underline{\nabla}^*.\underline{u}^* = 0. \tag{2.6b}$$

From this point onwards in this chapter, the asterisks denoting non-dimensional terms will now be dropped.

2.1.3 Newtonian fluid

Before we consider non-Newtonian fluids, it is important to consider the case for flows of Newtonian fluids, which have the simplest mathematical model that account for viscosity and the analytical and numerical results provide essential benchmarks for numerical simulations of non-Newtonian fluids with vanishing yield-stress ($\tau_0 \to 0$). The analytical velocity profiles are derived for pressure-driven Newtonian fluids through straight and curved channels by setting $\tau_0 = 0$.

Many fluids and gases which exist in every day life such as water, air, oil are examples of Newtonian fluids. Newton's law of viscosity, which was derived from the observations made by Isaac Newton in the late 17th century, states that "*the shear stress between adjacent fluid layers is proportional to the negative value of the velocity gradient between the two layers*" [Newton, 1728]. In other words, that the shear rate $\underline{\underline{\dot{\gamma}}}$ is directly proportional to the shear stress $\underline{\underline{\tau}}$ and the viscosity μ has no shear rate dependence:

$$\underline{\underline{\tau}} = \mu \underline{\underline{\dot{\gamma}}} \tag{2.7}$$

where $\underline{\underline{\dot{\gamma}}}$ can be written in terms of the gradient of velocity $\underline{u}$:

$$\underline{\underline{\dot{\gamma}}} = \left(\underline{\nabla}\ \underline{u} + (\underline{\nabla}\ \underline{u})^T \right). \tag{2.8}$$

These viscous stresses experienced by the flowing material are linearly proportional to the local strain-rate, i.e the rate of change of fluid deformation. In other words, a fluid or gas molecule will experience forces from surrounding fluid which includes force due to viscous stress which causes the molecule to deform. The size of the force (per unit area) can be approximated by eq. (2.7) and is denoted by $\underline{\underline{\tau}}$. All Newtonian fluids comply with Newton's law of viscosity.

For a 2D flow of fluid through a straight channel (as seen in fig. 2.5), the strain rate tensor has four non-zero components, namely the $\dot{\gamma}_{xx}$, $\dot{\gamma}_{xy}$, $\dot{\gamma}_{yx}$ and $\dot{\gamma}_{yy}$.

$$\underline{\underline{\dot{\gamma}}} = \begin{bmatrix} \dot{\gamma}_{xx} & \dot{\gamma}_{xy} & \dot{\gamma}_{xz} \\ \dot{\gamma}_{yx} & \dot{\gamma}_{yy} & \dot{\gamma}_{yz} \\ \dot{\gamma}_{zx} & \dot{\gamma}_{zy} & \dot{\gamma}_{zz} \end{bmatrix} = \begin{bmatrix} 2\frac{\partial u_x}{\partial x} & \left(\frac{\partial u_x}{\partial y} + \frac{\partial u_y}{\partial x}\right) & 0 \\ \left(\frac{\partial u_x}{\partial y} + \frac{\partial u_y}{\partial x}\right) & 2\frac{\partial u_y}{\partial y} & 0 \\ 0 & 0 & 0 \end{bmatrix}$$

For a pressure driven flow (in the x-direction) through a straight channel, which is the focus of chap. 3, the only non-zero velocity component is u_x which depends only on y, the diagonal entries should become zero, while the off-diagonal entries are symmetric and equal to $\frac{\partial u_x}{\partial y}$. We will also consider a pressure driven flow (in the θ-direction) through a curved channel in chap. 4 (fig. 4.14), the only non-zero component of velocity is u_θ which only depends on r, which reduces the diagonal entries of the strain rate tensor to zero and the off-diagonal entries ($r\theta$ and θr component) to $r\frac{\partial}{\partial r}\left(\frac{u_\theta}{r}\right)$. In plane polar co-ordinates, the strain rate takes the form:

$$\underline{\underline{\dot{\gamma}}} = \begin{bmatrix} \dot{\gamma}_{rr} & \dot{\gamma}_{r\theta} & \dot{\gamma}_{rz} \\ \dot{\gamma}_{\theta r} & \dot{\gamma}_{\theta\theta} & \dot{\gamma}_{\theta z} \\ \dot{\gamma}_{zr} & \dot{\gamma}_{z\theta} & \dot{\gamma}_{zz} \end{bmatrix} = \begin{bmatrix} 2\frac{\partial u_r}{\partial r} & \frac{1}{r}\frac{\partial u_r}{\partial \theta} + r\frac{\partial}{\partial r}\left(\frac{u_\theta}{r}\right) & 0 \\ \frac{1}{r}\frac{\partial u_r}{\partial \theta} + r\frac{\partial}{\partial r}\left(\frac{u_\theta}{r}\right) & 2\frac{\partial u_\theta}{\partial \theta} & 0 \\ 0 & 0 & 0 \end{bmatrix}. \tag{2.9}$$

2.1.4 Yield stress fluid

The property of the yield stress is often important, for example in preventing fluid flow in the absence of applied forces, and on the other hand often complicates applications, for example in requiring large stresses to be applied before a contaminated sludge can be processed. In enhanced oil recovery [Farajzadeh et al., 2012], the yield stress of a foam allows it to act as a displacement fluid, pushing oil in front of it. In such an application it is necessary to predict in which parts of the fluid the stress will exceed the yield stress, and the material will flow, and where the stress is so low that either the material does not move at all, or moves as a solid plug.

Yield stress fluids are fluids that don't satisfy Newton's law of viscosity (i.e. the viscosity of the fluid is not independent of the shear rate [George and Qureshi, 2013]) everywhere. Examples include the flow of pastes [Ardakani et al., 2011; Smeplass, 1993], foam [Nastasa et al., 2015; Weaire and Hutzler, 2001], blood [Bingham and Roepke, 1944], slurries [Hanks et al., 1967; Laird, 1957], flow of material in landslides [Hild et al., 2002] and geomaterials [Dragoni et al., 1986; Walsh and Saar, 2008]. Yield-stress fluids behaves like a solid material at small applied stresses and a Newtonian fluid at large stresses.

Perhaps the simplest example of a continuum model for a yield stress fluid is due to Bingham [Bingham, 1922], almost a century ago (eqs. 2.13-2.14). This model assumes zero strain rate below a critical value of the stress, and is therefore inelastic; this is a visco-plastic model. This model has been extensively studied theoretically, for example for steady pressure-driven flow in straight channels of different cross-sections [Bird et al., 1983; Norouzi et al., 2015; Taylor and Wilson, 1997] and for boundary-driven flow in annuli [Bird et al., 1983; Muravleva et al., 2010b] and numerically, for example for flow past a sphere [Blackery and Mitsoulis, 1997]. other models are commonly used such as the Herschel and Bulkley [1926] and Casson [1959] models, also discussed.

The proportion of fluid in the plug region is determined by the value of the yield stress of the fluid as well as the pressure gradient driving the flow. The position in the channel at which the two regions meet are called the yield surfaces, and occur when the stress is of equal magnitude to the yield stress of the fluid. For the straight channel flow, the yield surfaces are symmetric about the channel centerline and only depend on the yield stress τ_0 and the driving pressure-gradient G, where G is equal to the difference in inlet (p_{in}) and outlet (p_{out}) pressure, divided by the length of the channel L:

$$G = \frac{p_{in} - p_{out}}{L}. \tag{2.10}$$

When considering more complex channel geometries with channel curvature, approximating the locations of the yield surfaces positions becomes a more involved problem as they also depend on the channel curvature κ [Roberts and Cox, 2020].

Throughout this thesis, we consider two-dimensional flows of yield stress fluids through channels of various geometries. The simulations will be described in detail in chap. 2.2. Two-dimensional simulations produce accurate and fast (in comparison to 3D) simulations of a generalised problem, as the computational problem is much less complex (as the constitutive equation is linearised). Next, we discuss the different continuum models of viscoplastic fluids and outline the reasoning for our choice of continuum model to model the foam in sclerotherapy.

We present three different constitutive equations that model yield-stress fluid, listed as the Bingham model, Hershel-Bulkley model and Casson model, respectively. All three models are commonly used to simulate real life materials such as blood [Venkatesan et al., 2013], paint [Varela López and Rosen, 2002] and lava [Dragoni et al., 1986] and it is useful to know that all three could be applied to the sclerotherapy application. The added complexity of both Hershel-Bulkley and Casson models, shown in the following sections, cause the governing equations to become more complex to simulate.

Nevertheless, the results in the thesis are produced using the Bingham model, the simplest out of all three models. The simplicity of the Bingham model is one of the key reasons that it is used in this thesis as it allows us to produce accurate but fast simulations of foam flow through complex geometries, where all the information regarding the foam rheology is contained in the yield-stress term. Additionally, to validate our simulations in latter chapters, we compare with the analytical solutions for a flow of Bingham fluid in both straight and curved channels, where the analytical solution is known. The analytical solution is not known in a curved channel for both a Hershel-Bulkley and Casson models.

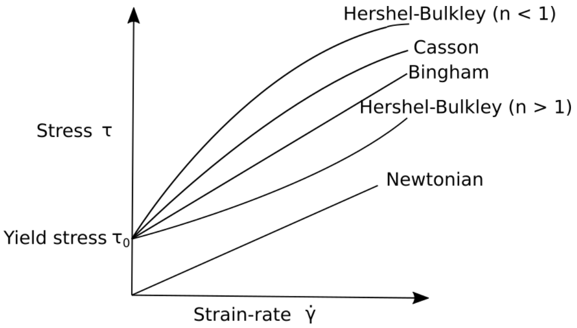

Figure 2.1: The stress-strain relationship for Newtonian and non-Newtonian fluid. The value of index n in eq. (2.20), determines if the fluid is shear thickening, thinning or Bingham fluid.

2.1.4.1 Bingham fluid

The Bingham model was formulated by Eugene Bingham in the 1920s, as a simple model for a yield-stress fluid. The constitutive equation of a Bingham fluid [Bingham, 1922] for a flow of yield-stress fluid takes the form:

$$\underline{\underline{\tau}} = \left(\mu + \frac{\tau_0}{|\underline{\underline{\dot{\gamma}}}|}\right)\underline{\underline{\dot{\gamma}}} \qquad \text{for} \quad |\underline{\underline{\dot{\gamma}}}| \geq \tau_0 \tag{2.11}$$

$$\underline{\underline{\dot{\gamma}}} = \underline{\underline{0}} \qquad \text{for} \quad |\underline{\underline{\dot{\gamma}}}| < \tau_0 \tag{2.12}$$

where $|\underline{\underline{\dot{\gamma}}}| = \sqrt{\frac{1}{2}\left(\underline{\underline{\dot{\gamma}}} : \underline{\underline{\dot{\gamma}}}\right)}$ is the second invariant of the strain rate tensor $\underline{\underline{\dot{\gamma}}}$ (eq. (2.8)).

The strain rate tensor $\underline{\underline{\dot{\gamma}}}$, is measure of the amount of change in the deformation of the fluid. When the tensor components are very small, the fluid is unyielded and flows like a solid plug. For channel flows, the regions of small rate of strain values are located at the centre of the channel. The rate of deformation is at its maximum at the channel walls, with friction creating velocity gradients leading to deformation.

Throughout this thesis, we will work with a Bingham model as it is has one of the simplest viscoplastic rheological models containing a yield-stress [Zengeni, 2016]. The yield-stress in the Bingham model has a non-linear contribution to the strain rate, which becomes linear (ofset by the yield stress) when considering unidirectional flows of Bingham fluids, which depend on only one variable space. Thus, the (linearised) Bingham constitutive equation becomes:

$$\tau_{xy} = \tau_0 + \mu\dot{\gamma}_{xy} \qquad \text{for} \quad |\tau_{xy}| \geq \tau_0 \tag{2.13}$$

$$\dot{\gamma}_{xy} = 0 \qquad \text{for} \quad |\tau_{xy}| < \tau_0. \tag{2.14}$$

This model assumes zero strain rate below a critical value, the yield stress, and above this value, the material flows such that the strain-rate is directly proportional to the applied shear stress. The relationship between the stress and strain for a Bingham fluid can be seen in fig. 2.1, where the slope of the line denoting a Bingham fluid is defined as the plastic viscosity of the fluid. Once the model is non-dimensionalised for a given two-dimensional system, all the information regarding the fluid properties is contained in a non-dimensional Bingham number B:

$$B = \frac{2\tau_0}{Gh} \tag{2.15}$$

where h denotes the channel width and the pressure gradient G is defined in eq. (2.10). By using the non-dimensional quantities from eq. (2.4), which were used to non-dimensionalise the governing Stokes equations, we can derive a non-dimensional form for the constitutive equations (eqs. (2.13) and 2.14):

$$\tau_{xy} = \frac{1}{2}B + \dot{\gamma}_{xy} \qquad \text{for} \quad |\tau_{xy}| \geq \frac{1}{2}B \tag{2.16}$$

$$\dot{\gamma}_{xy} = 0 \qquad \text{for} \quad |\tau_{xy}| < \frac{1}{2}B. \tag{2.17}$$

In chap. 6, we associate the value of B, but in 3D, with the foam properties in sclerotherapy by using an empirical estimate for the yield stress [Princen and Kiss, 1989].

The model for a Bingham fluid has been used both analytically and numerically to explore many different flows of yield-stress fluids, such as a Poiseuille flow of Bingham fluid [Frigaard et al., 1994], Couette-Poiseuille flow [Chen and Zhu, 2008], exit and entry flows [Abdali et al., 1992], a flow around a cylinder [Roquet and Saramito, 2003] and a squeeze flow [Smyrnaios and Tsamopoulos, 2001] (with slip [Yang and Zhu, 2006]), to name a few. The model has been applied to avalanches [Hild et al., 2002], lava flows [Dragoni et al., 1986], blood [Bingham and Roepke, 1944], concrete [Smeplass, 1993] and slurries [Hanks et al., 1967].

2.1.4.2 Hershel-Bulkley model

The Hershel-Bulkley model was formulated by Winslow Herschel and Ronald Bulkley in the early 20th century, as a model for a non-Newtonian fluid which takes into account the flow index n (as for a power law fluid [Hemphill et al., 1993]) and yield-stress τ_0. The constitutive equation of a Hershel-Bulkley fluid [Herschel and Bulkley, 1926] for a flow of yield stress fluid takes the form:

$$\underline{\underline{\tau}} = \left(\mu + \frac{\tau_0}{|\dot{\underline{\underline{\gamma}}}|}\right)\dot{\underline{\underline{\gamma}}}^n \qquad \text{for} \quad |\dot{\underline{\underline{\gamma}}}| \geq \tau_0 \tag{2.18}$$

$$\dot{\underline{\underline{\gamma}}} = \underline{\underline{0}} \qquad \text{for} \quad |\dot{\underline{\underline{\gamma}}}| < \tau_0. \tag{2.19}$$

If we consider a unidirectional flow (in the x direction) of Hershel-Bulkley fluid through a straight channel, the non-linearity of the constitutive equations (2.18-2.19) are reduced to a linearised model when the velocity is a function of one independent variable i.e. for the straight channel, the velocity u_x has only dependence on y. This means that the only non-zero component of the strain rate tensor (and thus the stress) is the xy component. We simplify the above constitutive equation and assume a unidirectional flow which allows us to assume the following relationship between the stress and strain rate.

$$\tau_{xy} = \tau_0 + \mu(\dot{\gamma}_{xy})^n \qquad \text{for} \quad |\tau_{xy}| \geq \tau_0 \tag{2.20}$$

$$\dot{\gamma}_{xy} = 0 \qquad \text{for} \quad |\tau_{xy}| < \tau_0 \tag{2.21}$$

The focus of the thesis will consider the simplest model of a yield-stress fluid by setting $n = 1$ in eqs. (2.20 - 2.21), were the fluid labelled as a Bingham fluid, shown in fig. 2.1. For

$n \neq 1$, the fluid can be labelled as shear thinning ($n < 1$) or thickening ($n > 1$).

For $n > 1$, we have a non-Newtonian shear thickening fluid. That is, as seen in fig. 2.1, the value of the stress increases as a polynomial of order n for increasing shear rate. Shear thickening behaviour is usually seen in suspensions such as a mixture of cornstarch and water [Fall et al., 2012; White et al., 2010]. By stirring the mixture slowly, it behaves just like a fluid, but when a large stress is applied on the suspension, it suddenly behaves as a solid as particles clump together to create solid-like structures. Alternatively you could shape the mixture of cornstarch and water into a ball, which falls apart once pressure is not applied. It is a very useful property which is used in "liquid body armor" [Kang et al., 2012].

On the other hand, shear thinning materials ($n < 1$) are much more common in every day life, such as paint [Varela López and Rosen, 2002], blood and ketchup [Berta et al., 2016]. Contrary to shear thickening fluids, when large stresses are applied it behaves like a fluid behaves like a solid when at rest or being stirred slowly. Paint for instance, allows the user to brush or roll (introducing high shear) evenly on a surface but once applied the viscosity of the fluid increases which stops the effects of dripping and running.

2.1.4.3 Casson model

The Casson model [Casson, 1959] was developed in the 1950s when considering the flow equation for the oil suspension in printing ink, but it has since been used to model the flow of blood in narrow arteries [Chaturani and Samy, 1986; Srivastava, 2014; Venkatesan et al., 2013; Walawender et al., 1975]. The Casson model is a non-Newtonian fluid model with yield stress τ_0, and in the same way as a Bingham fluid, analytical velocity profiles can be derived for some geometries, such as flow through a pipe [Bird et al., 1983]. The constitutive equation for a one-dimensional flow of Casson fluid takes the form:

$$\sqrt{\tau_{xy}} = \sqrt{\tau_0} + \mu\sqrt{\dot{\gamma}_{xy}} \qquad \text{for} \quad |\tau_{xy}| \geq \tau_0 \tag{2.22}$$

$$\dot{\gamma}_{xy} = 0 \qquad \text{for} \quad |\tau_{xy}| < \tau_0 \tag{2.23}$$

Although Casson fluid will not be used in this thesis, we acknowledge the many choices of continuum yield-stress fluid models used throughout the field of non-Newtonian fluid dynamics, and their application to a wide variety of fluids. As a future avenue of research, modelling sclerotherapy as a displacement flow of one yield-stress fluid by another could make use of the Casson model in order to model blood.

2.1.5 Boundary conditions

Throughout the thesis, we implement one of the simplest (and most common) boundary conditions to the walls of the channel (or vein), namely the no-slip boundary condition [Batchelor, 2000; Lamb, 1993]. We assume that there is sufficient friction at the vein wall to induce a no-slip boundary condition there [Baker and Wayland, 1974; Sousa et al., 2011]. The condition certifies that the liquid molecules that contact the surface in question become stationary relative to the surface:

$$\underline{u}\Big|_{\text{boundary}} = \underline{0}. \tag{2.24}$$

We also consider the implementation of the Navier slip condition [Navier, 1823] on the walls of the channels. Slip at the walls is an interesting phenomenon which occurs in many industrial applications which use complex fluids, such as suspensions, polymer melts and emulsions [Barnes, 1995; Hatzikiriakos, 2012], such as shaping molten polymers into a mold [Denn, 2001]. In this thesis, we consider the no-slip boundary condition as a special case of the Navier slip condition, with a zero slip length.

In classical fluid dynamics, Newtonian fluids comply with the no-slip boundary conditions, implemented above. Contrary to this, experimental findings by Neto et al. [2005]

show the existence of wall slip in flows of Newtonian fluids through microchannels. The study focused on tracing the motion of fluorescent particles near a solid surface using the "FRAP" method [Pit et al., 2000]. The study by Neto concluded that factors affecting the slip of fluid at the boundary listed as surface wetness and roughness, shear stress, boundary curvature and the fluid viscosity. The extent of this slip has been experimentally examined by several others in microfluidic and nanofluidic channels [Arkilic et al., 1997; Einzel et al., 1990; Lauga et al., 2005; Tretheway and Meinhart, 2002]. Experimental results conducted by Neto et al. [2005] and Matthews and Hill [2008] give evidence to support the compliance of Newtonian fluids with the Navier slip boundary condition.

Viscoplastic materials are known to exhibit wall slip, "which arises due to a depletion of particles adjacent to the shearing surface" [Damianou and Georgiou, 2014]. These have been observed for polymer solutions, emulsions and particle suspensions [Barnes, 1995], pastes [Meeker et al., 2004] as well as hydrogels [Aktas et al., 2014]. Wall slip has a significant effect on flowing viscoplastic material [Meeker et al., 2004] and the extent of the slip which occurs for non-Newtonian fluids is said to depend on wall shear, temperature, the properties of the flowing material and the fluid/wall interface [Denn, 2001].

The degree of slip is determined by the Navier slip condition [Navier, 1823], a linear slip condition used commonly in theoretical analysis of lubrication flows and microflows [Laun et al., 1999], is controlled by the strain rate [Thompson and Troian, 1997] as well as the roughness of the surface [Pit et al., 2000], captured by slip length β. The Navier slip condition assures that the velocity of the fluid at the wall is proportional to the local strain rate normal to the wall of the channel, multiplied by a slip length β [Chen et al., 2014]:

$$u_x = \beta \frac{du_x}{dy}. \tag{2.25}$$

By setting $\beta = 0$, we regain the usual no-slip conditions. We achieve full slip in the limit $\beta \to \infty$.

The Navier slip is only one possible slip condition. Another possible slip condition used for non-Newtonian fluids is a "stick-slip" boundary condition that only allow slip above a certain yield-stress [Kaoullas and Georgiou, 2013], based on results in Damianou et al. [2013]. Alternative slip models could take into account the roughness of the boundary [Zampogna et al., 2019].

Couette-Poiseuille flow with Navier slip between two parallel plates was considered by Chen and Zhu [2008], providing analytical solutions for different flow profiles by varying the driving velocity and slip. Philippou et al. [2016] looked at the development of viscoplastic flow in tubes and channels with slip, noticing that the development length decreases with increasing B. Damianou and Georgiou [2014] considered a Poiseuille flow of Bingham fluid through a rectangular duct with slip, using the regularised Papanastasiou model [Papanastasiou, 1987]. Some further work of implementing a slip boundary condition using the finite element method can be seen by Yeow et al. [2006] and Karapetsas and Mitsoulis [2013]. The latter set an upperbound for the non-dimensional slip length β of the order of $\mathcal{O}(1)$ as larger choices of slip length leads to gross overestimation of the pressure-drops in the system.

The aim for this thesis is to stimulate discussion of how implementing partial slip on the walls of channels of various geometries affect the flow profiles of Bingham fluidsy. We restrict the slip length β to 10% of the channel width. This would then elucidate the consequences of slip in veins on the effectiveness of foam in sclerotherapy.

2.2 Numerical Methods

In this chapter, we outline the Finite Element method (FEM) that we use to solve the Stokes equations and the Bingham constitutive model. We use the regularised Papanstatiou model [Papanastasiou, 1987] that overcomes singularities that occur at the yield surfaces due to the vanishing strain-rate, justifying our choice of model in chap. 2.2.2.1. Before this, we outline the Augmented Lagrangian Method (ALM) (chap. 2.2.1), another popular method of modelling non-Newtonian fluid and summarize our reasoning against its use.

We validate the accuracy of the simulation in three different two-dimensional channel geometries; a straight channel (fig. 2.5), curved channel (fig. 4.14) and a straight channel connected to a curved channel (fig. 4.19), with the domain of the channel labelled by Ω. We implement both the Navier slip boundary conditions on the channel walls for slip lengths $\beta = 0$ (no-slip) and 0.1, denoted by $\partial\Omega$.

We will derive the form of the Stokes equations in their weak formulation (see §2.2.2.2). In a weak formulation, used by both the regularised method and the ALM on FreeFem++, an equation is no longer required to hold absolutely and has instead weak solutions only with respect to certain "test vectors" or "test functions". As mentioned above, the weak formulation solves a system of equations by turning a differential equation into an integral equation. We will use FreeFem++ to solve the weak form of the Stokes equations in cohesion with the Papanastasiou model.

2.2.1 Augmented Lagrangian Method

The ALM is an adapted Finite Element Method which uses the weak formulation approach and doesn't require use of a regularised model. The method is an adaption of the Lagrangian method and was formulated in order to model non-Newtonian fluids, where a functional is defined (see Saramito and Roquet [2001]), which is minimized by the correct solution [Dimakopoulos et al., 2018].

To model non-Newtonian fluids, the method introduces dummy variables, called Lagrange multipliers, which are related to the stress tensor, to iterate towards a solution in order to avoid the diverging effective viscosity in regions of zero strain rate. These regions of zero strain rate occur where the stress experienced by the fluid is smaller in magnitude than the value of the yield-stress, according to eqs. (2.18-2.19).

By using dummy variables, the method avoids the computation of the non-linear part of the Bingham model in equations (2.18) and (2.19) [Huilgol and You, 2005] which "aids in the relaxation of computing the velocity gradient" [Dimakopoulos et al., 2018]. Additionally, a "quadratic" term is incorporated in the functional to improve the convergence of the iteration. The Lagrange multipliers are multiplied by certain coefficients which are updated in each iteration according to a conjugate gradient method [Dimakopoulos et al., 2018].

Knowing the information provided above, we can now introduce the different steps that occur in the iterative process of the ALM. The Lagrange multipliers are denoted by $\underline{\underline{\Upsilon}}$ (otherwise labelled as a linear constraint [Roquet and Saramito, 2003]) and $\underline{\underline{\tau}}$. If n denotes the iteration number, the ALM takes the following form [Saramito and Roquet, 2001]:

- Step 1:

$$-r\underline{\nabla}.(\underline{\nabla}.\underline{u} + (\underline{\nabla}.\underline{u})^T)^{n+1} + \underline{\nabla}p^{n+1} = \underline{\nabla}.(\underline{\underline{\tau}}^n - r\underline{\underline{\Upsilon}}^n)$$

$$\underline{\nabla}.\underline{u}^{n+1} = 0$$

- Step 2:

$$\underline{\underline{\Upsilon}}^{n+1} = \begin{cases} 0 & \text{if} \quad ||\underline{\underline{M_n}}|| < B \\ (1 - \frac{B}{||\underline{\underline{M_n}}||})\underline{\underline{M_n}}\frac{1}{1+r} & \text{otherwise} \end{cases}$$

  where $\underline{\underline{M_n}} = (\underline{\underline{\tau}}^n + r\underline{\underline{\dot{\gamma}}}^{n+1})$.

- Step 3:

$$\underline{\underline{\tau}}^{n+1} = \underline{\underline{\tau}}^n + r(\underline{\underline{\dot{\gamma}}}^{n+1} - \underline{\underline{\Upsilon}}^{n+1})$$

This process is repeated until convergence has been reached (for any $r > 0$), when the velocities are settled and the sum of velocities change little between iterations. Step 1 requires solving the Stokes equations with has an additional term on the right hand side, consisting of both Lagrange multipliers. This additional term needs to be minimized in order to satisfy the Stokes equations and the scheme iterates and updates both $\underline{\underline{\Upsilon}}$ and $\underline{\underline{\tau}}$ in steps 2 and 3 in order to converge to the true solution of the Stokes equations. In this thesis, we refer to the ALM as an alternative method, other than using regularisation, to simulate flows of Bingham fluid in complex geometries.

2.2.1.1 Comparison between the ALM and regularised models

The ALM is used successfully by several authors in the field, such as Frigaard et al. [2017], Hewitt et al. [2016], Roquet and Saramito [2003], Moyers-Gonzalez and Frigaard [2004] and Roquet and Saramito [2003, 2008]. Muravleva et al. [2010a] considered the simulation of cessation flows of a Bingham plastic with the ALM [Glowinski, 1980] and compared the results against both the analytical results and numerical results of Chatzimina et al. [2005], who used the regularised Papansatasiou model. The results suggest that the ALM yields superior results in comparison to the regularised model for the locations of the yield surfaces and the limit of vanishing yield-stress (in agreement with [Roquet and Saramito, 2003; Saramito and Roquet, 2001]). The results also suggest that the regularised models predict larger plug regions in comparison to the ALM, which is known to give an accurate prediction of the yielded and plug zones [Huilgol and You, 2005; Saramito and Roquet, 2001]. Saramito and Roquet [2001] suggest that the accuracy of ALM can be improved by the addition of an adaptive finite element method where the mesh refinement is increased between iterations [Roquet and Saramito, 2003, 2008; Saramito and Roquet, 2001].

On the other hand, the work by Muravleva et al. [2010a] also suggests that the regularised Papansatsiou model produces accurate results in comparison to ALM and the differences between both results are not "that great", suggesting that the regularised model is much easier to implement and produces very fast results with modern computers. Dimakopoulos et al. [2013] also concluded that the Papansatasiou model produces detailed and accurate results for the flow field of viscoplastic fluid and the yield surface positions are accurately determined. Abdali et al. [1992] and Smyrnaios and Tsamopoulos [2001] are also in agreement that the Papansatsiou model accurately captures the extent and shape of the yielded regions (using a criterion on the stress).

Dimakopoulos et al. [2013] results suggest that the ALM method takes 10 times the computational time in comparison to the Papansatasiou model. The ALM is so computationally expensive, other accelerated algorithms have been formulated such as PAL (Penalized Augmented Lagrangian [Dimakopoulos et al., 2018]), which is more efficient than the ALM, requiring less than half the number of iterations to converge. These continuous regularised models for Bingham fluid are also easily implemented to simulations [Frigaard and Nouar, 2005; Saramito and Roquet, 2001].

The accuracy of the ALM was reinforced on FreeFem++ when compiling the algorithm by Roustaei [2014] through a straight channel, which provided very accurate results (although slow and computationally expensive). Contrary to the success of the algorithm [Roustaei, 2014] in the straight channel case, the method had reoccurring convergence problems in both a curved and sinusoidal channels (chaps. 4 and 5) and the method became unreliable and slow. The regularised Papanastasiou model provided efficient and accurate predictions of the flow profiles in both straight and curved geometries (chaps. 3.5.1 and 4.6.1). We eventually only consider simulations that use the regularised viscosity models.

2.2.2 Finite Element Method

Here we describe in further detail the simulation methods that are used to produce the numerical data throughout the thesis. In addition to the description of the numerical methods, we consider the appropriate convergence criteria and mesh resolution needed to produce accurate simulations of pressure-driven Bingham fluid. The software used for producing the numerical simulations is FreeFem++ [Hecht, 2012], which is a partial differential equation solver for non-linear multi-physics systems, both in 1D, 2D and 3D, using the finite element method. FreeFem++ is written in C++. The software solves a system of partial differential equations from a wide range of physical problems using a “fast” interpolation algorithm [Hecht, 2012].

The software uses the weak formulation to solve the relevant system of equations, by making use of several test functions corresponding to pressure and velocity. The relevant system in our case is solving the Stokes equations (eq. 2.6) with the Bingham constitutive equation [Bingham, 1922] described by eqs. (2.13) and (2.14). Our assumptions about the nature of the flow of foam in varicose veins allows us to linearise the Navier-Stokes equations in the limit of small Reynolds number ($Re \to 0$), allowing us to solve the Stokes equations in tensorial form:

$$-\underline{\nabla}.\underline{\underline{\tau}} + \underline{\nabla}p = \underline{0} \quad \text{(Conservation of Momentum)} \tag{2.26a}$$

$$\underline{\nabla}.\underline{u} = 0 \quad \text{(Conservation of Mass)} \tag{2.26b}$$

Next, we discuss possible viscosity models that overcome singularities in the Bingham continiuum model.

2.2.2.1 Viscosity model

We consider a Bingham fluid as a generalised Newtonian fluid using regularised continuous viscosity models which smooths over singularities at the yield surface positions, provides accurate representation of Bingham plastic behaviour [Mitsoulis and Zisis, 2001]. Singularities occur when using the Bingham model (eqs. 2.18-2.19) due to the vanishing strain rate at the yield surface positions, causing the term involving the yield stress τ_0 to “blow up”, thus regularisation is required. Several authors have compared the results using regularised models to exact solutions [Burgos et al., 1999; Frigaard and Nouar, 2005] and have been cited as accurate methods of simulating non-Newtonian behaviour of fluid [Abdali et al., 1992; Frigaard and Nouar, 2005; Smyrnaios and Tsamopoulos, 2001].

In this chapter, we discuss the possible choices of the regularised viscosity model used to model a Bingham fluid. We will use the FEM to solve the Stokes equations (2.5) along with the Bingham constitutive model, with B denoting the Bingham number (eq. (2.15)), which measures the significance of yield stress compared to viscous stress. By non-dimensionalising eqs. (2.18-2.19) (with $n = 1$) by using the quantities in eq. (2.4), the non-dimensional Bingham model in tensorial form becomes

$$\begin{aligned} \underline{\underline{\tau}} &= \left(1+\tfrac{B}{2|\dot{\underline{\underline{\gamma}}}|}\right)\dot{\underline{\underline{\gamma}}} && \text{for} \quad |\underline{\underline{\tau}}| > \tfrac{1}{2}B \\ \dot{\underline{\underline{\gamma}}} &= 0 && \text{for} \quad |\underline{\underline{\tau}}| \leq \tfrac{1}{2}B. \end{aligned} \tag{2.27}$$

The viscosity models, which we denote by η and dependents on the strain rate $|\dot{\underline{\underline{\gamma}}}|$, are derived initially from observation of eq. (2.27) for large stresses and adapting using regularisation parameters.

$$\eta = \left(1+\frac{B}{2|\dot{\underline{\underline{\gamma}}}|}\right) \tag{2.28}$$

There were several attempts during the 1980s to produce a model for η, using regularisation parameters to overcome its unbounded nature when $|\dot{\underline{\underline{\gamma}}}| = 0$ within the plug regions [Bercovier and Engelman, 1980; O'Donovan and Tanner, 1984; Papanastasiou, 1987] i.e. adjusting expression eq. (2.28) to become bounded in the limit $\dot{\underline{\underline{\gamma}}} \to 0$. All regularised models predict that in the limit of $\dot{\underline{\underline{\gamma}}} \to 0$ that the shear stress also becomes zero ($\underline{\underline{\tau}} \to 0$). This means that the material in the plug region is "no longer a rigid solid but a highly viscous fluid that approximates the ideal viscoplastic behaviour" [Burgos et al., 1999]. This is not the case for the constitutive equation (eq. (2.27)) as the stress is undefined within the plug region, with $\dot{\underline{\underline{\gamma}}} = 0$.

Bercovier and Engelman [1979, 1980] introduced the use of a regularisation parameter δ_b (dimensionally equivalent to the strain rate), to overcome the discontinuity in the constitutive equation:

$$\underline{\underline{\tau}} = \left(1+\frac{B}{2(|\dot{\underline{\underline{\gamma}}}|+\delta_b)}\right)\dot{\underline{\underline{\gamma}}} \tag{2.29}$$

The finite element method used by Bercovier and Engelman [1980] consists of replacing the

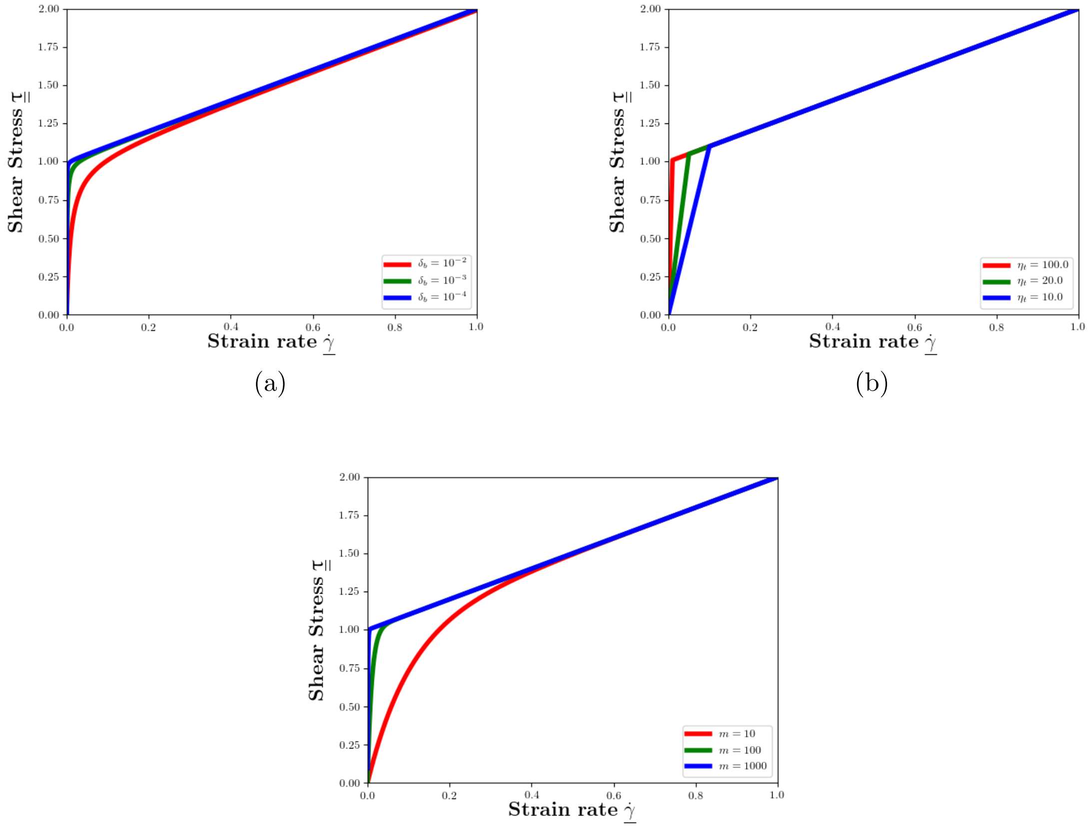

(a)

(b)

(c)

Figure 2.2: The stress-strain models for a Bingham fluid, with $B = 1$: (a) Bercovier [1980] model, (b) Tanner and Milthorpe [1983] bi-viscous model and (c) Papanastasiou [1987] model.

weak formulation of the Stokes equations with a penalty function approach [Bercovier, 1980; Zienkiewicz and Heinrich, 1979]. Saramito and Roquet [2001] reported that the practical difficulties of using this regularised model increases as δ_b approaches zero, which increases computational time. Equation (2.29) is plotted in fig. 2.2(a) for several different values of δ_b, showing that we recover the constitutive equation eq. (2.27) in the limit $\delta_b \rightarrow 0$. This model was used to solve the flow in a closed square cavity subject to a body force [Bercovier and Engelman, 1980], measuring the stagnant (dead) regions at the corners as well as the size of the plug region.

A further attempt of a viscosity model by Tanner and Milthorpe [1983] used a bi-viscous model. This gives two regions with different apparent viscosities instead of a jump in strain-rate, which are chosen such that the stresses match at a critical strain-rate $\dot{\gamma}_c$. The model can be written in terms of the plug viscosity $\eta_p = (1 + B/2\dot{\gamma}_c)$, and the yielded viscosity $\eta_y = (1 + B/2|\underline{\underline{\dot{\gamma}}}|)$, with $\eta_t = B/2\dot{\gamma}_c$:

$$\begin{aligned} \underline{\underline{\tau}} &= \left(1 + \tfrac{B}{2\dot{\gamma}_c}\right)\underline{\underline{\dot{\gamma}}} \qquad \text{for} \quad |\underline{\underline{\dot{\gamma}}}| \leq \dot{\gamma}_c \\ \underline{\underline{\tau}} &= \left(1 + \tfrac{B}{2|\underline{\underline{\dot{\gamma}}}|}\right)\underline{\underline{\dot{\gamma}}} \qquad \text{for} \quad |\underline{\underline{\dot{\gamma}}}| > \dot{\gamma}_c, \end{aligned} \tag{2.30}$$

where the results for different η_t are also plotted on fig. 2.2(b) and is a model which is a good match for the rheology of a Bingham fluid. This replaces the plug region by a slowly yielding flow to avoid the appearance of singularities [Lipscomb and Denn, 1984].

This model (eq. (2.30)) was also used by Beverly and Tanner [1989], who modelled die swell in viscoplastic materials. It was also used by Taylor and Wilson [1997], who considered a square and rectangular conduit flow of a incompressible Bingham fluid and reported that the model captured some dead regions of fluid but also captured unexpected situations where the concavity of the dead regions (regions in which the fluid is at rest [Brunn and Abu-Jdayil, 2007]) were inverted. Wang [1997] showed that the unexpected effects where down to insufficient numerical accuracy of the simulation [Saramito and Roquet, 2001]. Nirmalkar and Chhabra [2014] suggest that the value of η_t must be chosen carefully for the results to be independent of numerical artefacts. On the other hand, the model has been applied effectively to identify the yield surfaces of marine sediments [Jeong, 2013] and to model snow avalanche motion [Dent and Lang, 1983]

Following the attempts of Bercovier and Engelman [1980] and Tanner and Milthorpe [1983], Papanastasiou [1987] developed a continuous viscosity model for a Bingham fluid, using an exponential function to smooth over the different regions:

$$\underline{\underline{\tau}} = \left(1 + \frac{B(1 - \exp(-m|\underline{\underline{\dot{\gamma}}}|))}{2|\underline{\underline{\dot{\gamma}}}|}\right)\underline{\underline{\dot{\gamma}}}. \tag{2.31}$$

The viscosity model takes form

$$\eta = \left(1 + \frac{B(1 - \exp(-m|\underline{\underline{\dot{\gamma}}}|))}{2|\underline{\underline{\dot{\gamma}}}|}\right),$$

where m denotes a regularisation parameter that controls the exponential growth of stress. We investigate the influence of this parameter in fig. 2.2(c) (as well as chap. 3.5). Papanastasiou [1987] used eq. (2.31) to study several simple flows, such as a one-dimensional channel flow, a two-dimensional boundary layer flow and an extrusion flow. Since the late 80s, the model has been used by Ellwood et al. [1990] for laminar jets of Bingham fluid, Abdali et al. [1992] for entry and exit flows of Bingham fluids, Smyrnaios and Tsamopoulos [2001] for squeeze flows of Bingham fluids, Mitsoulis and Zisis [2001] for lid-driven cavities and for flow around the cylinder [Zisis and Mitsoulis, 2002], to name a few.

Both the Bercovier and Engelman [1980] (eq. (2.29)) and Papanastasiou [1987] (eq. (2.31)) models are differentiable, unlike the Tanner bi-viscous model (eq. (2.30)), and provide a smooth approximation to the ideal model in eq. (2.27), with the discrepancies between the viscosity and ideal model dependent on the choice of regularisation parameters δ_b and m. Therefore, due to the discontinuity of the Tanner model and the associated literature questioning the models accuracy [Saramito and Roquet, 2001; Wang, 1997], the bi-viscous model will not be considered further.

In order to provide as accurate results as possible, the parameter δ_b for the Bercouvier and Engelman model must be as small as possible, although making the value of δ_b small will affect the accuracy of the model in numerical simulations [Saramito and Roquet, 2001]. The regularisation parameter m in the Papanastasiou model must be as large as possible in order to accurately approximate the Bingham model. For each chosen value of m, there exists a critical shear rate below which solutions become inaccurate. The critical shear rate is inversely proportional to the value of m, meaning that the critical shear rate becomes smaller as the regularisation parameter increases.

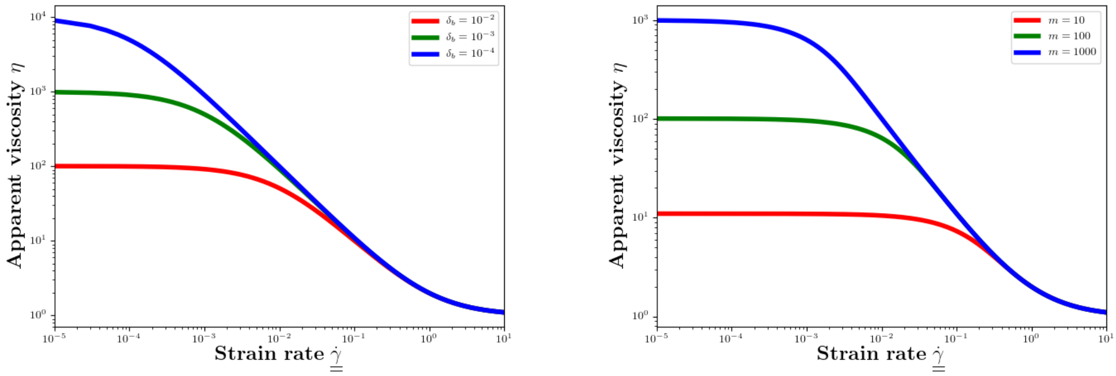

(a) (b)

Figure 2.3: The apparent viscosity η as a function strain-rate $\underline{\underline{\dot{\gamma}}}$ with $B = 1$: (a) Bercovier [1980] model and (b) Papanastasiou [1987] model for three different regularisation parameters.

Work by several other authors [Abdali et al., 1992; Ellwood et al., 1990; Smyrnaios and Tsamopoulos, 2001] suggest that the value of m should be greater than 10^2 to provide an accurate prediction of Bingham plastic behaviour and providing that $m \geq 10^4$, the results are not affected by the choice of m. At this choice of m, the critical strain rate would be equal to 10^{-4}, meaning that only results below this value of $\underline{\underline{\dot{\gamma}}}$ are inaccurate. Work by Dimakopoulos et al. [2013] suggests that increasing the value of m increases the accuracy results further and $m = 10^6$ is required for their simulations. The reasoning behind this is that increasing m decreases this critical strain rate (to 10^{-6}) in the Papanastasiou model, thus providing more accurate solutions and a smaller range of strain rate at which the results are inaccurate.

In fig. 2.3, we plot the apparent viscosities as functions of the strain rate $\underline{\underline{\dot{\gamma}}}$ on log-log scales. For very small strain rates, the value of the viscosity for the Bercouvier and Engelman model is of the order of B/δ_b and for the Papanastasiou model, the apparent viscosity is of the order m. Therefore choosing a large as possible m would be beneficial for the accuracy of the simulation as suggested above in context with the critical strain rate.

Many authors have considered the most common regularised models [Burgos et al., 1999;

Frigaard and Nouar, 2005] as discussed above and suggest that the Papanastasiou model [Papanastasiou, 1987], with an appropriate value of m, is the better choice of regularisation model. To support this, Tokpavi et al. [2008] suggests that the Papansatasiou model provides "the best velocity of convergence and accurately predicts shape and position of the rigid zones" out of all regularised models available. We therefore consider the Papansatsiou viscosity model (eq. (2.31)) as the regularised viscosity model for our finite element simulations in this thesis.

2.2.2.2 Weak formulation

In weak form, we solve Stokes equations (eq. (2.6)) as an integral function instead of solving a differential equation. We acknowledge that for the two-dimensional Stokes flows, the strain rate tensor is symmetric ($\underline{\nabla}\ \underline{u} = (\underline{\nabla}\ \underline{u})^T$), which allows us to write the Stokes equations (from eq. (2.6)) in the form

$$-2\underline{\nabla}.(\eta\underline{\nabla}\ \underline{u}) + \underline{\nabla}p = \underline{0} \quad \text{in} \quad \Omega \tag{2.32a}$$

$$\underline{\nabla}.\underline{u} = \underline{0} \quad \text{in} \quad \Omega \tag{2.32b}$$

The method requires multiplying throughout by a differentiable test function $\underline{v} \in V$ where $V \subset \Omega$ is a finite element space satisfying $\underline{v} = \underline{0}$ on the boundary $\partial\Omega$ i.e. $V = \{\underline{v} \in \Omega \mid \underline{v} = \underline{0} \text{ on } \partial\Omega\}$. By integrating equations (2.32a) over the whole domain Ω we get [Fang and Li, 2018]:

$$-\int_{\Omega} 2(\underline{\nabla}.(\eta\underline{\nabla}\ \underline{u})).\underline{v}\ d\Omega + \int_{\Omega} (\underline{\nabla}p).\underline{v}\ d\Omega = 0 \quad \forall \quad \underline{v} \in V. \tag{2.33}$$

Using integration by parts, Green's identity [Strauss, 2007] and applying $\underline{v} = \underline{0}$ on $\partial\Omega$, eq. (2.33) takes the form

$$\int_{\Omega} 2\eta\,(\underline{\nabla}\ \underline{u} : \underline{\nabla}\ \underline{v})\ d\Omega - \int_{\Omega} p.(\underline{\nabla}.\underline{v})\ d\Omega = 0 \quad \forall \quad \underline{v} \in V \tag{2.34}$$

which is the required form for the finite element method. Additionally, we need to consider the same process for equation (2.32b), integrating over the domain Ω, but multiplying by a test function for the pressure $q \in Q$, where $Q = \{q \in \Omega \mid q = 0 \text{ on } \partial\Omega\}$:

$$\int_{\Omega} (\underline{\nabla}.q).\underline{u} \; d\Omega = 0 \quad \forall \quad q \in Q. \tag{2.35}$$

Collecting equations (2.34) and (2.35), defines the Finite Element Method for the Stokes equations (eq. (2.32)) for a Bingham fluid; find $\underline{u} \in V$ such that

$$a(\underline{u}, \underline{v}) + b(p, \underline{v}) = 0 \quad \forall \quad \underline{v} \in V, \tag{2.36}$$

$$b(q, \underline{u}) = 0 \quad \forall \quad q \in Q, \tag{2.37}$$

where a and b are bilinear functionals of the form:

$$a(\underline{u}, \underline{v}) = \int_{\Omega} 2\eta(|\underline{\underline{\dot{\gamma}}}|)\Big(\underline{\nabla}\;\underline{u} : \underline{\nabla}\;\underline{v}\Big) \;\; d\Omega$$

$$b(q, \underline{v}) = -\int_{\Omega} (\underline{\nabla}.\underline{v}).q \; d\Omega.$$

We assume that this problem admits a unique solution with sufficient regularity that it can be evaluated point-wise [Apoung Kamga, 2020]. The weak form is equivalent to the strong formulation and is a re-formulation of the original PDE in eq. (2.32). An advantage of the weak formulation is that the velocity $\underline{u}$ is required only to be continuously differentiable on the first partial derivative in comparison to the second partial derivative in the strong formulation [Singh, 2009]. The system is non-dimensionalised with respect to the non-dimensional quantities in eq. (2.4). We notice in this system in the limit of vanishing yield-stress $B \to 0$, we return to the Finite Element Method for a viscous fluid.

2.2.2.3 Developing the viscosity model

To develop the viscosity model, the algorithm is iterated several times, introducing the dependence of the viscosity on the strain rate at the second iteration ($i = 1$), where the first iteration is the Newtonian solution ($i = 0$). This process is continued until the sum of velocities have settled below a certain convergence criterion, labelled by δ. This δ controls the extent of the convergence reached by the simulation. This follows a similar procedure of developing the Papanastasiou viscosity model in simulations of Bingham fluids as used by Blackery and Mitsoulis [1997], Mitsoulis et al. [1993] (for a Hershel-Bulkley fluid) as well as Abdali et al. [1992].

At the first iteration $i = 0$, we initiate the simulation by setting the viscosity of the fluid as being equal to 1, i.e a Newtonian fluid with viscosity 1, and achieve the Newtonian solution as the first approximation i.e. the simulation commences with $B = 0$. At the second iteration $i = 1$, we introduce the Papanastasiou viscosity model η (eq. (2.31)) with a non-zero value for B, which sharply increases the change in the sum of velocities between iterations as we develop the viscosity model. As i increases, we see the the sum of velocities between iterations becomes smaller until the simulation converges i.e. the velocities are deemed to be "settled".

For $i \geq 1$, we measure the difference between velocities at each iteration i and $i + 1$, characterised by δ which is a measure of how much the velocities have converged. The simulation continues until the difference in the sum of velocities between iterations fall below the value of the tolerance δ:

$$\delta > \sqrt{\sum_j \left(u^{sim}\left(x_j, y_j\right)_{i+1} - u^{sim}\left(x_j, y_j\right)_i\right)^2}. \tag{2.38}$$

Reducing the value of δ would yield a "better" convergence and a more accurate solution, but if it is too small it would lead to increased computation time or the simulation would never finish due to its inability to achieve such small sums of velocity between iterations. We will examine the effects of varying this parameter δ across a range $[10^{-6}, 10^{-2}]$ when validating the simulation. As the value of δ becomes smaller, certainly the amount of iterations needed for the convergence increases, as well as the compilation time, which will also be a factor considered. Blackery and Mitsoulis [1997] suggest that the number of iterations (and indeed compilation time) increases with increasing Bingham number B.

2.2.2.4 Finite element spaces

The channel domain Ω is divided into smaller parts i.e. finite elements, and the approximation for $\underline{u}$ is calculated over these smaller regions, allowing us to establish an approximation for $\underline{u}$ over the whole channel [Singh, 2009]. We consider an approximation over a two-dimensional triangulated mesh (see sec. 2.2.2.6). The channel domain Ω is discretized into nodes, which can be located on either a vertex or edge of each mesh triangles, then FreeFem++ [Hecht, 2020c] completes a triangulating process dependent on the nodes using a Delaunay-Voronoi algorithm [Hecht, 2012; Lee and Schachter, 1980]. For each finite element space, each triangle T_k has at least 3 nodes, located at the vertices, with the possibility that a node is shared by several different triangles. Depending on finite element space, nodes can also be located on the triangle edges i.e. finite element space $\mathbb{P}^3_h$.

For the two-dimensional mesh, we define a basis functions for each node on the mesh, labelled by $\phi_k(x, y)$ (eqs. (2.41-2.43)). The basis function is dependent on the choice of finite element space for the velocity. We consider the velocities in both finite element spaces $\mathbb{P}^1_h$ and $\mathbb{P}^3_h$, (and note the differences in results in chaps. 3.5.1 and 4.6.1), with the pressures p contained in finite element space $\mathbb{P}^1_h$, which are piecewise linear continuous finite elements.

Figure 2.4 shows an illustration of the finite element spaces $\mathbb{P}^1_h$ (a) and $\mathbb{P}^3_h$ (b) on a triangle in the mesh. We see that changing the finite element mesh from $\mathbb{P}^1_h$ to $\mathbb{P}^3_h$ will increase the number of nodes on each triangle T_k. If the velocities are in $\mathbb{P}^3_h$, each triangle has a node at every vertex as well as two other nodes on each side i.e. for equilateral triangles each side has nodes on each endpoint as well as two positioned at 1/3 and 2/3 along each side. We

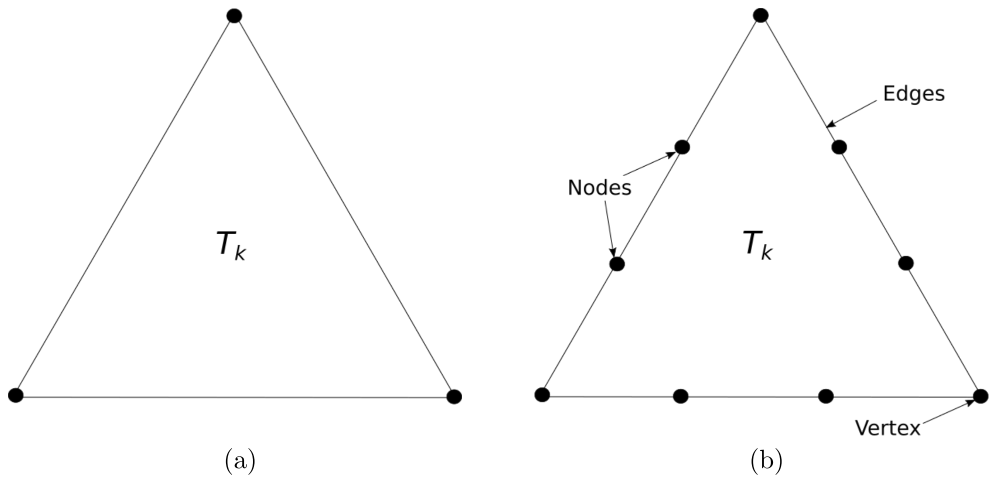

Figure 2.4: Finite element mesh triangles T_k (a) $\mathbb{P}_h^1$ and (b) $\mathbb{P}_h^3$. For more information, see [Hecht, 2020b].

denote the triangles that make up the finite element mesh as T_k for $k = 1, 2, .., N$, where N denotes the number of triangles of the mesh.

For all triangles T_k on the mesh Ω, if P_1 denotes the set of polynomials of $\mathbb{R}^2$ of degree ≤ 1 then the finite element space $\mathbb{P}_h^1$ takes the form:

$$\mathbb{P}_h^1 = \{\underline{v} \in H^1(\Omega) \mid \forall k \in T_h, v_{|k} \in \mathrm{P}_1\} \tag{2.39}$$

where $H^1(\Omega)$ denotes a Hilbert space. A Hilbert space is a complete inner product space, where the inner product is defined by:

$$||\underline{v}|| = \sqrt{(\underline{v}, \underline{v})} \quad \text{where} \quad (\underline{v}, \underline{v}) = \int_\Omega \underline{v}^2 \; d\Omega.$$

Knowing that the set P_3 denotes the set of polynomials of $\mathbb{R}^2$ of degrees ≤ 3, the finite element space $\mathbb{P}_h^3$ takes the similar form:

$$\mathbb{P}_h^3 = \{\underline{v} \in H^1(\Omega) \mid \forall k \in T_h, v_{|k} \in \mathrm{P}_3\} \tag{2.40}$$

In comparison to triangles in $\mathbb{P}_h^1$, which have 3 nodes related to the velocity, located at the vertices, triangles in $\mathbb{P}_h^3$ have 9 nodes, shown in fig. 2.4.

For finite element space in $\mathbb{P}_h^1$ (see both fig. 2.4(a) and eq. (2.39)), for each vertex q^{k_i} located on a triangle T_k, there is a basis function $\phi_k(x, y)$ of order 1 for all $x, y \in T_k$. The basis function takes the form [Hecht, 2012]:

$$\phi_k(x, y) = a_i^k + b_i^k x + c_i^k y \text{ for } (x, y) \in T_k \tag{2.41}$$

$$\phi_k(q^j) = 1 \tag{2.42}$$

$$\phi_k(q^i) = 0 \text{ if } i \neq j. \tag{2.43}$$

For finite element space $\mathbb{P}_h^3$, the basis function becomes a function of order 3 as suggested by the illustration in fig. 2.4. We denote nodal basis functions of the finite element spaces for velocity and pressure as $\{\phi_i\}_{1\leq i\leq N}$ and $\{\xi_i\}_{1\leq i\leq K}$, respectively. For a mesh of N triangles, FreeFem++ approximates all $\underline{u}$ and p as functions of $\hat{\underline{u}}$ and $\hat{p}$ as [Hecht, 2020b]

$$\hat{\underline{u}} = \sum_{j=1}^{N} \underline{u}_i \phi_i \quad \hat{p} = \sum_{j=1}^{K} p_i \xi_i. \tag{2.44}$$

In addition to this, FreeFem++ also approximates $\underline{v}$ and q from eq. (2.36) as $\hat{\underline{v}}$ and $\hat{q}$:

$$\hat{\underline{v}} = \sum_{j=1}^{N} \underline{v}_j \phi_j \quad \hat{q} = \sum_{j=1}^{K} q_j \xi_j. \tag{2.45}$$

Substituting the approximations $\hat{\underline{u}} \in \mathbb{R}^N$ and $\hat{\underline{v}} \in \mathbb{R}^K$ in eqs. (2.44) and (2.45) into the weak form of the Stokes equations eqs. (2.36) and (2.37) gives an equivalent system of the form:

$$\begin{bmatrix} \mathcal{A} & \mathcal{B} \\ \mathcal{B}^T & 0 \end{bmatrix} \begin{bmatrix} \hat{\underline{u}} \\ \hat{p} \end{bmatrix} = \begin{bmatrix} 0 \\ 0 \end{bmatrix} \tag{2.46}$$

where $\mathcal{A} \in \mathbb{R}^{N\times N}$ and $\mathcal{B} \in \mathbb{R}^{K\times N}$ take the form [Reusken, 2020]:

$$\mathcal{A}_{ij} = \int_{\Omega} 2\nabla\phi_i.\nabla\phi_j \; d\Omega$$

$$\mathcal{B}_{ij} = -\int_{\Omega} \xi_i \nabla.\phi_j \; d\Omega.$$

which is solved by FreeFem++ [Hecht, 2020e] using the Uzawa Algorithm and conjugate gradients [Glowinski, 2003; Glowinski and Pironneau, 1978; Roberts and Thomas, 1993] (see [Hecht, 2020d]). We label the finite element space which contains the velocity components by V_h, which is "a space of continuous functions affine in x and y on each triangle T_k" [Hecht, 2020e].

2.2.2.5 Boundary conditions

A no-slip boundary condition is easy to implement in FreeFem++ [Hecht, 2020e], and is defined as scalar-valued Dirichlet boundary condition. The Dirichlet boundary condition [Morse and Feshbach, 1954] is used to apply a constant value to the velocities or pressure on the relevant boundaries. To implement the boundary condition on the velocity in FreeFem++ at the boundary b_i, the no-slip case takes the form [Hecht, 2020e]:

$$\mathrm{on}(b_i, u_x = 0, u_y = 0).$$

The Navier slip condition is more tricky to implement. In FreeFem++, we are required to write the condition in weak form (see eq. (2.36)). As the slip velocity at the channel walls is dependent on the strain-rate, the condition becomes an integral of the velocity gradient over the boundaries. In order to write the Navier slip (eq. (2.25)) in weak form [Karapetsas and Mitsoulis, 2013; Venkatesan and Ganesan, 2015], we multiply by the test function on velocity $\underline{v} \in V$ and integrate over the boundary of the channel wall:

$$\int_{\partial\Omega} \underline{u}.\underline{v} = \beta \int_{\partial\Omega} \left(\underline{\underline{\dot{\gamma}}}.\underline{\hat{n}}\right).\underline{v} \; d\Omega. \tag{2.47}$$

The boundary condition is solved by FreeFem++ along with eq. (2.46) using the Uzawa Algorthim [Glowinski, 2003; Glowinski and Pironneau, 1978; Roberts and Thomas, 1993]. The accuracy of the Navier slip condition will be verified by using the analytical results. The results for $\beta \to 0$ match the no-slip solutions.

2.2.2.6 Mesh

Here we discuss the finite element meshes generated by FreeFem++ in our simulations. At the start of each simulation, the text file (extension - edp) is executed by FreeFem++ which builds a mesh, either by importing mesh commands by loading a (G)msh file used to create 3D meshes, or by using the "*buildmesh*" command [Hecht, 2020c]. We use the latter "*buildmesh*" command, which constructs the mesh using a list of defined boundaries.

The boundaries of the mesh, labelled by b_i, are expressed as functions of x and y, using the command "*border*". The boundaries are defined as piecewise parametrized curves and they can only intersect at the endpoints of each curve. For each boundary b_i, an integer value $k \in \mathbb{Z}$ is given, which indicates the number of nodes taken at each boundary (edge) to produce the mesh, such as $b_i(k)$. The sign of integer k indicates the orientation of the boundary points, with $k > 0$ indicating that the node orientation is on the left with respect to parametrised boundary direction. More information can be found on the FreeFem++ website [Hecht, 2020c].

The "*buildmesh*" command uses the defined boundaries b_i to triangulate the mesh and the mesh gets finer with increasing k. One can set an upper bound for the value of vertices taken on the mesh using the parameter "*nbvx*", which can be a useful parameter for mesh adaption between iterations. The mesh fineness can be adjusted between iterations using "*adaptmesh*". The "*adaptmesh*" function in FreeFem++ [Hecht, 2012] uses a "anisotropic mesh generator" [Hecht, 1998] which allows one to adapt the location of mesh nodes between iterations.

Roquet and Saramito [2003] suggest that implementing an adaptive mesh in their finite element simulations provides a more accurate representation of the locations and shapes of the plug regions [Roquet et al., 2000]. Roquet and Saramito [2003] used an adaptive mesh method to concentrate points in regions of large velocity gradients in a flow of Bingham fluid around a cylinder (and for slip in a square pipe [Roquet and Saramito, 2008]). Concentrating points at these locations in the channel allow us to define a smooth and definite boundary between both regions.

We measure mesh fineness as the amount of triangles per unit area, N/A_c. The meshes used in the straight channel case has an even distribution of triangles across the mesh due to the simplicity of the flow. For more complex situations such as the curved channel case in chap. 4 and the sinusoidal channel in chap. 5, some regions on the mesh require a greater mesh fineness N/A_c to determine the yield surfaces positions.

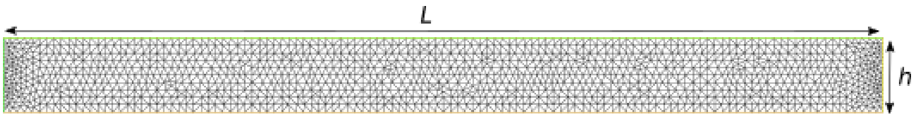

Figure 2.5: An example of a finite element mesh for a straight channel of length $L = 10$ and $h = 1$ on FreeFem++.

We plot an example of a straight channel mesh in fig. 2.5. The mesh is defined by 4 boundaries, two horizontal boundaries of length $L = 10$ connected to two vertical boundaries of length $h = 1$. As we consider a steady Stokes flow, the analytical velocity profile has no dependence on the x-position, providing that the x-position is far enough away from the channel inlet (and outlet). The inflow and outflow effects are considered for both the straight channel and curved channels in chapters 3 and 4, respectively.

2.2.2.7 Calculating the plug area

We characterize the effectiveness of foam in sclerotherapy by quantifying the size of the plug region within the vein. We concluded in chap. 1.4.4 that the large (apparent) viscosity of the foams' rigid plug region provides a stable and effective displacement of blood. We use the constitutive equations (eqs. (2.16-2.17)) to provide a criterion for identifying the regions of fluid within the plug and use numerical methods to calculate the area of plug for each considered channel geometry. Treskatis et al. [2016] states that the regularised models have some "numerical noise" near the yield surfaces. It is therefore a requirement to introduce a parameter, labelled as B_ϵ, to define the boundaries of the yielded and plug regions as satisfying $|\underline{\underline{\tau}}| = \frac{1}{2}\left(B + B_\epsilon\right)$, where B_ϵ is of the order 10^{-3} [Dimakopoulos et al., 2018] (shown to be the case in chap. 3.5.2). One can think of B_ϵ as a small simulation parameter which helps to identify the location of the yield surfaces and provide accurate plug areas (i.e. matching the numerical and analytical plug areas).

In order to find the plug area of fluid, denoted by A_p, we integrate over a step function $H(|\underline{\underline{\tau}}|)$ in eq. (2.48) below, which is dependent on the stress and identifies whether fluid is contained in the plug region or not. The step function gives a value of 1 where the stress exerted on the fluid is equal or less than the quantity $\frac{1}{2}\left(B + B_\epsilon\right)$ and 0 for the fluid where the stress $|\underline{\underline{\tau}}|$ is greater than $\frac{1}{2}\left(B + B_\epsilon\right)$. The step function takes the form

$$H(|\underline{\underline{\tau}}|) = \begin{cases} 1 & |\underline{\underline{\tau}}| \leq \frac{1}{2}\left(B + B_\epsilon\right) \\ 0 & |\underline{\underline{\tau}}| > \frac{1}{2}\left(B + B_\epsilon\right). \end{cases} \tag{2.48}$$

In the chapters to follow, we consider the relative plug area, which compares the plug area with the total channel area, denoted by A_t. The total channel area is found by integrating 1 over the channel domain Ω and matches the analytical value for the area exactly. The values of B_ϵ are identified in a straight channel for a range of Bingham numbers in chap. 3.5.2, which are then used to identify plug areas in more complex channel geometries (chaps. 4.7 and 5).

Freefem++ uses a quadrature formula [Hecht, 2020f] to calculate the values of integrals over the two-dimensional mesh. We do not only identify the plug areas using integrals but also the flow rate Q of fluid, which is found by integrating the speed over a domain of channel Ω in the FreeFem++ simulations:

$$Q = \iint_{\Omega_s} |\underline{u}| \; d\Omega. \tag{2.49}$$

In the following chapters, we use these numerical methods to determine the effectiveness of foam (characterized as a Bingham fluid) in sclerotherapy for several vein-like geometries.

3 A flow of a Bingham fluid in a straight channel

3.1 Introduction

Due to the existence of a yield-stress in foam (chap. 1.4.2.3), we model the foam as a Bingham fluid (see chap. 2). We consider this as a basic model of a flow of foam through straight veins. In this chapter, we will consider the flow of a pressure-driven Bingham fluid through a straight channel with the Navier slip [Navier, 1823] boundary condition and consider the special case $\beta = 0$ as the no-slip condition. The well-known analytical velocity profile for a Bingham fluid, shown in chap. 3.3, is derived from the governing Stokes equations and used to validate the accuracy of our finite element simulations in chap. 3.5.

For a Bingham fluid with a no-slip boundary condition, the velocity profile is well known (fig. 3.1) and has been derived by Bird et al. [1983]. A derivation of an analytical flow profile of a Poiseuille flow of viscoplastic fluid with wall slip has also been considered by several groups, such as Potente et al. [2006], Kalyon and Malik [2012] and Ellahi et al. [2010] (Oldroyd fluid), and the result for a Bingham fluid is shown in eq. (3.20).

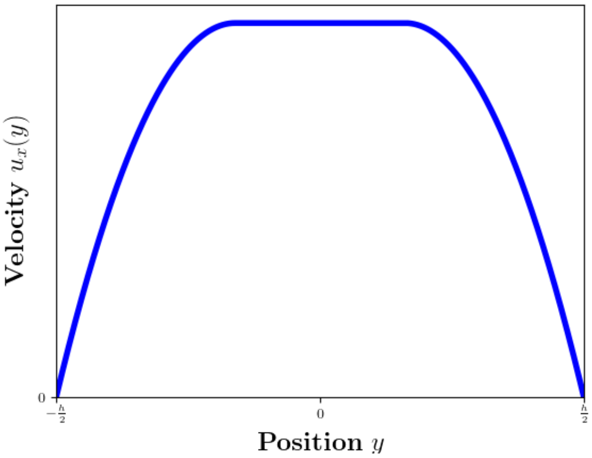

Figure 3.1: An example of a velocity profile of a Bingham fluid through a straight channel.

For the simulation of arterial walls, the usual no-slip condition is commonly used [Bux-

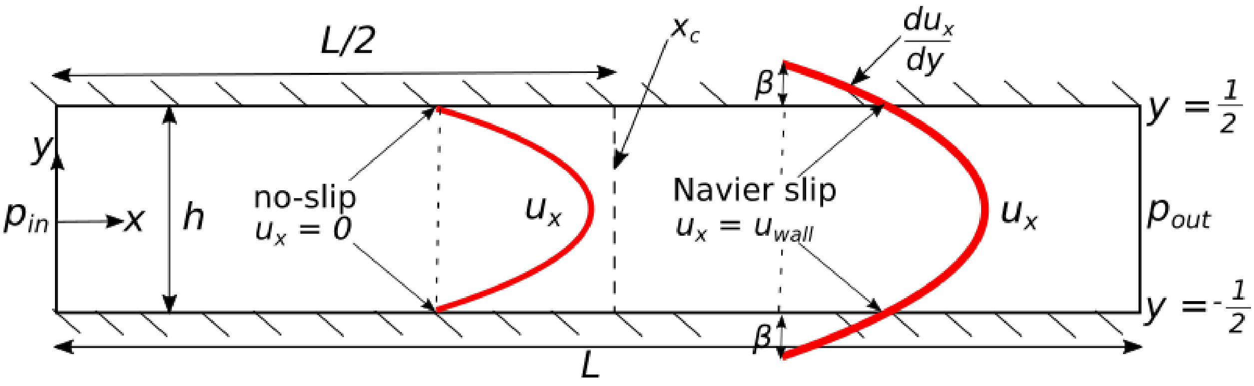

Figure 3.2: A diagram of the flow profiles and boundary conditions of a flow of Newtonian fluid in a straight channel for the case $\beta = 0$ (no-slip) and non-zero slip lengths β.

ton and Clarke, 2006; Chow and Mak, 2006; Pedley et al., 2000], but the presence of slip was theoretically justified for arterial walls by Brunn [1975] and experimentally by Bennett [1967] and has been since become an investigated phenomenon [Misra and Shit, 2007; Reddy and Srikanth, 2015; Sinha et al., 2013]. In the application of foam in sclerotherapy, it is not evident that a no-slip boundary condition is the appropriate choice for veins. Therefore, we will present analytical velocity profiles for a range of slip lengths.

For a Bingham fluid, we produce an error analysis, evaluating the disparity between the analytical velocity profile and the simulation velocity data. This allows us to obtain the optimal values for each of the simulation parameters, which produce small error values per mesh point, of the order 10^{-4}, and assert confidence in the numerical simulations. The error is measured for several mesh and convergence parameters.

3.2 Governing equations

The foam flows within veins are considered to be relatively slow due to the slow injection during the treatment (for example 2 – 2.5ml over 10 – 15 seconds [Bradbury et al., 2010]). For a foam with density $\rho = 125\text{kg/m}^3$, flowing through a vein of width $h = 5\text{mm}$ at a velocity of 3mm/s provides a flow with a small Reynolds number of $Re = 1.875 \times 10^{-2}$. We therefore assume that Re (eq. (2.3)) is small, with a typical foam speed of around 3mm/s.

We also make the assumption that the flow is steady and laminar (no time dependence), to maintain a steady displacement of blood form the vein. The assumptions allow us to consider the Stokes equations.

Therefore, we consider a steady, slow and unidirectional flow of Bingham fluid through a straight channel of width h, of the same geometry as in fig. 3.2. The fluid is driven by a constant pressure gradient G acting in the x-direction, which can be written in terms of the inlet and outlet pressures p_{in} and p_{out} and the length of the channel L:

$$G = \frac{p_{out} - p_{in}}{L}. \tag{3.1}$$

The Stokes' equations (shown in tensorial form in eq. (2.6)) equate the pressure gradient to the divergence of the stress. For a unidirectional flow of Bingham fluid through a straight channel, the only non-zero components of the stress and strain rate tensors $\underline{\underline{\tau}}$ and $\underline{\underline{\dot{\gamma}}}$ are τ_{xy} and $\dot{\gamma}_{xy}$ (eq. (2.9)) and the only non-zero component of velocity is $u_x(y)$, which allows us to write the Stokes' x-momentum equation in the form:

$$-G = \frac{\partial}{\partial y}\left(\tau_{xy}\right). \tag{3.2}$$

Along with this equation, we consider the constitutive equation that characterises a Bingham fluid [Bingham, 1922], outlined previously in eqs. (2.13-2.14). The constitutive equation takes a linear form:

$$\begin{aligned} \tau_{xy} &= \pm\tau_0 + \mu\frac{\partial u_x}{\partial y} && \text{for} \quad |\tau_{xy}| > \tau_0 \\ \dot{\gamma}_{xy} &= 0 && \text{for} \quad |\tau_{xy}| \leq \tau_0. \end{aligned} \tag{3.3}$$

The ± that appears from the constitutive equation is required as the stress is positive on the channel wall $y = h/2$ and negative on the other at $y = -h/2$.

At the channel walls we impose the Navier slip boundary condition [Navier, 1823], which allows the fluid to satisfy no-slip, partial slip and full slip. The condition states that the velocity at the channel wall is determined by the strain rate normal to the wall $\dot{\gamma}_{xy}$ and a slip length β. From fig. 3.2, we deduce that the Navier slip condition in a straight channel takes the form

$$\mp \frac{du_x}{dy}\bigg|_{y=\pm h/2} = \frac{u_x}{\beta}\bigg|_{y=\pm h/2} \iff u_x\bigg|_{y=\pm h/2} = \mp\beta\frac{du_x}{dy}\bigg|_{y=\pm h/2}. \tag{3.4}$$

The sign change in eq. (3.4) is required as the gradient of velocity changes sign due to the axisymmetry of the velocity profile (fig. 3.3) and assures that the speed is positive at each wall. The gradient $\frac{\partial u_x}{\partial y}$ is positive at the top wall (at $y = h/2$) and negative at the bottom wall (at $y = -h/2$).

We consider the governing equations in dimensionless form relative to the non-dimensional quantities in eq. (2.4), where the length scale is equal to the channel width h and the velocity scale can be written in terms of the pressure-gradient $U = Gh^2/\mu$:

$$y^* = \frac{y}{h}, \quad u_x^* = \frac{u_x\mu}{Gh^2}, \quad \underline{\nabla}^* = h\underline{\nabla}, \quad \underline{\underline{\tau}}^* = \frac{\underline{\underline{\tau}}}{Gh}, \quad \beta^* = \frac{\beta}{h}. \tag{3.5}$$

Equation (3.2) becomes

$$-1 = \frac{\partial}{\partial y^*}\left(\tau^*_{xy}\right), \tag{3.6}$$

and eq. (3.3) becomes:

$$\begin{aligned} \tau^*_{xy} &= \pm\tfrac{1}{2}B + \frac{\partial u_x^*}{\partial y^*} && \text{for} \quad |\tau^*_{xy}| > \tfrac{1}{2}B \\ \dot{\gamma}^*_{xy} &= 0 && \text{for} \quad |\tau^*_{xy}| \leq \tfrac{1}{2}B. \end{aligned} \tag{3.7}$$

Both the yield-stress of the fluid τ_0 and the viscosity μ are absorbed into the dimensionless Bingham number, which is a measure of the importance of yield stress to viscous stress:

$$B = \frac{2\tau_0}{Gh}. \tag{3.8}$$

The value of the Bingham number B depends on both the fluids' properties and the flow itself. Large Bingham numbers result from a slow flow of fluid, which can be caused by either a large yield-stress τ_0 or small pressure gradient G driving the flow. B also depends on the width of the channel h, with narrower channels resulting in larger Bingham numbers. We include an additional factor of two in the numerator of eq. (3.8), in order to be consistent with the non-dimensional terms used for a pressure-driven Bingham fluid through an annulus in chap. 4. We show illustrations of the flow profiles for $B = 0$ in fig. 3.2 and for non-zero B in fig. 3.3.

The Naiver slip condition, eq. (3.4), in dimensionless form becomes

$$u_x^*\bigg|_{y=\pm 1/2} = \mp\beta^* \frac{\partial u_x^*}{\partial y}\bigg|_{y=\pm 1/2}. \tag{3.9}$$

From this point onwards in the chapter, we drop the asterisk notation denoting dimensionless quantities.

3.3 Analytic solution

First of all, we focus our interest on the yielded regions of the channel, where the value of the xy-component of the stress is taken to be greater than $\frac{1}{2}B$. These regions are located close to the walls, where the large stresses are induced by the fluid interaction with the channel wall. We integrate eq. (3.6) with respect to y to find a solution for the stress profile

$$\tau_{xy} = -y + C \tag{3.10}$$

where C denotes a constant of integration. The integration constant can be set to zero by the condition that $\dot{\gamma}_{xy} = 0$ at $y = 0$ as u_x is symmetric about the channel centreline. We can therefore write the stress profile as

$$\tau_{xy} = -y, \tag{3.11}$$

which is linear in y and independent of the fluid yield stress (and hence the Bingham number B), plotted in fig. 3.5. This means that the yield surfaces $\mp y_c$, which are the points in the channel where the magnitude of the stress is equal to $\frac{1}{2}B$ are symmetric about $y = 0$, as indicated in fig. 3.3. We apply this condition to eq. (3.11) in order to find an expression for y_c in terms of B:

$$\tau_{xy}\Big|_{y=\mp y_c} = (-y)\Big|_{y=\mp y_c} = -(\mp y_c) = \pm\frac{1}{2}B \implies y_c = \frac{1}{2}B. \tag{3.12}$$

These yield surfaces are plotted with the stress profiles in fig. 3.5, displaying the linear relationship between the stress and the y-position along the cross-section.

Given the stress profile, we can substitute the expression of the stress in the yielded region (eq. (3.7)) into eq. (3.11). As the flow profiles are symmetric about the channel centerline ($y = 0$) [Bird et al., 1983], we consider the case $y > 0$:

$$\frac{du_x}{dy} = -y + \frac{1}{2}B. \tag{3.13}$$

We integrate eq. (3.13) with respect to y in order to find the velocity in terms of y, B and integration constant D:

$$u_x = -\frac{1}{2}y^2 + \frac{1}{2}By + D. \tag{3.14}$$

The value of D is determined by applying the Navier slip boundary conditions (eq. (3.9)). We can substitute the expressions found in eq. (3.13) and (3.14) into the Navier slip condition (eq. (3.9) at $y = 1/2$:

$$\left(-\frac{1}{2}y^2 + \frac{1}{2}By + D\right)\Bigg|_{y=1/2} = -\beta\left(-y + \frac{1}{2}B\right)\Bigg|_{y=1/2} \tag{3.15}$$

which allows us to express D in terms of B and β:

$$D = \frac{1}{8} - \frac{1}{4}B + \frac{1}{2}\beta\left(1 - B\right). \tag{3.16}$$

The expression for D can be substituted back into eq. (3.14) in order to find the velocity profile in the yielded region:

$$u_x = \frac{1}{2}\left(\left(\frac{1}{2}\right)^2 - y^2\right) - \frac{1}{2}B\left(\frac{1}{2} - y\right) + \frac{1}{2}\beta\left(1 - B\right). \tag{3.17}$$

By considering the same derivation for the yielded region with $y < 0$, we see a change in sign for the term of order y, meaning that the velocity profile for the yielded regions becomes

$$u_x = \frac{1}{2}\left(\left(\frac{1}{2}\right)^2 - y^2\right) - \frac{1}{2}B\left(\frac{1}{2} - |y|\right) + \frac{1}{2}\beta\left(1 - B\right). \tag{3.18}$$

Once we know the velocity profile for both yielded regions, the plug velocity is easy to find. The fluid within the plug is moving at constant speed, $u_x = U_0$, for some constant U_0, which can be derived from the constitutive equation (3.7):

$$\frac{\partial u_x}{\partial y} = 0 \implies u_x = U_0$$

The value of the constant U_0 is determined by making sure that the velocity is continuous between the yielded and plug regions. We match the velocities at $y = y_c$, using eq. (3.18) and that for the plug region, $u_x = U_0$:

$$U_0 = \frac{1}{2}\left(\left(\frac{1}{2}\right)^2 - y_c^2\right) - \frac{1}{2}B\left(\frac{1}{2} - |y_c|\right) + \frac{1}{2}\beta\left(1 - B\right).$$

From the above, we deduce that the plug velocity takes the form:

$$u_x = \frac{1}{2}\left(\left(\frac{1}{2}\right)^2 - y_c^2\right) - \frac{1}{2}B\left(\frac{1}{2} - |y_c|\right) + \frac{1}{2}\beta\left(1 - B\right). \tag{3.19}$$

We combine both equations (3.18) and (3.19) to find the full velocity profile:

$$u_x(y) = \begin{cases} \frac{1}{2}\left(\left(\frac{1}{2}\right)^2 - y^2\right) - \frac{1}{2}B\left(\frac{1}{2} - |y|\right) + \frac{1}{2}\beta\left(1 - B\right), & \text{for} \quad |y| > y_c, \\ \frac{1}{2}\left(\left(\frac{1}{2}\right)^2 - y_c^2\right) - \frac{1}{2}B\left(\frac{1}{2} - |y_c|\right) + \frac{1}{2}\beta\left(1 - B\right), & \text{for} \quad |y| \leq y_c. \end{cases} \tag{3.20}$$

where y_c denotes the yield surface found in eq. (3.12). This analytical velocity profile will be the basis for the validation of our numerical simulations of a Bingham fluid through straight channels. The yield surfaces y_c (eq. (3.12)) move towards the walls of the channel as B increases. The flow of fluid ceases when the yield surfaces reach the channel walls i.e. when $y_c = \frac{1}{2}$. Therefore, using eq. (3.12), the value of B at which the fluid becomes stationary is

$$y_c = \frac{1}{2}B = \frac{1}{2} \implies B = 1. \tag{3.21}$$

This means that the Bingham number is bounded between 0 and 1, where $B = 0$ indicates the results for a Newtonian fluid and at $B = 1$, the fluid becomes stationary.

We can use the velocity profile in eq. (3.20) to derive an expression for the one-dimensional flow rate Q, which (in this 2D example) is the area of fluid which passes a cross-section per unit time. We can integrate eq. (3.20) with respect to y between $-1/2$ and $1/2$ to find the flow rate Q and consider its value for different values of B and β. The flow rate is

$$\begin{aligned} Q = & \int_{-1/2}^{1/2} u_x(y)\ dy = 2\int_{y_c}^{1/2} u_x(y)\ dy + 2\int_{0}^{y_c} u_x(y)\ dy \\ = & \frac{1}{12} - \frac{1}{8}B + \frac{1}{12}B^3 + \frac{1}{2}\beta\left(1 - B\right). \end{aligned} \tag{3.22}$$

From the conclusions in eq. (3.21), we see that $Q = 0$ when $B = 1$.

3.4 Results

By setting $B = 0$ in eq. (3.20), the flow profiles for a Poiseuille flow of Newtonian fluid with no-slip (setting $\beta = 0$) and Navier slip ($\beta > 0$) (also given by [Ferrás et al., 2012; Matthews and Hill, 2007]) boundary conditions are derived. In fig. 3.2, we sketch the boundary conditions in the straight channel case and give an examples of a parabolic velocity profile in the absence of yield-stress for the cases of no-slip and slip (eq. (3.9)).

The one-dimensional flow of Bingham fluid through a straight channel with no-slip

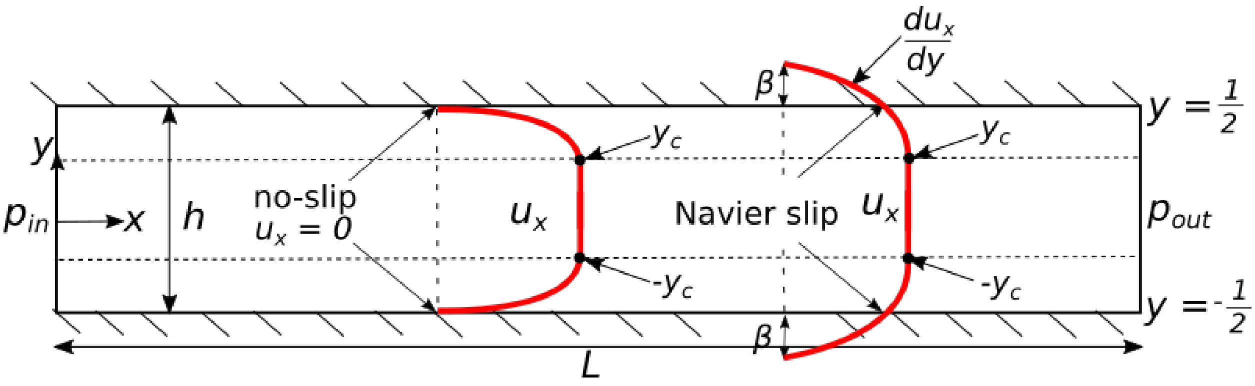

Figure 3.3: The geometry of the straight channel, showing the flow profile of a pressure driven Bingham fluid which satisfies the no-slip boundary condition. The pressure gradient is defined by the inlet and outlet pressure, p_{in} and p_{out} respectively.

($\beta = 0$) has been a focus of many authors throughout the 20th century, in particular the velocity profile in Poiseuille flow of Bingham fluid [Bird et al., 1983], shown in eq. (3.20) (as well as other flow profiles have also been derived [Norouzi et al., 2015; Taylor and Wilson, 1997]). The stability of the Poiseuille flow was considered by Frigaard et al. [1994] who performed a linear stability analysis; results show the stabilizing effect of an increasing yield stress (albeit for a flow dominated by inertial effects i.e. large Re). For the application of foam in sclerotherapy, increasing the value of the yield-stress of a foam i.e. making B larger, would increase stability of the flow as is desired.

In fig. 3.3, we show the channel geometry and flow profile of a Bingham fluid. For positive B, the parabolic yielded regions are separated by a rigid plug region of width B, located at the centre of the channel.

3.4.1 Velocity

For a flow of pressure-driven Bingham fluid through a straight channel with an implemented Navier slip condition, we derived an expression for the flow profile u_x in eq. (3.20) (also derived by Damianou and Georgiou [2014]) with the yield surface position equal to $y_c = \frac{1}{2}B$, according to eq. (3.12). In fig. 3.4, we plot the velocity profile from eq. (3.20) by varying both the slip length β and Bingham number B.

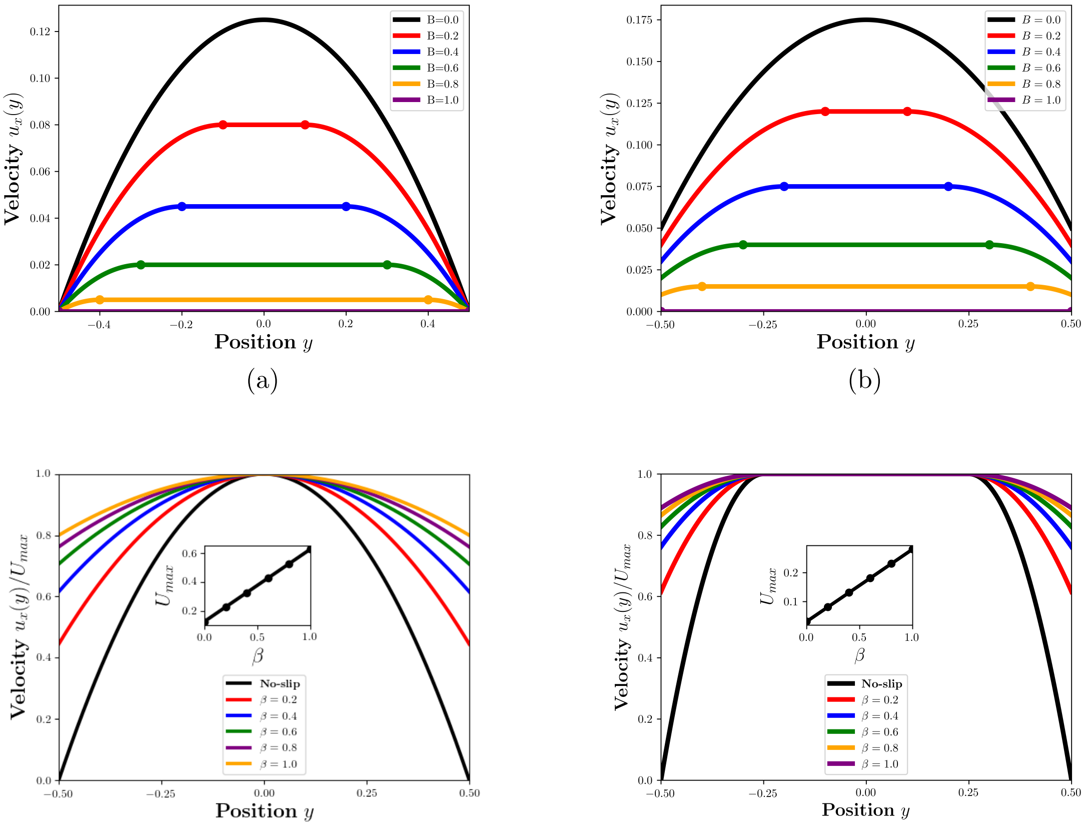

(a) (b)

(c) (d)

Figure 3.4: For a pressure-driven Bingham fluid in a straight channel, we plot the velocity profile u_x for: (a) $\beta = 0$ and a range of B between 0 and 1, (b) $\beta = 0.1$ and a range of B between 0 and 1, (c) $B = 0$ for a range of β between 0 and 1 and (d) $B = 0.5$ for a range of β between 0 and 1. For (c) and (d), we scale by the maximum velocity U_{max} in each case.

The flow profile of a Newtonian fluid ($B = 0$) for the no-slip case ($\beta = 0$) is a well-known parabolic profile is shown in fig. 3.4(a), with a maximum velocity located at the centre of the channel ($y = 0$) of value $U_{max} = \frac{1}{8}$. When B is non-zero, we see the appearance of yield surfaces, marked by dots, and a plug region located at the centre of the channel, moving with $U_{max} = \frac{1}{8}(1 - B)^2$. The width of the plug region increases with B, causing the yield surfaces to move closer towards the walls of the channel. A large plug region is more suitable in industrial and medical applications, in particular for the purpose of a displacement of another immiscible fluid [Frigaard et al., 2017]. In addition to this, increasing the value of B causes the fluid velocity to decrease as less of the fluid is un-yielded by the choice of

B. This means that the flow rate of the fluid also reduces as Bingham number is increased until the fluid becomes stationary for $B = 1$.

In fig. 3.4(b), we fix a slip length of $\beta = 0.1$ and vary the value of B between 0 and 1. As expected, the fluid with the smallest value of B has the largest velocity, with the fluids' velocity decreasing with increasing B before becoming stationary at $B = 1$. The yield surfaces (described by eq. (3.12)) are independent of β and move linearly towards the channel walls with increasing B. This is useful information from an industrial application standpoint as one would be able to maintain a constant plug width of the Bingham fluid through pipes and increase the velocity (and flow rate) of the fluid with the addition of slip, as the plug region is the useful part for displacing other fluids [Frigaard et al., 2017].

In fig. 3.4(c), by setting $B = 0$ in eq. (3.20), we plot u_x for values of β between 0 and 1, scaled by the maximum velocity U_{max}. This parabolic velocity profile again has a maximum value located at the centre of the channel ($y = 0$), equal to $U_{max} = \frac{1}{8} + \frac{1}{2}\beta$. By increasing β, we see the velocity increases by $\frac{1}{2}\beta$ everywhere, thus the velocity (and flow rate) increases with larger slip lengths as expected. The wall velocity increases relative to the maximum velocity with increasing β and for $\beta = 1$, the velocity at the wall becomes $u_\theta = \frac{4}{5}U_{max}$.

By fixing a value of $B = 0.5$ in fig. 3.4(d), we consider u_x scaled by $U_{max} = \frac{1}{8}(1 - B)^2 + \frac{1}{2}\beta(1 - B)$ for different slip lengths β and notice similar behaviour as seen for the case $B = 0$ (fig. 3.4(c)). We regain the no-slip profile by setting $\beta = 0$ in eq. (3.20), where the velocity is stationary at the walls of the channel. As B increases, the value of the velocity at the wall becomes closer to U_{max}. For example, choosing $\beta = 1$, the value of the velocity at the walls is close to 90% the value of U_{max}, 10% more than the case for $B = 0$. The yield surfaces are located in the same position for each value of β as they are only dependent on B. Also, the value of maximum velocity increases with β for fixed B.

The velocity profile derived in eq. (3.20) is used to validate the accuracy of the numerical simulations for both slip lengths $\beta = 0$ and 0.1 in chap. 3.5.1. The flow profile will also be the benchmark for the curved channel analytical velocity profile in the limit of infinitely small channel curvature.

3.4.2 Shear stress

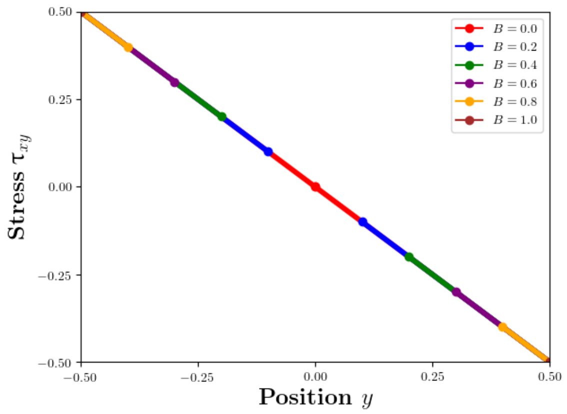

Figure 3.5: The stress profile τ_{xy} (eq. (3.11)) for a Bingham fluid through a straight channel. The profile is independent of Bingham number B and slip length β and depends only on the y-position in the channel. The yield surfaces are denoted by markers for each value of B.

The stress profile τ_{xy} (eq. (3.11) is axisymmetric about the centreline of the channel, equal to zero at the channel centreline (as is the strain rate) and linear in y, plotted in fig. 3.5. It is unchanged for non-zero B and β, although the region where the stress is defined becomes smaller with increasing B (see eq. (3.7)). The stress profiles are important in a yield stress fluid, where the positions of the yield-surfaces (denoted by dots) are dependent on the value of stress and the stress is undefined for τ_{xy} less than $\frac{1}{2}B$ (i.e. between the markers in fig. 3.5), where the strain rate is zero. As B is increased, the width of the plug region increases, meaning that the stress is only defined in the yielded region close to the channel walls. For a Bingham fluid (and in fact a Newtonian fluid) flowing through a straight channel, the maximum stress $|\tau|_{max}$ occurs at the channel walls $y = \pm\frac{1}{2}$ with $|\tau|_{max} = \frac{1}{4}$.

3.4.3 Flow rate

We derive an expression for the one-dimensional flow rate Q in eq. (3.22) in terms of B and β. From fig. 3.4(b) and (d), we can deduce that increasing the value of B will certainly decrease the value of Q until it becomes zero at $B = 1$. By fixing the Bingham number B, Q will become larger with increasing β, as the velocities increase by $\frac{1}{2}\beta(1 - B)$ everywhere for each β.

We derive an expression for the flow rate Q (eq. (3.22)) in order to investigate how the yield-stress, channel geometry (chaps. 4 and 5) and wall slip effects the flow rate of fluid. The flow rate of a Newtonian fluid with slip is derived by setting B to zero in eq. (3.22):

$$Q = \frac{1}{12} + \frac{1}{2}\beta. \tag{3.23}$$

As expected, for $\beta = 0$ (i.e. no-slip), $Q = \frac{1}{12} \approx 0.083$. The inclusion of the Navier slip condition introduces an extra $\frac{1}{2}\beta$ factor to the flow rate, thus by setting a non-zero value for β, the flow rate increases.

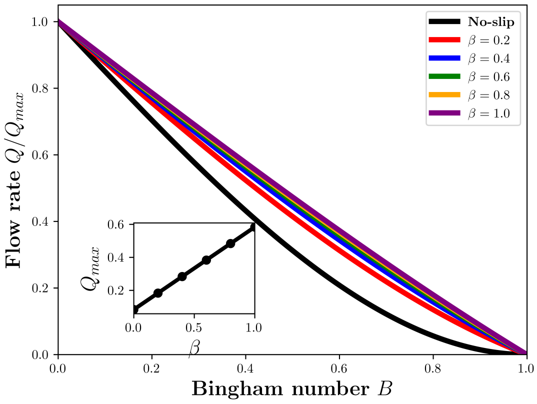

Figure 3.6: The flow rate Q (eq. (3.22) of a Bingham fluid through a straight channel with slip as a function of B for different values of the slip length β and scaled by Q_{max} (equal to eq. (3.23)).

In fig. 3.6, we consider the flow rate Q/Q_{max} as a function of B for different values of

β. We scale Q by Q_{max} (the flow rate for the case $B = 0$ for each β in eq. (3.23)) so that all cases scale to 1 at $B = 0$. Setting $\beta = 0$ (no-slip), we see that Q/Q_{max} decreases linearly with increasing B for $B \leq 0.6$. For $B > 0.6$, we see the cubic term in eq. (3.22) starting to influence the value of flow rate Q, meaning that the gradient of the curve saturates as the fluid nears the point of becoming stationary. At $B = 1$, we see the flow rate Q become equal to zero as the flow ceases at the point where the yield surfaces have reached the channel walls. Increasing the value of β from zero causes the relationship between Q/Q_{max} and B to become more linear for all B, since the term involving β in eq. (3.22) dominates the B^3 term.

We also consider the value of Q_{max} against β, noticing that Q_{max} increases with slip length β. One should note that the fluid's flow rate Q is equal to the area under the flow profiles shown in fig. 3.4, thus we clearly see that with increasing B, the value of Q decreases.

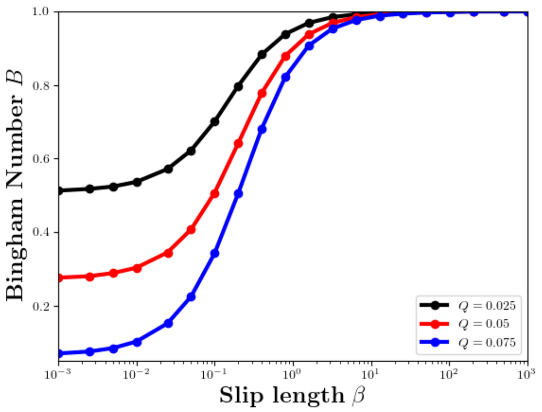

Figure 3.7: The relationship between Bingham number B and slip length β for fixed flow rates $Q = 0.025$, 0.05 and 0.075, described by eq. (3.22).

To maintain a constant flow rate Q, one needs to consider the relationship between the yield-stress τ_0, the driving pressure gradient G as well as the channel width h, all captured by the Bingham number (eq. (3.8)). For the no-slip case, fixing the Bingham number B is sufficient to maintain Q, so that for a fixed channel width h, the ratio of τ_0/G must be constant (i.e. larger τ_0 requires larger G and vice versa).

For non-zero slip length β, fixing the flow rate Q of a flow of Bingham fluid in a straight channel (or pipes in industrial applications), one would need to achieve a balance between the value of the Bingham number B and slip length β. The value of the flow rate for the case $\beta = 0$ ranges between $\frac{1}{12} \approx 0.083$ (eq. (3.23)) and 0, depending on the value of B, so fixing the value of Q for a range of β would require Q to fall between those values. For example, we set Q to 0.025, 0.05 and 0.075 in fig. 3.7 and see that for small slip lengths $\beta \leq 10^{-3}$, that the value of B required to maintain Q is around 0.51, 0.27 and 0.07, respectively. For small slip lengths β, fixing a value of Q closer to $\frac{1}{12}$ decreases the value of B towards 0 and fixing smaller flow rates Q closer to 0, the value of B required would increase and become closer to 1 (and for $Q = 0 \implies B = 1$ for each β i.e. fluid is stationary).

As the slip length β is increased from 10^{-3} to 10^{1}, the value of B required to fix Q is sharply increased to close to 1, as the fluid needs to be nearly at the point of becoming stationary to prevent the fluids' velocity getting very large. This trend continues for $\beta > 10^{1}$ as the B gets ever closer to 1 with increasing slip length β.

3.5 Simulation validation

Here we investigate the accuracy of our FEM simulations. The difference between the derived analytical velocity profiles (eq. (3.20)) and the numerical data produced by the finite element simulation (chap. 2.2.2) is labelled as the error ϵ. This error is measured as a function of the mesh fineness N/A_c, denoting the number of triangles per unit area, regularisation parameter m, related to the implemented viscosity model (eq. (2.31)) and the convergence parameter δ (eq. (2.38)), determining the extent of convergence. In addition to this, we consider the choice of the finite element space of the velocities on the accuracy of our simulation, choosing between $\mathbb{P}_h^1$ and $\mathbb{P}_h^3$.

We start by defining the error as a mathematical quantity. For each mesh node, the value of velocity is taken with reference to a mesh co-ordinate (x_j, y_j). As the analytical velocity profile u_x, depends only on the y-position, we calculate the value of u_x in eqn. (3.20) for each y_j. We compute the value of the error by calculating the rms root of the sum of the squared differences between u_{sim}, the numerical data, and u_x at each point y_j. The last part needed to define ϵ is to divide by the number nodes on the mesh M. This gives us a measure of the expected error on each particular node

$$\epsilon = \frac{1}{M}\sqrt{\sum_j \left(u_{sim}(x_j, y_j) - u_x(y_j)\right)^2} \tag{3.24}$$

and can be thought to be the value of the errorbar on each entry of velocity data. We will use eq. (3.24) to validate the simulation in both straight and curved channel geometries (chap. 4).

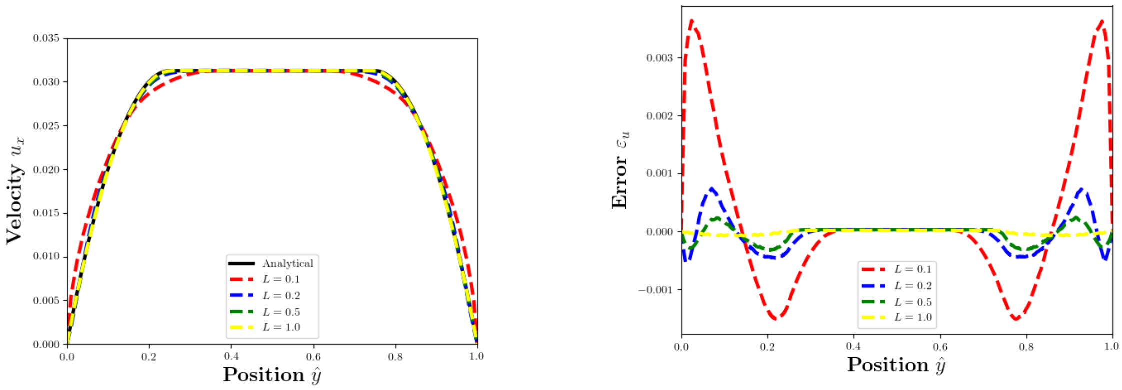

(a) (b)

Figure 3.8: (a) The velocity data for u_x with $B = 0.5$ in a straight channel for different values of channel lengths L, with the data taken from a cross-section x_c, located $L/2$ away from the channel inlet and outlet (fig. 3.2), (b) The difference between both the simulation data and analytical velocity profiles $\varepsilon_u = u^{sim} - u^{anal}$ associated with finite size.

To determine the appropriate "awayness", we investigate different velocity cross-sections of a channel of length L and width h. The fluid flows in response to a pressure gradient which is set by a difference in pressure at the inlet and outlet. By fixing the outlet pressure to zero ($p_{out} = 0$), the inlet pressure p_{in} is set so that the pressure gradient is equal to one, thus depends on the length of the channel. We fix a no-slip boundary condition at the channel walls.

In fig. 3.8(a), we show the velocity data for u_x with $B = 0.5$ and $\beta = 0$ taken at a cross-section at x_c, located directly at the centre of a straight channel i.e. $L/2$ away from the channel inlet (fig. 3.3) for different channel lengths L, and plot against the respective analytical velocity profile (eq. (3.20)). The disparities between both curves is easier seen by considering the quantity $\varepsilon_u = u^{sim} - u^{anal}$ (fig. 3.8(b)). We see distinct differences between the analytical prediction and the red curve denoting $L = 0.1$, shown in fig. 3.8(b), suggesting that the velocity is influenced by an inflow or outflow effect. Increasing L to 0.2 and 0.5, allows us to obtain a good agreement between the velocity data and analytical flow profile (shown in eq. (3.20), with slight disparities near the yield surfaces and yielded regions. Increasing to $L = 1$ shows little difference between both, highlighted by quantity ε_u in fig. 3.8(b).

We conclude that to avoid the inflow and outflow effects on the values of velocity u_x and numerical error ϵ, we must exclude the data from the inflow and outflow sections of length 0.5. For all cases in chap. 3.5.1, we have a straight channel of length $L = 5$ and $h = 1$, thus the channel area is $A_c = 5$ (which is equal to 4 when neglecting the inflow and outflow sections of length 0.5). The value of the error is calculated on the area of channel (a half width) away from the inflow and outflow regions, which allows us to avoid any additional increase to the quantity ϵ that would be incurred by including data tainted by the entrance effects. In order to avoid the finite-length effects of the channel inlet and outlet, one could impose an exact solution boundary condition as we know the form of the velocity profile. This would remove the need to consider the difference between the analytical and numerical velocity at the inlet and outlet.

3.5.1 Error analysis

A error analysis is performed for slip lengths $\beta = 0$ (no-slip) and $\beta = 0.1$ in order to attain confidence in the accuracy of the implementation of the Navier slip boundary condition. Wall slip is implemented by writing the Naiver slip condition (eq. (2.25)) in weak form as shown in eq. (2.47). We set a slip length of $\beta = 0.1$ as an upperbound for our numerical simulation, as larger slip lengths decrease the accuracy of the numerical methods [Karapetsas and Mitsoulis, 2013]. Here, the influence of the values of tolerance δ, regularisation parameter m as well as the mesh fineness N/A_c on the error ϵ is investigated.

For choices of m less than 100, the accuracy of the regularized viscosity model decreases significantly (as expected by fig. 2.2). Abdali et al. [1992] suggest that a choice of $m > 100$ provides a good estimation of Bingham plastic behaviour. Abdali et al. [1992] and Ellwood et al. [1990] suggest that using values larger than $m = 10^4$ has no effect on their results. Indeed in our case, we see no improvement in the accuracy of results for any choice of m greater than 5000. Smyrnaios and Tsamopoulos [2001] results on a squeeze flow of Bingham fluid suggest that for each order of B, there exists a critical value of exponent m for which above it the results are unaffected by the choice of m. For sufficiently small m, the results become dependent on its value. We choose a range of m between 100 and 5000 as an appropriate span to investigate the influence of the regularisation parameter.

In fig. 3.9, the error ϵ decreases as the tolerance δ becomes smaller, meaning that the accuracy of the simulation improves for smaller δ. This is expected as a small δ indicates that the difference in the sum of velocities between iterations is small i.e. velocities become settled. For larger tolerances $\delta \geq 10^{-2}$, the values of ϵ for all m follow the same trend and are mostly inseparable. These larger tolerances are too big for our purpose, which allows the simulation to terminate before fully “converging”, hence providing larger values of ϵ.

For $\delta \leq 10^{-5}$, we gain little accuracy as the error saturates for all m. This suggests that $\delta = 10^{-5}$ is an optimum value for tolerance δ which provides an accurate solution with ϵ of order 10^{-4}. The effect of increasing m causes the error ϵ to decrease and provide a more accurate prediction of a flow of Bingham fluid. By taking into account the conclusions from the associated literature [Abdali et al., 1992; Ellwood et al., 1990; Smyrnaios and Tsamopoulos, 2001] and the results in fig. 3.9, we select an optimal value of $m = 5000$.

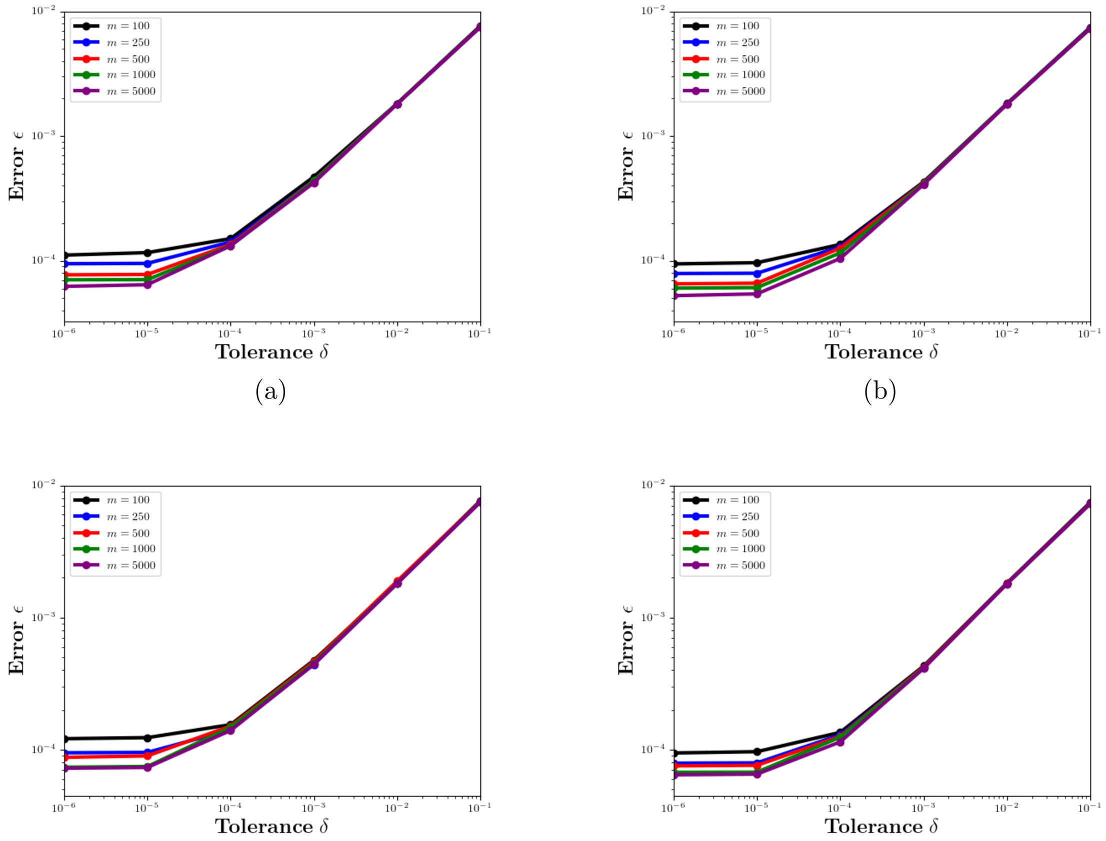

(a) (b)

(c) (d)

Figure 3.9: The error ϵ against the value of the tolerance δ for different values m. The simulation was executed with $B = 0.5$ and $N/A_c = 19.6 \times 10^3$: (a) for the velocities in $\mathbb{P}_h^1$ with $\beta = 0$, (b) for the velocities in $\mathbb{P}_h^3$ with $\beta = 0$, (c) for the velocities in $\mathbb{P}_h^1$ with $\beta = 0.1$, (d) for the velocities in $\mathbb{P}_h^3$ with $\beta = 0.1$

By direct comparison of fig. 3.9, the error ϵ is reduced for $\mathbb{P}_h^3$ in comparison to $\mathbb{P}_h^1$ for each regularisation parameter m. For $\delta = 10^{-5}$ and $m = 5000$, the error ϵ for $\beta = 0$ decreases by 18% from 6.42×10^{-5} to 5.42×10^{-5} by choosing $\mathbb{P}_h^3$ (fig. 3.9(b)) over $\mathbb{P}_h^1$ in (fig. 3.9(a)). For $\beta = 0.1$, we see an 11% decrease in the error ϵ by choosing $\mathbb{P}_h^3$ (fig. 3.9(d)) over $\mathbb{P}_h^1$ (fig. 3.9(c)). This indicates that a choice of finite element space $\mathbb{P}_h^3$ for the velocities provides a more accurate results in comparison to $\mathbb{P}_h^1$.

In fig. 3.10, we consider the error ϵ for a range of tolerances δ and different mesh fineness N/A_c for both finite element spaces and slip lengths $\beta = 0$ and 0.1 with $m = 5000$. For each

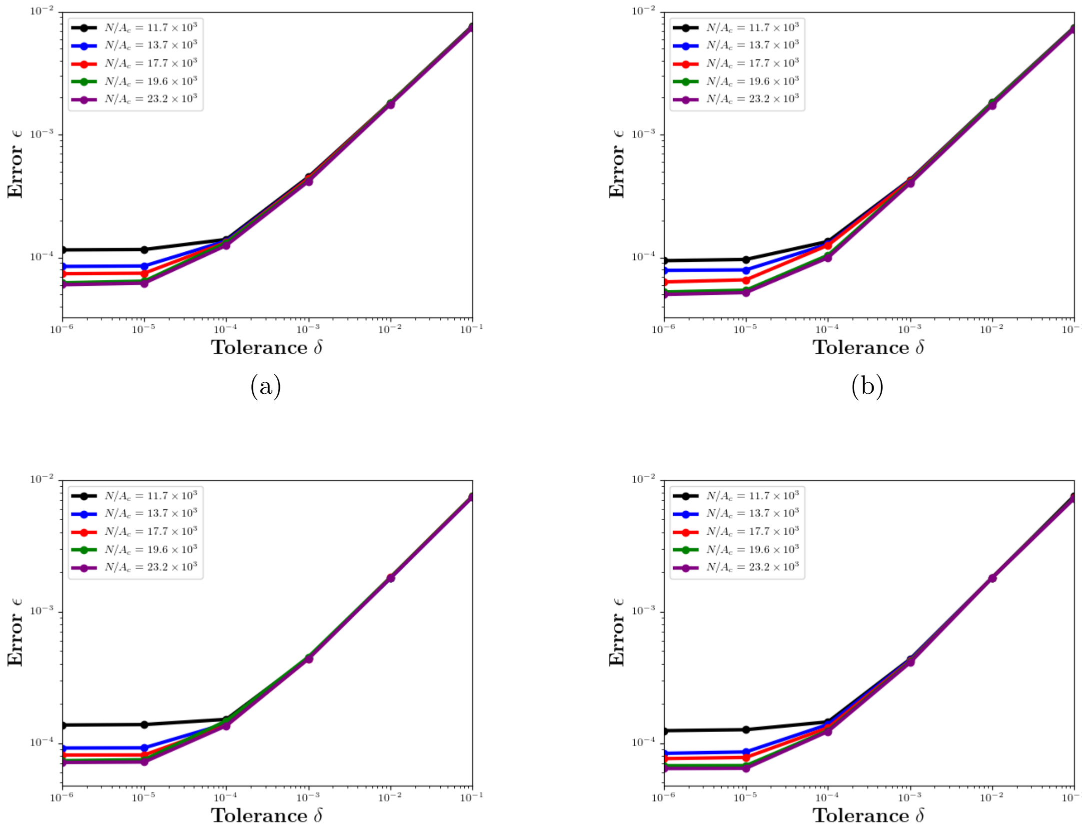

(a) (b) (c) (d)

Figure 3.10: The error ϵ against the value of the tolerance δ for different mesh fineness N/A_c. The simulation was executed with $B = 0.5$ and $m = 5000$: (a) for the velocities in $\mathbb{P}_h^1$ with $\beta = 0$. (b) for the velocities in $\mathbb{P}_h^3$ with $\beta = 0$. (c) for the velocities in $\mathbb{P}_h^1$ with $\beta = 0.1$. (d) for the velocities in $\mathbb{P}_h^3$ with $\beta = 0.1$.

simulation, the channel area remains constant $A_c = 4$ (by excluding the inflow and outflow channel sections as suggested by fig. 3.8). Increasing mesh fineness N/A_c causes the error ϵ to decrease as expected. The error curves for the two finest meshes N/A_c (which provide the smallest values of ϵ for each δ) more or less overlap, suggesting that we gain very little accuracy (at most 3%) by increasing N/A_c from 19.6×10^3 to 23.2×10^3. We therefore deduce that the smallest value of the two is a sufficient to provide accurate results for both the finite element space $\mathbb{P}_h^1$ and $\mathbb{P}_h^3$.

For $N/A_c = 19.6 \times 10^3$ in fig. 3.10, the results for $\mathbb{P}_h^3$ yields more accurate solutions for slip lengths $\beta = 0$ and $\beta = 0.1$ in comparison to $\mathbb{P}_h^1$ i.e. the error ϵ reduces by 18% and

12%, respectively. Using the optimal simulation parameters and velocity in $\mathbb{P}_h^3$, ϵ is equal to 5.42×10^{-5} and 6.75×10^{-5} for $\beta = 0$ and $\beta = 0.1$, respectively. The addition of wall slip increases ϵ by 25%.

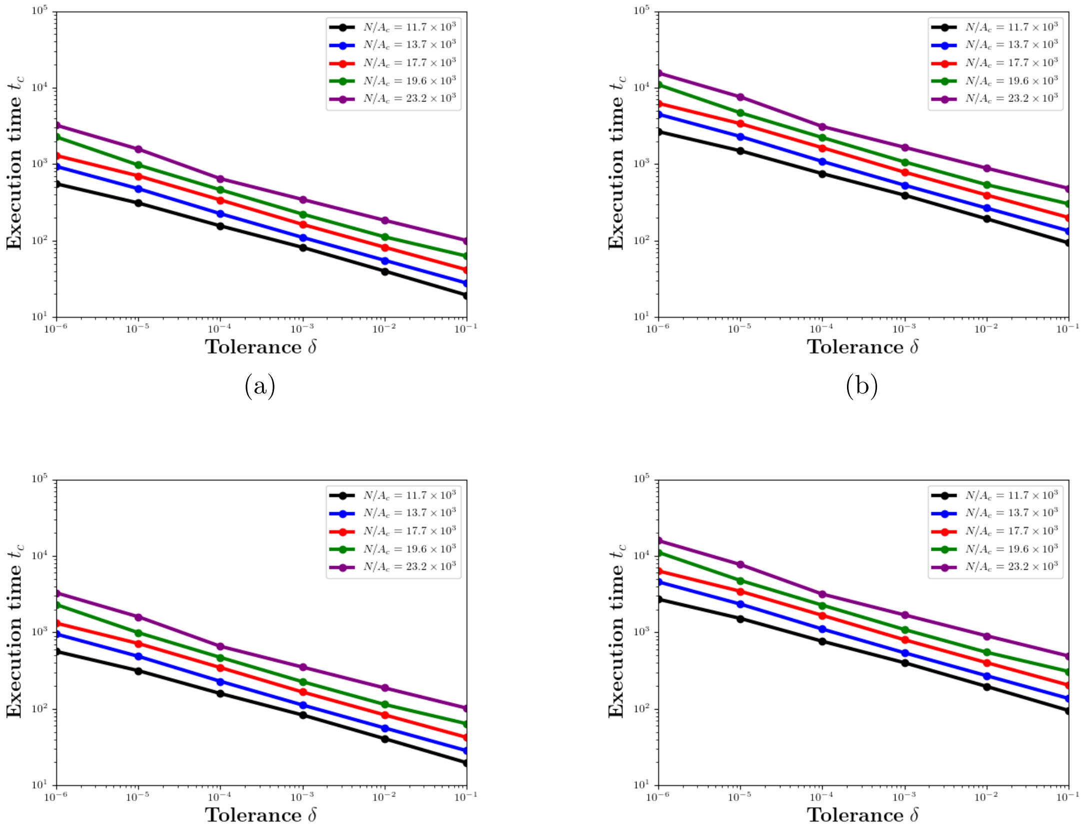

(a) (b)

(c) (d)

Figure 3.11: The execution time for each simulations for different tolerances with $m = 5000$: (a) for the velocities in $\mathbb{P}_h^1$, with $\beta = 0$, (b) for the velocities in $\mathbb{P}_h^3$, with $\beta = 0$, (c) for the velocities in $\mathbb{P}_h^3$, with $\beta = 0.1$, (d) for the velocities in $\mathbb{P}_h^3$, with $\beta = 0.1$.

In fig. 3.11, we consider the relationship between mesh fineness N/A_c on the the execution time t_c for the simulation. The execution time is the time taken for the simulation to run through the iterations until convergence has been reached (satisfying eq. (2.38)), which increases as the tolerance δ decreases and N/A_c increases. The gradient of the slope m_s of the execution time against δ remains roughly constant for all simulations in all cases and is estimated using

$$\log(t_c) = m_s \log(\delta) \implies t_c = \delta^{m_s} \tag{3.25}$$

and is $m_s \approx -0.2$. The results for $\beta = 0$ in figs. 3.10 and 3.11 show a 3% gain in the accuracy between meshes $N/A_c = 19.6 \times 10^3$ and $N/A_c = 23.2 \times 10^3$ (for $m = 5000$ and $\delta = 10^{-6}$), but the computation time increases by 42% for both finite element spaces, from 37.8 minutes to 53.9 minutes and 182.4 to 259.6 minutes for $\mathbb{P}^1_h$ and $\mathbb{P}^3_h$, respectively. For $\beta = 0.1$, there is a 45% increase in the execution times for the same simulation parameters, suggesting that the Navier-slip condition has no significant effect on the computation time ($\approx$ 1.8% increase). The simulations that involve $\mathbb{P}^3_h$ take considerably longer to converge in comparison to $\mathbb{P}^1_h$ i.e. for $\delta = 10^{-6}$ and $N/A_c = 23.2 \times 10^3$, the former takes an additional three hours to converge compared to the latter. Using the gradient m_s, we can use this estimation of the execution time for simulations of any mesh fineness N/A_c.

To conclude, we have determined the optimal values for parameters δ, m and N/A_c that provide the most accurate approximation of a pressure-driven Bingham fluid through a straight channel for slip lengths $\beta = 0$ and 0.1. The optimal values are determined by evaluating the value of the error ϵ (eq. (3.24)), a measure of the disparity between the simulation data and analytical profile, per node. The optimal values list as $m = 5000$ and $N/A_c = 19.6 \times 10^3$ and $\delta = 10^{-5}$, and the velocities should be contained in finite element space $\mathbb{P}^3_h$. This produces an error of $\epsilon = 5.42 \times 10^{-5}$ and 6.75×10^{-5} for $\beta = 0$ and 0.1, respectively. By running the simulation with the velocities contained in $\mathbb{P}^3_h$ compared to $\mathbb{P}^1_h$ yield more accurate solutions (although the computation time becomes over 4 times longer). One could potentially reduce the error further by introducing an adaptive mesh process as seen in the work by Saramito and Roquet [2001] and Roquet et al. [2000].

3.5.2 Identifying the plug regions

Here we identify the values of B_ϵ (discussed in chap. 2.2.2.7), which is a small simulation parameter which allows us to identify the correct locations of the plug regions and yield surfaces in a straight channel by assuring that the simulated plug area is in agreement with the analytical prediction. The requirement for a small parameter was also cited by both

Treskatis et al. [2016] and Dimakopoulos et al. [2018], to deal with “noise” near the yield-surfaces in regularised models. The requirement and value of B_ϵ is related to our choice of regularisation paramter m. For each m, there exists a critical value of the strain rate at which below it, the results are inaccurate. The range of strain rates at which results are inaccurate becomes smaller as the regularisation parameter is increased. This critical strain rate discussed here is related to the value of B_ϵ. We will show below that the estimated values of B_ϵ are of the order 10^{-3} and vary little over a range of B, which is the case when $m = 5000$.

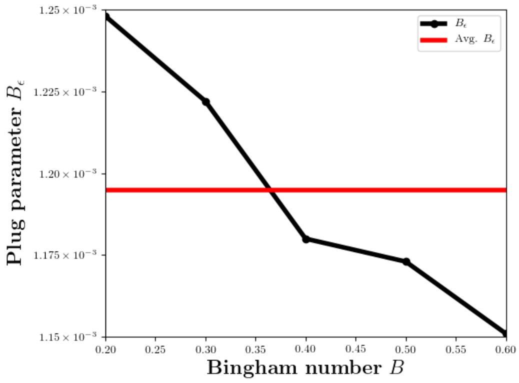

Figure 3.12: The values of B_ϵ for a range of B between 0.2 and 0.6 with mesh fineness $N/A_c = 19.6 \times 10^3$ and regularisation parameter $m = 5000$. We also calculate the average value of B_ϵ, which is equal to 1.195×10^{-3}.

The values of B_ϵ are approximated when the simulated plug areas (relative to the total channel area) is equal to the analytical prediction for a channel of width 1. We adjust the value of B_ϵ until the simulated areas satisfy criterion

$$\frac{A_p}{A_t} = B, \tag{3.26}$$

with A_p and A_t denoting the plug and total area (see §2.2.2.7). As mentioned above, the value of B_ϵ is associated with our choice of regularisation parameter, which is $m = 5000$ from sec. 3.5. The ideal values for B_ϵ which satisfy the criterion in eq. (3.26) are shown in fig. 3.12 for a range of B between 0.2 and 0.6 and mesh fineness $N/A_c = 19.6 \times 10^3$ (fig. 3.10). The value of B_ϵ varies very little for all B (±4% in comparison to the average of $B_\epsilon \approx 1.195 \times 10^{-3}$) and at most 0.6% in comparison with the size of its respective Bingham number. We see that the values of B_ϵ decrease with increasing B from 1.248×10^{-3} for $B = 0.2$ to 1.151×10^{-3} for $B = 0.6$.

As the values of B_ϵ are of the order 10^{-3}, one could imply that they are inversely proportional to the value of m i.e. $B_\epsilon \approx 1/5000$. Additionally, as the choice of B_ϵ is affected by m, one could also notice how the values of B_ϵ are weakly affected by the choice of Bingham number from the Papanastasiou [1987] viscosity model (shown in eq. (2.31)). The results in fig. 3.12 indicate that the simulation requires a greater value of B_ϵ as B gets smaller to accurately estimate the plug areas for fixed $m = 5000$. This could be due to the larger speed of the fluid for smaller B (i.e. larger velocity gradients), which makes it harder to identify the locations of the yield surfaces as the gradient the viscosity model (which is inversely proportional to the strain rate in eq. (2.31)) increases in the yielded regions.

3.6 Concluding remarks

In chap. 3.4, we have presented analytical velocity profiles for a flow of pressure-driven Bingham fluid through a straight channel with the Navier slip boundary conditions (chap. 2.1.5). The velocity profile in eq. (3.20) suggests that the addition of slip sees an addition of a quantity $\frac{1}{2}\beta(1 - B)$ to the velocity at each position. We present the velocity in figs. 3.4(c) and (d) scaled by the its maximum velocity U_{max}, where we see that the velocity at the channel walls increases (relative to U_{max}) with increasing slip length β.

One measure of the performance of foam in sclerotherapy is the proportion of the channel that is filled by the unyielded plug region. Both the plug and yielded regions are determined by the locations of the yield surfaces, the positions at which the stress $|\underline{\underline{\tau}}|$ is equal to $\frac{1}{2}B$, according to the constitutive equation (eq. (3.7)). The yield surfaces in the straight channel depend only on the Bingham number and are independent of the slip length β (eq. (3.12)), therefore the effectiveness of the foam for sclerotherapy through straight veins is not affected by the presence of wall slip.

By integrating the flow profiles, an expression for the flow rate Q was derived (eq. (3.22)). According to fig. 3.7, the relationship between the Bingham number and slip length is considered in order to fix a flow rate Q of Bingham fluid. This could be useful in industrial applications of viscoplastic fluids and will be considered for curved channels. To fix a flow rate Q in fig. 3.7, for small slip lengths β requires a small Bingham number B and for larger slip lengths β, B is required to be close to 1, in order to prevent the flow rate becoming very large.

The flow profiles, derived from the governing Stokes equations (eq. (3.2)), are used here to validate the accuracy of our simulation data. We consider the effect of varying δ (eq. (2.38), m (eq. (2.31) and N/A_c on the accuracy of the simulation results, captured by ϵ in eq. (3.24). The error for both the no-slip and slip cases is small ($\leq 10^{-4}$) and are both of the same order, for $m = 5000$, $N/A_c = 19.6 \times 10^3$ and $\delta = 10^{-5}$. This reassures us that the results approximating the flow of Bingham fluid through straight are realistic and accurate.

From figs. 3.9 and 3.10, we determine optimum values for the simulation parameters ($\delta = 10^{-5}$, $m = 5000$ and $N/A_c = 19.6 \times 10^3$) with the velocities in $\mathbb{P}_h^3$. The optimum values of δ, m and N/A_c for the slip boundary conditions are the same as for the no-slip case and implementing slip has little effect on the accuracy (fig. 3.10) or execution time (fig. 3.11) of the simulation.

In preparation for later chapters, we calculate the values for plug parameter B_ϵ using the finite element simulation over a range of B. The values of B_ϵ allow us to match the analytical prediction of plug area satisfying eq. (3.26). The plug areas are calculated using the methods introduced in chap. 2.2.2.7, by integrating over step-function $H(\underline{\underline{\tau}})$ (eq. (2.48)). This will allow us to measure any additional yielding of the plug region that occurs in more complex vein geometries (in chaps. 4 and 5) relative to the case for a straight vein.

The finite element simulation on FreeFem++ [Hecht, 2012] is now validated for the straight channel geometry. We investigate more complex channel geometries in chaps. 4 and 5, to investigate the effectiveness of foam in sclerotherapy and how the geometry of the vein impairs or improves its performance. The plug region of fluid is the essential region for displacing the blood within the vein (as mixing occurs in the yielded regions) and is proportional to the value of B. So for a straight channel (or vein), the effectiveness of the foam in the treatment solely depends on the value of B. The larger the value of B, the wider the plug region and the less mixing that occurs between the foam and blood. This statement is consistent with both no-slip and slip cases. This is not true for more complex channel geometries, such as an annulus (chap. 4). One should note that although the size of the plug region is not affected by slip, the foam velocity within the vein would be greatly affected by β, as U_{max} is proportional to β (fig. 3.4), which should also be considered during treatment.

4 A flow of a Bingham fluid in a curved channel

4.1 Introduction

To widen the applicability of the results in chap. 3, we consider the one-dimensional, steady flow of a Bingham fluid through a curved channel. We derive analytical velocity profiles for a Bingham fluid flowing through a curved channel (or annulus), applying wall slip to the channel walls.

We consider the slow 2D pressure-driven (Poiseuille) flow of a Bingham fluid in a curved duct. The curvature of the channel κ is determined by the ratio of the channel width h and the radius of curvature of the channel midline R_c i.e. $\kappa = h/R_c$. The Dean number is defined as the product of the Reynolds number Re (defined in eq. (2.3)) and the square root of the curvature κ:

$$De = Re\sqrt{\kappa}.$$

As we consider a creeping flow of fluid in this thesis, the Reynolds number is assumed to be small (of the order 10^{-2} - see §3.2). The channel curvature κ in our simulations is considered to be less than one. Therefore, the Dean number is assumed to be small ("creeping" Dean flow), so that we neglect inertia, centripetal forces and any consequent secondary flows. In chap. 4.2 we give the governing equations of the flow, the constitutive equation for the fluid, and outline our solution, which requires determination of the radial positions of the yield surfaces. We describe predictions for the velocity and stress fields for the Navier slip condition in chap. 4.5, considering slip lengths between 0 and h.

We consider special cases for the problem, such as the flow profiles in the absence of yield stress i.e. a Newtonian fluid by setting B to zero, or in the absence of wall slip i.e. the no-slip case with $\beta = 0$. We therefore have four distinct cases to investigate (as in chap. 3), with the case for a Bingham fluid with no-slip shown also in [Roberts and Cox, 2020].

In presenting our results for $B \neq 0$, we scale the Bingham number B by its critical value B_c, to represent the magnitude of the yield stress, and for all cases shift radial position to represent distance from the inner wall of the channel, $\hat{r} = r - \frac{1}{\kappa}$. These analytical profiles will be benchmarks for the finite element simulations of Bingham fluid flow in an annulus as well as a more complex channel geometry in chap. 4.7.

Using the same analyses as for the straight channel, we conduct an error analysis for the curved channel case. Considering the disparities between the simulation data and the analytical velocity profiles, derived in chap. 4.3, allows us to evaluate the accuracy of the results produced by the simulations in a curved channel geometry for both slip lengths $\beta = 0$ and 0.1. We expect the errors to be larger for the latter as the velocities grow in relation to the value of the slip length β.

Upon validation, we tie up the findings from both chapters 3 and 4 by describing the numerical simulations of the flow of a Bingham fluid from a straight into an annulus (considered in [Roberts and Cox, 2020]) in chap. 4.7. We describe the distance over which the velocity profile makes the transition from one solution to another and consider the amount of plug "lost" due to the flow transitioning from the straight to curved channel geometry. Finally, in chap. 4.8, we discuss the implications of our work for flow in narrow curved channels, such as the yielding of the foam that occurs during the process of varicose vein sclerotherapy.

A Newtonian fluid flowing in a curved channel was considered by Gibson and Cook [1974], Lighthill and Rosenhead [1963] and Joshi and Denn [2003], but the original derivation of the velocity profile is unknown. Lamb [1993] derived a solution of both velocity and flow rate in an annular channel. Dean [1928] considered for a flow of pressure-driven fluid between two stationary concentric cylinders spaced by length d, where d is considerably smaller than the radius of the inner cylinder R_i as does Gibson and Cook [1974].

The literature for the slip boundary condition for Newtonian fluids on curved surfaces is sparse. Neto et al. [2005] suggests that wall slip is dependent on the boundary curvature. In addition to this, Chen et al. [2014] state that the Navier slip condition is readily extended to surfaces of any shape, and the velocities close to the wall are proportional to the local strain rate. Fan et al. [2001] considered a flow of both viscous and viscoplastic fluid through a curved channel, noting that a drag of a viscoplastic flow in a curved pipe is larger than that of a corresponding straight pipe, even for small deviations. Norouzi et al. [2018] conducted a theoretical study of an Oldroyd-B fluid through a curved pipe with wall slip. The work provides a benchmark for numerical simulations and experimental investigations of polymer flow, using first order perturbations to characterise on the onset of secondary flows for values of Re, β and the Weissenberg number We, the ratio of elastic to viscous forces.

Wall slip on curved boundaries has been intensely investigated for Newtonian fluids. Einzel et al. [1990] suggested that the slip length β required an additional contribution due to channel curvature, seconded by Tibbs et al. [1997]. The conclusions drawn from their experimental work supports that a more valid approximation of wall slip experienced by a fluid in a curved boundary is in fact the velocity of the fluid is proportional to the strain rate component normal at the wall ($r\theta$-component), not the gradient of velocity normal to the wall [Einzel et al., 1990; Tropea and Yarin, 2007] as Navier [1823] (and later Maxwell [1878]) suggested. We see the additional contribution of channel curvature by expanding the expression for the $r\theta$ component of the strain rate, which is the only non-zero component of the strain rate that exists for the considered flow in a curved channel:

$$\dot{\gamma}_{r\theta} = r\frac{\partial}{\partial r}\left(\frac{u_\theta}{r}\right) = \frac{\partial u_\theta}{\partial r} - \frac{1}{r}u_\theta. \tag{4.1}$$

This is a justification for using the expression for the strain rate in the Navier slip boundary condition. Notice that this reduces to the chap. 3 case in the limit $R_i \to \infty$ as the second term in eq. (4.1) becomes negligible.

A great deal of work on Bingham fluids is concerned with Couette flow [Bird et al., 1983], as in a Couette viscometer, in which the fluid is held between concentric cylinders and one of the cylinders moves tangentially. Away from the laboratory, many flows of yield stress fluids are pressure-driven, often in curved or bent pipes [Spedding et al., 2004]. To the best of our knowledge, closed form analytic solutions for pressure-driven flow in an annulus have not been previously derived. Norouzi et al. [2015] proposed the use of an infinite series solution for the velocity profile in a curved three-dimensional channel with a rectangular cross-section. We take a different approach and, for simplicity, consider the equivalent 2D case, but seek a closed form expression for the velocity and stress profiles.

4.2 Governing equations

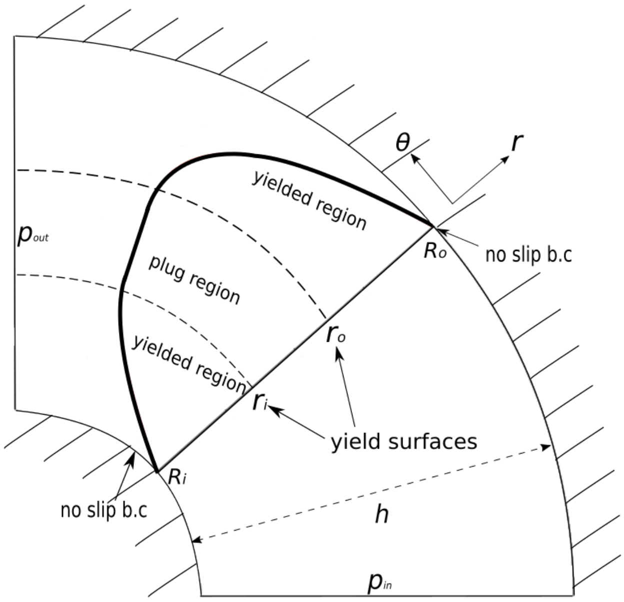

Figure 4.1: The diagram indicates the geometry of the channel under consideration. Relative to plane polar coordinates r and θ, the channel has inner radius R_i and outer radius R_o. Fluid flows in the positive θ direction due to a pressure difference $p_{\text{in}} - p_{\text{out}}$. An example of a velocity profile is shown in red, with a plug region between yield surfaces at $r = r_i$ and $r = r_o$.

We consider the steady, unidirectional flow of a Bingham fluid in the annular channel shown in fig. 4.1, described by polar coordinates r and θ. The annulus has inner and outer radii R_i and R_o respectively, giving a channel of width $h = R_o - R_i$.

The fluid moves in response to a constant pressure gradient G acting in the θ-direction, which can be written in terms of the inlet and outlet pressures p_{in} and p_{out} and the position of the centreline of the channel, $R_c = \frac{1}{2}(R_i + R_o)$ as $G = (p_{out} - p_{in})/\theta R_c$. Here we impose a fixed pressure gradient along the midline of the channel (at $r = R_c$) by selecting the inlet p_{in} and outlet p_{out} pressures to appropriate scalar values such that $G = 1$ at $r = R_c$. Note therefore that the pressure gradient G always appears with the length-scale R_c [Norouzi et al., 2015; Rieger and Šesták, 1973] to take into account that the distance between the ends of the annular region increases with r. Therefore, the effective pressure gradient at each r should decrease with increasing radial position as $G \approx (p_{out} - p_{in})/\theta r$.

According to Stokes' equations this pressure gradient is balanced by the divergence of the stress. For this unidirectional flow the only non-zero component of the stress tensor $\underline{\underline{\tau}}$ is $\tau_{r\theta}$ (chap. 3.2), so this becomes

$$-\frac{R_c}{r}G = \frac{1}{r^2}\frac{\partial}{\partial r}\left(r^2\tau_{r\theta}\right). \tag{4.2}$$

Similarly, the only non-zero component of the strain-rate tensor $\underline{\underline{\dot{\gamma}}}$ is the $r\theta$ component and the fluid velocity is $u_\theta(r)$. In consequence, the tensorial form of the constitutive equation for a Bingham fluid [Denn and Bonn, 2011] simplifies and the condition for yielding no longer requires calculation of the second invariant of the strain-rate tensor but becomes simply $|\tau_{r\theta}| > \tau_0$ (as in chap. 3.2). The constitutive equation is therefore linear:

$$\begin{aligned} \tau_{r\theta} &= \pm\tau_0 + \mu r\frac{\partial}{\partial r}\left(\frac{u_\theta}{r}\right) && \text{for} \quad |\tau_{r\theta}| > \tau_0 \\ \dot{\gamma}_{r\theta} &= 0 && \text{for} \quad |\tau_{r\theta}| \leq \tau_0. \end{aligned} \tag{4.3}$$

We then consider three distinct regions in the flow. The sign in front of the Bingham number is positive in the inner yielded region, where the stress is positive, and negative in the outer yielded region, where the stress is negative. In the centre of the channel, where the magnitude of the shear stress $\tau_{r\theta}$ is below the yield stress, there is a "plug" of fluid with zero strain-rate. At each side of the core "plug" region we have regions of yielded fluid, close to the walls of the channel, where the magnitude of the shear stress is greater than the fluids' yield stress. In these two regions the velocity profile is parabolic, while in the plug region the fluid undergoes solid body rotation with u_θ proportional to r.

At the channel walls we impose the Navier slip condition [Navier, 1823], which allows the fluid to satisfy no-slip, partial slip and full slip behaviour at the channel walls, dependent on the choice of the slip length β:

$$u_\theta = \pm\beta r \frac{\partial}{\partial r}\left(\frac{u_\theta}{r}\right). \tag{4.4}$$

The sign in front of the slip length is required due to the change in sign of the $r\theta$ component of the strain rate and again is positive in the inner yielded region (at $r = R_i$) and negative in the outer yielded region (at $r = R_o$).

We consider the governing equations in dimensionless form relative to the length-scale h and the velocity scale $U = Gh^2/\mu$. Denoting dimensionless quantities with an asterisk we use

$$r^* = \frac{r}{h}, \quad u_\theta^* = \frac{u_\theta \mu}{Gh^2}, \quad \underline{\nabla}^* = h\underline{\nabla}, \quad \tau^* = \frac{\tau}{Gh}, \quad \beta^* = \frac{\beta}{h}. \tag{4.5}$$

Introducing the channel curvature $\kappa = h/R_i$, the momentum balance eq. (4.2) becomes

$$-\left(\frac{1}{\kappa} + \frac{1}{2}\right) = \frac{1}{r^*}\frac{\partial}{\partial r^*}\left(r^{*2}\tau_{r\theta}^*\right), \tag{4.6}$$

where the left hand side arises from writing $R_c = R_i + h/2$. The constitutive equation (4.3) becomes

$$\begin{aligned} \tau_{r\theta}^* &= \pm\tfrac{1}{2}B + r^*\frac{\partial}{\partial r^*}\left(\frac{u_\theta^*}{r^*}\right) && \text{for} \quad |\tau_{r\theta}^*| > \tfrac{1}{2}B \\ \dot{\gamma}_{r\theta}^* &= 0 && \text{for} \quad |\tau_{r\theta}^*| \leq \tfrac{1}{2}B. \end{aligned} \tag{4.7}$$

The yield-stress τ_0 and viscosity μ are absorbed into a dimensionless Bingham number, representing the ratio of the yield stress to the viscous stresses [Bingham, 1922]:

$$B = \frac{2\tau_0}{Gh}. \tag{4.8}$$

For small values of B the profiles of velocity and stress will be similar to those for a Newtonian fluid of comparable viscosity. Increasing B at fixed pressure gradient causes a widening plug region to develop in the centre of the channel and results in a decrease in the fluid flux.

The Navier slip condition in dimensionless form becomes

$$u_\theta^* = \pm \beta^* r^* \frac{\partial}{\partial r^*} \left(\frac{u_\theta^*}{r^*} \right). \tag{4.9}$$

From this point onwards, we drop the asterisks denoting dimensionless quantities.

4.3 Analytic solution

In the yielded regions, the solution to eq. (4.6) takes the form

$$\tau_{r\theta} = -\left(\frac{2+\kappa}{4\kappa} \right) + \frac{C}{r^2}, \tag{4.10}$$

where C is a constant of integration. In principle the constant of integration could be different in each region of the flow, but matching the stresses at each yield surface, or by applying a balance between pressure and stress at a selected control volume [Laird, 1957], indicates that they are equal. Therefore the shear stress decreases quadratically across the gap, taking its maximum value at the inner wall $r = 1/\kappa$, where the pressure gradient is greatest.

According to the constitutive equation, eq. (4.7), the fluid yields when the magnitude of the shear stress is equal to $B/2$. We can therefore find the positions of the inner and outer yield surfaces, r_i and r_o, at the points where $\tau_{r\theta} = B/2$ and $-B/2$ respectively:

$$r_i^2 = \frac{2C}{\left(\frac{2+\kappa}{2\kappa}\right) + B}, \quad r_o^2 = \frac{2C}{\left(\frac{2+\kappa}{2\kappa}\right) - B}. \tag{4.11}$$

Eliminating C gives a relationship between the positions of the inner and outer yield surfaces, written in terms of modified Bingham numbers $B^{\pm} = \frac{1}{2}\left(\left(\frac{2+\kappa}{2\kappa}\right) \pm B\right)$:

$$B^{+} r_i^2 = B^{-} r_o^2. \tag{4.12}$$

In addition, substituting for C in eq. (4.10) gives two equivalent expressions for the stress in terms of the position of either yield surface:

$$\tau_{r\theta} = -\left(\frac{2+\kappa}{4\kappa}\right) + B^{+}\frac{{r_i}^2}{r^2} \quad \text{and} \quad \tau_{r\theta} = -\left(\frac{2+\kappa}{4\kappa}\right) + B^{-}\frac{{r_o}^2}{r^2}. \tag{4.13}$$

These only apply in each of the two yielded regions of the flow, $\frac{1}{\kappa} \leq r \leq r_i$ and $r_o \leq r \leq \frac{1}{\kappa}+1$, where substitution into the constitutive equation (4.7) gives the velocity profile there.

Up to this point, the choice of boundary condition have had no effect on the derivation. The Navier slip condition is used when obtaining values for the integration constants which appear in both yielded regions. We can match the expressions for the stress $\tau_{r\theta}$ from eqs. (4.7) and (4.13) in both yielded regions. These can be rearranged to the form

$$r\frac{\partial}{\partial r}\left(\frac{u_\theta}{r}\right) = -B^{+} + B^{+}\frac{r_i^2}{r^2} \quad \text{and} \quad r\frac{\partial}{\partial r}\left(\frac{u_\theta}{r}\right) = -B^{-} + B^{-}\frac{r_o^2}{r^2}. \tag{4.14}$$

The dependence of the strain rate on slip length β is contained in the yield surface positions r_i and r_o. These equations are integrated with respect to r, which allows us to write an expression for the velocity profiles u_θ in both yielded regions in terms of integration constants D_1 and D_2:

$$u_\theta = B^{+}\left(-r\ln(r) - \frac{r_i^2}{2r} + D_1 r\right) \quad \text{and} \quad u_\theta = B^{-}\left(-r\ln(r) - \frac{r_i^2}{2r} + D_2 r\right). \tag{4.15}$$

The integration constants D_1 and D_2, for the inner and outer yielded regions, respectively are determined using the Navier slip boundary condition eq. (4.9).

In the inner yielded region (at $r = 1/\kappa$), we can substitute the expression for u_θ from eq. (4.15) and the strain rate $r\theta$ component from eq. (4.14) into the Navier slip condition at $r = 1/\kappa$:

$$B^+ \left(-\frac{1}{\kappa} \ln\left(\frac{1}{\kappa}\right) - \frac{1}{2} r_i^2 \kappa + D_1 \frac{1}{\kappa} \right) = \beta B^+ \left(-1 + r_i^2 \kappa^2 \right) \tag{4.16}$$

which is rearranged to find the value of integration constant D_1:

$$D_1 = \ln\left(\frac{1}{\kappa}\right) + \frac{1}{2}(r_i\kappa)^2 + \beta\left(-\kappa + r_i^2\kappa^3\right). \tag{4.17}$$

We substitute the value of D_1 back into eq. (4.15) and conclude that the velocity profile for the inner yielded region becomes:

$$u_\theta = B^+ \left(\frac{r_i^2}{2}\left(\kappa r - \frac{1}{r}\right) - r\ln(\kappa r) + \beta r\left(-\kappa + r_i^2\kappa^3\right)\right). \tag{4.18}$$

Applying the Navier slip condition for $r_o \leq r \leq 1/\kappa + 1$, the velocity profile for the outer yielded region takes the form:

$$u_\theta = B^- \left(\frac{r_o^2}{2}\left(\frac{r}{(1/\kappa + 1)^2} - \frac{1}{r}\right) - r\ln\left(\frac{r}{1/\kappa + 1}\right) - \beta r\left(\frac{-1}{1/\kappa + 1} + \frac{r_o^2}{(1/\kappa + 1)^3}\right)\right). \tag{4.19}$$

Notice that the sign in front of the slip length β in both regions is opposite, as suggested by eq. (4.9), as the extent of the slip is proportional to the local strain rate at the wall i.e the gradient of velocity (which changes sign from the inner to the outer wall) and an additional term dependent on curvature (eq. (4.1)).

Between these yielded regions, the fluid moves in a solid-like plug. In this region of zero strain-rate flowing under solid body rotation, $\frac{\partial}{\partial r}\left(\frac{u_\theta}{r}\right) = 0$, which implies $u_\theta = Ar$ with A a constant found by ensuring that the velocity is continuous at the yield surfaces. We find A by matching the velocities at $r = r_i$, and use the condition at $r = r_o$ to find the analytical location of both yield surfaces. Alternatively, one could find A by matching the velocities at $r = r_o$ and use the condition at $r = r_i$ to find the yield surface locations. Joining all three regions allow us to derive the full velocity profile, which takes the form:

$$u_\theta(r) = \begin{cases} B^+ \left(\frac{r_i^2}{2} \left(\kappa r - \frac{1}{r} \right) - r \ln(\kappa r) + \beta r \left(-\kappa + r_i^2 \kappa^3 \right) \right) & \text{for} \quad \frac{1}{\kappa} \leq r \leq r_i \\ B^+ r \left(\frac{1}{2} \left(r_i^2 \kappa^2 - 1 \right) - \ln\left(r_i \kappa \right) + \beta \left(-\kappa + r_i^2 \kappa^3 \right) \right) & \text{for} \quad r_i \leq r \leq r_o \\ B^- \left(\frac{r_o^2}{2} \left(\frac{r\kappa^2}{(\kappa+1)^2} - \frac{1}{r} \right) - r \ln\left(\frac{r\kappa}{\kappa+1} \right) - \beta r \left(\frac{-\kappa}{\kappa+1} + \frac{r_o^2 \kappa^3}{(\kappa+1)^3} \right) \right) & \text{for} \quad r_o \leq r \leq \frac{1}{\kappa} + \end{cases} \tag{4.20}$$

By matching the velocities at the outer yield surface $r = r_o$ (or $r = r_i$ if the condition at the outer yield surface was used to find A) and using eq. (4.12), we derive a condition to determine the position of the yield surface r_i:

$$\begin{gathered} B^+ \left(\frac{1}{2} \left(r_i^2 \kappa^2 - 1 \right) - \ln(r_i \kappa) + \beta(-\kappa + r_i^2 \kappa^3) \right) = \\ B^- \left(\frac{1}{2} \left(\frac{r_o^2 \kappa^2}{(\kappa+1)^2} - 1 \right) - \ln\left(\frac{r_o \kappa}{\kappa+1} \right) - \beta \left(-\frac{\kappa}{\kappa+1} + \frac{r_o^2 \kappa^3}{(\kappa+1)^3} \right) \right). \end{gathered} \tag{4.21}$$

Having found r_i, eq. (4.12) gives the position of the outer yield surface r_o. To solve eq. (4.21) for r_i, we collect terms in $\ln(r_i)$ and r_i^2 to write it in the form

$$-2B \ln(r_i) + A_1 r_i^2 + A_2 = 0. \tag{4.22}$$

The constants are

$$A_1 = \frac{1}{2} B^+ \left(\kappa^2 - \frac{\kappa^2}{(\kappa+1)^2} \right) + \beta B^+ \left(\kappa^3 + \frac{1}{(1/\kappa+1)^3} \right),$$

$$A_2 = -B - B^+ \ln(\kappa) + B^- \ln\left(\sqrt{\frac{B^+}{B^-}} \frac{\kappa}{\kappa+1} \right) - \beta \left(B^+ \kappa + \frac{B^- \kappa}{\kappa+1} \right).$$

Equations of the form (4.21) have an exact solution in terms of the Lambert W function [Corless et al., 1996]:

$$r_i = \sqrt{\frac{B}{A_1} W\left(-1, -\frac{A_1}{B} \exp\left(-\frac{A_2}{B} \right) \right)}. \tag{4.23}$$

where the -1 branch is used because the second argument is negative. Notice that the position of the yield surfaces r_i and r_o depend on κ, B and β. In the appendix, we show the full derivation (chap. A.1) of the analytic solution for r_i. Alternatively, it is straightforward to find the root r_i numerically using a root-finding algorithm to solve eq. (4.12). This provides the necessary input to give the velocity profile $u_\theta(r)$ in equation (4.20) in terms of the channel curvature κ, Bingham number B and slip length β, against shifted radial position $\hat{r} = r - \frac{1}{\kappa}$.

The one-dimensional flow rate Q of a pressure-driven Bingham fluid through an annulus with slip is defined as the amount of fluid which crosses a particular cross-section per unit time. The quantity Q is found by integrating the velocity profile in eq. (4.20) with respect to r between $1/\kappa$ and $1/\kappa + 1$. This allows us to explore the influence of the slip parameter β, Bingham number B and channel curvature κ on the flow rate:

$$\begin{aligned}
Q &= \int_{\frac{1}{\kappa}}^{\frac{1}{\kappa}+1} u_\theta \mathrm{d}r \\
&= \int_{\frac{1}{\kappa}}^{r_i} u_\theta \mathrm{d}r + \int_{r_i}^{r_o} u_\theta \mathrm{d}r + \int_{r_o}^{\frac{1}{\kappa}+1} u_\theta \mathrm{d}r \\
&= B^+ \left(\frac{{r_i}^2}{2} \left(\frac{1}{2} - \ln\left(r_i \kappa\right) \right) - \frac{{r_o}^2}{2} \left(\frac{1}{2} + \ln\left(r_i \kappa\right) \right) - \frac{1}{4\kappa^2} + \frac{r_o^2 r_i^2 \kappa^2}{4} \right) \\
&+ B^- \left(r_o^2 \ln\left(\frac{r_o}{1/\kappa + 1} \right) + \frac{(1/\kappa + 1)^2}{4} - \frac{{r_o}^4}{4(1/\kappa + 1)^2} \right) \\
&+ \frac{1}{2}\beta \left(B^+ \left(-\kappa + r_i^2 \kappa^3 \right) \left(r_o^2 - \frac{1}{\kappa^2} \right) - B^- \left(-\frac{1}{\kappa} - 1 + \frac{2r_o^2}{1/\kappa + 1} - \frac{r_o^4}{(1/\kappa + 1)^3} \right) \right).
\end{aligned} \tag{4.24}$$

In order to fix the flow rate of fluid in an annulus of curvature κ, one needs to consider a balance between B and β.

4.4 Constraints on the solution

A Bingham fluid flowing through a straight channel of width 1 due to a unit pressure gradient will flow provided that B is less than 1 (chap. 3.3). That is, below a critical Bingham number B_c, the shear stress induced at the walls of the channel will not exceed the yield stress, and then the material will not move. The critical value is found when the yield surfaces at $y = \pm B/2$ reach the walls at $y = \pm 1/2$, see eq. (3.21).

In the curved channel that we consider here, an indication that flow can cease is that for the velocity profile to be defined in eq. (4.21) we must have B^- positive, giving an upper bound for the Bingham number:

$$B \leq \frac{2+\kappa}{2\kappa}, \tag{4.25}$$

indicated by the red line in fig. 4.2.

When the fluid is stationary everywhere the yield surfaces coincide with the walls of the channel, i.e. $r_i = \frac{1}{\kappa}$ and $r_o = \frac{1}{\kappa} + 1$. Then eq. (4.12) gives

$$\left(B + \left(\frac{1}{\kappa} + \frac{1}{2}\right)\right)\left(\frac{1}{\kappa}\right)^2 = \left(-B + \left(\frac{1}{\kappa} + \frac{1}{2}\right)\right)\left(\frac{1}{\kappa} + 1\right)^2. \tag{4.26}$$

This can be rearranged to give a critical Bingham number

$$B_c = 1 - \frac{\kappa^2}{2((\kappa+1)^2+1)}, \tag{4.27}$$

shown in figure 4.2, above which the flow stops. For small κ, B_c tends to one and we recover the result for the straight channel. As the channel curvature increases, either through reducing the inner radius R_i or increasing the width h, the value of B_c is reduced towards a value of 0.5, indicating that a larger pressure gradient is required to induce flow. Thus a small amount of channel curvature has a surprisingly large effect on inhibiting flow. Even though the position of the yield surfaces (and therefore the plug width) has a dependence on the slip length β, the value of B_c is independent of the choice of boundary condition.

Although there are no restriction on the value of slip parameter β, we choose to limit our choices of β to values between 0 and $10^0 = 1$ as within this range, we see all the "interesting" flow profiles i.e. the range of β at which the fluid transitions from no-slip to close to full slip. In the finite element simulations, we set an upper bound for β as 0.1, explained in chap. 3.5.1.

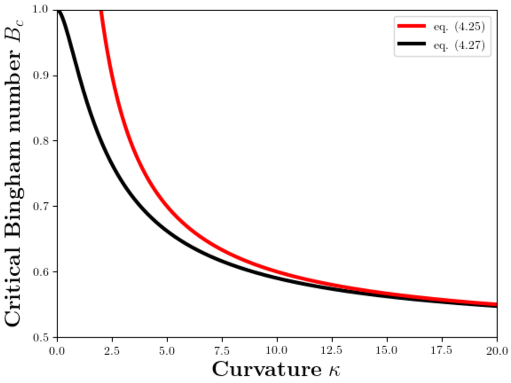

Figure 4.2: The value of the critical Bingham number B_c (eq. (4.27)), above which flow ceases, decreases with increasing channel curvature κ. The red line indicates the upper bound for B in eq. (4.25).

4.5 Results

We consider a pressure-driven Bingham fluid through an annulus with Navier slip boundary condition. In this next chapter, we plot the expressions of velocity, stress and flow rate found in chap. 4.3. We investigate the affect of slip on a Bingham fluid in an annulus and its implication in the effectiveness of foam in sclerotherapy. In presenting our results we scale the Bingham number B by its critical value B_c, to represent the magnitude of the yield stress, and shift radial position to represent distance from the inner wall of the channel, $\hat{r} = r - \frac{1}{\kappa}$.

4.5.1 Velocity

For a given Bingham number B, slip length β and channel geometry set by κ, we can find the positions of the yield surfaces r_i and r_o which allows us to plot the velocity profile u_θ. The positions of the yield surfaces are shown in eq. (4.23) are used to plot the velocity profile in eq. (4.20), and the profiles are plotted in both figs. 4.3 and 4.4. In the limit $\kappa \to 0$ we obtain the velocity profile for the straight channel case (see chap. 3).

In fig. 4.3(a), we consider a Newtonian fluid with no-slip (by setting $B = 0$ and $\beta = 0$)

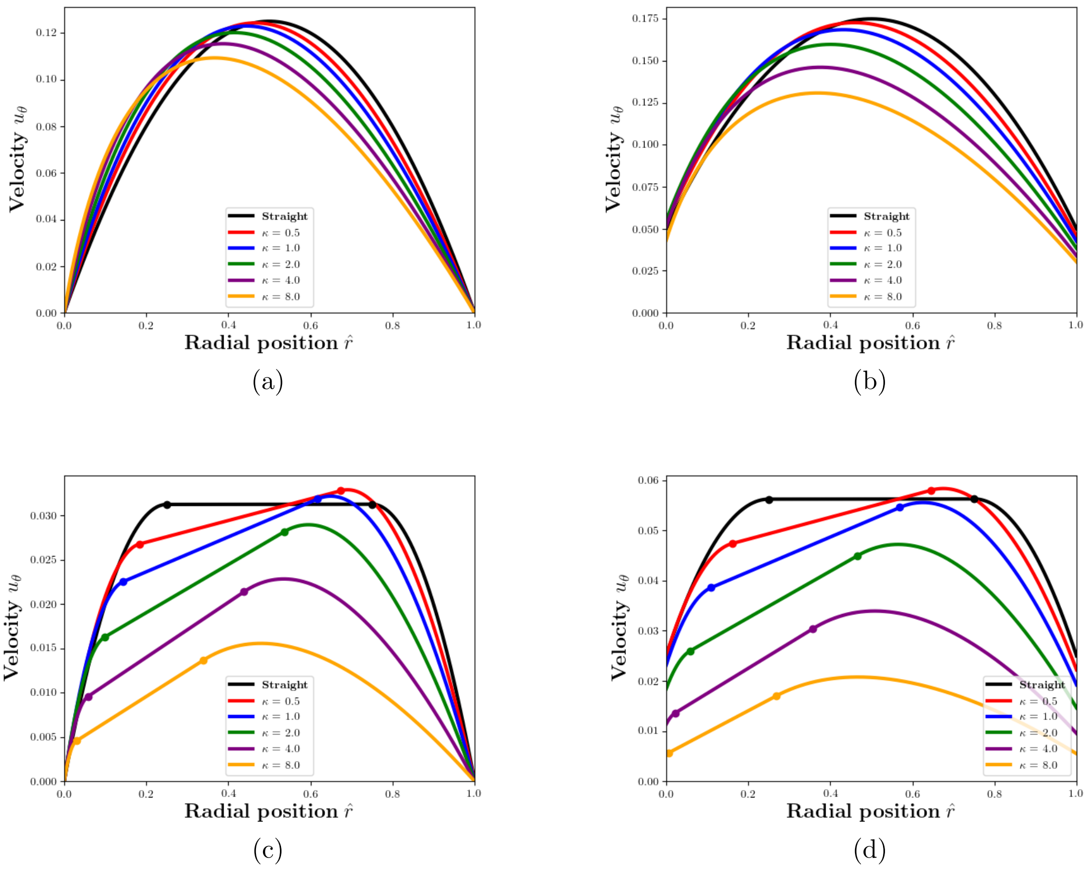

(a) (b) (c) (d)

Figure 4.3: The velocity profiles u_θ for different values of channel curvatures κ, plotted against radial position $\hat{r} = r - \frac{1}{\kappa}$: (a) u_θ for a Newtonian fluid with no-slip ($B = 0$ and $\beta = 0$), (b) u_θ for a Newtonian fluid with Navier-slip ($B = 0$ and $\beta = 0.1$), (c) u_θ for a Bingham fluid with no-slip ($B = 0.5$ and $\beta = 0$), (d) u_θ for a Bingham fluid with Navier-slip ($B = 0.5$ and $\beta = 0.1$). The dots in parts (c) and (d) indicate the yield surface positions.

for different values of κ. For $\kappa = 0$ i.e. the straight channel case (fig. 3.4(a)), the velocity profile is symmetric about the channel centerline with the position of maximum velocity located at 0.5, directly on the channel centerline. By increasing the channel curvature κ, we see a shift in the velocity towards the inner wall of the channel, where the radius of curvature (and pressure-gradient) is largest, and the fluids' velocity decreases. By considering a Newtonian fluid with a non-zero slip length $\beta = 0.1$ in fig. 4.3(b), we see that increasing channel curvature decreases the fluids velocity everywhere including the channel walls and the point of maximum velocity moves towards the inner channel wall with increasing channel curvature κ, as was the case for fig. 4.3(a). The velocity at the outer wall decreases more in comparison to the inner wall with increasing κ.

Fig. 4.3(c) shows for the no-slip case, how the velocity profile is affected by changes in channel curvature with fixed fluid properties $B = 0.5$. Increasing the channel curvature κ reduces the velocity, particularly in the inner half of the channel, although for intermediate values of $\kappa = 0.5$ and 1.0, we see a region of fluid close to the outer yield surface moving faster than the straight channel case. The slope of the velocity in the plug region is high for large curvatures κ corresponding to high curvature of the stress profile (see fig. 4.9). In the limit $\kappa \to 0$ we obtain the velocity profile seen in chap. 3 which is included in both fig. 4.3(c) and (d). In fig. 4.3(d), we consider u_θ by varying the value of κ for fixed $\beta = 0.1$ and $B = 0.5$. For $\kappa = 0.5$, we see one again that there is a value of u_θ which is larger than the straight channel case. As we increase the value of κ, the velocity of the fluid decreases everywhere as does the plug width.

By fixing $\kappa = 2$ in fig. 4.4, we consider the affects of both B and β on the flow profiles. For fixed $\beta = 0$ and 0.1 and varying B, the results in figs. 4.4(a) and (b) show that the fluid velocity decreases and the plug width increases as the yield stress is increased. As B approaches B_c (which is equal to 0.8 for $\kappa = 2$), the flow stops. By direct observation of figs. 4.4(a) (no-slip) and (b) (slip with $\beta = 0.1$), we note that the plug widths are shifted closer to the inner wall of the channel and slightly narrow due to wall slip.

In fig. 4.4(c), we plot u_θ for a Newtonian fluid ($B = 0$) for fixed $\kappa = 2$ and different slip lengths β. The case $\beta = 0$ is also shown in part (a). As β is increased, we see that the velocity increases everywhere, with the velocity at the inner wall larger than the outer. Increasing β further causes the velocity at the outer wall to become larger than the inner wall and the position of maximum velocity moves towards the outer wall. This suggests that there is a value of β and κ at which both wall velocities are equal (considered in fig. 4.6).

For the Bingham case ($B = 0.5$) fig. 4.4(d), we vary the value of β between 0 and 1 for

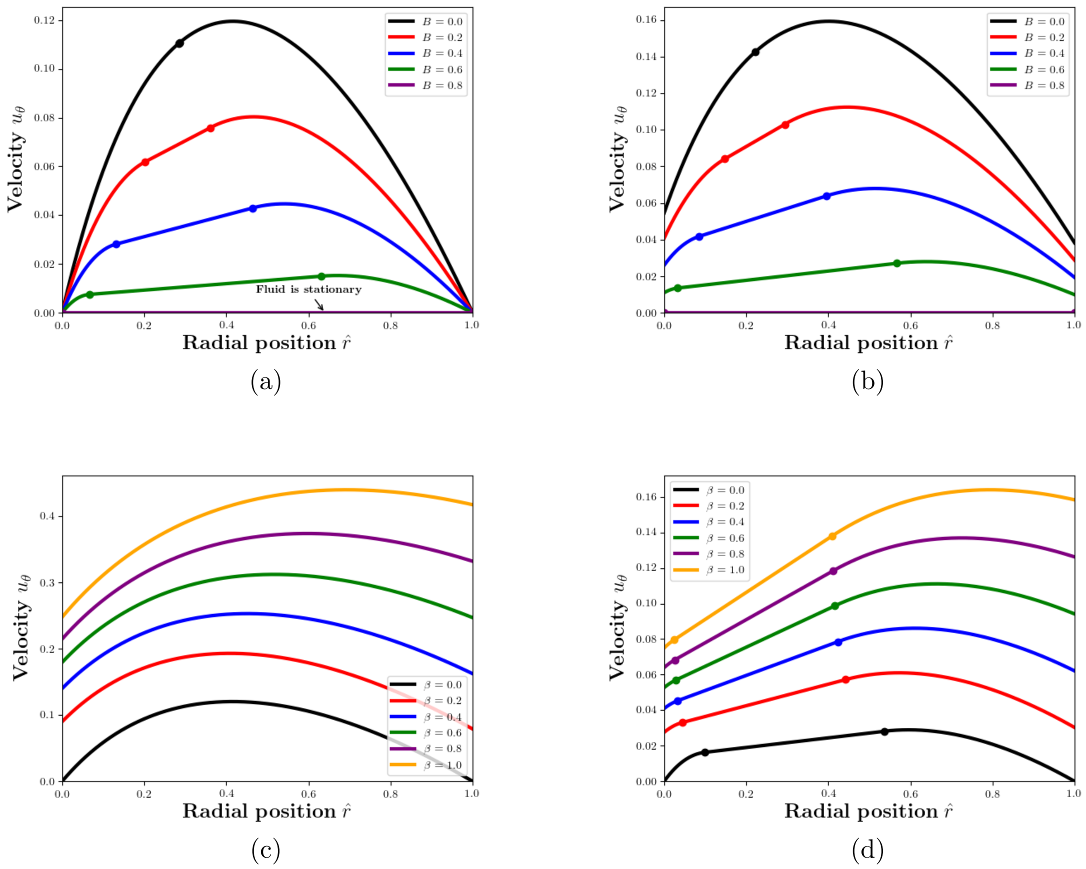

(a) (b) (c) (d)

Figure 4.4: We plot the velocity profiles u_θ for a Bingham fluid through an annulus with fixed $\kappa = 2$; we vary the Bingham number for (a) no-slip and (b) slip ($\beta = 0.1$) boundary conditions and vary the slip length β for (c) $B = 0$ and (d) $B = 0.5$. The dots in part (b) and (d) indicate the locations of the yield surfaces.

fixed $\kappa = 2$, which shows that the value of maximum velocity moves towards the outer wall with increasing β. There is little difference in the plug width with increasing β (see fig. 4.8) but the plug region is shifted towards the inner wall. As for the Newtonian case, we see that the maximum velocity increases with β, as expected.

4.5.1.1 Maximum velocity

From inspection of figs. 4.3 and 4.4, it is possible to see that the maximum velocity is located between the outer yield surface and the outer wall. As the velocity profile in the outer yielded region is parabolic, we can find the position of maximum velocity, denoted by

r_{max}, by differentiating the outer yielded region of eq. (4.20) with respect to r:

$$\frac{d}{dr}\left(u_\theta(r)\right) = B^- \left(\frac{r_o^2}{2}\left(\frac{\kappa^2}{(\kappa+1)^2}+\frac{1}{r^2}\right) - \left(\ln\left(\frac{\kappa r}{\kappa+1}\right)+1\right) - \beta\left(\frac{-\kappa}{\kappa+1}+\frac{r_o\kappa^3}{(\kappa+1)^3}\right)\right)$$

which we equate to zero to give an expression for r_{max}. This can be rearranged to an equation of the form:

$$A_3 \ln\left(\frac{1}{r_{max}^2}\right) + \frac{1}{r_{max}^2} + A_4 = 0 \qquad (4.28)$$

where the constants are:

$$A_3 = \frac{1}{r_o^2}, \quad A_4 = \frac{1}{(1/\kappa+1)^2} + \frac{2}{r_o^2}\left(\ln(1/\kappa+1)-1\right) - \frac{2}{r_o^2}\beta\left(\frac{-\kappa}{\kappa+1}+\frac{r_o\kappa^3}{(\kappa+1)^3}\right).$$

Then equation (4.28) can be solved using the Lambert W-function in the same way as in eq. (4.23) to find an exact solution to r_{max}:

$$r_{max} = \frac{1}{\sqrt{A_3 W\left(0, \frac{1}{A_3}\exp\left(-A_4/A_3\right)\right)}} \qquad (4.29)$$

where the 0 branch is used because the second argument is positive.

Figures 4.5(a) and (c) show that the radial position for the maximum velocity is always greater than or equal to the outer yield surface r_o. The point of maximum velocity, close to $r = r_o$, moves away from the outer wall as κ increases, but the value of the velocity there does not change monotonically: for intermediate curvature (e.g. $\kappa = 1.0$) the maximum velocity of the fluid exceeds the value in a straight channel (in figs. 4.3(c) and (d)).

The value of r_{max} from eq. (4.29) is shown in figs. 4.5(a) for $\beta = 0$ and (c) for $\beta = 0.1$. As channel curvature κ decreases, the point of maximum velocity approaches a linear interpolation between the midpoint of the channel for $B = 0$ and the outside of the channel for $B = B_c$, as for a straight channel. As B increases relative to B_c, the slope of the velocity profile in the plug region is reduced (and the fluid velocity also decreases). Hence r_{max}

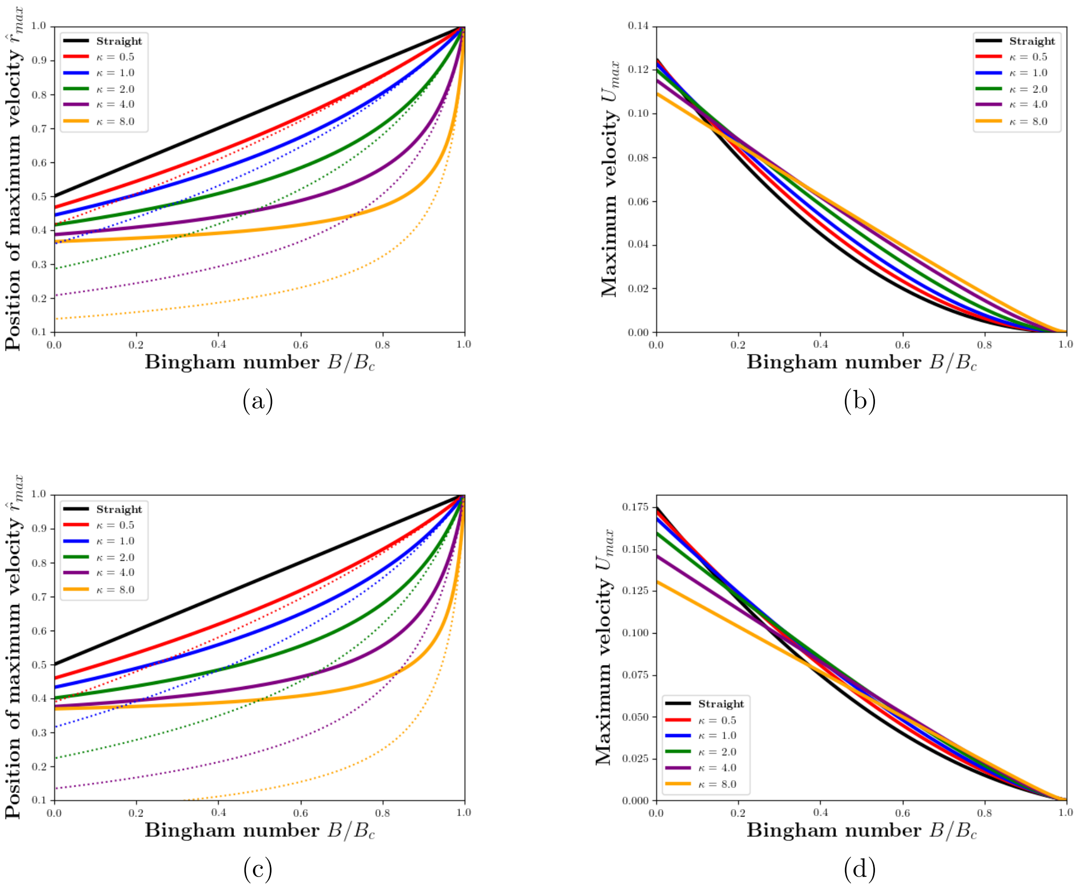

(a) (b)

(c) (d)

Figure 4.5: The point of maximum velocity r_{max} with fixed channel curvatures κ as a function of Bingham number B/B_c. The radial position of the maximum velocity (thick lines), compared with the position of the outer yield surface (thin lines) for several values of channel curvature κ for (a) $\beta = 0$ and (c) $\beta = 0.1$. Parts (b) and (d) show the values of the maximum velocity when $r = r_{max}$ for $\beta = 0$ and 0.1, respectively.

approaches the outer yield surface and they eventually coalesce (fig. 4.5(a) and (c)). For less-curved channels, this coalescence is seen at smaller values of B/B_c. The existence of wall slip $\beta = 0.1$ in fig. 4.5(c) causes the coalescence to occur at larger ratios of B/B_c, albeit no extreme change in values.

The value of the maximum velocity itself, U_{max}, is shown in fig. 4.5(b) and (d) for different channel curvatures κ as the Bingham number B changes. For $B = 0$, i.e. a Newtonian fluid, the maximum velocity of the fluid increases as the channel curvature decreases (smaller κ). As B/B_c is increased, we notice a crossover where channels with greater curvature induce a flow with a higher maximum velocity, and this point occurs at a radial position further away from the outer wall. For the no-slip case, the crossover for each κ occurs at smaller values of B/B_c (i.e. between 0.1 and 0.2) than in comparison to the slip case in part (d), where the crossovers occur over a much larger range of B/B_c.

At the crossover, the yield-stress is relatively small for $\beta = 0$ and slightly larger for $\beta = 0.1$, but nonetheless indicates the competition between the curvature of the channel and the yield stress of the fluid in determining the fluid motion. The position of the point of maximum velocity is far enough from the outer wall that the no slip condition is not dominant, but not so close to the inner wall that the higher curvature there induces larger stresses.

4.5.1.2 Wall velocity

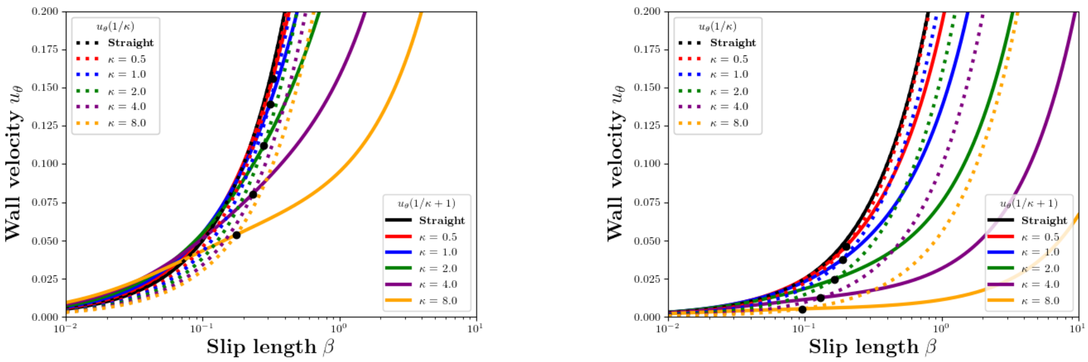

(a) (b)

Figure 4.6: The wall velocity of a Bingham fluid in a curved channel as a function of slip parameter β: (a) for $B = 0$ and (b) $B = 0.5$. The dashed and full lines denote the velocity on the inner and outer wall, respectively.

In fig. 4.6, we consider the values of the velocity at the inner and outer walls of the channel as functions of slip parameter β for different κ for; (a) Newtonian fluid (b) Bingham fluid with $B = 0.5$. The wall velocity is of particular interest as for small β, u_θ is larger on the inner wall before it becomes larger on the outer wall for larger β (see fig. 4.4), meaning that there is a transition point at which they must be equal, denoted by the black marks. We see that for a Newtonian fluid, these black marks fall between $\beta = 0.17$ and 0.32 for the considered range of κ (between 0 and 8), with the critical value of β decreasing with increasing κ. A value of $B = 0.5$ (fig. 4.6(b)) causes the critical values of β to decrease from the Newtonian case (see fig. 4.6(a)) to between 0.09 and 0.2 with increasing curvature κ.

4.5.2 Yield surface positions and plug width

The radial positions of the yield surfaces, from eq. (4.23), are shown in fig. 4.7. In the limit $B \to 0$, the material behaves like a Newtonian fluid: there are no yield surfaces and the values r_i and r_o coincide at a point close to the middle of the channel. As the curvature of the channel increases this point moves towards the inner wall. The existence of slip ($\beta = 0.1$ in fig. 4.7(b)) causes the point to move even closer to the inner wall in comparison to fig. 4.7(a). As $\kappa \to 0$ they meet at $\hat{r} = \frac{1}{\kappa} + \frac{1}{2}$, as in a straight channel.

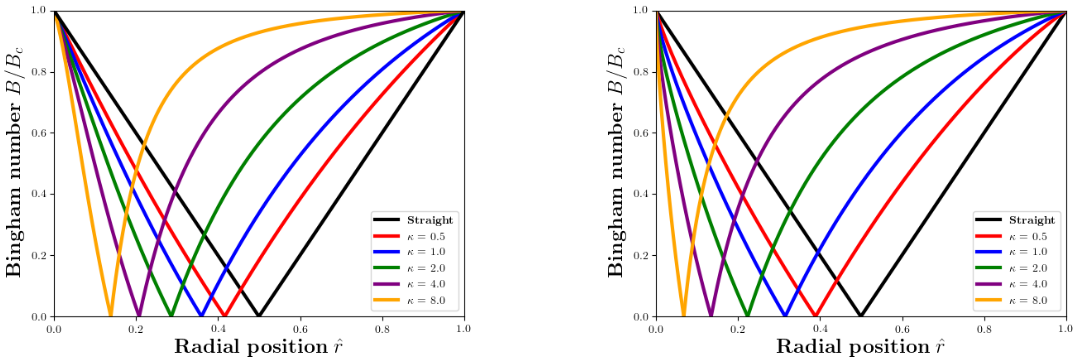

(a)

(b)

Figure 4.7: We plot the yield surfaces r_i and r_o against B/B_c for a Bingham fluid through an annulus with slip for different channel curvatures κ; (a) For the no-slip boundary condition $\beta = 0$ and (b) for the Navier slip boundary condition with $\beta = 0.1$.

As B increases, the two yield surfaces move apart, reaching the inner and outer walls precisely when B reaches B_c. For large channel curvatures κ the outer yield surface remains close to the centre of the channel until B reaches about half of its critical value, while the position of the inner yield surface is almost linear in B/B_c in all cases.

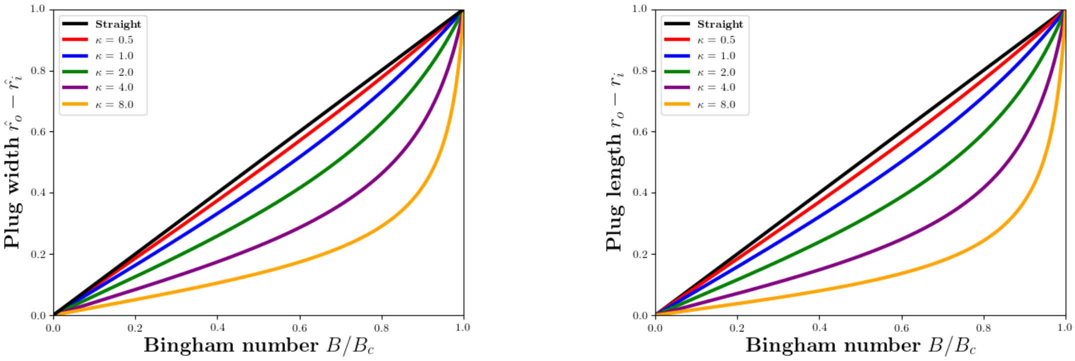

(a) (b)

Figure 4.8: We plot the plug length $r_o - r_i$ against B/B_c for a Bingham fluid through an annulus with slip; (a) For a fixed $\beta = 0.1$, we vary the channel curvature κ, (b) For fixed $\kappa = 2$, we vary the value of β.

The distance between the yield surfaces is the plug width, the region of low stress in which the material moves as a solid body, shown in fig. 4.8 and is equal to zero for $B = 0$ and 1 for $B = B_c$. As $B \to B_c$ the plug width increases until it spans the whole channel. For channels of larger curvature κ, the plug width increases more slowly with B and then sharply increases as B approaches B_c. This implies that increasing channel (or vein) curvature causes in plug length of fluid to decrease, thus decreasing the effectiveness of foam in sclerotherapy treatment. The addition of slip in fig. 4.8(b) sees the plug widths slightly decrease for each κ, although it is clear to see that channel curvature has a much greater influence than the slip length β on the plug width. For weakly curved channels (small κ), the plug width becomes linear in B/B_c.

4.5.3 Shear stress

The shear stress $\tau_{r\theta}$ of a Bingham fluid in a curved channel with slip is shown in eq. (4.13). Equation (4.13) shows that the shear stress decreases from the inner to the outer wall, since the pressure gradient is greatest at the inner wall. In fig. 4.9(a), we vary the channel curvature κ between 0 and 8, and consider the stress in the Newtonian case with a no-slip boundary

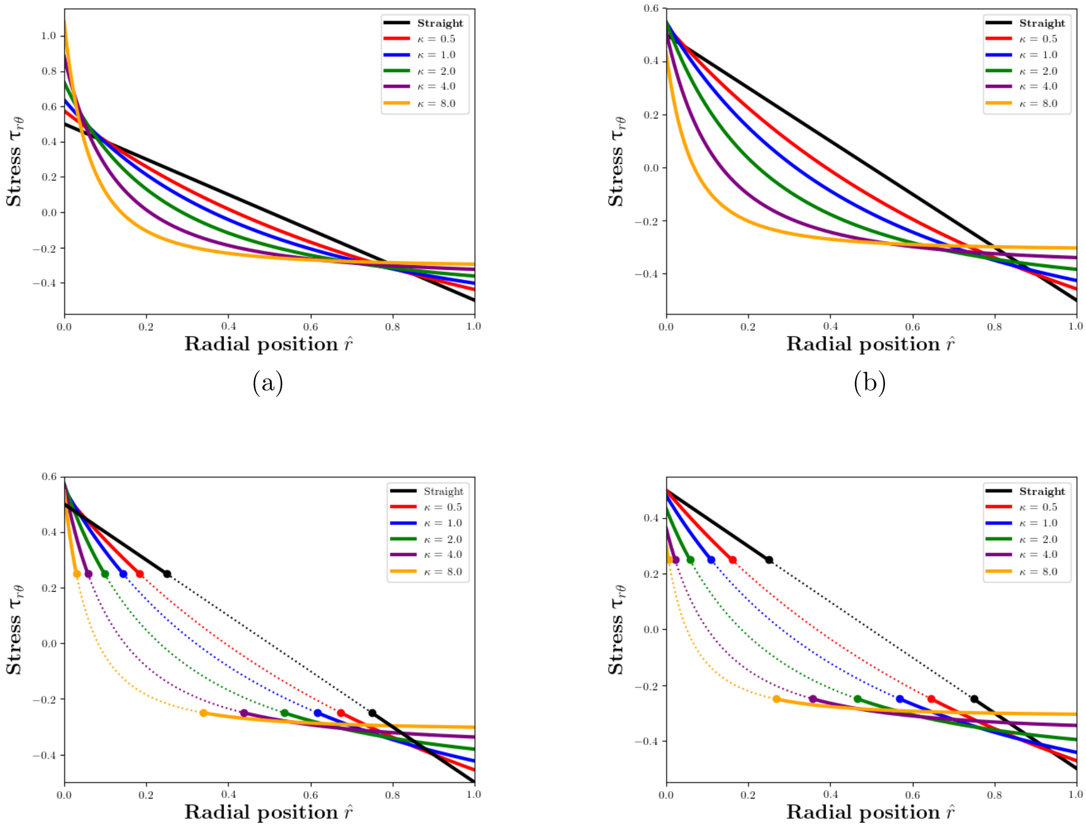

(a)

(b)

(c)

(d)

Figure 4.9: The stress profiles $\tau_{r\theta}$ for different values of channel curvatures κ, plotted against radial position $\hat{r} = r - \frac{1}{\kappa}$: (a) $\tau_{r\theta}$ for a Newtonian fluid with no-slip ($B = 0$ and $\beta = 0$), (b) $\tau_{r\theta}$ for a Newtonian fluid with Navier-slip ($B = 0$ and $\beta = 0.1$), (c) $\tau_{r\theta}$ for a Bingham fluid with no-slip ($B = 0.5$ and $\beta = 0$), (d) $\tau_{r\theta}$ for a Bingham fluid with Navier-slip ($B = 0.5$ and $\beta = 0.1$). The dashed lines in parts (c) and (d) indicate the regions of the fluid where the stress is undefined and the fluid moves as a plug.

condition ($B = 0$ and $\beta = 0$). Recall that for a Newtonian (and in fact Bingham) fluid with $\kappa = 0$ (fig. 3.5), the profile is linear and axisymmetric about the channel centreline, shown in black in fig. 4.9. By increasing κ, we lose the antisymmetry of the stress, as the pressure gradient on the inner wall becomes greater than the outer wall. This causes the shear stress to increase at the inner wall of the channel and to decrease on the outer channel wall with increasing κ. For $\kappa = 8$, we see that the shear stress becomes very large at the inner wall (over double the value for the case $\kappa = 0$). Its value decreases sharply between $\hat{r} = 0$ and 0.2 and then becomes remains roughly constant (at around -0.25) for $\hat{r}$ between 0.2 and 1.0.

In fig. 4.9(b), we consider the stress for a Newtonian fluid with slip and set $\beta = 0.1$. We notice that increasing channel curvature decreases the absolute value of stress at the outer wall. The stress on the inner wall increases from the straight channel case for small curvature ($\kappa = 0.5$ and 1) before decreasing as the choice of κ becomes larger. The effect on the stress of varying the channel curvature κ is significant. In fig. 4.9(c), as κ decreases, the plug width increases and the stress profile becomes straighter, approaching the linear profile found in a straight channel. As κ increases the stress on the inner wall increases slightly and decreases significantly on the outer wall, resulting in a smaller region of unyielded fluid, in agreement with fig. 4.8.

In fig. 4.9(d), we fix $B = 0.5$ and $\beta = 0.1$ and vary the channel curvature κ. Increasing the channel curvature κ removes the stress from the linearly decreasing profile for the straight channel case and causes the plug region to narrow and move towards the inner wall as the stress at $r = \frac{1}{\kappa} + 1$ decreases. We notice, contrary to the no-slip case, the stress at the inner wall decreases with increasing κ for $\beta = 0.1$.

Figure 4.10(a) shows the profile of stress in a channel with $\kappa = 2$ for different values of the Bingham number B. As B increases towards B_c, the stress decreases everywhere. In fig. 4.10(b) $\beta = 0.1$ are fixed as we vary B between 0 and 0.8. As for the no slip case, we see that increasing B decreases the value of the stress everywhere, although setting $\beta = 0.1$ reduces the rate of reduction in stress with increasing B. Increasing the Bingham number causes the stress at the inner wall to decrease at a greater rate compared to the outer wall, where lines for all B ar bunched up at $\hat{r} = 1$ i.e. the outer wall.

In fig. 4.10(c), we consider the shear stress profiles for a Newtonian fluid with fixed $\kappa = 2$ for different slip lengths β. We notice that increasing the value of β decreases the stress everywhere with the greatest decrease in stress occurring at the inner wall $r = \frac{1}{\kappa}$. In the no-slip case, it is the case that the maximum (magnitude) of stress occurs at the inner wall. Notice that for $\beta = 1.0$, we see that the maximum magnitude of stress $|\tau|_{max}$ is located

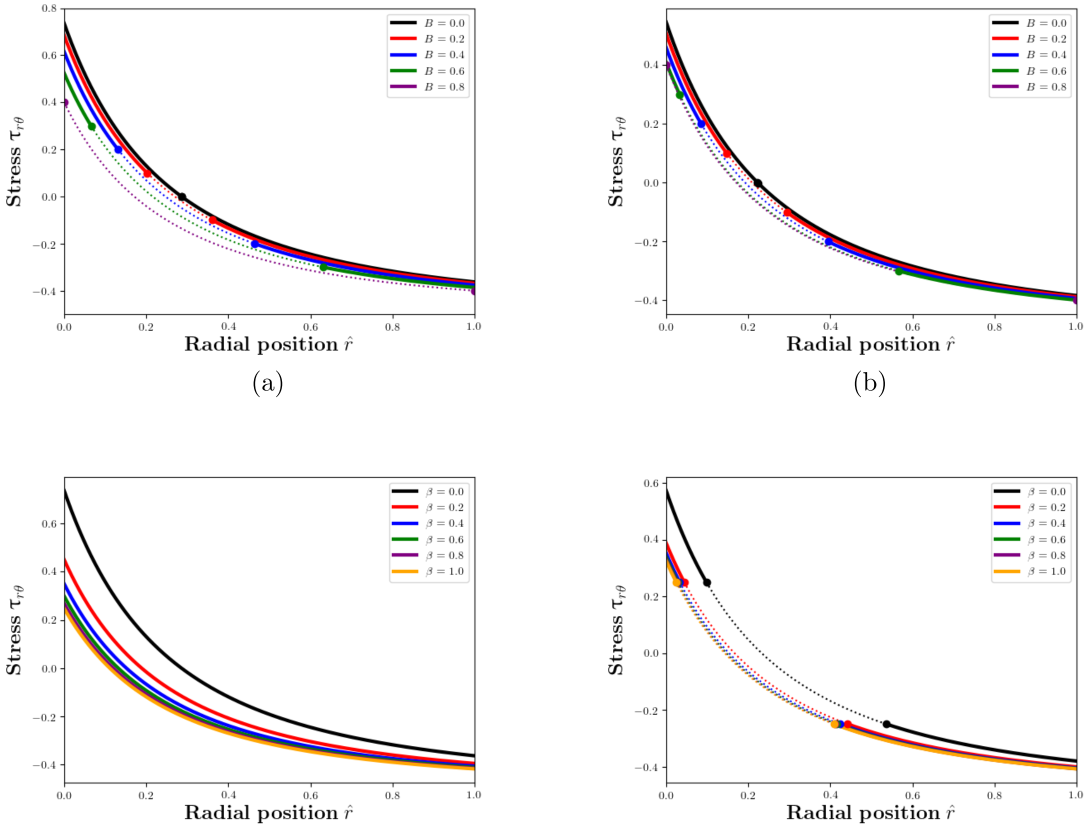

(a) (b)

(c) (d)

Figure 4.10: We plot the stress profiles $\tau_{r\theta}$ for flow through an annulus with slip; For fixed $\kappa = 2$ and in part (a) set $\beta = 0$ and (b) as $\beta = 0.1$, we vary the value of B, and in part (c) set $B = 0$ and (d) $B = 0.5$ and vary the value of the slip length β. The dots denote the positions of the yield surfaces, which are positions at which the stress is equal to $\frac{1}{2}B$. The dashed lines in parts (c) and (d) indicate the regions of the fluid where the stress is undefined and the fluid moves as a plug.

at the outer wall $r = \frac{1}{\kappa} + 1$, which implies that the maximum magnitude of stress differs from the maximum stress providing that there is wall slip. In fig. 4.10(d), where $B = 0.5$, we see that if β is large enough, the magnitude of stress can become greater at the outer wall, compared to the inner wall (notice curve denoting $\beta = 1.0$). We see that the effect of increasing β causes the stress to decrease everywhere and the plug is shifted towards the inner radius of curvature.

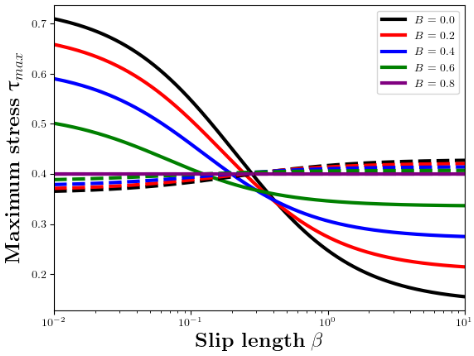

Figure 4.11: The maximum stress τ_{max} as a function of β for fixed $\kappa = 2$ (hence $B_c = 0.8$) different B between 0 and 0.8.

4.5.3.1 Maximum stress

From figs. 4.9 and 4.10, we notice that the largest value of the stress, denoted by τ_{max} for a Bingham fluid always occurs at the inner wall $r = 1/\kappa$. Therefore, τ_{max} is found by evaluating the eq. (4.13) at the inner wall:

$$\tau_{max} = -\left(\frac{2+\kappa}{4\kappa}\right) + B^{+} r_i^2 \kappa^2 \tag{4.30}$$

Our findings in figs. 4.10(c) and (d) suggest that the maximum magnitude of stress, denoted $|\tau|_{max}$, can occur at either the inner or outer wall, depending on the value of slip length β:

$$|\tau|_{max} = \max\left(\left|\tau_{r\theta}\left(\frac{1}{\kappa}\right)\right|, \left|\tau_{r\theta}\left(\frac{1}{\kappa}+1\right)\right|\right). \tag{4.31}$$

In fig. 4.11, for fixed $\kappa = 2$ we consider the value τ_{max} (as well as $|\tau_{r\theta}(\frac{1}{\kappa}+1)|$) for a range of slip lengths β between 10^{-2} and 10. The full curves denote the value of τ_{max} and the dashed lines denote $|\tau_{r\theta}(\frac{1}{\kappa}+1)|$ for each case. The black curve denotes the results for the Newtonian fluid, which has the largest τ_{max} at small β and its value decreases with increasing β. By increasing B, the maximum stress at small slip length β decreases and at large β increases until the fluid ceases when the maximum stress is equal to $\frac{1}{2}B$. As for $|\tau|_{max}$ from eq. (4.31), we see that a crossover for critical values of the slip length β between 10^{-1} and 10^{0} in fig. 4.11, for which the magnitude of the stress $|\tau|_{max}$ is equal to τ_{max} for the smaller slip length

β if B is larger and equal to $|\tau_{r\theta}(\frac{1}{\kappa}+1)|$ for larger β for smaller B.

4.5.4 Flow rate

Recognising that the flow rate is the area beneath the velocity curves in fig. 4.3, we expect Q to tend to zero as the Bingham number approaches its critical value B_c, while for $B = 0$ the flux Q is the value for a Newtonian fluid in the same channel. Fig. 4.12 shows that this is indeed the case, with part (a) corresponding to the no-slip case and (b) to the Navier-slip case with $\beta = 0.1$.

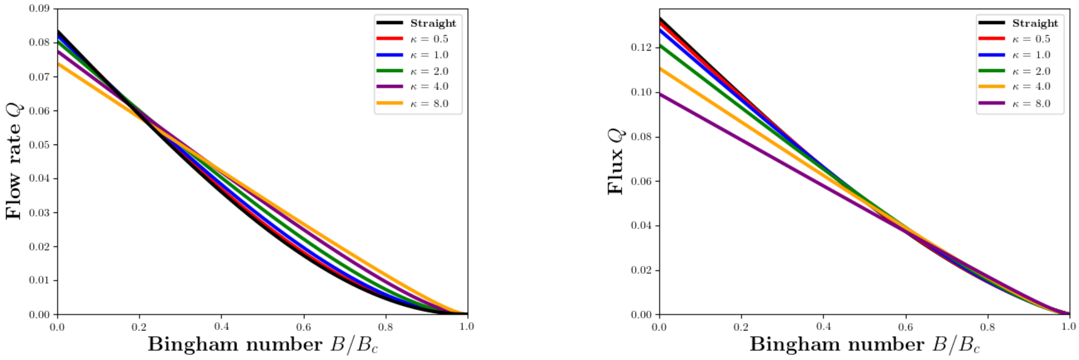

(a) (b)

Figure 4.12: The flow rate Q of Bingham fluid in a curved channel is investigated as a function of B/B_c for different channel curvatures κ; (a) for $\beta = 0$ and (b) for $\beta = 0.1$.

Fig. 4.12 also shows that at low Bingham number the flow rate is greatest for weakly-curved channels: increasing curvature of the channel reduces the amount of material moving through the channel. However, just as for the maximum velocity (fig. 4.5(b) and (d)) there is a crossover at a moderate value of B/B_c close to 0.2 for part (a) and at larger value of B/B_c close to 0.6 for part (b), and the flow through a curved channel is greater for given B/B_c. Note that B_c depends on the channel geometry κ so this is not equivalent to an increase of flow rate due to increased channel curvature κ for fixed B. As the curvature increases the flow rate becomes almost linear in B/B_c.

To maintain a constant flow rate Q, there exists a balance between the Bingham number B and the slip length β. The larger the slip length, the larger B which is required in order to slow up the fluid flow. In fig. 4.13, we consider the relationship between the Bingham number B and slip length β for a fixed flow rate $Q = 0.05$ for different channel curvatures κ and we scale by B_c (eq. (4.27)), which decreases with increasing κ. For small slip lengths β, the value of B/B_c increases with channel curvature κ but not monotonically. For larger values of β, the value of B required increases (with the rate at which it increases decreasing with κ) until it becomes close to B_c at very large slip lengths ($\geq 10^1$).

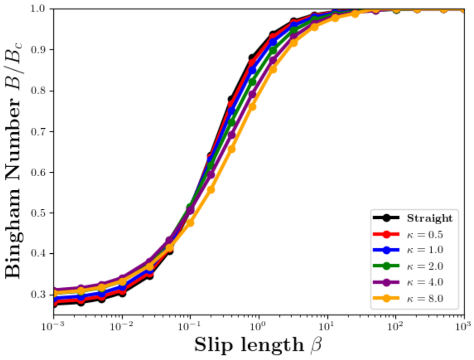

Figure 4.13: The relationship between the Bingham number B and slip length β in order to maintain a fixed flow rate $Q = 0.05$ for different channel curvatures κ between 0 and 8.

4.6 Simulation validation

We validate the accuracy of the results from our FEM simulation of a pressure-driven Bingham fluid in a curved channel. The aim of the simulation is to to validate the accuracy of the finite element method in curved channels, using the analytical work outlined earlier in the chapter, with the idea of relating the simulation to a more vein-like geometry in sec. 4.7 and in chapter 5. Producing accurate FEM simulations of a Bingham fluid in vein-like geometries is desirable in order to assess the performance of foam in sclerotherapy. We evaluate the effectiveness of the foam by determining the size of the rigid plug region, which vary depending on the Bingham number and channel curvature.

The accuracy of the simulation is determined by the value of the error ϵ, defined in eq. (3.24), and is calculated for different values of the tolerance δ, regularisation parameter m (eq. (2.31)), mesh fineness N/A_s and finite element space $\mathbb{P}_h^3$ using the same process undertaken in chap. 3.5. As the finite element simulation is written in Cartesian co-ordinates, we compare the speed data with the magnitude of u_θ from eq. (4.20).

We set the value of channel curvature $\kappa = 0.4$ (i.e. $R_i = 5$ and $h = 2$) and $B = 0.5$ and we consider the value of the error ϵ for two slip lengths $\beta = 0$ (no-slip) and 0.1. Obtaining small values of ϵ will give us confidence in the validity of the simulation results in a curved channel.

The channel geometry is shown in fig. 4.14. The cross-sections' of velocity for the numerical data are taken at an angle of 0, directly halfway along the annulus in order to avoid any effects of inflow and outflow, to ensure that the flow profiles are settled. The distance required in order to achieved a settled flow profile is considered for a curved channel (fig. 4.15) and also investigated further in the flow from straight to curved channel in chap. 4.7.

4.6.1 Error analysis

We consider an annular channel where both inner and outer channel walls are semi-circles for which the angle θ ranges between $-\pi/2$ and $\pi/2$, shown in fig. 4.14. The inner channel wall is at fixed radial position $r = \frac{1}{\kappa}$ and outer wall located at $r = \frac{1}{\kappa} + 1$ such that $h = 1$. From fig. 4.14, we show an example of a finite element mesh for the curved channel, with a number of triangles are around $8,000$ and present our results using the quantity N/A_c. The results of the simulations below require a much denser meshes than the example shown in fig. 4.14, thus the slight disordered appearance of the mesh plays no significant factor in the accuracy of the simulations.

The conditions on the inlet and outlet pressure are chosen such that the pressure gradient along the centreline of the annulus is set to one ($G = 1$). To simplify the condition, we set

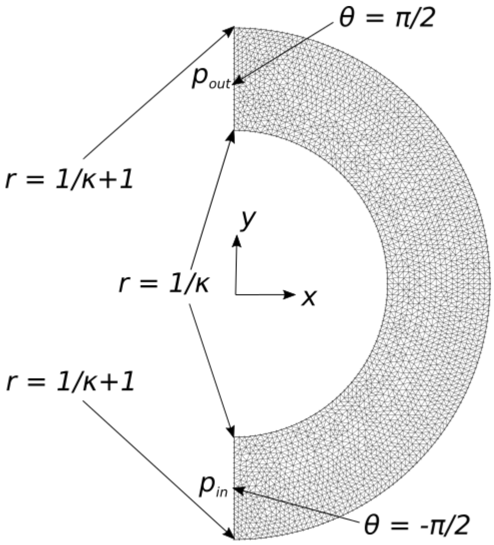

Figure 4.14: The mesh for the curved channel, a semi-circular annulus of angle π. We set the outlet pressure $p_{out} = 0$ and the inlet pressure according to eq. (4.32) to satisfy $G = 1$. The radial positions are between $\frac{1}{\kappa}$ and $\frac{1}{\kappa} + 1$. The mesh consists of around $8,000$ triangles.

$p_{out} = 0$ and vary the value of p_{in} according to:

$$p_{in} = \pi\left(\frac{1}{\kappa} + \frac{1}{2}\right). \tag{4.32}$$

The boundary conditions on the velocities at $r = \frac{1}{\kappa}$ and $\frac{1}{\kappa} + 1$ are the Navier slip boundary conditions, which depend on the chosen slip length β.

In fig. 4.15 we determine the appropriate "awayness" for the curved channel case. For $B = 0.5$, $\beta = 0$ and $\kappa = 0.4$, we consider the velocity cross-sections at different θ away from the outlet through a curved channel shown in fig. 4.14 (with θ between $-\frac{\pi}{2}$ and $\frac{\pi}{2}$), against the analytical velocity profiles in eq. (4.20). We see that there are distinct differences for the red curve denoting $\theta = \frac{23}{48}\pi$ and the analytical prediction, suggesting that the velocity is influenced by the outflow effects. As θ decreases, we see that the major differences located near the outer yield surfaces decreases until we see excellent agreement at $\theta = \frac{3\pi}{8}$. Therefore, we exclude these inflow and outflow regions of the channel of angle $\theta = \frac{\pi}{8}$ (with arc-length $\frac{\pi}{8}\left(\frac{1}{\kappa} + \frac{1}{2}\right) \approx 1.178$) from the results for the error analysis below, as we did for the straight channel case.

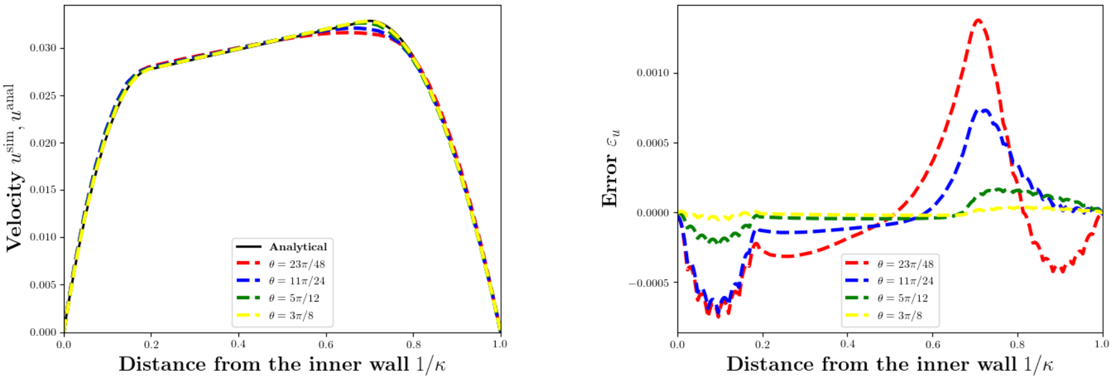

(a) (b)

Figure 4.15: (a) The velocity data for u_θ with $B = 0.5$ in a curved channel of curvature $\kappa = 0.4$ for different channels of arclengths $2\theta\left(\frac{1}{\kappa} + \frac{1}{2}\right)$, with the data taken from a cross-section at $\theta = 0$ (see fig. 4.14), located θ angle away from the channel inlet and outlet, (b) The error between both the simulation data and analytical velocity profiles $\varepsilon_u = u^{sim} - u^{anal}$.

In fig. 4.16, for a range of tolerances δ between 10^{-2} to 10^{-6}, we consider the error ϵ for different regularisation parameters m with fixed mesh fineness $N/A_c = 20.4 \times 10^3$. Taking smaller tolerances δ (and larger m) reduces the error ϵ as the velocities are allowed to converge further with decreasing δ, thus increasing the accuracy. The value of ϵ plateaus at $\delta \leq 10^{-5}$, meaning that we gain very little accuracy ($\approx 1.5\%$) from choosing $\delta = 10^{-6}$ over 10^{-5}. We therefore reach the same conclusions as chap. 3.5, that $\delta = 10^{-5}$ (and $m = 5000$) are appropriate values for our finite element simulations.

Choosing the finite element space $\mathbb{P}_h^3$ for the velocities yields more accurate results compared to $\mathbb{P}_h^1$, with the error ϵ (for $\delta = 10^{-5}$) approximately 10% and 12% smaller for $\beta = 0$ and 0.1, respectively. Once again, this suggests $\mathbb{P}_h^3$ should be used for the velocities in the simulations. Comparing with the results in fig. 3.10, the error for $\delta = 10^{-5}$ is 24% smaller in the straight channel ($\kappa = 0$) case than the curved channel ($\kappa = 0.4$).

In fig. 4.17, the error ϵ decreases with increasing mesh fineness N/A_c, particularly for $\delta \leq 10^{-5}$. The error for the two largest N/A_c vary little, implying that increasing N/A_c further past 20.4×10^3 yields little further accuracy. For a mesh fineness $N/A_c = 20.4 \times 10^3$ (and the velocity in $\mathbb{P}_h^3$), $\epsilon \approx 7.3$ and 11.2×10^{-5} for $\beta = 0$ and 0.1, respectively, suggesting

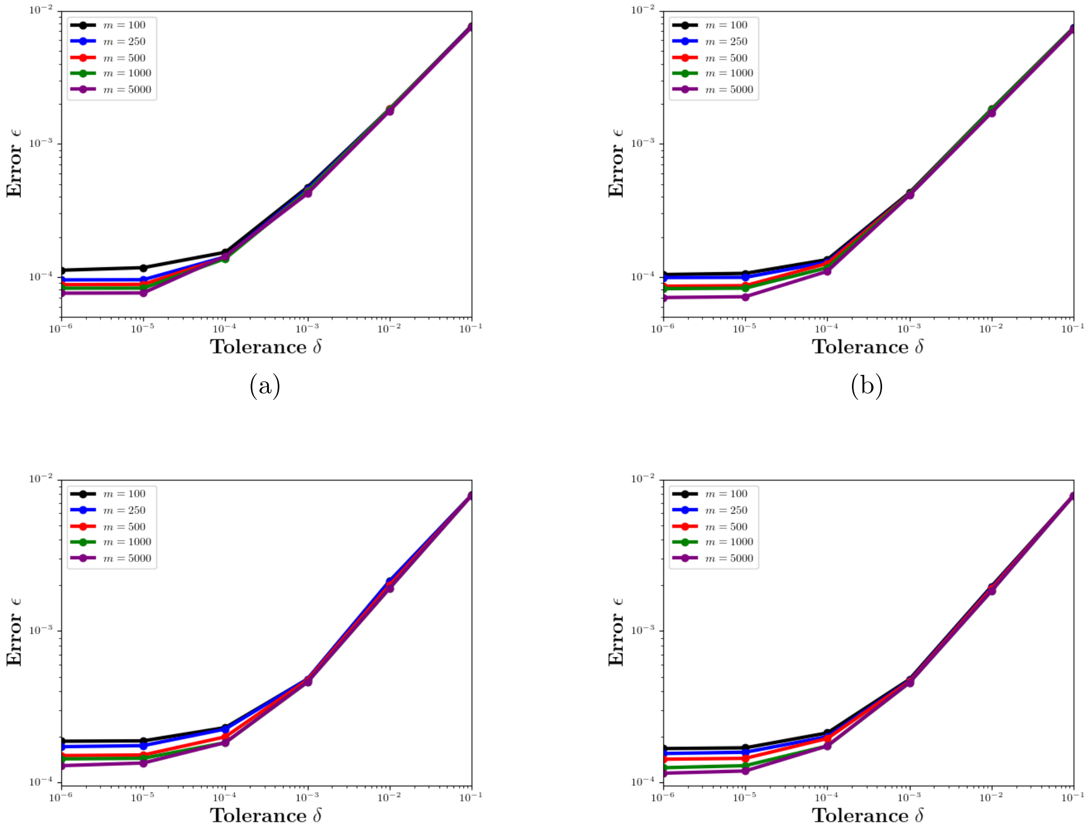

(a) (b)

(c) (d)

Figure 4.16: The error ϵ against the value of the tolerance δ for different values regularisation parameter m, $B = 0.5$, $N/A_c = 20.4 \times 10^3$ and: (a) for the velocities in $\mathbb{P}_h^1$ with $\beta = 0$, (b) for the velocities in $\mathbb{P}_h^3$ with $\beta = 0$, (c) for the velocities in $\mathbb{P}_h^1$ with $\beta = 0.1$, (d) for the velocities in $\mathbb{P}_h^3$ with $\beta = 0.1$,

that the error ϵ increases by 53% with increasing the slip length from 0 to 0.1.

In fig. 4.18, the execution time t_s for the simulation increases significantly from choosing $\mathbb{P}_h^3$ over $\mathbb{P}_h^1$ i.e for $\delta = 10^{-5}$ and $N/A_c = 20 \times 10^3$, t_c increases from 16 to 78 minutes. The slope of the relationship between the execution time and tolerance δ is approximated as $m_c \approx -0.2$ using eq. (3.25), which is in agreement with fig. 3.11 for the straight channel case.

The implementation of the Naiver slip boundary condition has only a very small effect on the execution time t_c i.e. for $N/A_c = 20.4 \times 10^3$ and $\delta = 10^{-5}$, t_c increases by 0.1% for $\beta = 0.1$ in compared to the case $\beta = 0$ (fig. 4.18).

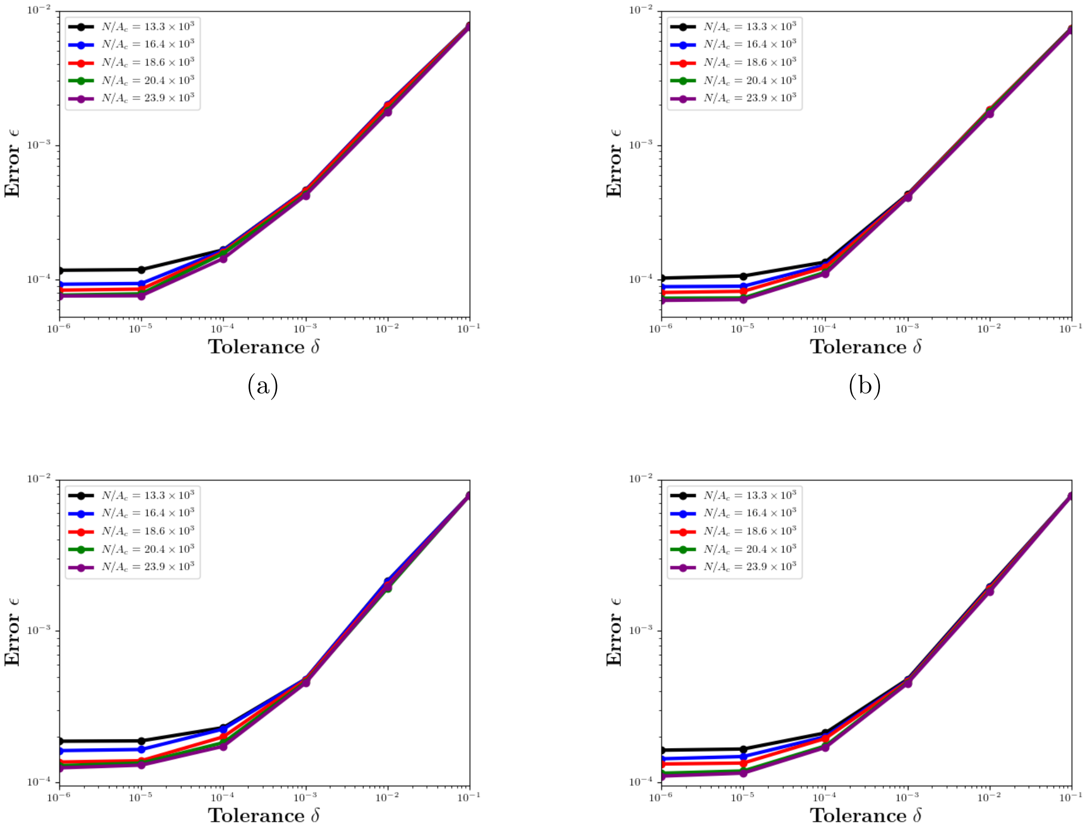

(a) (b) (c) (d)

Figure 4.17: The error ϵ against the value of the tolerance δ for different mesh fineness N/A_c, $B = 0.5$ and $m = 5000$: (a) the error for velocity contained in $\mathbb{P}_h^1$ and $\beta = 0$, (b) the error for velocity contained in $\mathbb{P}_h^3$ and $\beta = 0$, (c) the error for velocity contained in $\mathbb{P}_h^1$ and $\beta = 0.1$, and (d) the error for velocity contained in $\mathbb{P}_h^3$ and $\beta = 0.1$.

4.7 Flow from a straight to a curved channel

We have derived the velocity profile for a Bingham fluid in a curved channel (eq. (4.20)), but the question remains as to how this profile is established when fluid enters such a channel. We consider the velocity profile for slip lengths $\beta = 0$ (no-slip case considered by Roberts and Cox [2020]) and for $\beta = 0.1$.

We therefore consider a geometry in which a straight channel is connected to a curved channel of the same width (fig. 4.19). Fluid in the straight section, far from the join, flows

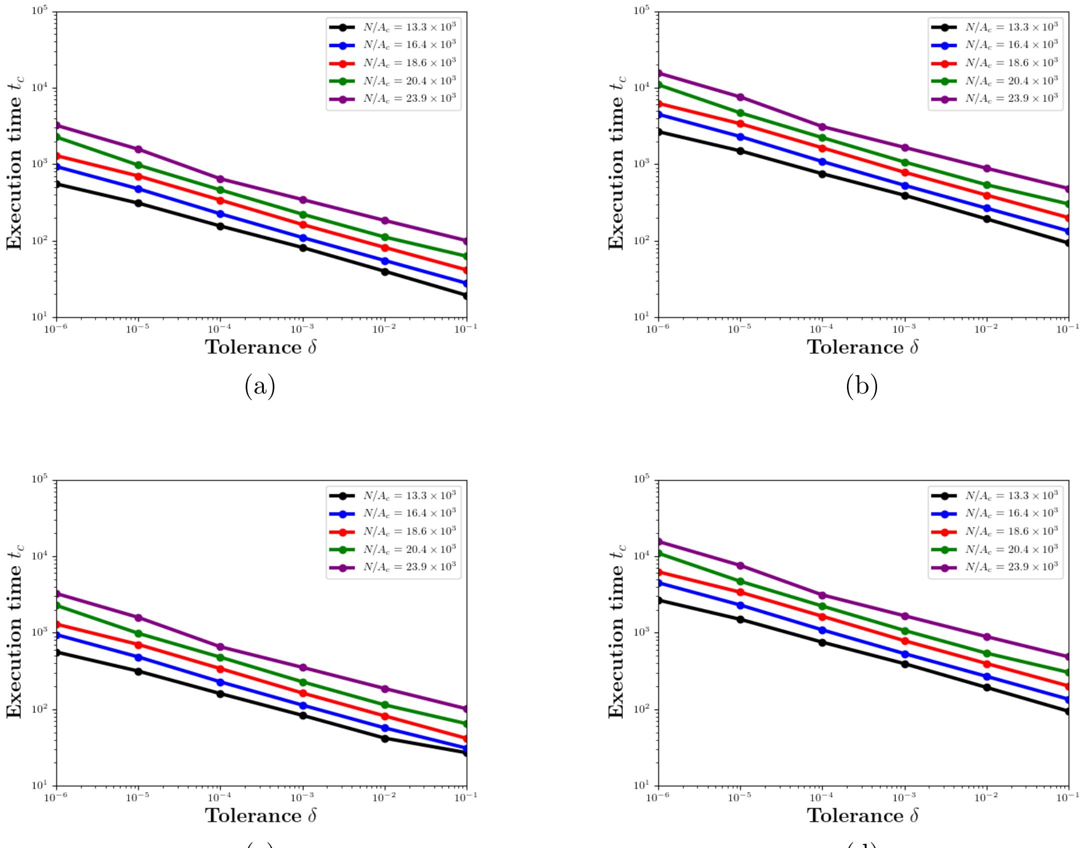

(a) (b)

(c) (d)

Figure 4.18: The execution time for each simulations for different tolerances with $m = 5000$: (a) for the velocities in $\mathbb{P}_h^1$ and $\beta = 0$, (b) for the velocities in $\mathbb{P}_h^3$ and $\beta = 0$, (c) for the velocities in $\mathbb{P}_h^1$ and $\beta = 0.1$, and (d) for the velocities in $\mathbb{P}_h^3$ and $\beta = 0.1$,

with the usual profile (eq. (3.20)) with yield surfaces at $y_c = 1/2 \pm B/4$, while fluid in the annular section, again far from the join, flows with the velocity profile in eq. (4.20). In between, there is a transition region whose length may depend on Bingham number B, slip length β and/or channel curvature κ. The flow is steady, but nonetheless we require a numerical solution of the governing equations, described below, to determine the flow in the transition region.

We choose the straight channel length to be $L = 5$, i.e. five channel widths long. The mesh for the joined straight and curved channel consists of $N = 198,564$ triangles, with highest density close to the walls of the channel and around the region where the channels meet (fig. 4.19). We take a unit pressure gradient, which is achieved by setting the inflow

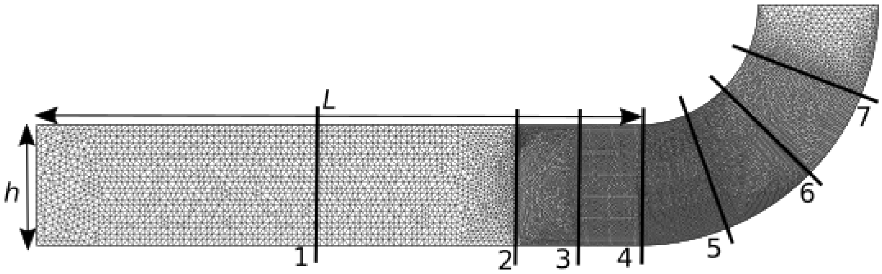

Figure 4.19: The channel geometry and finite element mesh used in the simulations to examine the transition between the velocity profile in a straight and a curved channel. The cross-sections 1-7 are used to probe the development of the velocity profile as fluid flows through the channel. The mesh in the figure is made of around $30,000$ triangles, approximately 5 times coarser than the meshes used in the simulations.

pressure to $p_{in} = 5 + \frac{\pi}{2}\left(\frac{1}{\kappa} + \frac{1}{2}\right)$ and outflow pressure to zero, and record two measures of the flow to determine the properties of the transition region:

- the velocity profile across different cross-sections of the channel. From this we can find the distances upstream and downstream of the join between channel sections at which the velocity profiles coincide with the analytic ones.
- the area of the unyielded plug region, normalized by the channel area. This gives a broader indication of the disruption to the flow caused by the transition to a curved channel.

The cross-sections are taken at three positions along the straight channel (fig. 4.19), at distances $2.5h$, $0.5h$ and $0.25h$ upstream of the join; at one cross-section where they join; and at three further cross-sections at angles of $\pi/8$, $\pi/4$ and $3\pi/8$ from the join in the curved channel.

4.7.1 Velocity profiles

We first set the Bingham number to $B = 0.6$ and slip length to $\beta = 0$ and show the velocity profiles for fixed channel curvature $\kappa = 0.4$ in fig. 4.20(a). At cross-section 1 the velocity profile takes the form of the straight channel velocity profile, symmetric about the channel centerline. At cross-sections 2 and 3, closer to the start of the curved region, there

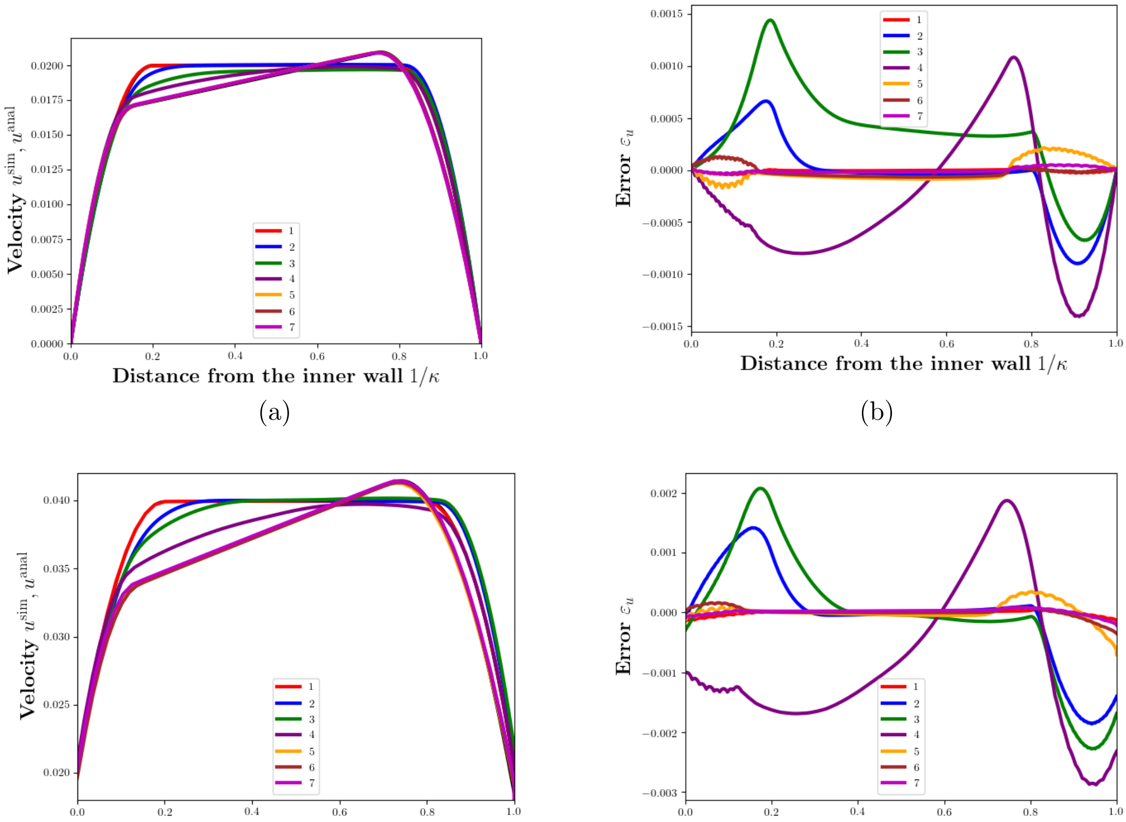

(a) (b)

(c) (d)

Figure 4.20: The velocity profiles in the transition region, shown at the numbered cross-sections indicated in fig. 4.19 and the difference between the simulation data and the appropriate analytical velocity profile, denoted by ε_u. Channel curvature is $\kappa = 0.4$ and Bingham number is $B = 0.6$ with parts (a) and (b) showing results for $\beta = 0$ and (c) and (d) denoting results for $\beta = 0.1$.

is a clear deviation from this profile and the beginning of a smooth transition towards the curved channel velocity profile, with fluid moving more slowly in the inner yielded region. By cross-section 5 the velocity profile almost overlaps the curved channel velocity profile, with just a small discrepancy near the outer yield surface. In cross-sections 6 and 7 it isn't possible to see a difference between the curves.

In fig. 4.20(c), we introduce slip and set $B = 0.6$, $\kappa = 0.4$ and $\beta = 0.1$ and show the velocity profiles at all 7 cross sections in fig. 4.19. At cross-section 1, the velocity profile matches the straight channel velocity profile. At both cross-sections 2 and 3, located closer to the start of the curved channel, the flow profile begins the deviation towards the expected velocity profile for the curved channel (eq. (4.20)), with the fluid de-accelerating towards the inner yielded region. We see that the profiles overlap by cross-section 5, in the same way as the no-slip case.

A more precise indication of convergence is given by the discrepancy in the velocity along each cross-section, defined as

$$\varepsilon_u = u^{\mathrm{sim}} - u^{\mathrm{anal}}, \tag{4.33}$$

where the superscript $^{\mathrm{anal}}$ refers to the straight channel profile for cross-sections 1 to 3 and to the curved channel profile for cross-sections 4-7. Fig. 4.20(b) ($\beta = 0$) shows that the main differences occur in the yielded regions, close to the yield surfaces, and particularly (but not unexpectedly) around the join (cross-sections 3 and 4) between the two channels. Cross sections 1 and 5-7 show very small values for ε_u, indicating that a distance $2.5h$ or an angle $\pi/8$ away from the join the fluid is moving with an unchanging analytically-predictable profile. For $\beta = 0.1$ in fig. 4.20(d), we see that the discrepancy ε_u in eq. (4.33) is very small for cross-sections 1 and $6 - 7$ as there is very little difference between the the analytical velocity profile and numerical data. The main differences occur at the yield surface positions and the outer channel wall, due to slip, at cross-sections 3 and 4 (at the join). There is some discrepancy ε_u near the outer wall of the channel at cross-section 5 but not enough to imply that the transition length has been increased by the existence of slip. The velocities for $\beta = 0.1$ are much larger than for $\beta = 0$ (the plug velocity is approximately doubled) which results in larger differences ε_u.

4.7.2 Yielded regions

Fig. 4.21 shows examples of the shape of the unyielded regions as the fluid moves from a straight to a curved channel for different Bingham numbers B and curvatures κ, for $\beta = 0$ (no-slip). Just after leaving the straight part of the channel the plug region narrows until the fluid is yielded. The plug then reforms over roughly the same distance in the curved part

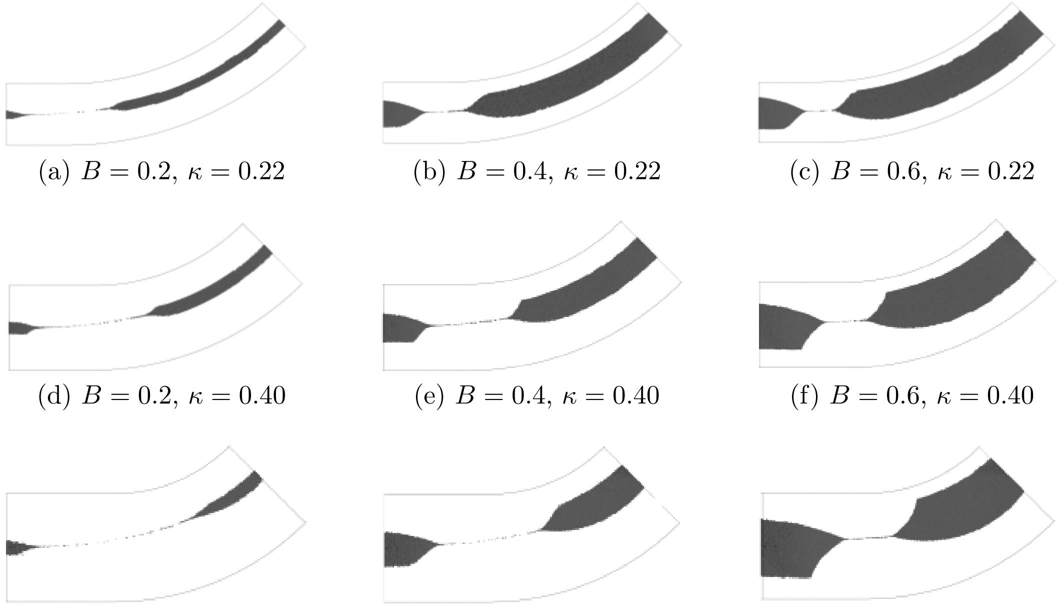

(a) $B = 0.2$, $\kappa = 0.22$ (b) $B = 0.4$, $\kappa = 0.22$ (c) $B = 0.6$, $\kappa = 0.22$

(d) $B = 0.2$, $\kappa = 0.40$ (e) $B = 0.4$, $\kappa = 0.40$ (f) $B = 0.6$, $\kappa = 0.40$

(g) $B = 0.2$, $\kappa = 0.66$ (h) $B = 0.4$, $\kappa = 0.66$ (i) $B = 0.6$, $\kappa = 0.66$

Figure 4.21: The outline of the plug region between cross sections 2 and 6 is shown for three different values of the Bingham number B, three different values of the channel curvature κ and slip length $\beta = 0$. Note how the fluid yields just downstream of where the straight channel meets the curved channel.

of the channel. The distance over which the fluid yields increases as the annulus curvature κ increases and as the Bingham number decreases. The width of the plug is smaller in the curved channel as expected from fig. 4.8.

For the case $\beta = 0.1$ in fig. 4.22, we see the similar behaviour to the no-slip case. The plug regions are slightly reduced, which can be seen in the most distinctively in part (i) (compared to fig. 4.21(d)). The slight reduction in unyielded plug region is expected from fig. 4.8(b) as the introduction of wall slip causes a slight narrowing in the plug length of a flow of Bingham fluid through an annulus with increasing β. The distance over which the fluid yields increases with increasing κ and decreasing B as seen in the no-slip case, the results in fig. 4.22 suggest that β between 0 and 0.1 has little influence on the length of this transitioning region, supported by fig. 4.20.

If there was an abrupt change from a uniform flow in the straight part of the channel to

(a) $B = 0.2$, $\kappa = 0.22$ (b) $B = 0.4$, $\kappa = 0.22$ (c) $B = 0.6$, $\kappa = 0.22$

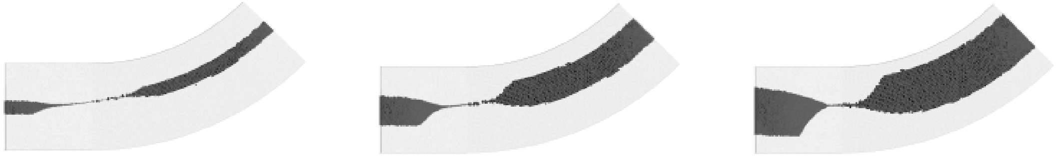

(d) $B = 0.2$, $\kappa = 0.40$ (e) $B = 0.4$, $\kappa = 0.40$ (f) $B = 0.6$, $\kappa = 0.40$

(g) $B = 0.2$, $\kappa = 0.66$ (h) $B = 0.4$, $\kappa = 0.66$ (i) $B = 0.6$, $\kappa = 0.66$

Figure 4.22: The outline of the plug region between cross sections 2 and 6 is shown for three different values of the Bingham number B and three different values of the channel curvature κ, with slip length $\beta = 0.1$.

a uniform flow in the curved part of the channel, the area of the plug region between cross sections 2 and 6 would be

$$A_p^{\text{anal}} = 0.5hB \; + \; \frac{1}{2}(r_o^2 - r_i^2)\frac{\pi}{8}. \tag{4.34}$$

Clearly the actual area of the plug in this transition region is much less than this. We therefore compare the area of the plug region found in the simulations between these cross-sections, A_p^{sim}, with this idealised value. In the limit $\kappa \to 0$ we expect $A_p^{\text{sim}} \to A_p^{\text{anal}}$.

Fig. 4.23 shows the relative yielded plug area for three different Bingham numbers and two different slip lengths as a function of channel curvature, with $\beta = 0$ indicating the no-slip case and dashed lines denoting the results for $\beta = 0.1$. We choose to show $1 - A_p^{\text{sim}}/A_p^{\text{anal}}$, which is a measure of the "missing" area of unyielded fluid between cross-sections 2 and 6. Relative to our naive prediction A_p^{anal}, this extra area of yielded fluid increases as the channel becomes more curved, indicating that the transition region becomes longer, in agreement

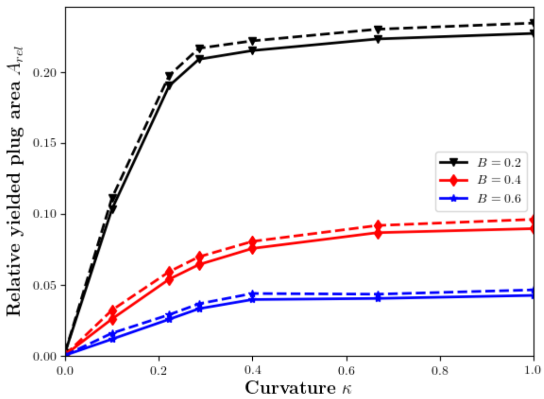

Figure 4.23: The relative yielded plug area $A_{rel} = 1 - A_p^{\text{sim}}/A_p^{\text{anal}}$ as a function of channel curvature κ in the region between cross-sections 2 and 6. The data for $\kappa = 0.0$ is from a simulation of an equivalent area of a straight channel with $h = 1.0$. The full lines indicate the no-slip condition ($\beta = 0$ in fig. 4.21) and the dashed lines show the results for $\beta = 0.1$ (fig. 4.22).

with fig. 4.21. This effect is stronger for small Bingham numbers, for which the plug is narrowest. The addition of slip increases the quantity $1 - A_p^{\text{sim}}/A_p^{\text{anal}}$ for all $\kappa > 0$, meaning that additional area of the unyielded region is lost relative to A_p^{anal}, which would (slightly) reduce the effectiveness of foam in sclerotherapy. The difference between no-slip and slip ($\beta = 0.1$) curves is less than 1% of the relative yielded plug areas, with the difference between both curves increasing with decreasing B (the difference between both curves are approximately 0.8%, 0.6% and 0.4% for $B = 0.2$, 0.4 and 0.6, respectively), meaning that for sclerotherapy, minimal slip and large B are essential for an effective treatment.

Lastly, we briefly consider what is going on in the region where the plug vanishes by considering the quantity $\log(|\underline{\underline{\dot{\gamma}}}|)$. Considering the value of $\log(|\underline{\underline{\dot{\gamma}}}|)$ allows us to see whether regions of fluid are moving as a yielded fluid, a plug fluid or "pseudo-plugs" [Balmforth and Craster, 1999; Muravleva, 2015; Walton and Bittleston, 1991], which are regions of fluid that experience values of stress very close to the yield-stress of the fluid. In the "pseudo-plug" regions, the fluid is not truly rigid but demonstrates close to plastic behaviour [Balmforth and Craster, 1999]. In fig. 4.24, a value of $\log(|\underline{\underline{\dot{\gamma}}}|)$ close to "0" would indicate that the strain-rate is large and the material is very highly sheared thus fully yielded, where a value close to "−14" indicates that the strain-rate is small thus moving as a plug. Here our regions of interest are regions that display an intermediate value of $\log(|\underline{\underline{\dot{\gamma}}}|)$, which imply pseudo-plug behaviour [Balmforth and Craster, 1999].

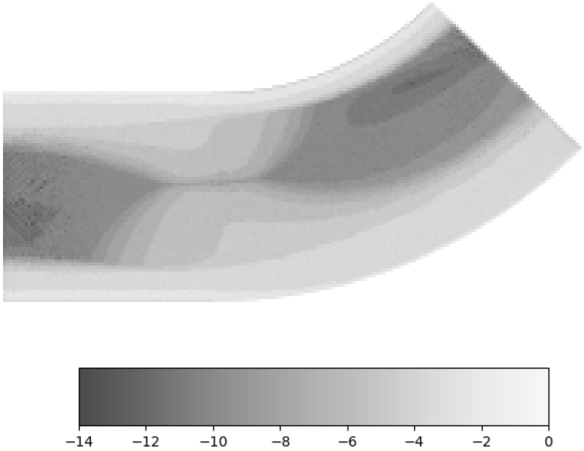

Figure 4.24: The logarithm of the second invariant of the strain rate tensor $\log(|\underline{\underline{\dot{\gamma}}}|)$ in a curved channel for a curvature of $\kappa = 0.66$ for $B = 0.6$ with slip length $\beta = 0.0$. Dark regions indicate regions of small strain-rates $\underline{\underline{\dot{\gamma}}}$ and lighter regions indicate regions of highly sheared material close to the channel walls.

In fig. 4.24, we consider the logarithm of the second invariant of the strain rate tensor $\log(|\underline{\underline{\dot{\gamma}}}|)$ for a Bingham numbers $B = 0.6$ and channel curvature $\kappa = 0.66$. We notice that the regions that appear to be highly sheared regions of yielded fluid in fig. 4.21(i) display intermediate values of $\log(|\underline{\underline{\dot{\gamma}}}|)$, implying that the fluid in the transitioning region is moving as a pseudo-plug with small strain-rates (but large enough to satisfy the criterion of being classified as yielded). Therefore, the results here imply that the transitioning region of yielded fluid may not be fully yielded and is actually fluid moving as a pseudo-plug. This news would be beneficial for sclerotherapy as the foam would maintain a motion which closely resembles a plug flow around a bend in a curved channel, which would allow for an effective displacement of blood.

4.8 Concluding remarks

Poiseuille flows of yield stress fluids in curved channels have attracted relatively little attention. It is clear that the scenario we describe, of a pressure-driven flow in a curved channel, is difficult to implement in an experiment in isolation. Instead, it could be thought of as one element of, for example, a network of pipes conveying some yield stress fluid, which due to certain constraints must be made to turn a corner.

Our predictions allow the effect of such a situation to be determined, for example the drop in flux associated with such a bend, as a function of the material parameters of the fluid. This work also provides a more stringent test against which to validate simulation codes for rheological models in non-trivial geometries and as a base flow which is perturbed when the flow-rate increases and secondary flows may arise.

Our main result, eq. (4.20), provides detailed insight into the dependence of the flow on the dimensions of the channel and the slip length β. It allows us to identify non-monotonicity in the flow, in particular in the region of maximum velocity (fig. 4.5(b) and (d)), stress (figs. 4.9 and 4.10) and flux (fig. 4.12) in the channel.

In terms of the Bingham number B, we consider two extreme situations. For small B, the fluid behaves like a Newtonian fluid, with relatively large velocity and large stress on the inner wall $\frac{1}{\kappa}$. Such a material is likely to be ineffective at displacing a second fluid (in the example of varicose vein treatments, this second fluid is the blood that initially fills the vein), because it will be prone to instabilities such as viscous fingering.

In the other limit, as $B \to B_c$, the flow is dominated by the yield stress of the fluid and is relatively slow. The majority of the material moves as a large plug which almost completely spans the channel (fig. 4.8). In applications, it is this plug region which is essential for displacing another fluid. So a large Bingham number is required in varicose vein sclerotherapy.

Our result also indicates that the degree of curvature of the channel κ affects the efficacy of a displacement flow. For a given Bingham number B, the width of the plug region is smaller for channels with greater curvature. In the varicose vein example, a vein that is manipulated in such a way to reduce its curvature should be treated more effectively. We have also shown that the value of β also has a role in the effectiveness of foam in sclerotherapy as the existence of slip induces smaller plug regions (fig. 4.8) for each B/B_c, reducing the capability of foam in the treatment.

We considered the maximum stress for the fluid (fig. 4.11), which is always located at $r = \frac{1}{\kappa}$, and noticed a general trend that the introduction of slip decreases the maximum stress (as well as the stress (fig. 4.10)) and also leads to the maximum magnitude of stress occuring at $r = \frac{1}{\kappa} + 1$. Therefore in industrial applications of slow flows of viscoplastic fluid through a pipe of curvature κ, one could regulate whether the inner or outer sections of a bent channel would wear at a greater rate by determining the value of β and B as the fluid would attribute a force over a chosen area of pipe.

Validating our numerical simulations (chap. 4.6.1) will allow us to examine more complex vein-like geometries and draw conclusions on the affect of B, κ and β in foam sclerotherapy. We conclude that the same optimal simulation parameters are valid for the flow in an annulus as for the straight channel from chap. 3.5.1. We conclude that for the no-slip and slip case choosing FE space $\mathbb{P}_h^3$ over $\mathbb{P}_h^1$ reduces the error ϵ by 10% and 12%, respectively, but the execution time is greatly increased (fig. 4.18).

Our simulations of the transition in the velocity profile as fluid moves from a straight channel to a curved one in chap. 4.7 indicate that in this region the fluid yields (fig. 4.21), albeit over a short distance, which depends on both B and κ but not small $\beta \leq 0.1$. The results for $\beta = 0.1$ suggest that the performance of foam wouldn't be hindered by wall slip as the relative plug areas are reduced by less than 1% (fig. 4.23) for $\beta = 0.1$. Therefore, wall slip could be beneficial for the purposes of displacing one another (less viscous fluid) fluid as the size of the plug regions are largely unaffected i.e. the regions essential for effective displacement but the velocities increase proportionally to β leading to a quicker displacement. In this yielded region there is likely to be a good deal of mixing between blood and foam during sclerotherapy, which again highlights the importance of keeping the vein as straight as possible during treatment.

5 A flow of Bingham fluid in a sinusoidal channel

5.1 Introduction

In this chapter, we consider the flow of Bingham fluid in a more complex geometry than the straight and curved channels investigated in chapters 3 and 4 as we which to extend the research to more complex channel geometries that might represent a more typical vein geometry. The aim of the thesis is to determine the effectiveness of foam, which we model as a yield-stress fluid, in sclerotherapy. Veins, in particular varicose veins, are usually tortuous thus we are required to consider how the treatment is affected by the vein geometry. Here, we produce simulations of a pressure-driven Bingham fluid in a sinusoidal channel and consider the consequence of deviating away from a straight vein on the size of the foams plug region and thus the effectiveness of the blood displacement.

A sinusoidal channel is an interesting problem to study as we expect that by increasing the amplitude of the channel, it causes additional yielding of the foams plug region, as seen in the previous chapter in an annulus. This yielding of the plug region in our application is detrimental but could be a useful for industrial applications of yield-stress fluids, which would like to enhance situations where the fluid is being yielded or in order to mix with another fluid.

We again investigate the extent of relative yielding A_{rel} (i.e. the yielded area of the plug region) and position of the plug areas as considered for the flow from the straight to curved channel in chap. 4.7. We measure the relative area of the plug region for different Bingham numbers and channel amplitudes. As the channel geometry deviates from a straight channel, there is more yielding.

We record the speed $|\underline{u}|$ of the fluid at two cross sections within the sinusoidal region. Plotting the contours of speed shows that the global maximum of speed is not necessarily at the centre of the sinusoidal region. In chap. 5.5.3.1, we identify the maximum $|\underline{u}|_{max}$ and trace its position for different channel amplitudes and Bingham numbers. Closely related to the speed, we also calculate the flow rate Q, identifying the effect of geometry on Q. The effects induced by a sinusoidal channel (chap. 5.5.1.1) on A_{rel}, Q and $|\underline{u}|_{max}$ could be beneficial for industrial purposes, for example if one would like to cause complete yielding of the plug, or to increase the flow rate without considerably increasing the value of the driving pressure gradient G.

Despite the complexity of the channel geometry, similar sinusoidal geometries have been examined for Newtonian fluids, both experimentally and numerically, though a variety of channels and pipes with wavy boundaries. Burns and Parkes [1967] considered the peristaltic motion (i.e. the phenomenon of fluid transport in organs [Mittra and Prasad, 1974]) of a two-dimensional Stokes flow in a symmetric sinusoidal channel and derived expressions for the flow profile by using a Fourier series, concluding that the flux per unit length is roughly proportional to the channel width h, for each amplitude. Bizzarri et al. [2002] also considered Stokes flow in a sinusoidal channel, where an approximate solution is constructed by using a series expansion, deriving an expression for the velocity components and validating the reversibility of the flow, for the purpose of studying solute transport in rough-walled fractures. Song et al. [2018] modelled surface roughness on Stokes flow in sinusoidal pipes, noticing that increasing the amplitude of the sinusoidal function at the wall causes an increase in the pressure drop, leading to larger stresses. The conclusions are connected with the results for $B = 0$ in fig. 4.9 and 4.10 for a curved channel, that curvature of the channel walls induce larger stresses. We can link flows of Newtonian fluids in sinusoidal channels with industrial applications, such as flows in the oil displacement industry [Otomo et al., 2015].

Hemmat and Borhan [1995] numerically determined critical geometrical parameters leading to secondary viscous eddies for a shear flow of viscous fluid past sinusodially corrugated walls, which is one example of many studies into the onset of flow reversal past wavy walls

[Higdon, 1985; Munson et al., 1985; Pozrikidis et al., 1992]. When the amplitude of the sinusoidal walls is sufficiently large, streamlines indicate the existence of eddies, supported by the numerical simulations of Pozrikidis et al. [1992] in 2D and by Malevich et al. [2006] in 3D. In yield-stress fluids, the locations of eddies in Newtonian fluids coincide approximately with locations of static plugs for Bingham fluids, also called "dead regions" [Brunn and Abu-Jdayil, 2007], which we determine for our channel geometry in chap. 5.5.1.3.

The Navier [Navier, 1823] slip condition is commonly used for flows of Newtonian fluids in straight geometries [Brunn, 1975; Ebert and Sparrow, 1965; Lauga and Stone, 2003], as discussed in chaps. 3 and 4. The related literature for slip flows along complex geometries is limited, although channels can be intentionally wavy and corrugated in order to enhance flow (or do so unintentionally), due to the amplitude of the channel geometry. The flow profile for a fluid in a longitudinally corrugated channel with slip was derived by Chu [1996] and went on to consider a Newtonian flow through a pipe [Chu, 1999a] and an annulus [Chu, 1999b, 2000]. We provide results for two different slip lengths using the slip (eq. (2.25)) boundary conditions, which allows us to identify the effect of wall slip on A_{rel}, $|\underline{u}|$ and Q which allows us to stimulate further discussions about the implications of wall-slip on the sclerotherapy process.

The flow of a yield-stress fluid through sinusoidal channels is much less investigated. Roustaei and Frigaard [2013] considered the phenomenon of "fouling layers" (see fig. 5.1) i.e. dead regions where the fluid becomes stationary in layers next to the walls of wavy-walled channels. Their expansion-contraction channel geometry, with sinusoidal walls is wider at the centre of the sinusoidal region as it's symmetric about the x and y axis, causing large dead regions of stationary plug to form in the region where the channel is wider, with the aid of the conservation of mass. Dead regions occur at the widest regions, which depend on B, for example in fig. 5.1 we see that the size of dead regions become larger at larger amplitudes. Roustaei's [2016] work on flows of yield-stress fluids along fractures, will also be related to the results from our FEM simulations. A channel of identical geometry was

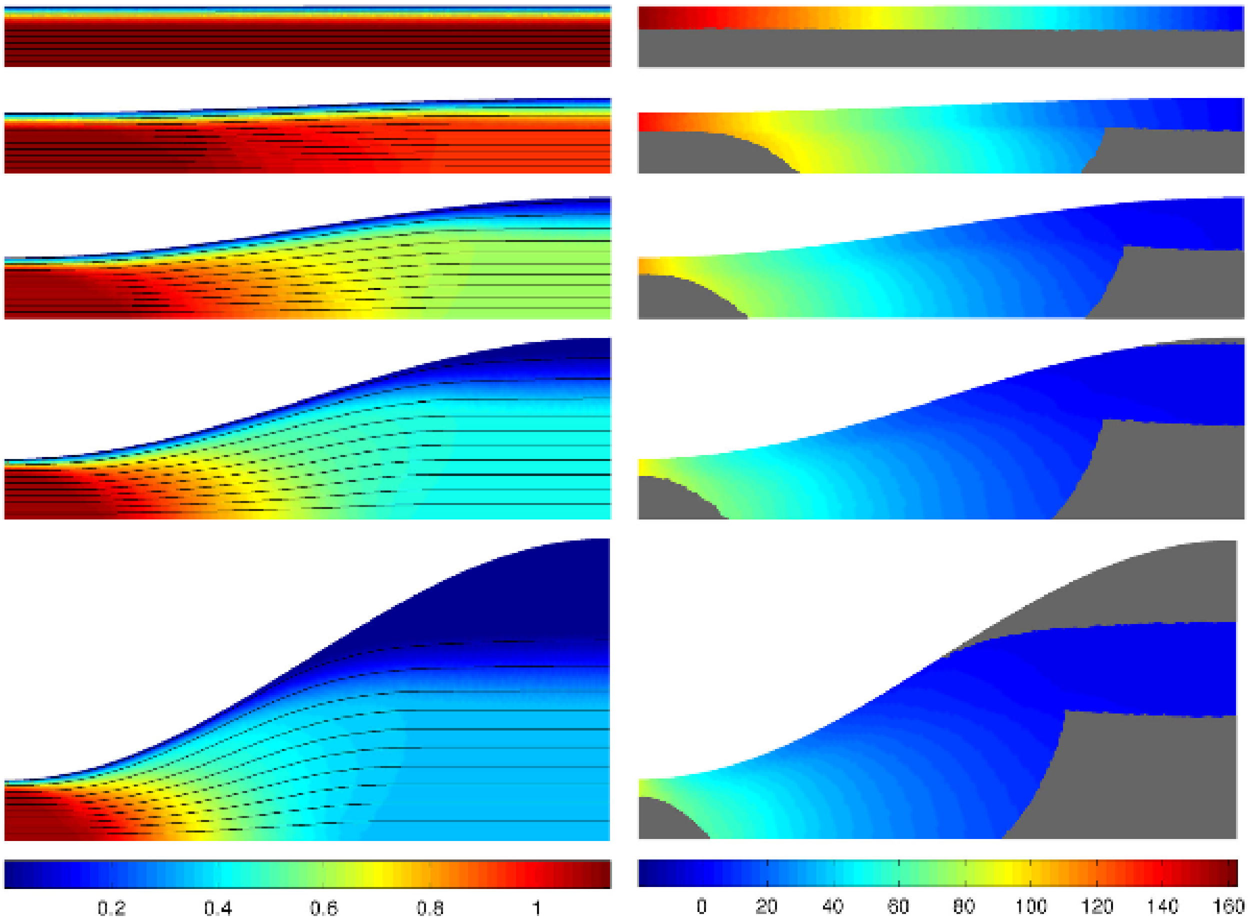

Figure 5.1: The dead regions of fluid that occur in sinusoidal channels presented by Roustaei and Frigaard [2013], for fixed B and different values of amplitude y_0, which increases the further down the figure you go. The left hand sides are the plot of speed and on the right we have pressure, with the unyielded plug coloured in grey.

investigated by Roustaei [2016] (see fig. 5.2) who noted that the "the fastest travelling fluid moves at the larger radius of curvature (i.e. towards the outer channel wall) while the plug regions are displaced at each bend".

5.2 Geometry of the sinusoidal channel

We consider a flow of Bingham fluid through a sinusoidal channel of "almost" constant width with wavy walls described by a sinusoidal function and investigate the effect of the channel geometry on the fluid's flow profile and the size of the plug regions. The channel consists of two straight channel sections, the inflow and outflow regions; between these straight channel

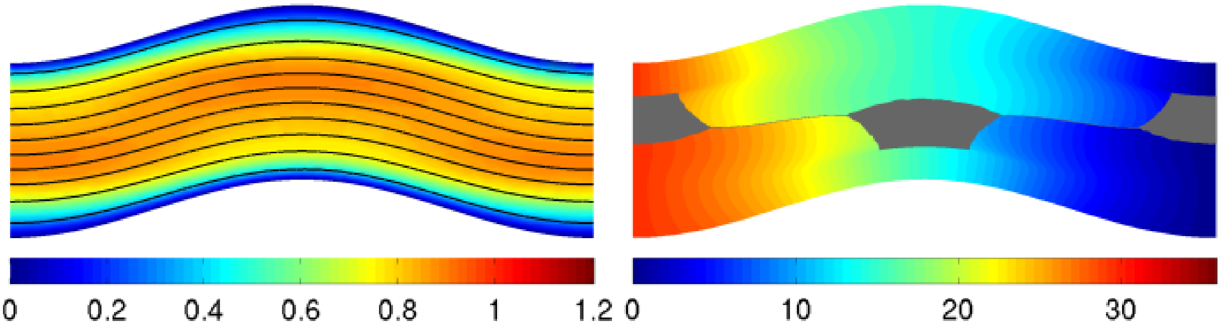

Figure 5.2: Computed examples of a flow of Bingham fluid through a sinusoidal channel with no-slip boundary condition, taken from Roustaei [2016]; the left diagram shows the speed and streamlines and the right show the contours of pressure p and plug regions in gray.

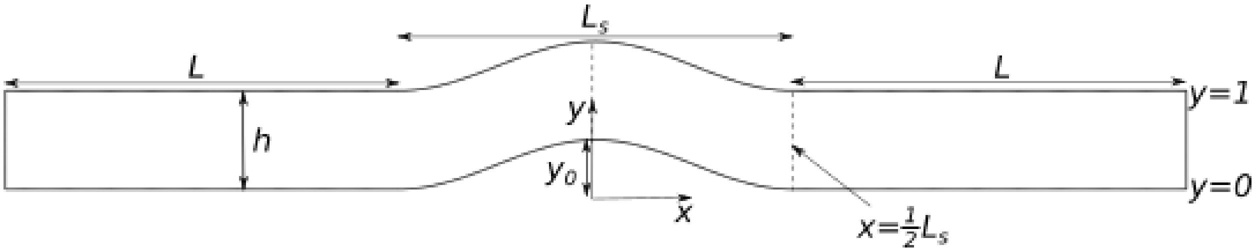

Figure 5.3: The geometry of the sinusoidal channel. We vary the value of y_0 the shape of the sinusoidal section is given by eq. (5.1).

sections is a sinusoidal region. The shape of the walls is determined by one period of a sinusoidal function, which determines the deviation from a straight channel.

The straight channel inlet and outlet regions are of length L and width $h = 1$ (shown in fig. 5.3). The length L is chosen such that the inflow and outflow effects occur far from the sinusoidal region. All simulations are run with $L = 5$. As identified from fig. 3.8, this is not an optimal minimum length to avoid inflow effects, which is in fact around $L \approx 0.5$.

Joining these straight regions is the sinusoidal region, of length L_s. The walls of the sinusoidal channels are functions

$$y = W(x) = \frac{1}{2}y_0\left(1 - \cos\left(\frac{2\pi}{L_s}\left(x - \frac{L_s}{2}\right)\right)\right). \tag{5.1}$$

Eq. (5.1) describes the bottom wall of the channel. The amplitude y_0 is varied between

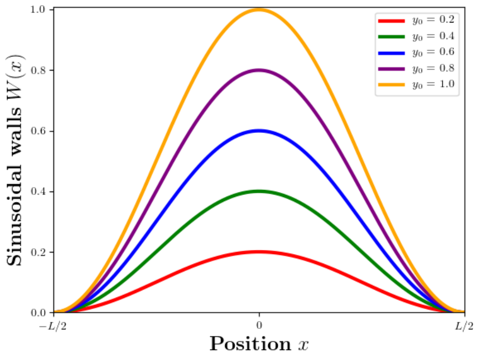

Figure 5.4: The function $W(x)$, the shape of the sinusoidal part of the channel, shown in eq. (5.1) for different values of y_0.

0 and h (fig. 5.4), and we trace the effects of varying its value on the size of the plug regions within the central sinusoidal region. The channel is symmetric about $x = 0$, such that $|x| \leq L_s/2$ denotes the sinusoidal region and $|x| \geq L_s/2$ denotes the straight channel sections. We consider two cross-sections of speed, one at $|x| = 0$, denoted by χ_1 and the second at $|x| = L_s/2$, denoted by χ_2.

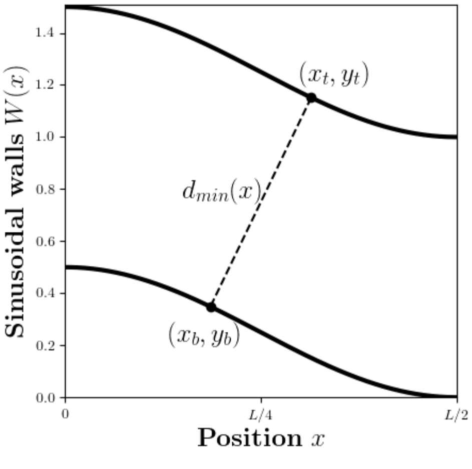

Figure 5.5: A diagram showing the location of the minimum distance $d_{min}(x_t, x_b)$ in a sinusoidal channel for $h/L_s = 0.33$ and $y_0 = 0.5$.

The channel has constant vertical width 1 but doesn't have a constant channel width perpendicular to the wall (shown in figs. 5.5 and 5.6) with increasing amplitude y_0. In regions between cross-sections χ_1 and χ_2, we notice that the minimum distance between

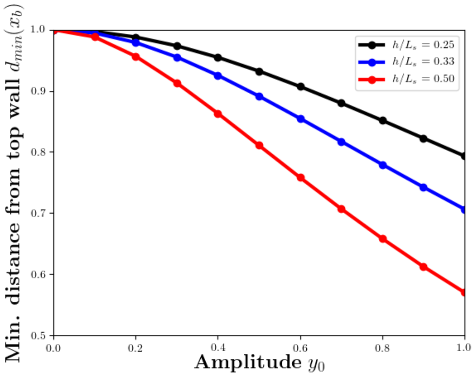

Figure 5.6: The minimum distance, defined as the minimum value of $d(x_b)$ (eq. (5.2)) from (x_t, y_t) on the top wall to (x_b, y_b) on the bottom wall for different ratios $h/L_s = 0.25$, 0.33 and 0.5.

the bottom and top wall becomes less than one, as shown for $h/L_s = 0.33$ and $y_0 = 0.5$ in fig. 5.5, where $d_{min} \approx 0.9$. The method used to identify the co-ordinates (x_t, y_t) on the top wall, which are perpendicular to the bottom wall at position (x_b, y_b) is described in the appendix (§A.2). Once co-ordinates (x_b, y_b) are identified, we investigated the minimum (perpendicular) distance from a point (x_b, y_b) on the bottom wall to (x_t, y_t) on the top wall in fig. 5.6, measured as the minimum of

$$d(x_b) = \sqrt{(x_t - x_b)^2 + (W(x_t) + h - W(x_b))^2} \tag{5.2}$$

we notice that increasing the amplitude y_0 decreases this distance, particularly for larger channel lengths h/L_s. This narrowing of the channel width (which occurs near $x = L_s/4$) is one reason we expect the flow rate to increase with increasing y_0. The minimum distance is reduced by up to 43% for $y_0 = 1$. The narrowing of the perpendicular channel width will induce additional yielding of the plug region and cause the fluids velocity to increase.

As we concluded in chap. 4.7, the introduction of curvature to the channel walls introduces additional yielding and larger stresses. This chapter will reiterate the importance of keeping veins as straight as possible during treatment.

5.3 Setting a constant pressure gradient

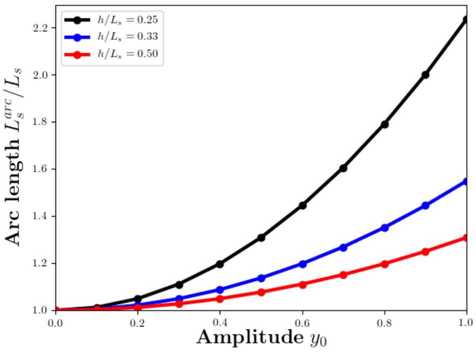

Figure 5.7: The arc length of the sinusoidal region L_s^{arc}, divided by L_s, for different values of y_0 and $h/L_s = 0.25$, 0.33 and 0.5.

In setting the pressure-gradient it is important to consider that the introduction of non-zero amplitudes y_0 makes the channel length longer. The channel length is equal to $2L + L_s^{arc}$ (fig. 5.3), where L_s^{arc} is the (arc) length of the sinusoidal region. It is possible to calculate L_s^{arc} between $-L_s/2$ and $L_s/2$ as it is described by $W(x)$ from eq. (5.1) (which is smooth (C^∞) between $-L_s/2$ and $L_s/2$), by evaluating the line integral [Larson et al., 2006]

$$\begin{aligned} L_s^{arc} &= 2\int_0^{L_s/2} \sqrt{1 + \left(\frac{dW(x)}{dx}\right)^2}\, dx \\ &= 2\int_0^{L_s/2} \sqrt{1 + \left(y_0 \frac{\pi}{L_s} \cos\left(\frac{2\pi}{L_s}\left(x + \frac{L_s}{2}\right) + \frac{\pi}{2}\right)\right)^2}\, dx. \end{aligned} \tag{5.3}$$

Eq. (5.3) is evaluated numerically because it's an "elliptic integral" which has no analytical solution. We use the "quad" integration tool in Python to find the values of L_s^{arc} and the results are plotted on fig. 5.7 for different values of h/L_s, scaled by L_s. Increasing the value of y_0 for different ratios of h/L_s increases the arc length of the sinusoidal region. The values for L_s^{arc} are stored for each given y_0 and h/L_s and are used by FreeFem++ to set the value of the pressure gradient, which is dependent on the length of the channel (see eq. (3.1)). The numerical uncertainty for the arc length is of the order 10^{-14}.

We fix the pressure gradient at $G = 1$ for channel amplitude y_0. The pressure gradient

G is set by fixing the values of the inlet p_{in} and outlet p_{out} pressure, as in chap. 3 and 4. The pressure gradient is equal to the difference between p_{in} and p_{out} divided by the length of the channel, which increases with amplitude y_0. To simplify our approach, we set the outlet pressure to zero ($p_{out} = 0$) and determine the required value of the inlet pressure p_{in}, for each amplitude y_0, to give $G = 1$. Using eq. (5.3), we find the length of the channel in order to set p_{in}:

$$G = \frac{p_{in} - p_{out}}{2L + L_s^{arc}} = 1 \implies p_{in} = 2L + L_s^{arc}.$$

Our predominant focus is on the sinusoidal region at the centre of the channel, thus we choose to present results of the data positioned within the sinusoidal region, which has a domain labelled as Ω_s, denoting the whole sinusoidal region of the channel i.e. $|x| \leq L_s/2$. This allows us to exclude any irrelevant yielding that occurs at the inlet and outlet of the channel far away from the region of interest. We will evaluate the value of the plug area for five different Bingham numbers in the range $0.2 - 0.6$ for amplitudes y_0 between 0 and 1.

5.4 Numerical Method

We consider a pressure-driven Bingham fluid through the sinusoidal channel and consider the results for two different slip lengths; $\beta = 0$ (no-slip) and $\beta = 0.1$. For a (vertical) channel width of $h = 1$, we vary the length of the sinusoidal region between $L_s = 2$ and 4 and consider its effects in chap. 5.5.1.3. Initially we set $L_s = 4$ thus $h/L_s = 0.25$. The geometry of the channel is changed by the parameter y_0, denoting the channel amplitude, where the walls of the channel in the sinusoidal region are described by eq. (5.1). We investigate the impact of increasing its value (thus deviating from the straight channel) on the plug region and the speed within the sinusoidal section i.e. for x between $-L_s/2$ and $L_s/2$. The case $y_0 = 0$ will replicate the results provided in chap. 3.

We focus on calculating the area of the plug region of fluid within the sinusoidal region. The plug area is an essential quantity to estimate for the purpose of sclerotherapy as it is determines the extent of effectiveness of the displacement of blood by the foam from a vein. We measure the relative yielded plug area as

$$A_{rel} = 1 - A_p^{\text{sim}}/A_p^{\text{anal}} \tag{5.4}$$

which provides $A_{rel} = 0$ in a straight channel. Here the remaining plug area is considered relative to A_p^{anal}, the analytical plug area of the straight channel case $y_0 = 0$, as the analytical locations of the yield surface positions are unknown for such a channel geometry. Using the same approach to calculate the plug areas as outlined in chap. 2.2.2.7 and using appropriate choices of B_ϵ (chap. 3.5.2), we plot the yielded regions in chap. 5.5.1 for each y_0 to draw preliminary conclusions on the effect of the amplitude y_0. Following this, we consider other quantities such as the maximum speed $|\underline{u}|_{max}$, its position and the flow rate, in chap. 5.5.3.1. Using the previous error analysis (chap. 3.5 and 4.6.1), we know that for accurate simulation results requires a mesh fineness of at least $N/A_c = 20.4 \times 10^3$, which we set for all meshes in this chapter.

As mentioned previously, we consider two different cross-sections of speed in a sinusoidal channel: located directly at the centre (denoted by χ_1) as well as at the inflow (denoted by χ_2), as indicated on fig. 5.3. At these cross-sections, we also find the locations of the yield surfaces and the fluids' plug width.

5.5 Results

5.5.1 Plug areas in the sinusoidal region

The plug areas of fluid in the numerical simulations are regions which experience "local" stress (in this case $|\underline{\underline{\tau}}| = \sqrt{\frac{1}{2}(\underline{\underline{\tau}} : \underline{\underline{\tau}})}$) with a magnitude less than $\frac{1}{2}(B + B_\epsilon)$. We also know from the constitutive equation that the value of $|\dot{\underline{\underline{\gamma}}}|$ within the plug region is zero (eq. (2.16) and (2.17)). Recall that by using a regularised Papanastasiou model, the plug region is not a rigid solid but a "highly viscous fluid that approximates ideal viscoplastic behaviour"

[Burgos et al., 1999]. We quantify the relative area A_{rel} for different amplitudes y_0, Bingham numbers B and channel lengths h/L_s.

5.5.1.1 The effect of varying the amplitude in the no-slip case on the plug area

In figs. 5.8, 5.9 and 5.11, we plot the plug areas for fixed channel length $h/L_s = 0.25$ and slip length $\beta = 0$, for different amplitudes y_0 between 0 and 1 and for Bingham numbers $B = 0.2, 0.4$ and 0.6. In all cases, we see that increasing y_0 causes further yielding within the sinusoidal region, with the extent of this additional yielding dependent on B.

In fig. 5.8 ($B = 0.2$), we see that small values of y_0 between 0 and 0.3 causes little further yielding of the plug region. The introduction of a small amount of curvature in this limit is not sufficient to increase the stress to yield all the fluid at the centre of the channel. As the Bingham number is smaller, the yield surfaces lie closer to the centre of the channel; this flow requires a larger amplitude y_0 to cause further yielding of the plug region in comparison to fluids with larger yield-stresses B. At $y_0 = 0.4$, the plug region in the sinusoidal region becomes separated from the plug region situated (nearly - see fig. 5.36) outside the sinusoidal region (i.e. $|x| \geq L_s/2$) as the fluid is (nearly) completely yielded close to the inlet of the sinusoidal region, with the plug region in the sinusoidal section taking a "crescent"-like shape. At $y_0 = 0.7$, the crescent-shaped plug splits into three parts as the plug in the straight channel region extends further from the inlet of the sinusoidal region. We see very little difference in the shape or size of the plug regions between $y_0 = 0.8$ and 1 as there is very little further yielding of the plug region outside the sinusoidal region. The bulk of the plug fluid remains a consistent distance away from the inlet.

In fig. 5.9, the results for $B = 0.4$ provides more extreme yielding patterns even for small $y_0 \leq 0.2$. The introduction of curvature causes two large "chunks" of un-yielded plug to exist within the sinusoidal region, one at the inlet and one at the centre near $x = 0$. The fluid is nearly completely yielded outside these "chunks" of plug with a small connecting line of

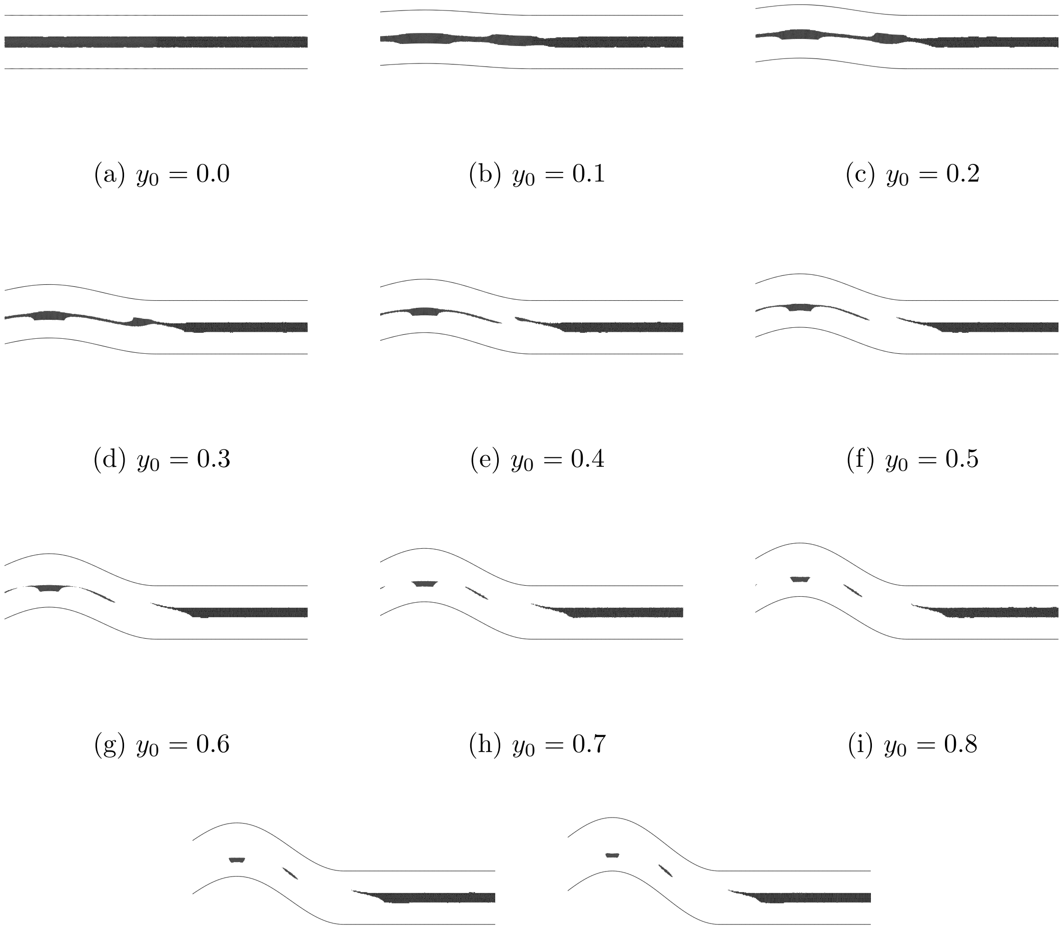

(a) $y_0 = 0.0$ (b) $y_0 = 0.1$ (c) $y_0 = 0.2$

(d) $y_0 = 0.3$ (e) $y_0 = 0.4$ (f) $y_0 = 0.5$

(g) $y_0 = 0.6$ (h) $y_0 = 0.7$ (i) $y_0 = 0.8$

(j) $y_0 = 0.9$ (k) $y_0 = 1.0$

Figure 5.8: The shapes of the plug regions are shown in black for $B = 0.2$ and channel amplitudes y_0 between 0 and 1.

plug joining them both. Referring back to chap. 4.5, the analytical stress profiles derived in eq. (4.13) and plotted in figs. 4.9 and 4.10 show that for curved channels there is an increase in the stress within the channel for larger B. The additional stress due to curvature causes additional yielding to occur, which is the origin of the isolation of the chunks of plug. For larger values of $y_0 > 0.2$, the behaviour is very similar to the case $B = 0.2$, with a crescent shape forming at the centre before breaking into three parts. Notice that for the values of y_0 considered, the complete yielding of the fluid in the sinusoidal region is never achieved.

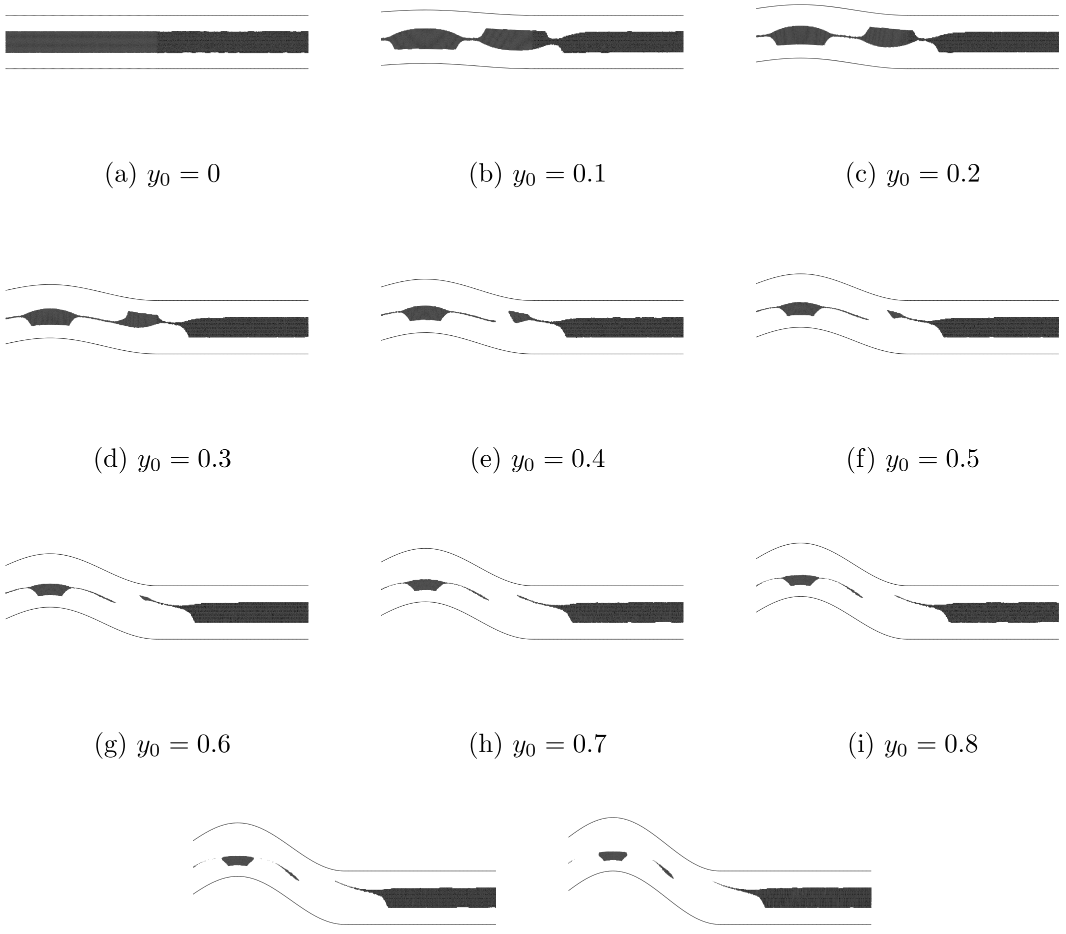

(a) $y_0 = 0$ (b) $y_0 = 0.1$ (c) $y_0 = 0.2$

(d) $y_0 = 0.3$ (e) $y_0 = 0.4$ (f) $y_0 = 0.5$

(g) $y_0 = 0.6$ (h) $y_0 = 0.7$ (i) $y_0 = 0.8$

(j) $y_0 = 0.9$ (k) $y_0 = 1.0$

Figure 5.9: The shapes of the plug regions are shown in black for $B = 0.4$ and channel amplitudes y_0 between 0 and 1.

The largest value of B considered is $B = 0.6$ and the results are plotted for y_0 between 0 and 1 in fig. 5.11. Recall that in the curved channel case (chap. 4), the value of B at which fluid flow ceases, labelled as B_c (eq. 4.27), decreases as the curvature increases. We are unable to derive the value of B_c analytically for the sinusoidal case, but we can be certain that it is less than 1 (for non-zero y_0) and its value can be estimated using the simulations. An approximation for B_c was found by running the simulation for increasing B until the flow rate reduced to $Q \approx 10^{-4}$. In fig. 5.10, we show the estimated values for B_c as a function of y_0 for $h/L_s = 0.25$. B_c decreases between $y_0 = 0$ and 0.6 to $B_c \approx 0.92$. For larger values of y_0, the perpendicular distance between the sinusoidal walls becomes narrower in the sinusoidal region near $x = L_s/4$ (see fig. 5.6), causing a large amount of yielding of the plug region and as a result causes B_c to increase.

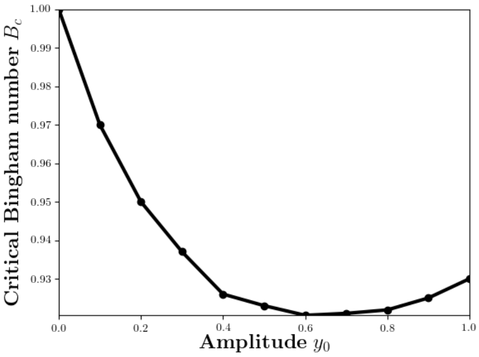

Figure 5.10: Estimate of the critical Bingham number B_c for different values of y_0 for $h/L_s = 0.25$.

The case $B = 0.6$ (figure 5.11) follows in similar fashion to the case $B = 0.4$: we see a large amount of yielding occurring for y_0 in the range $0 - 0.2$ and two chunks of plug are formed by parts of the channel becoming almost completely yielded. It is for this value of B that the extent of the yielding of plug regions that small deviations from a straight channel can cause, becomes apparent. In the case $B = 0.6$, the tips of the crescents, formed between $y_0 = 0.4$ and 0.8, are much thicker than for the previous cases and remain thick even as the crescent splits into three. For all B, a large area of plug still remains at the centre of the sinusoidal region, close to $x = 0$. The point where the fluid achieves its maximum velocity is near the outer wall of the channel, suggestive of solid body rotation. This replicates the findings in a curved channel (fig. 4.20) and the findings of Roustaei [2016].

5.5.1.2 Calculating the relative plug area in the no-slip case

We next investigate the value of the relative yielded plug area A_{rel} (cf fig. 4.23) as a function of y_0. We fit a tanh function to the results for A_{rel} which allows us to approximate the effect of the Bingham number B on the relative area A_{rel}.

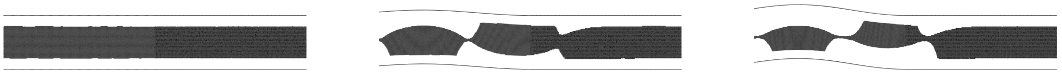

(a) $y_0 = 0$ (b) $y_0 = 0.1$ (c) $y_0 = 0.2$

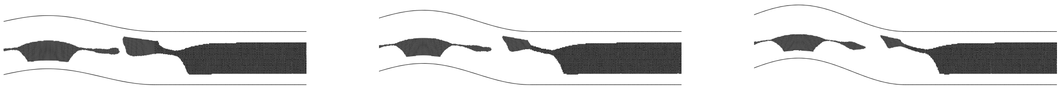

(d) $y_0 = 0.3$ (e) $y_0 = 0.4$ (f) $y_0 = 0.5$

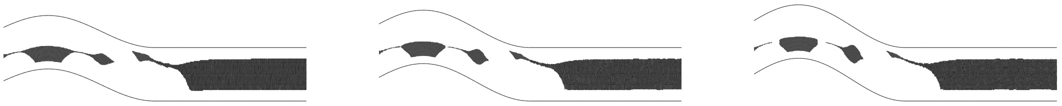

(g) $y_0 = 0.6$ (h) $y_0 = 0.7$ (i) $y_0 = 0.8$

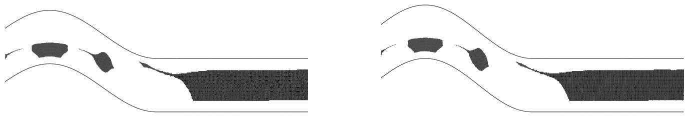

(j) $y_0 = 0.9$ (k) $y_0 = 1$

Figure 5.11: The shapes of the plug regions are shown in black for $B = 0.6$ and channel amplitudes y_0 between 0 and 1.

Here we explore the effect that changing the channel geometry has on the size of the plug areas for fixed $h/L_c = 0.25$. (We repeat the process for $h/L_c = 0.33$ and 0.5 in section 5.5.1.3) and $\beta = 0$ (we consider non-zero slip lengths in section 5.5.1.4). Using the same approach as in fig. 4.23, we present the results as the relative plug area but now as a function of channel amplitude y_0 (instead of channel curvature κ).

From eq. (5.4), A_p^{sim} is equal to the area of plug divided by the total channel area A_p/A_t

and A_p^{anal} is equal to B, the analytical prediction of plug area per unit area in the straight channel case. Here we assume that the analytic result for $y_0 = 0$ case applies for all choices of y_0, thus A_{rel} measures the proportion of plug area that becomes yielded from the straight channel with increasing amplitude y_0. Thus the relative yielded plug area is written as

$$A_{rel} = 1 - \frac{(A_p/A_t)}{B} \tag{5.5}$$

where A_p/A_t denotes the plug area per unit area of the channel and is bounded between 0 and B. When $y_0 = 0$, we know that from eq. (3.26), $A_p/A_t = B$ is achieved by our choice of B_ϵ, and therefore $A_{rel} = 0$ for all B. As y_0 increases, we would expect to see additional yielding occur due to the introduction of curvature (cf. §4.5), causing A_p to become smaller. In the extreme situation where the fluid becomes completely yielded ($A_p = 0$), we achieve the maximum of the relative yielded area, $A_{rel} = 1$.

In fig. 5.12, we consider the relative yielded plug area A_{rel} (eq. (5.5)) for a range of y_0 between 0 and 1. Increasing the amplitude y_0 from 0 to 0.4 increases the relative yielded area A_{rel} from 0 to close to 0.8 for all B, meaning that relative to the case $y_0 = 0$ we see that 80% of the fluids plug area becomes yielded. For larger amplitudes y_0, the gradient of the curve A_{rel} saturates before settling to final values of A_{rel} for y_0 between 0.8 and 1. The final values of A_{rel} seem to have a dependence on the choice of B, with larger B providing smaller values of A_{rel} at $y_0 = 1$.

For example, for $B = 0.2$ the value of A_{rel} for $y_0 = 1$ is 0.9684, meaning that the fluid only has 3.16% of the original plug area that it had at $y_0 = 0$. This suggests that the fluid becomes close to becoming completely yielded. For $B = 0.6$ the value of A_{rel} for $y_0 = 1$ is 0.8734, which suggests that the larger the Bingham number, the more (relative) plug area remains at large amplitudes $y_0 = 1$. From this, we can work out that the remaining plug area A_p is 12 times larger for $B = 0.6$ than for $B = 0.2$. This can be seen clearly in figs. 5.8, 5.9 and 5.11, where the area of plug within the sinusoidal region decreases with increasing y_0.

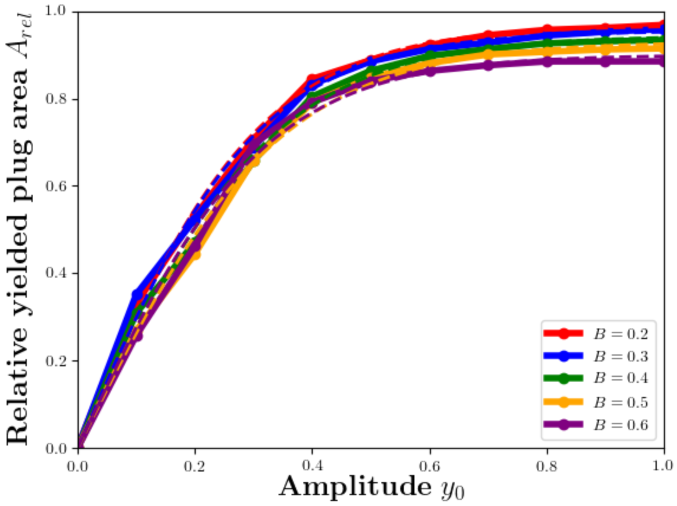

Figure 5.12: The relative yielded plug area A_{rel} increases with the deviation from the straight channel, the amplitude y_0, for different values of the Bingham number B.

We consider the data for the relative yielded plug area A_{rel} as a function of y_0 in fig. 5.12. In addition to this, we fit a hyperbolic tangent function to the resulting curve, as the data in fig. 5.12 suggests that A_{rel} is a monotonically increasing function and settles to final values of A_0 at $y_0 = 1$ and is equal to 0 at $y_0 = 0$. We suggest two fitting parameters A_0 and ϵ_0, assumed to be dependent on B. The values of parameters A_0 and ϵ_0 control the saturated value of A_{rel} for large y_0 and the amount of yielding of the plug at smaller values of y_0, respectively. The fitting function takes the form:

$$A_{fit} = A_0(B) \tanh\left(y_0/\epsilon_0(B)\right). \tag{5.6}$$

The values of parameters A_0 and ϵ_0 are determined using non-linear least squares; the values of the rms error of the parameters A_0 and ϵ_0 are very small, of the order 10^{-5}.

Fig. 5.13 shows the values of the fitted parameters A_0 and ϵ_0. We conclude that ϵ_0 remains more or less constant for each value of B, $\epsilon_0 \approx 0.32$, which suggests that the gradient of the curve A_{rel} for $y_0 \leq 0.4$ is the same for all B. This means that the amount of yielding of the plug region of the fluid with increasing y_0 is the same irrespective of the value of B.

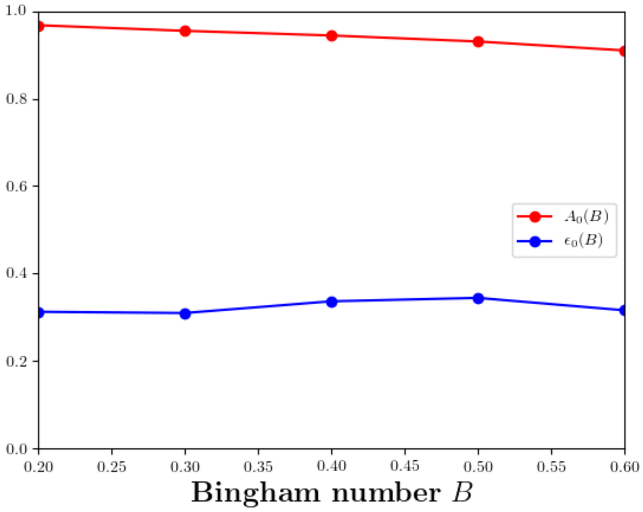

Figure 5.13: The fit parameters A_0 and ϵ_0 plotted as functions of B. The error bars are smaller than the point size when plotted and are of the order 10^{-5}.

On the other hand, we see that A_0 decreases slightly with increasing B. We assume a linear decrease and approximate the value of A_0 as

$$A_0 = 1 - 0.164B \quad (\approx 1 - 0.5\epsilon_0 B) \tag{5.7}$$

We will see (in §5.5.1.3) that the assumption that A_0 depends on ϵ_0 is not coincidental. Combining the value $\epsilon_0 = 0.32$ with the approximation in eq. (5.7), we rewrite the fit for A_{rel} in eq. (5.6) as

$$A_{fit} = (1 - 0.164B) \tanh\left(y_0/0.32\right).$$

This means that for larger choices of y_0 (when $\tanh(y_0/\epsilon_0)$ becomes close to 1), we expect to see that $A_{fit} \approx A_0$, suggesting that the relative yielded plug area A_{rel} at large y_0 is only dependent on B (eq. (5.7)). The results also suggest that the plug area A_{rel} should not increase further by increasing y_0 above 1. In fact, we see in cases of smaller lengths L_s (i.e. larger h/L_s), that A_{rel} can in fact decrease due to the formation of dead regions of fluid (see [Roustaei and Frigaard, 2013]).

5.5.1.3 The effect of varying the length of the sinusoidal region on the plug area

We consider the relative yielded plug area A_{rel} for different ratios h/L_s, the ratio of the (vertical) channel width h to the length of the sinusoidal region L_s. As the length of L_s becomes shorter, the sinusoidal region becomes steeper and the channel width becomes narrower (fig. 5.6). Increasing the value of y_0 causes additional yielding of the plug region, which increases A_{rel} towards one (see chap. 5.5.1.2).

Figs. 5.14 and 5.15 show the plug regions of the fluid with $h/L_s = 0.5$ for $B = 0.2$ and 0.6 respectively. Here we focus on the sinusoidal region in particular as we trace the degradation of the plug and the formation of regions of stationary plug for each B. In fig. 5.14 ($B = 0.2$), we see that the plug region in the sinusoidal region becomes separated from the plug region outside the sinusoidal region for $y_0 \geq 0.2$, which is half the value of the case $h/L_s = 0.25$ in fig. 5.8. The yielding patterns differs for each amplitude y_0 in the case $h/L_s = 0.5$ than $h/L_s = 0.25$ and sees a greater amount of yielding to the point that the fluid becomes nearly completely yielded at $y_0 = 0.8$. With $y_0 = 0.9$ and 1.0, we see the formation of small dead regions at the top wall. For $B = 0.6$ (fig. 5.15), even for small amplitudes we see significant yielding of the plug such that the plug in the sinusoidal region becomes separated from the plug outside the region. For amplitude y_0 between 0.2 and 0.6, the plug region of the fluid takes a crescent-shaped form, which breaks into three for larger y_0. We also see that that the size of the dead regions are much larger than for $B = 0.2$ and are seen for $y_0 \geq 0.5$ and grow with amplitude y_0, which will be evident when measuring the area of the plug region.

In fig. 5.16, we show the plug regions of fluid for a very large value of $B = 0.9$, close to the critical Bingham number B_c (fig. 5.10) for $h/L_s = 0.5$ over a range of amplitudes y_0. When the Bingham number is large, the fluid is close to becoming stationary i.e. completely plugged up. This occurs when the driving pressure gradient isn't large enough in proportion to the fluids yield stress to cause flow in such a channel. For the case $y_0 = 0$ in part (a), we see thin regions of yielded fluid close to the channel walls with the majority of the channel

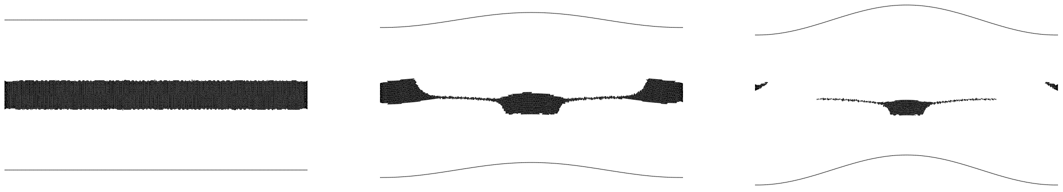

(a) $y_0 = 0.0$ (b) $y_0 = 0.1$ (c) $y_0 = 0.2$

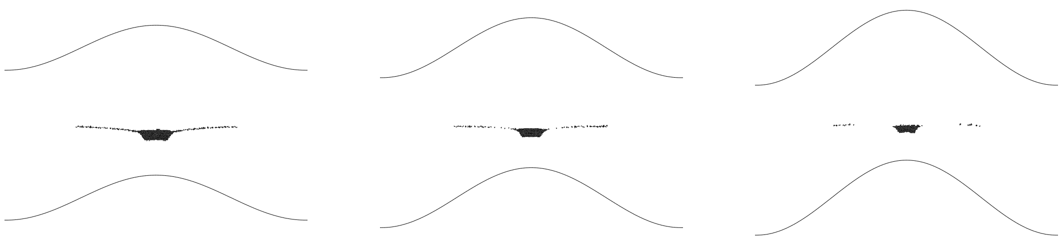

(d) $y_0 = 0.3$ (e) $y_0 = 0.4$ (f) $y_0 = 0.5$

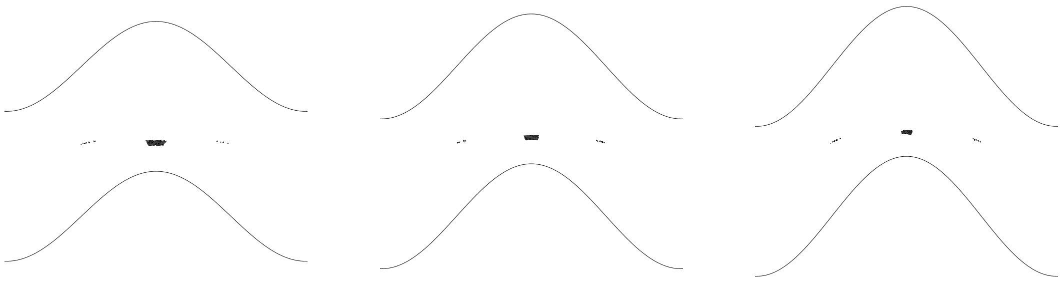

(g) $y_0 = 0.6$ (h) $y_0 = 0.7$ (i) $y_0 = 0.8$

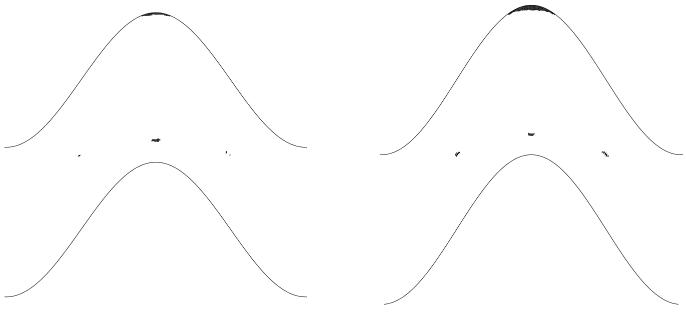

(j) $y_0 = 0.9$ (k) $y_0 = 1.0$

Figure 5.14: For $B = 0.2$ and $h/L_s = 0.5$, we vary the amplitude y_0 between 0 and 1 and consider the shapes of the plug regions (coloured in black).

filled with plug flow (in this case, 90% of the channel area is filled with plug region). An amplitude of $y_0 = 0.1$ has little effect on the size of the plug and yielded regions, with the

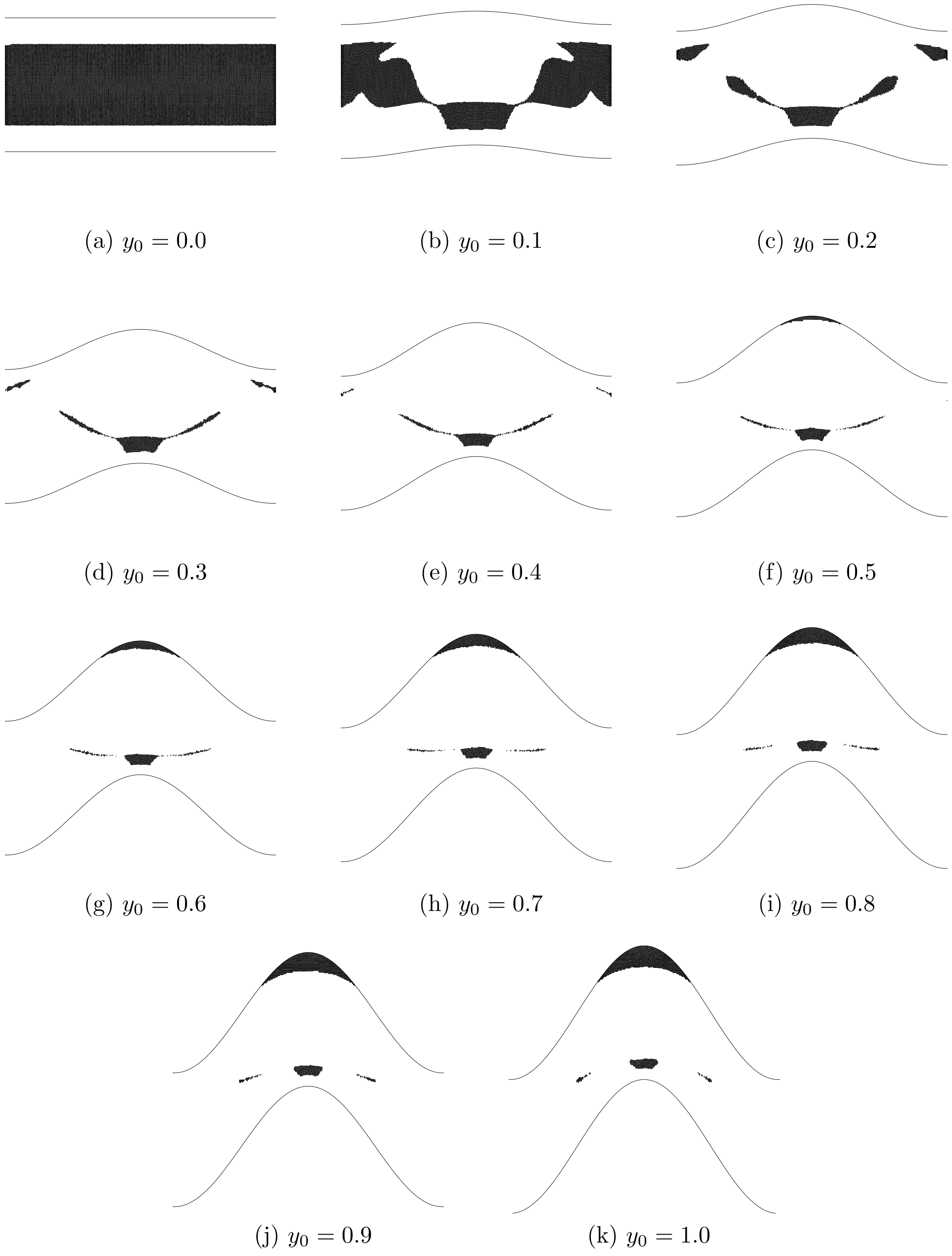

(a) $y_0 = 0.0$ (b) $y_0 = 0.1$ (c) $y_0 = 0.2$

(d) $y_0 = 0.3$ (e) $y_0 = 0.4$ (f) $y_0 = 0.5$

(g) $y_0 = 0.6$ (h) $y_0 = 0.7$ (i) $y_0 = 0.8$

(j) $y_0 = 0.9$ (k) $y_0 = 1.0$

Figure 5.15: For $B = 0.6$ and $h/L_s = 0.5$, we vary the amplitude y_0 between 0 and 1 and consider the shapes of the plug regions (coloured in black).

large plug region still separating two thin regions of yielded fluid located near the channel walls.

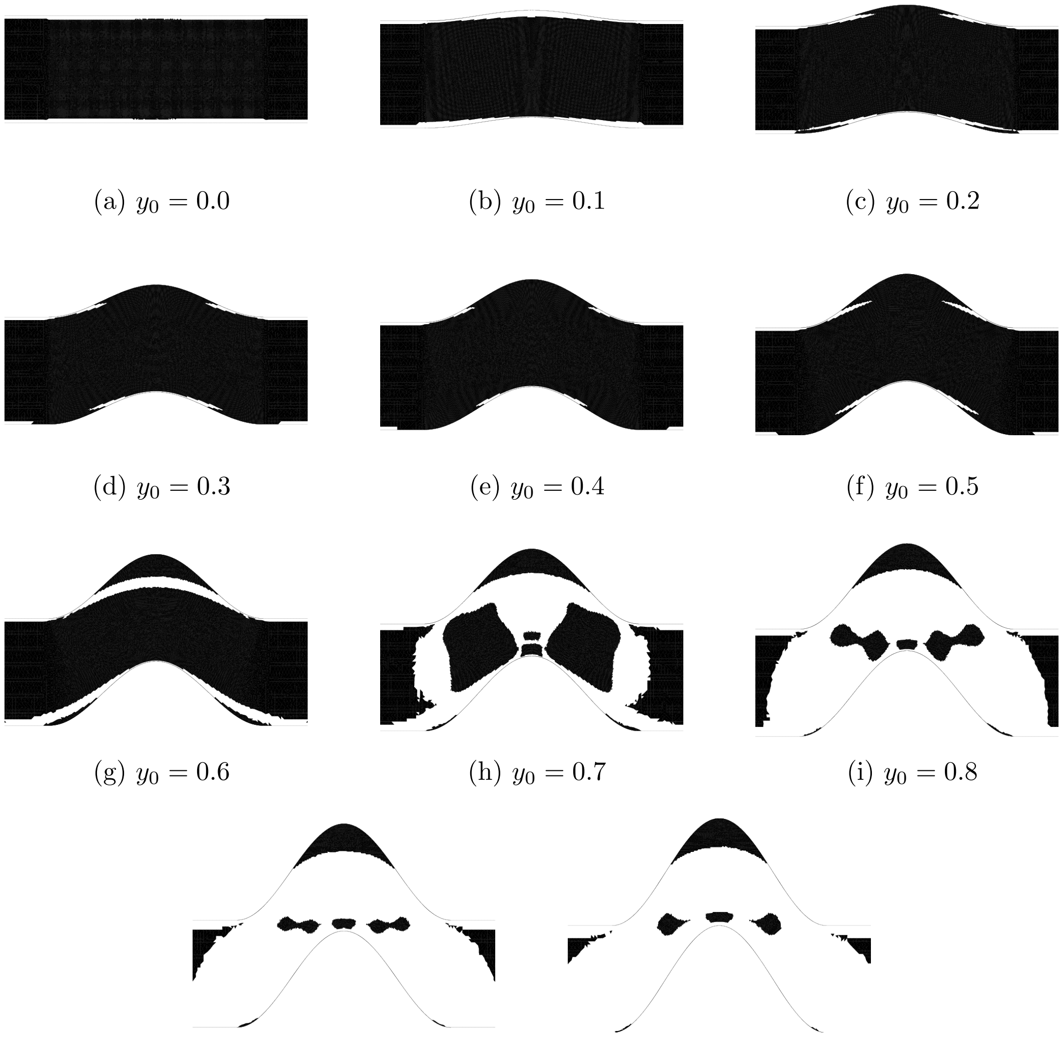

(a) $y_0 = 0.0$ (b) $y_0 = 0.1$ (c) $y_0 = 0.2$

(d) $y_0 = 0.3$ (e) $y_0 = 0.4$ (f) $y_0 = 0.5$

(g) $y_0 = 0.6$ (h) $y_0 = 0.7$ (i) $y_0 = 0.8$

(j) $y_0 = 0.9$ (k) $y_0 = 1.0$

Figure 5.16: For $B = 0.9$ and $h/L_s = 0.5$, we vary the amplitude y_0 between 0 and 1 and consider the shapes of the plug regions (coloured in black).

By increasing y_0 in figs. 5.16(b)-(f), we notice that the yielded regions of fluid (in white) are removed from the top wall of the channel as the fluid becomes stagnant within the bump of the sinusoidal section, forming a dead region of fluid. Increasing y_0 to 0.6 in fig. 5.16(g) sees the formation of a thin region of yielded fluid, which cuts off the dead region of fluid at the top wall and the channel effectively becomes narrower. As the channel amplitude y_0 is increased past 0.6 (parts (h)-(k)), the size of the stagnant dead region at the top wall increases but the majority of the plug region close to the centerline of the channel becomes yielded, leaving three small regions of plug close to the centre of the sinusoidal section, as was the case for $B = 0.6$ (fig. 5.15). This supports our findings in fig. 5.10 that the critical Bingham number B_c increases at larger amplitudes y_0, as the channel moves from being nearly filled completely with fluid moving in a plug motion at $y_0 = 0.4$ to becoming majority yielded at $y_0 = 1.0$.

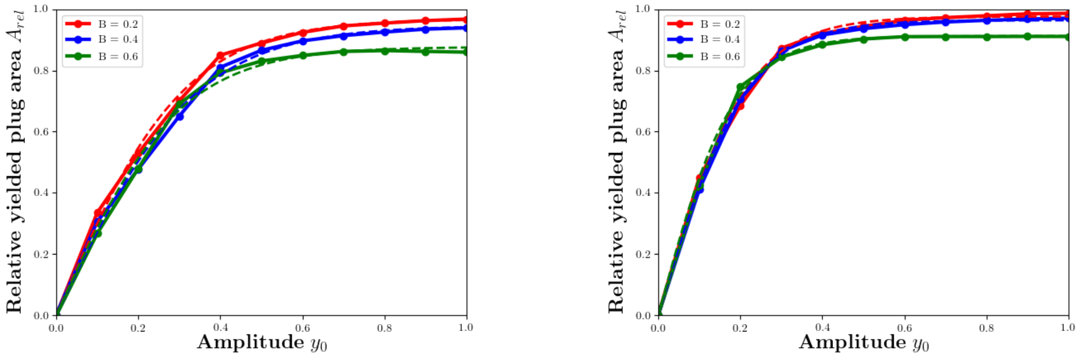

(a) $h/L_c = 0.25$ (b) $h/L_c = 0.33$

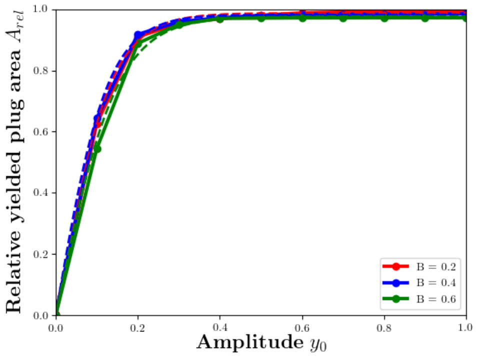

(c) $h/L_c = 0.5$

Figure 5.17: The relative yielded plug areas A_{rel} for different channel lengths ratios h/L_s.

In fig. 5.17, we show the relative yielded plug area A_{rel} for different ratios h/L_s (with channel width $h = 1$) and we increment L_s between 2 and 4 (and B between 0.2 and 0.6). We see that the effect of increasing h/L_s causes the rate of yielding of A_{rel} to increase between 0 and 0.2 (i.e. the curves become steeper) and the value A_{rel} becomes closer to 1 with increasing h/L_s. The curves denoting different B become closer together with increasing h/L_s (in effect, increasing channel curvature) reducing the effect of B on the saturated values of A_{rel} near $y_0 = 1$. For $h/L_s = 0.5$, the value of A_{rel} becomes smaller at larger y_0, for $B = 0.6$. This is caused by the formation of dead regions located directly at the centre of the sinusoidal region near the top wall.

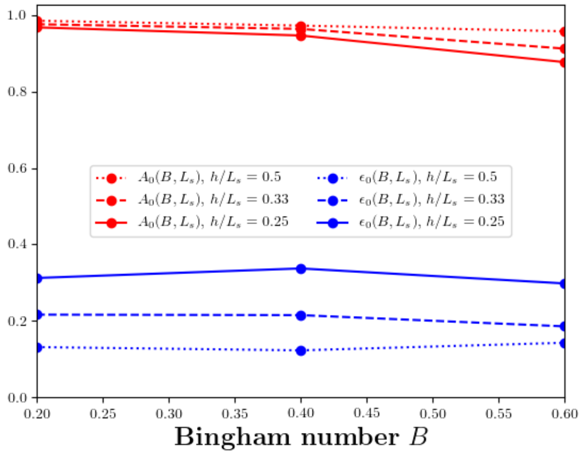

Figure 5.18: The fit parameters A_0 and ϵ_0, denoting the saturated value of A_{rel} at large y_0 and the amount of yielding experienced at small y_0, respectively, from eq. (5.7) plotted as functions of B.

As for fig. 5.12, we fit a tanh function (eq. (5.7)) to the data for A_{rel} in fig. 5.17. The estimated fitting parameters are shown in fig. 5.18. Increasing h/L_s has an evident effect on the values of A_0 and ϵ_0 for each amplitude y_0. For the case $h/L_s = 0.25$ in 5.13, we concluded that the parameter A_0 has a slight dependence on B (eq. (5.7)) and found the value $\epsilon_0 \approx 0.32$. Increasing the ratio h/L_s causes the values of ϵ_0 to decrease (approaching zero for larger h/L_s), suggesting that increasing h/L_s causes the amount of yielding of the plug to increase for small y_0, as expected. Additionally, increasing h/L_s, the value of A_0 becomes independent of B. As $h/L_s \to \infty$, the results suggest that $A_0 \to 1$ and $\epsilon_0 \to 0$. We adjust the approximation (eq. (5.7)) for A_0 in order to account for the variation in h/L_s:

$$A_0 \approx 1 - \frac{2\epsilon_0 h}{L_s} B.$$

The value of A_0 is an approximation to the saturated value of A_{rel} at large y_0. The fitted tanh function provides excellent approximations for A_{rel} in the absence of dead regions (fig. 5.12).

In conclusion, we suggest that increasing the ratio h/L_s causes a greater amount of plug to be lost at fixed y_0. At fixed amplitude y_0, increasing h/L_s causes the sinusoidal region to become steeper and narrower which dislodges the plug region and induces additional yielding. The "amount" of yielding of the plug area also increases for larger h/L_s, meaning that much more of the plug region is lost for small amplitudes from the straight channel if h/L_s is larger. If one would want to yield the fluid completely, increasing h/L_s would be beneficial, but increasing it too much would lead to the formation of static dead regions.

5.5.1.4 The effect of increasing the slip length on the plug area

We fix $h/L_s = 0.25$ and consider the effect of non-zero slip lengths (eq. (2.25)) on A_{rel} for a range of y_0 between 0 and 1, extending the results of sec. 5.3. We consider slip lengths up to 10^{-1} for $B = 0.2$ - 0.6 and compare the results with the no-slip case (fig. 5.12). Recall from chap. 3 that wall slip has no effect on the yield surface positions in the case $y_0 = 0$. For non-zero y_0 this is not the case. The position of the yield-surfaces within the sinusoidal region depend on the slip length β (due to channel curvature - see chap. 4.5.2).

In fig. 5.19, we show the relative yielded plug areas A_{rel} for three different non-zero slip lengths $\beta = 10^{-3}$, 10^{-2} and 10^{-1} for three different Bingham numbers $B = 0.2, 0.4$ and 0.6. As for all cases $A_{rel} \approx 0$ for $y_0 = 0$, this implies that the appropriate value of B_ϵ (for each B) is independent of β (or at the most, vary little with β).

The slope of A_{rel} at the smaller values of y_0 increases for larger slip lengths β, indicating that a greater amount of plug is lost at smaller amplitudes y_0 with increasing β. For larger values of y_0, the value of A_{rel} saturates and approaches 1 with increasing β, suggesting that wall slip causes further yielding within the sinusoidal region. This is in agreement with the analytical predictions for plug widths in fig. 4.8 and the simulation results for plug area in fig. 4.23. The results also suggest that A_{rel} is independent of B for the case $\beta = 10^{-1}$, which

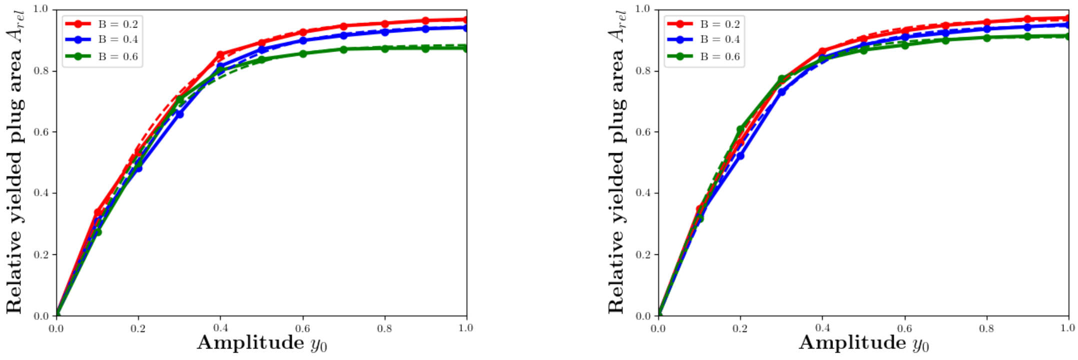

(a) $\beta = 10^{-3}$

(b) $\beta = 10^{-2}$

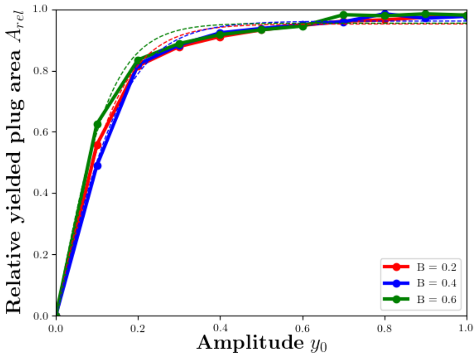

(c) $\beta = 10^{-1}$

Figure 5.19: The relative yielded plug areas A_{rel} for the sinusoidal channel with $h/L_s = 0.25$ for different slip lengths β: (a) $\beta = 10^{-3}$, (b) $\beta = 10^{-2}$ and (c) $\beta = 10^{-1}$.

is not the case for $\beta = 0$ (fig. 5.19).

We fit a tanh function to the numerical plug data A_{rel} and find fitting parameters A_0 and ϵ_0 in eq. (5.6). For $\beta = 0$, we investigated the dependence of these parameters on both B and h/L_s and the results in fig. 5.19 suggest that they also depend on β. In fig. 5.20, we see that as β increases, the values of A_0 become independent of B and constant which is supported by fig. 5.19(c) as all curves overlap. The values of ϵ_0 also remain roughly constant but as β increases, the value of ϵ_0 decreases. We would expect that for large β, ϵ_0 will decrease towards 0, while $A_0 \approx 1$, similar to the inference of fig. 5.17. We see little or no difference between the values of A_0 and ϵ_0 for the no-slip case $\beta = 0$ and $\beta = 10^{-3}$ implying that a slip length of the order 10^{-3} has minimal effect on the flow, which is expected as the

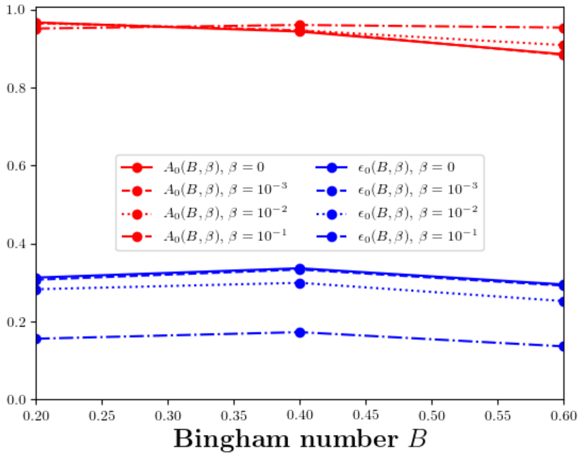

Figure 5.20: The value of the fitting parameters (from eq. (5.7)) for all curves plotted in fig. 5.19 with $h/L_s = 0.25$.

slip length β in comparison to the channel width is small (10% the value of h).

5.5.2 Speed profiles in the sinusoidal region

The fluid's speed is an important part of our investigation: It allows us to estimate the shape of the flow front expected for foam through sinusoidal veins and hence how the channel/vein geometry affects the displacement of blood (chap. 1.3.3).

We plot the speed profiles along cross-sections χ_1 and χ_2 of the channel (fig. 5.3). These locations were chosen by observing in figs. 5.8, 5.9 and 5.11 that the plug region becomes completely yielded at χ_2 with increasing y_0 but at χ_1, there always exists some un-yielded plug for each y_0. Furthermore, by increasing h/L_s to 0.5, we see the development of fouling layers at χ_1 (figs. 5.15 and 5.17(c)).

5.5.2.1 The effect of varying the amplitude in the no-slip case on the speed

Here we consider the fluids speed within the sinusoidal region for the case $h/L_s = 0.25$ and for $\beta = 0$ (no-slip) for a range of amplitudes y_0 between 0 and 1. This allows us to draw conclusions on the effects of amplitude and Bingham number on the speed.

In fig. 5.21-5.23, we plot the contours of speed $|\underline{u}|$. The figures are useful to understand how the speed of the fluid changes for different values of y_0. For the case $y_0 = 0$, all three cases have a plug region of fluid moving at constant speed, labelled as U_{SC} (see chap. 3.3), located at the centre of the channel. All contours of speed below U_{SC} are in the yielded region, where the fluid is flowing like a Newtonian fluid and the velocity gradient is at its largest i.e. providing a good approximation of a parabolic flow profile, as the velocity ranges between 0 and U_{SC}.

For $B = 0.2$ (fig. 5.21), for an amplitude of $y_0 = 0.1$, we see a light pink contour (circled in black) which is moving faster than U_{SC}; this is located close to the cross-section χ_1. As we increase y_0, the contours which represent the faster speeds (in pink close indicating that $|\underline{u}|$ is close to 0.08) grow and stretch throughout the sinusoidal region, with the maximum velocity for the whole channel located somewhere within the sinusoidal region. For $y_0 \geq 0.8$, the contour representing the largest velocities splits into two with a dark pink contour appearing at some point between cross-sections χ_1 and χ_2, i.e. near $|x| = L_s/4$. We trace the value and position of $|\underline{u}|_{max}$ in chap. 5.5.3.1.

We see similar behaviour for the cases $B = 0.4$ (fig. 5.22) and 0.6 (fig. 5.23) although speed contours take considerably smaller values as B increases (as implied by figs. 3.4 and 4.3 that increasing B decreases the fluids velocity). In both cases at small values of $y_0 \leq 0.4$, we see a light pink contour forming containing the maximum velocity located close to χ_1 and the light pink contours grow and stretch throughout the sinusoidal region. Contrary to the findings for $B = 0.2$, the pink contours don't split (but they are starting to and would do at larger y_0) as we saw in fig. 5.21, by tracing the maximum velocity later on, we can determine the effect of the amplitude and B on the location and value of $|\underline{u}|_{max}$.

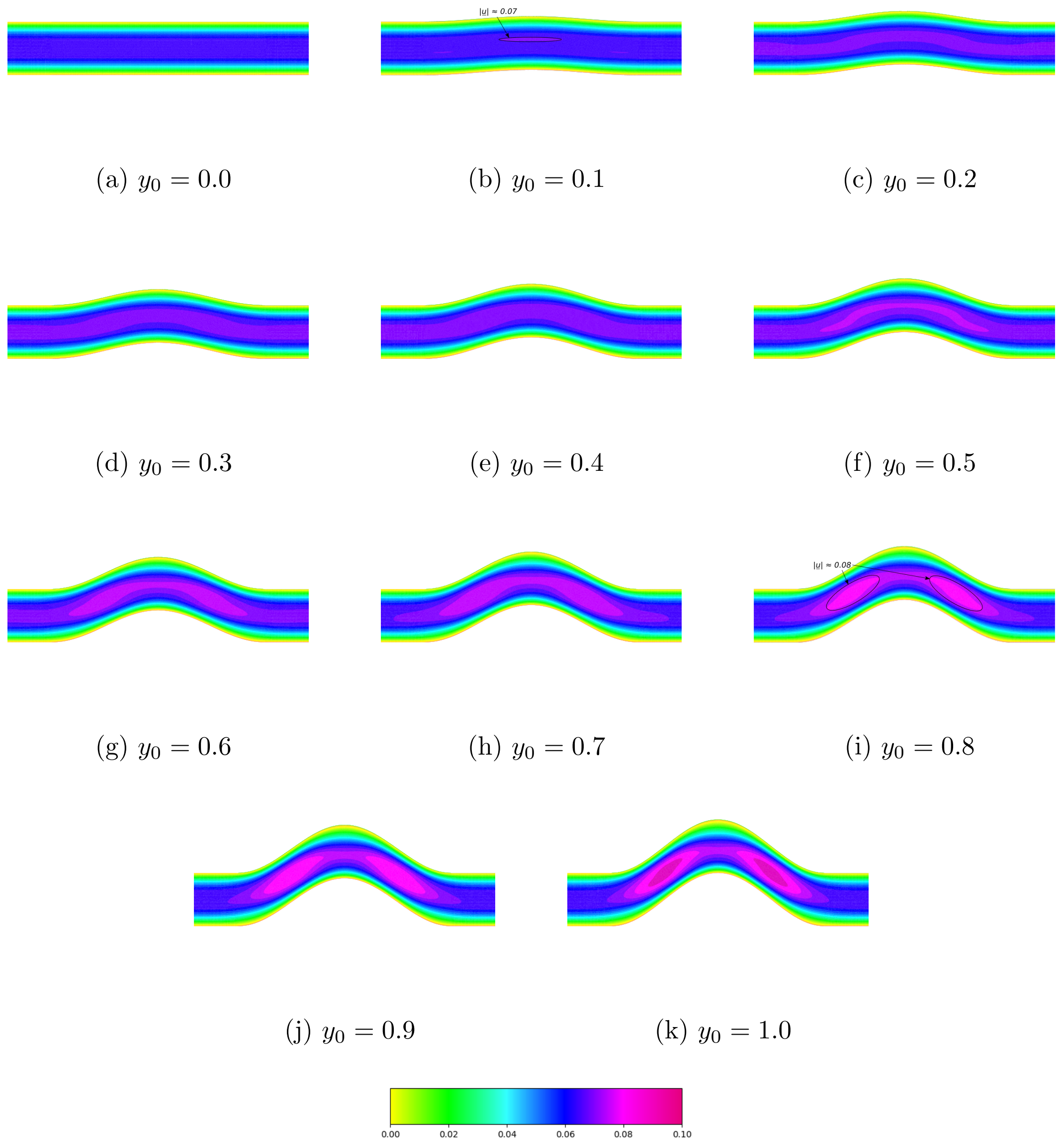

(a) $y_0 = 0.0$ (b) $y_0 = 0.1$ (c) $y_0 = 0.2$

(d) $y_0 = 0.3$ (e) $y_0 = 0.4$ (f) $y_0 = 0.5$

(g) $y_0 = 0.6$ (h) $y_0 = 0.7$ (i) $y_0 = 0.8$

(j) $y_0 = 0.9$ (k) $y_0 = 1.0$

Figure 5.21: The speed contours for channel amplitudes y_0 between 0 and 1 for $B = 0.2$ and $h/L_s = 0.25$.

5.5.2.2 The effect of varying the amplitude for the no-slip case on the speed profile

The speed profiles $|\underline{u}|$ located at two different cross-sections along the channel. Recall that χ_1 is located at the midpoint of the sinusoidal region at $x = 0$ and χ_2 at the inlet, at $x = L_s/2$ (due to reversibility of Stokes flow $x = -L_s/2$ is equivalent). They are also locations have fixed channel widths of 1, unlike for x between χ_1 and χ_2 (see fig. 5.6). The

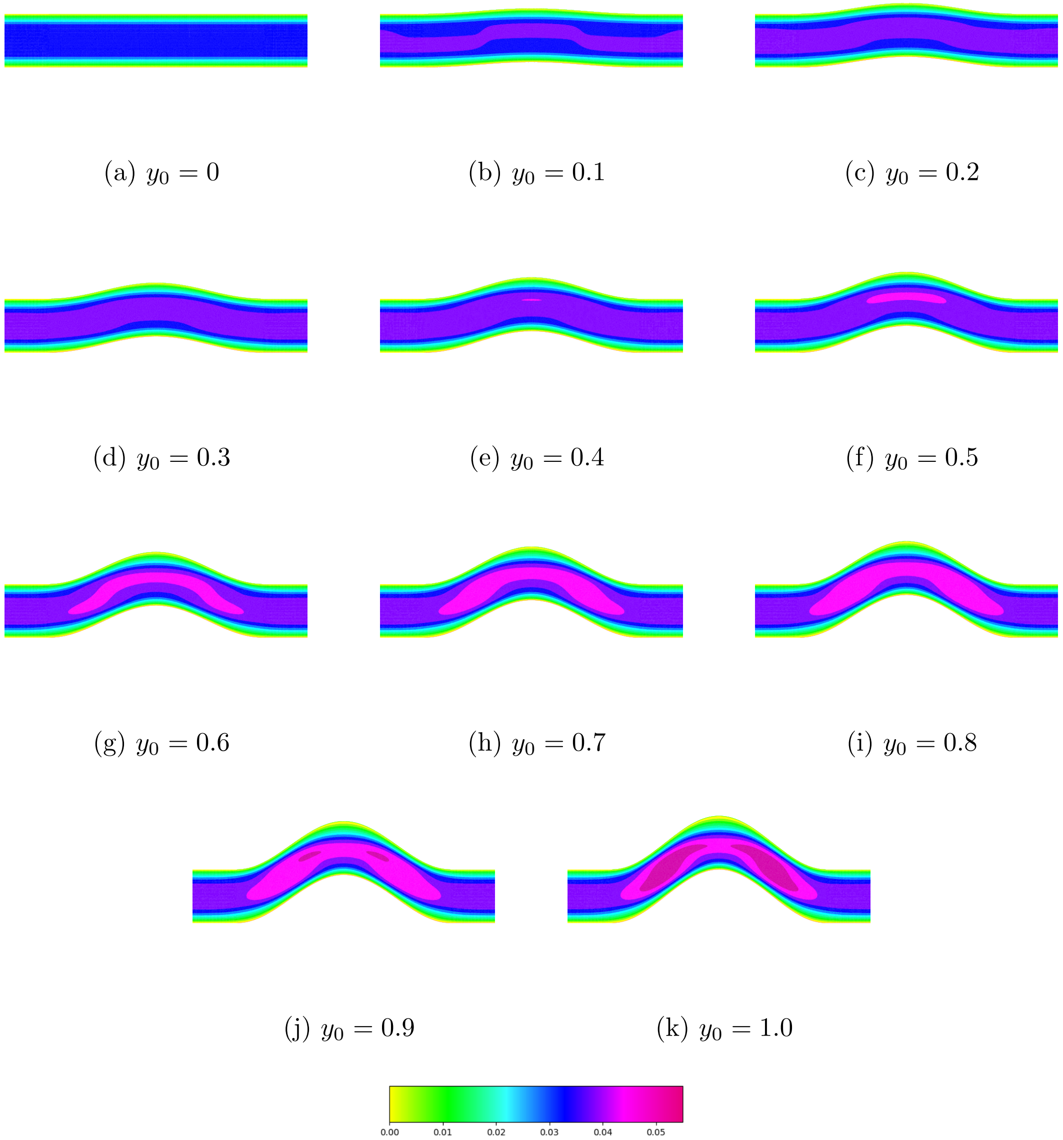

(a) $y_0 = 0$

(b) $y_0 = 0.1$

(c) $y_0 = 0.2$

(d) $y_0 = 0.3$

(e) $y_0 = 0.4$

(f) $y_0 = 0.5$

(g) $y_0 = 0.6$

(h) $y_0 = 0.7$

(i) $y_0 = 0.8$

(j) $y_0 = 0.9$

(k) $y_0 = 1.0$

Figure 5.22: The speed contours for channel amplitudes y_0 between 0 and 1 for $B = 0.4$ and $h/L_s = 0.25$.

smoothness of the streamlines (fig. 5.2) along with the fact that the majority of cases will contain fully-yielded fluid suggest that χ_1 and χ_2 are representative and other cross-sections would yield similar results. We plot the profiles of $|\underline{u}|$ against $\hat{y}$, where $\hat{y} = y - W(x)$ such that $\hat{y}$ is rescaled between 0 and 1 for all cases. Note that at χ_1 and χ_2, that $W(0) = \frac{1}{2}y_0$ and $W(L_s/2) = 0$, respectively.

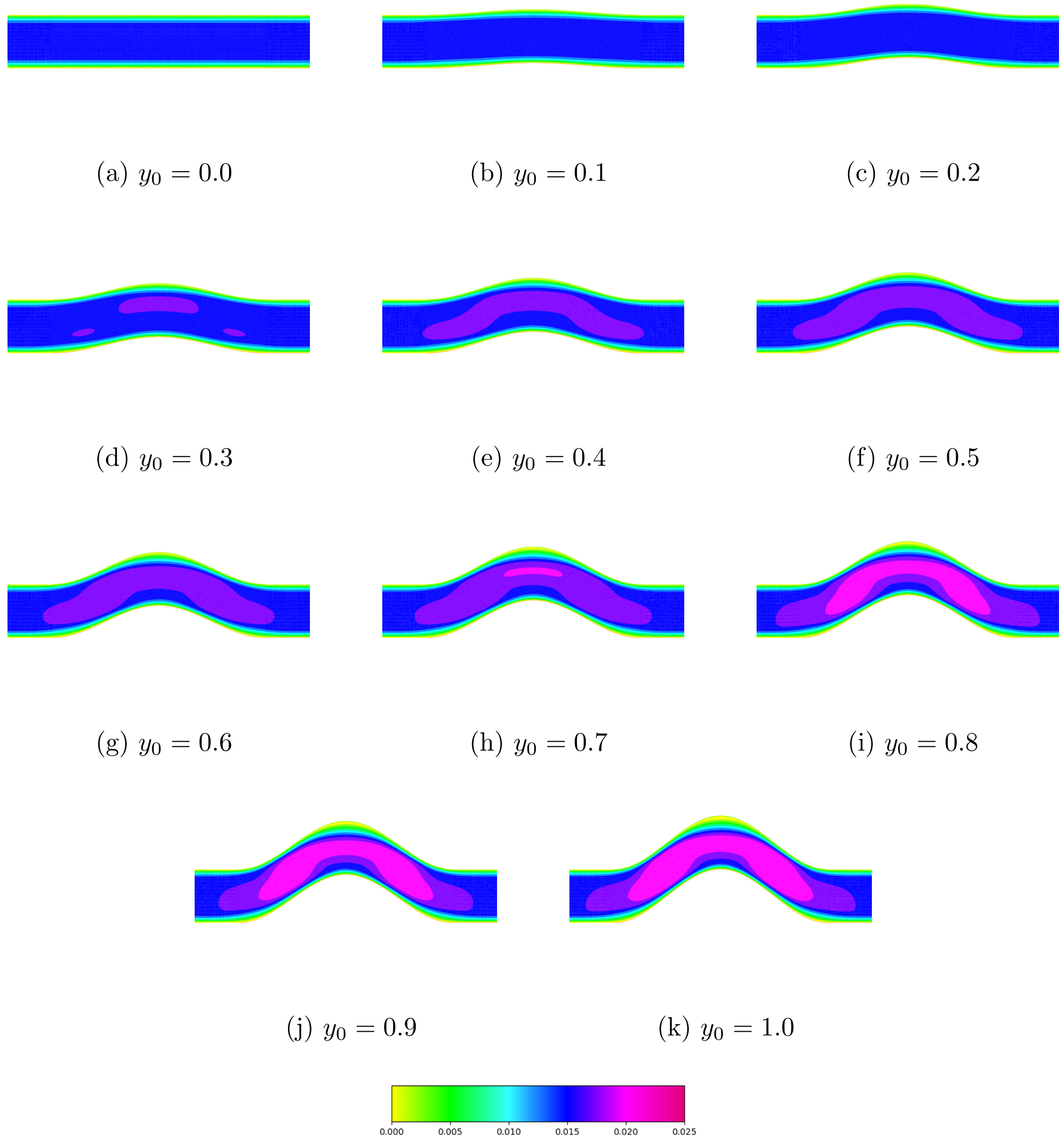
(a) $y_0 = 0.0$ (b) $y_0 = 0.1$ (c) $y_0 = 0.2$

(d) $y_0 = 0.3$ (e) $y_0 = 0.4$ (f) $y_0 = 0.5$

(g) $y_0 = 0.6$ (h) $y_0 = 0.7$ (i) $y_0 = 0.8$

(j) $y_0 = 0.9$ (k) $y_0 = 1.0$

Figure 5.23: The speed contours for channel amplitudes y_0 between 0 and 1 for $B = 0.6$ and $h/L_s = 0.25$.

We know that increasing the curvature of the channel wall causes the stress to increase across the cross sections which in turn will cause more of the fluid to yield. We quantify this additional yielding as A_{rel} (in chap. 5.5.1) and as the amplitude y_0 increases, the fluid in the sinusoidal region is nearly completely yielded. But what effect does this have on the speed profiles at χ_1? The speed increases and the plug width decreases with increasing y_0.

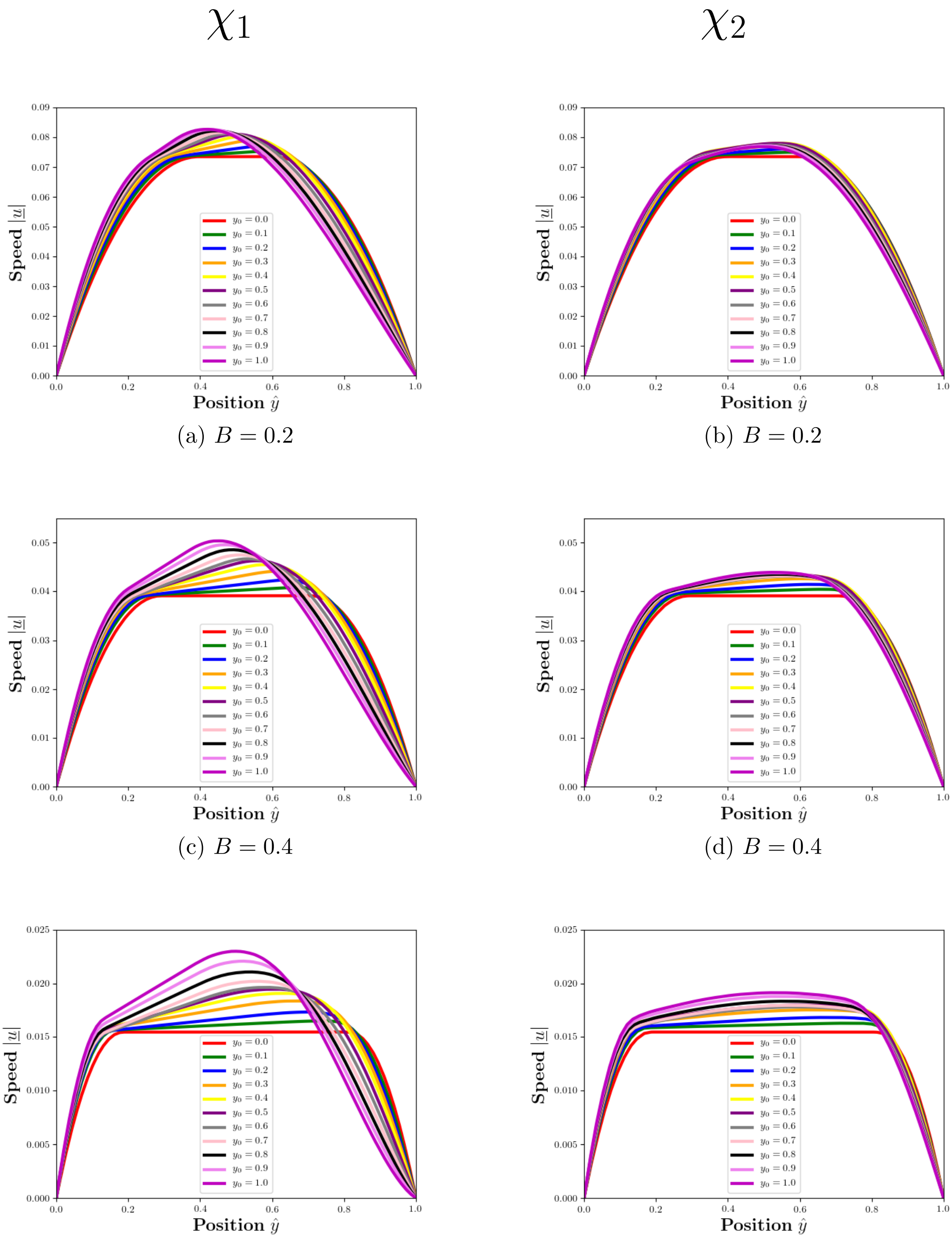
χ_1

χ_2

(a) $B = 0.2$

(b) $B = 0.2$

(c) $B = 0.4$

(d) $B = 0.4$

(e) $B = 0.6$

(f) $B = 0.6$

Figure 5.24: The speed profiles against $\hat{y} = y - W(x)$ for different values of y_0 for $h/L_s = 0.25$ at cross-sections: (a) χ_1 and (b) χ_2.

Do we suggest the same prediction for the flow profiles for the cross-section χ_2? Figs. 5.8, 5.9 and 5.11 indicate that by increasing y_0, the fluid becomes fully yielded at χ_2. As for the speed, from figs. 5.21-5.23 we see that larger amplitudes y_0 increases in speed, but we expect the speed to be less at χ_2 in comparison to χ_1.

In fig. 5.24, we show $|\underline{u}|$ at both cross-sections χ_1 and χ_2, for channel length $h/L_s = 0.25$ and Bingham numbers $B = 0.2$, 0.4 and 0.6. Increasing y_0 causes the maximum speed $|\underline{u}|_{max}$ to increase at both χ_1 and χ_2 for all B. For both cross-sections χ_1 and χ_2, the speed of the fluid (and location of $|\underline{u}|_{max}$) is shifted towards the inner radius of curvature i.e. the inner channel wall, where the stress (and pressure gradient) is at a maximum (also seen with increasing channel curvature in fig. 4.9). The gradient of the plug region increases with y_0 as the fluid begins to transition towards solid body rotation. Recall that the fluid with $B = 0.2$ moves considerably faster than for $B = 0.6$ (see fig. 5.24), as expected.

The changes in the speed at χ_1 are greater than χ_2 for each fixed amplitude y_0 i.e. the velocities increase more at χ_1. Notice that the increase in the speed relative to the case $y_0 = 0$ for each amplitude y_0 becomes greater for larger choices of the Bingham number B (see fig. 5.24(e)).

5.5.2.3 The effect of varying the length of the sinusoidal region on the speed profile

We consider the effect of varying the channel length L_s on the flow profiles for each amplitude. In fig. 5.15 (for $h/L_s = 0.5$ and $B = 0.6$), we saw the development of a dead region of static fluid at the top wall of the channel. The static fluid is located at cross-section χ_1, which we expect to grow with increasing both amplitude or yield-stress (or both) (figs. 5.14-5.15).

In figs. 5.25 and 5.26, we consider the speed profiles $|\underline{u}|$ for a range of amplitudes y_0 at both cross-sections χ_1 and χ_2 for channel lengths $h/L_s = 0.25$ and $h/L_s = 0.33$, respectively. At χ_1, the speed near the lower wall becomes larger with increasing amplitude y_0. The speed increases further as the channel width decreases (i.e. for larger h/L_s), which causes the sinu-

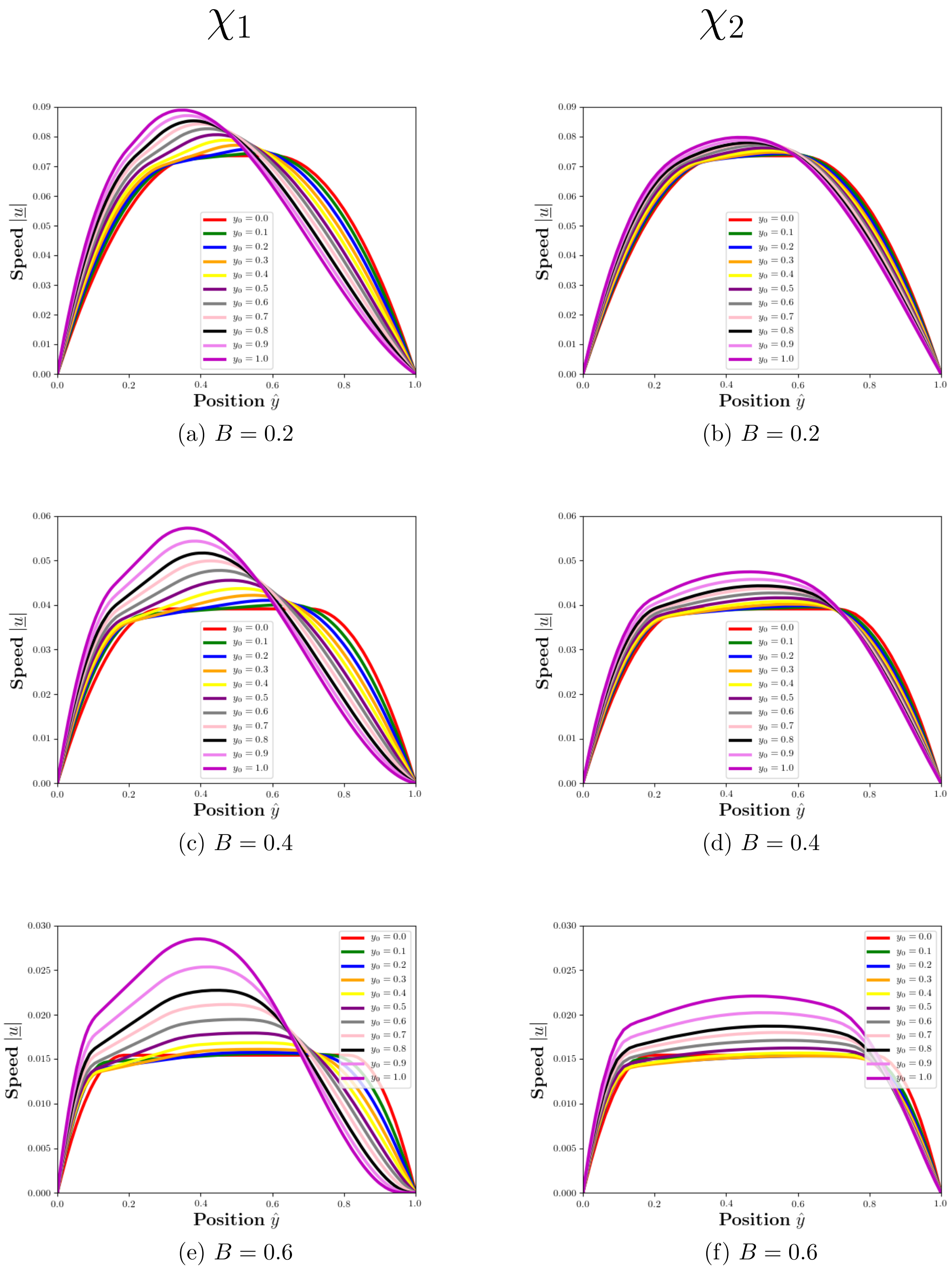

(a) $B = 0.2$ (b) $B = 0.2$

(c) $B = 0.4$ (d) $B = 0.4$

(e) $B = 0.6$ (f) $B = 0.6$

Figure 5.25: For $B = 0.2$,0.4,0.6, we show the speed at cross-sections χ_1 and χ_2 for $h/L_s = 0.33$ for y_0 between 0 and 1.

soidal region to become “steeper”. Again, we see the width of the plug region narrows with increasing amplitude y_0, particularly for larger h/L_s. For the case $h/L_s = 0.5$ and $B = 0.2$, we see complete yielding at χ_2 for choices of $y_0 \geq 0.3$.

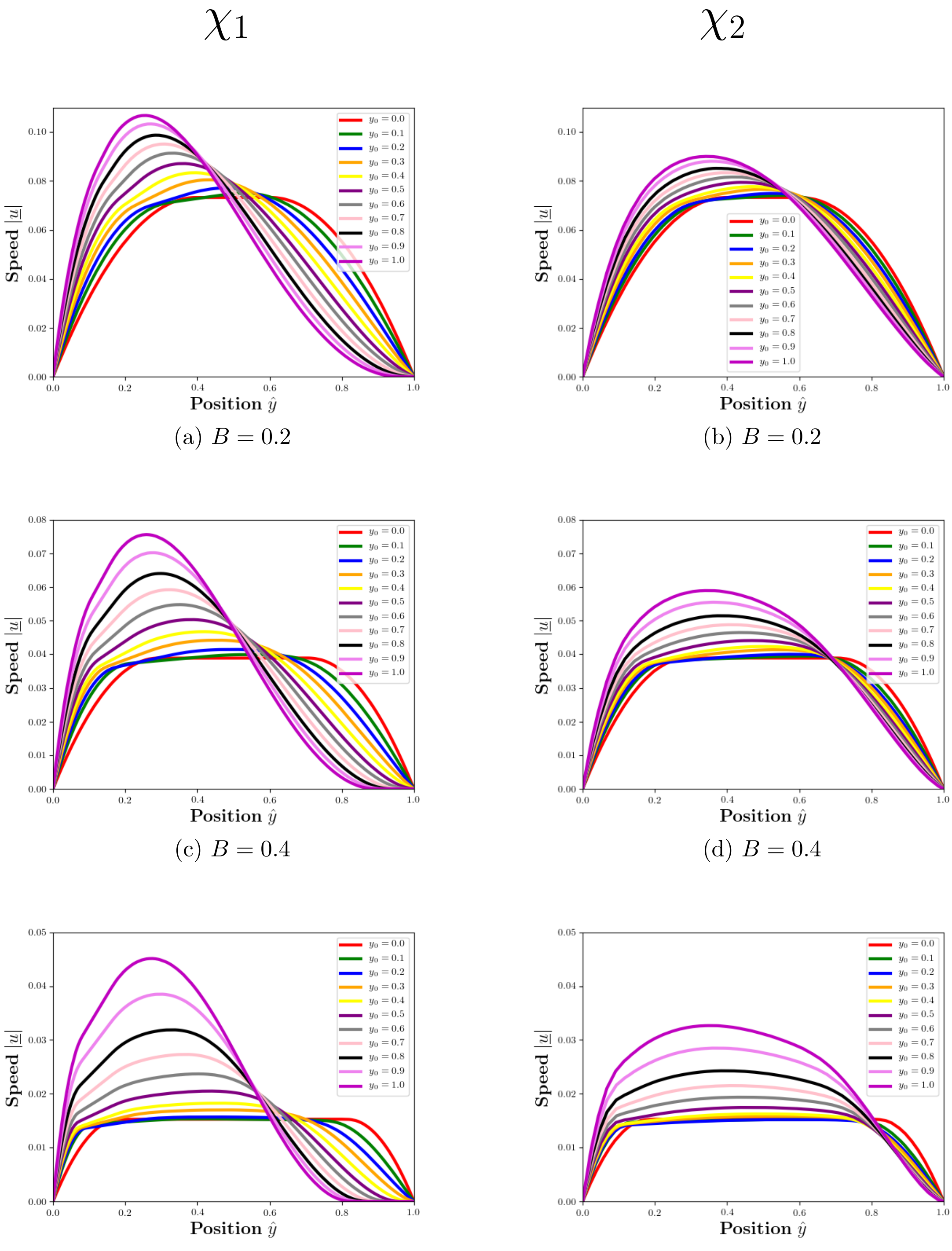

(a) $B = 0.2$

(b) $B = 0.2$

(c) $B = 0.4$

(d) $B = 0.4$

(e) $B = 0.6$

(f) $B = 0.6$

Figure 5.26: For $B = 0.2$,0.4,0.6, we show the speed at cross-sections χ_1 and χ_2 for $h/L_s = 0.5$ for y_0 between 0 and 1.

We identify a region of stationary fluid for $h/L_s = 0.5$ close to the top wall, in fig. 5.26 (also seen in fig. 5.25(e)). This suggests the presence of a region of static fluid experiencing small stresses, close to the outer wall. The width of this dead region at χ_1 increases with y_0 and B. The largest width of the dead region at cross-section χ_1 spans around a fifth of the channel width for the case $h/L_s = 0.5$, $y_0 = 1$ and $B = 0.6$.

For cross-section χ_2, we notice similar findings to the speed profiles in cases $h/L_s = 0.25$ (figs. 5.21-5.23). Increasing the amplitude y_0 for $h/L_s = 0.5$ causes the fluid to completely yield here for all values of B, with the critical amplitude y_0 for this to occur is identified in sec. 5.5.4.2. The fluid with smaller B yields completely at a smaller amplitude y_0, as expected. For both $h/L_s = 0.33$ and 0.5, we see that increasing the value of B causes the maximum speed (relative to U_{SC}) to increase.

5.5.2.4 The effect of increasing the slip length on the speed profile

From the findings in chap. 3 and 4, the implications of increasing the slip length β causes the speed (and flow rate) of the fluid to increase, and for curved channels, causes the plug region to narrow slightly. Here we investigate the effect of slip on the flow of Bingham fluid in sinusoidal channels.

In fig. 5.27, we consider the speed $|\underline{u}|$ for different slip lengths β, channel amplitudes y_0 and Bingham numbers B. The results for slip length $\beta = 10^{-3}$ in each case are nearly identical to the results for the no-slip case (fig. 5.24). For larger given slip lengths β, the fluids' speed increases everywhere, with the extent of the increase in speed dependent on the Bingham number B and amplitude y_0. The larger the Bingham number, the greater the speed gained relative to the no-slip case (see fig. 5.27(a) and (e)).

For a fixed slip length $\beta = 10^{-1}$ at cross-section χ_1, the maximum speed of the fluid increases (and plug width decreases) with increasing channel amplitude y_0, which becomes more evident for larger B. The speed at the channel walls decreases, in particular at the outer channel wall. At cross-section χ_2, larger slip lengths β causes the speed of the fluid

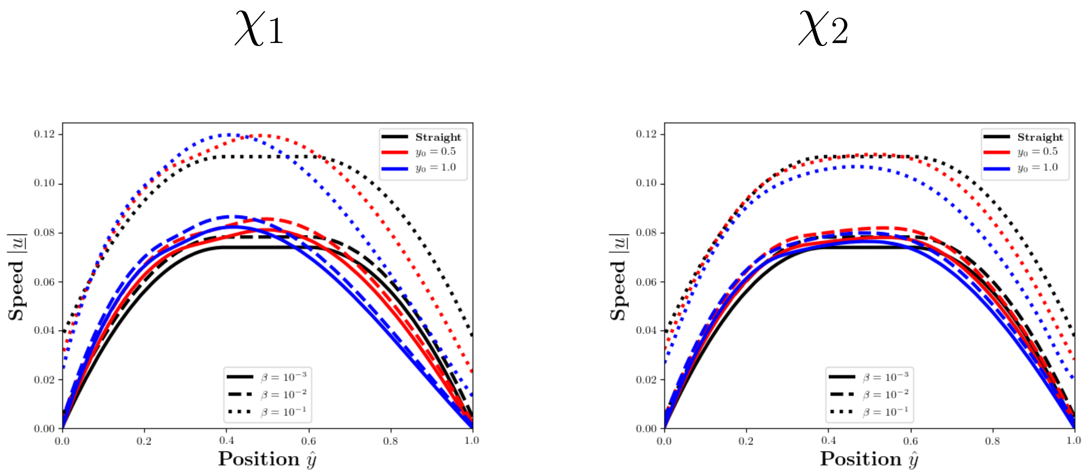

(a) $B = 0.2$ (b) $B = 0.2$

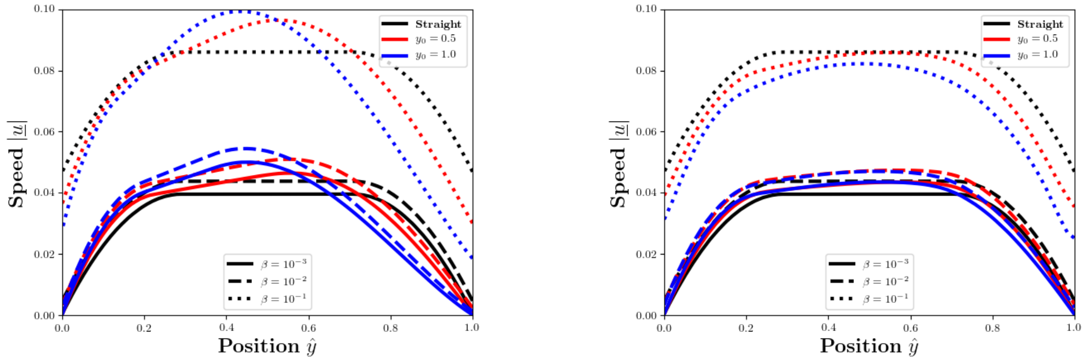

(c) $B = 0.4$ (d) $B = 0.4$

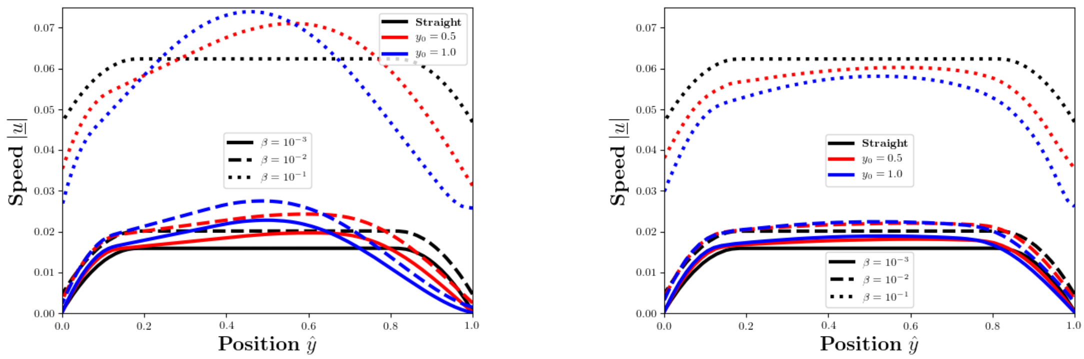

(e) $B = 0.6$ (f) $B = 0.6$

Figure 5.27: The speed at cross-sections χ_1 and χ_2 for Bingham numbers $B = 0.2$, 0.4 and 0.6, amplitudes $y_0 = 0.0$, 0.5 and 1.0 and slip lengths β with a fixed channel length $h/L_s = 0.25$.

to decrease everywhere (as seen in fig. 4.4 for larger considered κ), particularly for larger B. The implications of the results for sclerotherapy suggest that a larger slip lengths and amplitudes y_0 hinder the foams' ability to displace blood in sinusoidal veins.

5.5.3 The maximum speed in the sinusoidal region

For $y_0 = 0$, the fluid moves at its fastest when $B = 0$, i.e. the fluid has no yield-stress so there is no minimum stress required to overcome for the fluid to flow and $|\underline{u}|_{max}$ occurs at the channel centreline. For increasing B, the fluid's maximum speed decreases (with $|\underline{u}|_{max} = U_{SC}$) as the plug width increases, until the fluid ceases to flow at $B = 1$.

In chap. 4, we saw that the curvature of the annulus forces the maximum speed of the fluid to move towards inner radius as the plug region moves with solid body rotation and the stress becomes larger on the inner wall. Other effects include a decrease in the plug-width and decreasing B_c (eq. (4.27)). Also recall that for constant B, some intermediate values of channel curvature produce values of maximum velocity greater than the straight channel maximum velocity, shown in fig. 4.3(c) and (d). We locate the position of the max speed within the channel for different values of B and y_0. We also evaluate the flow rate Q within the sinusoidal region and consider if increasing the amplitude y_0 induces any increase or decrease in the flow rate. From fig. 5.6, we expect to see Q increase with increasing amplitude y_0 due to the narrowing of the average channel width (fig. 5.6) i.e. due to the conservation of mass. This is only part of the story as increasing the channel amplitude causes the yielding of the plug, which also contributes to the increasing flow rate.

We consider the position and value of the maximum speed for different channel lengths h/L_s which cause the average channel width to reduce further. We expect this to cause further yielding and to increase the flow rate.

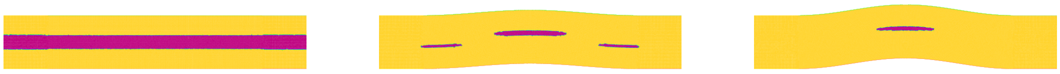

(a) $y_0 = 0.0$ (b) $y_0 = 0.1$ (c) $y_0 = 0.2$

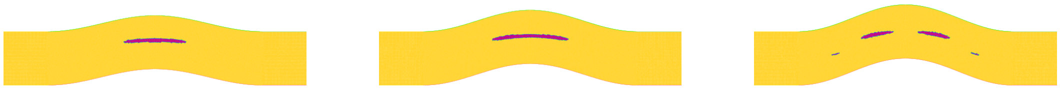

(d) $y_0 = 0.3$ (e) $y_0 = 0.4$ (f) $y_0 = 0.5$

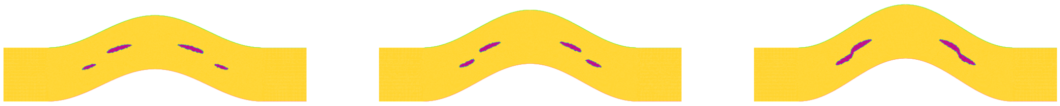

(g) $y_0 = 0.6$ (h) $y_0 = 0.7$ (i) $y_0 = 0.8$

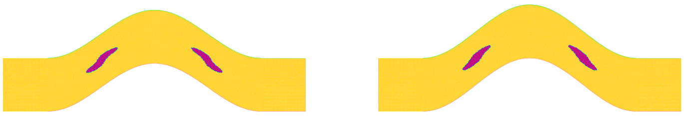

(j) $y_0 = 0.9$ (k) $y_0 = 1.0$

Figure 5.28: For $B = 0.2$ and $h/L_s = 0.25$, the region of speed which is within 0.5% of the global maximum speed for amplitudes y_0 between 0 and 1.

5.5.3.1 The effect of varying the amplitude in the no-slip case on the maximum speed

From inspection of fig. 5.24, the position of $|\underline{u}|_{max}$ (locally) at cross-sections χ_1 and χ_2 moves towards the inner wall and its value increases with increasing y_0. Figs. 5.21-5.23 show that the (global) maximum velocity occurs between both cross-sections. This sub-section will investigate the value of the global maximum as well as its position within the channel.

In figs. 5.28-5.30, the darker colored contour of fluid represents the fluid which is moving

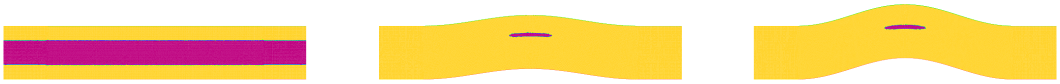

(a) $y_0 = 0.0$ (b) $y_0 = 0.2$ (c) $y_0 = 0.4$

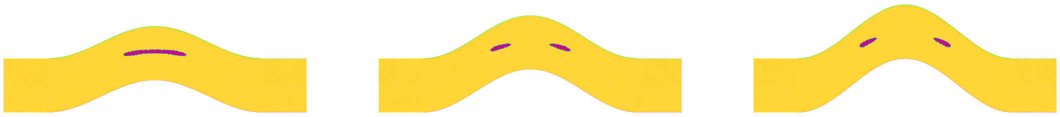

(d) $y_0 = 0.6$ (e) $y_0 = 0.8$ (f) $y_0 = 1.0$

Figure 5.29: For $B = 0.4$ and $h/L_s = 0.25$, the region of speed which is within 0.5% of the global maximum speed for amplitudes y_0 between 0 and 1.

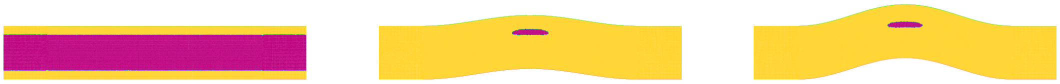

(a) $y_0 = 0.0$ (b) $y_0 = 0.2$ (c) $y_0 = 0.4$

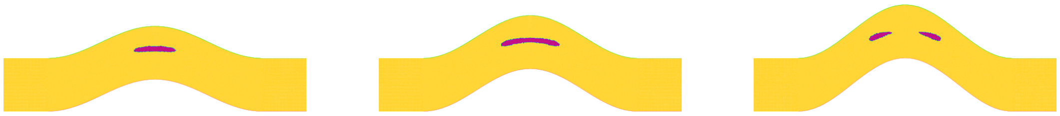

(d) $y_0 = 0.6$ (e) $y_0 = 0.8$ (f) $y_0 = 1.0$

Figure 5.30: For $B = 0.6$ and $h/L_s = 0.25$, the region of speed which is within 0.5% of the global maximum speed for amplitudes y_0 between 0 and 1.

within 0.5% of $|\underline{u}|_{max}$. We consider the cases $B = 0.2$, 0.4 and 0.6. For the case $y_0 = 0$, the fluid region which moves fastest within the channel is the plug region at the centre of the channel close to $\hat{y} = 0.5$. By choosing a non-zero amplitude, we see regions of fluid which is moving faster than the fluid within the plug region. We trace the value and position of the maximum velocity for each amplitude.

For $B = 0.2$ and $y_0 = 0.1$ (fig. 5.28) there exists three distinct regions of fluid moving with a speed which is within 0.5% of the maximum speed, with the largest region situated directly at the centre of the sinusoidal region. Increasing y_0 to a value between 0.2 and 0.4 leads to the disappearance of the smaller regions of colored fluid, leaving only the region located at the centre of the sinusoidal section, where it appears to stretch and become narrower towards $x = 0$ (cross-section χ_1). At an amplitude $y_0 = 0.5$, the maximum speed begins to move away from cross-section χ_1 as it is split into four (into two then four for some $0.4 < y_0 < 0.5$), with two large and two small regions. As y_0 increases from 0.6 to 0.7, the larger regions move towards the smaller regions of fluid i.e. further away from χ_1 towards χ_2, with the large regions reduce in size while the smaller ones grow and become attached at $y_0 = 0.8$. They remain attached for the rest of the range of y_0. Increasing the amplitude y_0 moves the position of $|\underline{u}|_{max}$ away from cross-section χ_1 towards χ_2.

Figs. 5.29 and 5.30 show the cases for $B = 0.4$ and 0.6. By choosing an amplitude y_0 between 0.2 and 0.6 shows only one region of fluid moving at close to the maximum speed located near χ_1. For $B = 0.4$, at an amplitude of $y_0 = 0.8$ the region is split into two and are positioned away from χ_1 in the same nature as the $B = 0.2$ case. For $B = 0.6$, the movement of the maximum speed away from χ_1 (i.e. the regions split) occurs at $y_0 = 1.0$. We notice that this splitting occurs at larger amplitudes y_0 as B increases, suggesting that the point of maximum speed remains closer to χ_1 for larger amplitudes y_0 by increasing the Bingham number B.

The value of $|\underline{u}|_{max}$ and its position is considered as a function of y_0 and is shown in fig. 5.31. We scale the maximum speed by U_{SC} as we are interested in the changes caused to $|\underline{u}|_{max}$ by deviating from a straight channel and increasing the amplitude y_0. We also scale the flow rate Q (which is found by the integral in eq. (2.49)), by Q_{SC}, which is the flow rate for $y_0 = 0$.

In fig. 5.31(a) and (b), we plot the coordinates of the maximum speed, denoted by

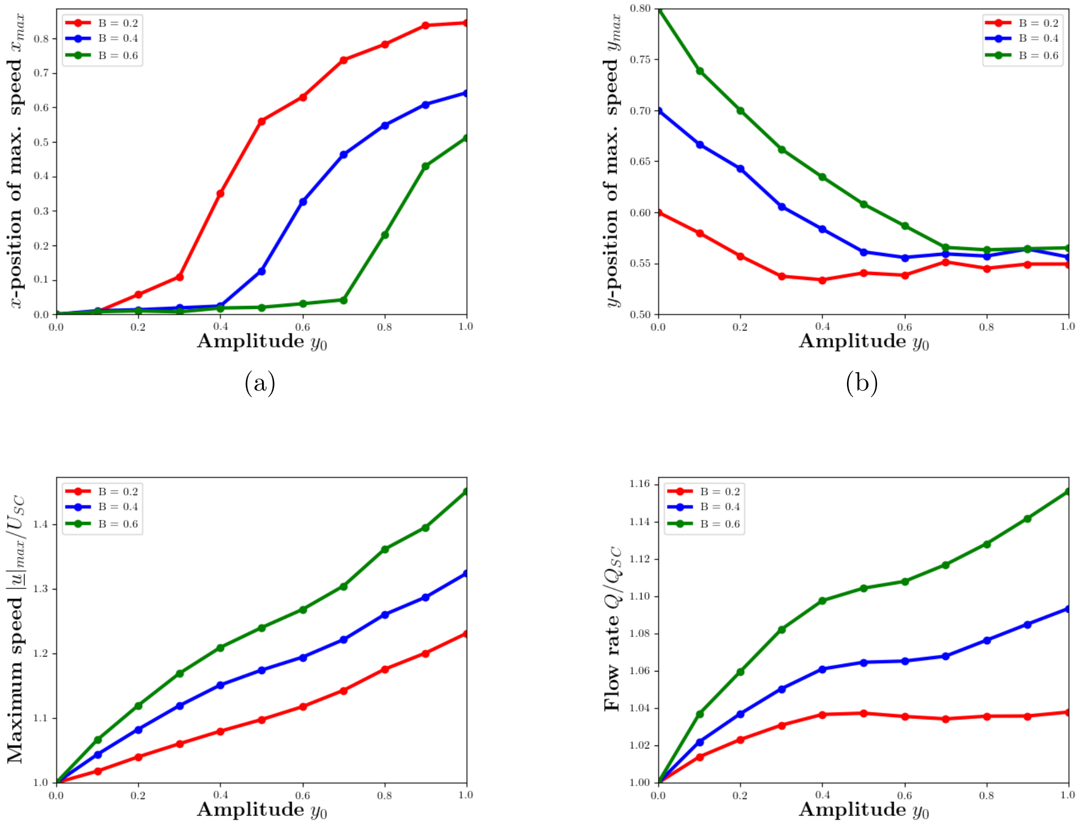

(a) (b)

(c) (d)

Figure 5.31: For $B = 0.2, 0.4, 0.6$, slip length $\beta = 0$ and channel length $h/L_s = 0.25$, we consider the following as functions of y_0: (a) The x-distance x_{max} of the position of maximum speed from the channel centre. (b) The y-distance $\hat{y}_{max}$ of maximum speed from the lower channel wall (i.e. $\hat{y} = 0$), (c) the value of the maximum speed scaled by U_{max} and (d) the flow rate Q scaled by Q_{SC}.

(x_{max},y_{max}). Due to the reversibility of Stokes flow, the maximum speeds' x-position, denoted by x_{max}, occurs in two positions symmetric about $x = 0$ (cross-section χ_1). The position y_{max} is measured from the bottom wall of the channel (described by eq. (5.1)). From fig. 5.3, we see that the value $\hat{y} = 0$ denotes the bottom wall and $\hat{y} = 1$ denotes the top wall of the channel. To maintain this notation in the sinusoidal region, we measure the $\hat{y}_{max}$ as the vertical distance from the bottom wall i.e. $\hat{y}_{max} = y_{max} - W(x)$.

The maximum speed $|\underline{u}|_{max}$ for $y_0 = 0$ is the equal to the plug speed so there is no particular position of maximum speed. The results from fig. 4.5 suggest that the position of max speed is close to the outer yield-surface for small channel curvatures. For very small y_0 (i.e. setting $y_0 = 0.01$), the position y_{max} is located near the outer yield surface, labelled by y_o^s, close to the outer channel wall at $\hat{y} \approx \frac{1}{2}B$. Therefore in fig. 5.31, we plot the position of the maximum speed for the case $y_0 = 0.01$ instead of $y_0 = 0.0$, which show of positions (x_{max},y_{max}) at very small amplitudes.

For all Bingham numbers B, we see (fig. 5.31(a)) that choosing a non-zero amplitude y_0 causes the value x_{max} to become positive (or negative, by symmetry) as x_{max} moves away from χ_1, implied by figs. 5.28-5.30. The value x_{max} remains close to 0 for a range of y_0 which is dependent on the Bingham number B i.e. $x_{max} < 0.04$ for y_0 between 0 and 0.7 for $B = 0.6$ in comparison to y_0 between 0 and 0.1 for $B = 0.2$. For smaller B, the value of x_{max} moves further away from χ_1 for each y_0 in comparison to larger B, with x_{max} increasing at amplitudes y_0 for smaller B.

In fig. 5.31(b), we consider y_{max} for a range amplitudes y_0 between 0 and 1. For y_0 close to 0, the position y_{max} is located near the outer yield surface for each B. y_{max} decreases with increasing amplitude y_0 for all B; it gets closer to the bottom wall of the channel. For both $B = 0.4$ and 0.6, the position y_{max} decreases approximately linearly from $y_0 = 0$ to 0.5 and 0.7, respectively and thereafter becomes constant for large y_0 at $y_{max} \approx 0.56$. For $B = 0.2$, y_{max} also decreases with increasing y_0 but for this smaller Bingham number, we see a slight overshoot in the value of y_{max} as it increases (moving towards the upper wall) for $y_0 \geq 0.4$. The value of y_{max} saturates at 0.55 for $y_0 \geq 0.7$. There is a correlation between x_{max} (fig. 5.31(a)) and y_{max} (fig. 5.31(b)) as x_{max} only increases if the value of y_{max} has saturated.

In fig. 5.31(c) and (d), we consider the maximum speed $|\underline{u}|_{max}/U_{SC}$ and flow rate Q/Q_{SC} as functions of y_0. Both $|\underline{u}|_{max}$ and Q increase in value with increasing amplitude y_0, with a greater increase seen for fluids with larger B. For example, the maximum speed $|\underline{u}|_{max}$, relative to U_{max}, increases by approximately 45% for $B = 0.6$ for $y_0 = 1$, where for $B = 0.2$ there is an increase of around 23% for the same amplitude y_0.

For the flow rate Q/Q_{SC}, the gradient of the curve decreases at intermediate amplitudes y_0. For $B = 0.2$, there is no increase in the flow rate for amplitudes greater than 0.5 as the curve stagnates at a value around 4% larger than the straight channel case $y_0 = 0$. For $B = 0.4$ and 0.6, the gradient of Q/Q_{SC} decreases for amplitudes y_0 between 0.4 and 0.6 before increasing for $y_0 > 0.6$. This decrease in gradient of the flow rate coincides the movement of the maximum speed away from the cross-section χ_1 and the stagnation in the yielding A_{rel} with increasing y_0. Fig. 5.31(d) indicates that flow rate can be increased or decreased by varying both the Bingham number B and channel amplitude y_0 which could be of particular interest in industrial applications of flowing yield-stress fluids through pipes.

The results suggest that for a pipe of amplitude $y_0 = 1.0$ and a fluid with Bingham number $B = 0.6$, one could induce a 16% increase in flow rate Q (relative to the case $y_0 = 0$), although this causes the majority of the fluid to become yielded (which is counterproductive for foam sclerotherapy). One should note that although Q/Q_{SC} becomes larger with increasing amplitudes y_0 for $B = 0.6$ than $B = 0.2$, the flow rate is measured in relation to straight channel case. In fact the flow rate decreases for larger Bingham numbers i.e. Q is over 3.5 times smaller for $B = 0.6$ than $B = 0.2$ for $y_0 = 0$.

5.5.3.2 The effect of varying the length of the sinusoidal region on the position of maximum speed

We consider the effect of shortening the length of the sinusoidal region L_s on the position of maximum velocity and present results in terms of channel length h/L_s.

In fig. 5.32(a), we trace x_{max} for a range of y_0 and for $h/L_s = 0.25$, 0.33 and 0.5. For small values of y_0 between 0 and 0.3, x_{max} remains close to 0 for all ratios h/L_s. For larger values of y_0, x_{max} shoots away from cross-section χ_1 at amplitudes y_0 between 0.3 and 0.4, depending on the value of the channel length h/L_s. A larger h/L_s causes x_{max} to move

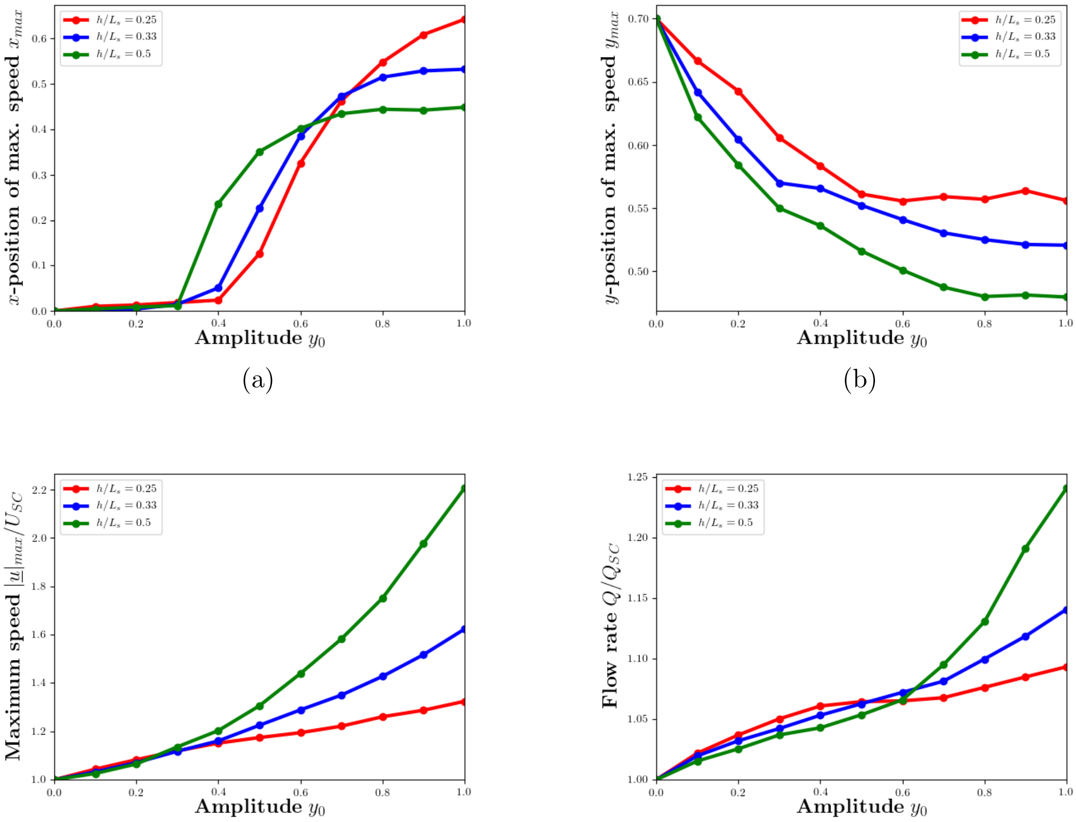

(a) (b)

(c) (d)

Figure 5.32: For channel lengths $h/L_s = 0.25$, 0.33, and 0.5, Bingham number $B = 0.4$ and slip length $\beta = 0$, we consider the following as functions of y_0: (a) The x-distance x_{max} of the position of maximum speed from the channel centre. (b) The y-distance y_{max} of maximum speed from the lower channel wall (i.e. $\hat{y} = 0$), (c) the value of the maximum velocity scaled by U_{max} and (d) the flow rate Q scaled by Q_{SC}.

away from χ_1 at smaller amplitudes y_0, although its effect is not as strong as varying the Bingham number (fig. 5.31). The position x_{max} then increases for larger amplitudes until and stagnates to a fixed value of $x_{max} \approx 0.4$ for $h/L_s = 0.5$ at $y_0 = 1$. Decreasing h/L_s causes the position x_{max} to move further away from χ_1 with increasing amplitude y_0 i.e. $x_{max} \approx 0.6$ for $h/L_c = 0.25$ and $y_0 = 1$.

As the amplitude y_0 increases, y_{max} (fig. 5.32(b)) moves from near the outer yield surface inwards towards the bottom channel wall, where the pressure gradient is largest. The effect of increasing h/L_s causes y_{max} to move closer to the bottom wall, saturating at approximately 0.45 for $y_0 = 1$ and $h/L_s = 0.5$.

For the maximum speed $|\underline{u}|_{max}$, scaled by the plug velocity U_{SC} in fig. 5.32(c), increasing the amplitude y_0 causes the maximum speed to increase for each ratio h/L_s. For small amplitudes $y_0 < 0.3$, the smallest channel length h/L_s provides the largest $|\underline{u}|_{max}/U_{SC}$. Increasing the channel amplitude past 0.3 sees the larger channel lengths h/L_s providing a larger "relative speeds". For the case $h/L_s = 0.5$, the maximum speed doubles for an amplitude of $y_0 = 1$.

Lastly, in fig. 5.32(d), by considering Q/Q_{SC} we see a cross over for different channel lengths h/L_s, where for $y_0 \leq 0.5$ that smaller h/L_s provide larger values of Q/Q_{SC} and for larger amplitudes the larger values of h/L_s become greater. The flow rate Q becomes 25% larger at $y_0 = 1.0$ in comparison to the straight channel case. This suggests that for industrial application of yield-stress fluids flowing at through pipes, flow rate can be induced by introducing pipes of a sinusoidal function with a large h/L_s.

One could roughly estimate the increase in the flow rate Q caused by a change in the channel amplitude y_0 by using the findings in fig. 5.6. The flow rate can be calculated for a straight channel (as in §3) based on the minimum channel width that the channel reduces to. For example, for $h/L_s = 0.5$ and $y_0 = 1.0$, the minimum distance d_{min} reduces by 43% to 0.57 which increases the flow rate of Bingham fluid with the same yield-stress through a straight channel by approximately 25%. This is a close approximation to the results shown in fig. 5.32(d). Therefore, when fluid becomes stagnant within the bump of the sinusoidal region, the increase in flow rate can be estimated by a mass-conservation argument where the reduction in channel width in a sinusoidal channel suggests the amount that the flow rate increases by using the straight channel results.

5.5.3.3 The effect of increasing the slip length on the position of maximum speed

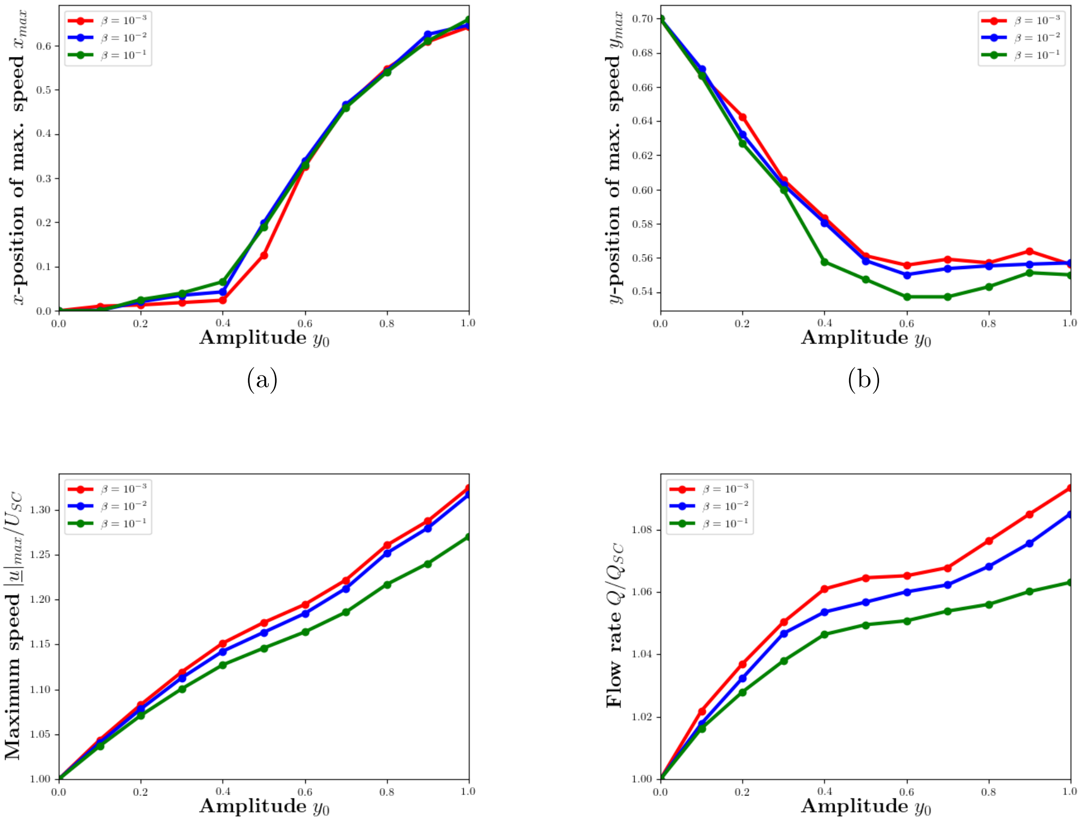

(a) (b)

(c) (d)

Figure 5.33: For $h/L_s = 0.25$, $B = 0.4$ and slip lengths $\beta = 0$, 10^{-2} and 10^{-1}, we plot: (a) the x-position x_{max}, (b) y-position y_{max} of maximum velocity, (c) the value of maximum velocity as well as (d) the flow rate Q/Q_{SC} for y_0 between 0 and 1.

Here we consider the effect of wall slip on the position and value of the maximum speed $|\underline{u}|_{max}$ (as well as flow rate Q) for a fixed channel length $h/L_s = 0.25$. In fig. 5.33(a) and (b), we consider the x and y position of maximum velocity, x_{max} and y_{max} for a range of amplitudes y_0. The positions x_{max} remain close to χ_1 ($x = 0$) for $y_0 \leq 0.4$ before moving towards χ_2 for larger amplitudes. The distance of x_{max} away from χ_1 increases for larger y_0 and is also dependent on the Bingham number i.e. having a smaller B means that the position of $|\underline{u}|_{max}$ moves closer to χ_2 compared to larger B (fig. 5.31). Increasing the slip length has little effect on the relationship between x_{max} and y_0.

The position y_{max} shifts towards the inner wall with increasing amplitude y_0, before saturating at larger y_0 to $y_{max} \approx 0.56$ for all slip lengths β. For the largest considered slip length $\beta = 10^{-1}$, we see a slight overshoot in position (at $y_0 = 0.6$ where $y_{max} \approx 0.54$) before y_{max} moves away from the bottom wall and saturates at 0.56.

In fig. 5.33(c) and (d), we consider the maximum speed $|\underline{u}|_{max}/U_{SC}$ and flow rate Q/Q_{SC} as functions of y_0. Both quantities increase with y_0 as expected as widths of the sinusoidal region becomes narrower with increasing amplitude y_0 (fig. 5.6). The amount of increase in $|\underline{u}|_{max}$ relative to the U_{SC} decreases as the slip length increases β. For example, for an amplitude of $y_0 = 1$, the maximum speed $|\underline{u}|_{max}/U_{SC}$ is 5% less for $\beta = 10^{-1}$ compared to the no-slip case.

In fig. 5.33(d), we see that the flow rate Q/Q_{SC} also increases with increasing amplitude y_0. For an intermediate amplitude y_0 close to 0.5, the curves flatten for all slip lengths β. For small slip lengths ($\leq 10^{-2}$), the curve becomes "steeper" for amplitudes $y_0 \geq 0.6$ as previously seen in fig. 5.31. This is not seen as clearly for larger slip lengths. We conclude that the main effect of wall slip on $|\underline{u}|_{max}$ and Q is that both quantities grow less relative to the straight channel case, than the no-slip case.

5.5.4 Yield surfaces

In chapters 3 and 4, we have focused on determining the locations of the yield-surfaces, which demarcates the plug region. For χ_1 and χ_2, we determine where the yield surfaces y_i^s and y_o^s cross the cross-sections χ_1 and χ_2 and use it to investigate the size of the plug width of Bingham fluid across each cross-section with increasing amplitudes y_0.

In chap. 5.5.1, we analysed the plug area for different values of y_0; here we use the same criterion on the stress to identify individual yield-surfaces on the two cross-sections. From figs. 5.8, 5.9 and 5.11, we see that as y_0 increases, the fluid becomes nearly completely yielded at χ_2 as $y_0 \to 1$. At cross-section χ_1, there is always a non-zero plug width for each amplitude y_0. The yield surfaces, are identified as the smallest and largest $\hat{y}$ for which the stress $|\underline{\underline{\tau}}|$ is below $\frac{1}{2}(B + B_\epsilon)$.

5.5.4.1 The effect of varying the amplitude on the yield surfaces

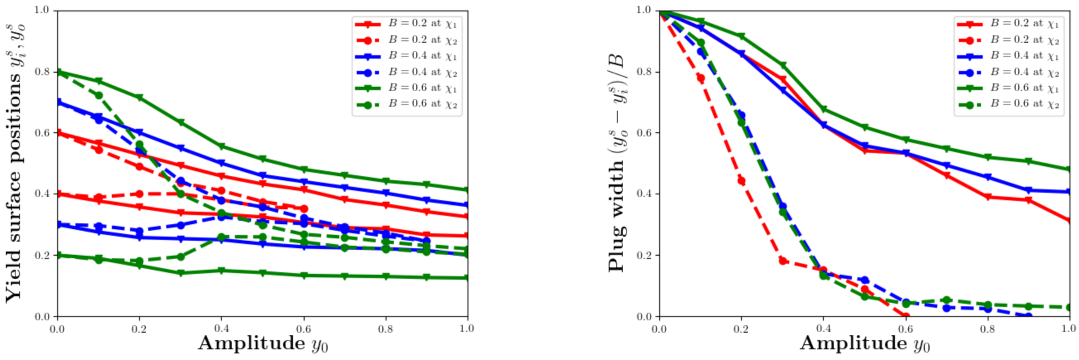

(a) (b)

Figure 5.34: For Bingham numbers $B = 0.2, 0.4, 0.6$, slip length $\beta = 0$ and channel length $h/L_s = 0.25$, we plot: (a) The yield surfaces y_i^s, y_o^s as a function of y_0 and (b) the plug width as a function of y_0 scaled by B.

In fig. 5.34(a) ($h/L_s = 0.25$ and $\beta = 0$), we consider the positions of the yield surfaces at cross-sections χ_1 and χ_2 for a range of amplitudes y_0 between 0 and 1 and Bingham numbers $B = 0.2$, 0.4 and 0.6. For small amplitudes y_0, the yield-surfaces become closer together and are positioned closer to towards the bottom wall of the channel (where the pressure gradient is largest). The yield surfaces at cross-section χ_2 become closer together in comparison to χ_1 for each B and y_0. At χ_2, the inner yield surface y_i^s remains close to the yield surfaces at χ_1 for amplitudes y_0 between 0 and $\frac{1}{2}B$. For larger amplitudes, the inner yield surface y_i^s moves closer to the outer yield surface y_o^s until at critical amplitudes, the fluid becomes completely yielded i.e. when the yield surfaces coincide. The critical amplitudes for complete yielding in the case $h/L_s = 0.25$ for $B = 0.2$ and 0.4 are $y_0 = 0.6$ and $y_0 = 0.9$, respectively. For $B = 0.6$, there is only a small plug width at χ_2 for a channel amplitude $y_0 = 1$.

At χ_1, we see that the inner yield surface deviates little from the positions at $y_0 = 0$ with increasing amplitude y_0, only moving slightly closer to the inner wall of the channel. The outer yield surface moves inwards towards the bottom wall causing the plug width to narrow.

In fig. 5.34(b), we plot the respective plug widths at cross-sections χ_1 and χ_2, defined as the distance between the yield surfaces and scaled by B such that for $y_0 = 0$, the plug width is 1. By increasing the amplitude y_0 causes the plug width to decrease at both cross-sections for all B, with a greater narrowing of the plug seen at χ_2 as expected (due to the large difference in curvature between the sinusoidal region and the straight channel). For some Bingham numbers and channel amplitudes i.e. $B = 0.2$ and $y_0 = 0.6$, we see complete yielding at χ_2.

5.5.4.2 The effect of varying the length of the sinusoidal region on the yield surfaces

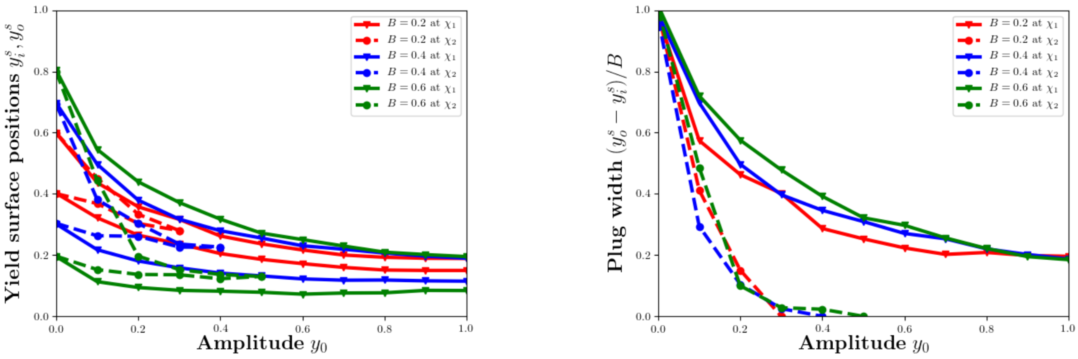

(a) (b)

Figure 5.35: (a) The position of the yield surfaces y_i^s, y_o^s as a function of the amplitude of the sinusoid y_0 and (b) the plug width as a function of y_0 scaled by B for $B = 0.2, 0.4, 0.6$ and $h/L_s = 0.5$.

In fig. 5.35, we consider the yield-surface positions (and respective plug length) for $h/L_s = 0.5$ for $B = 0.2$, 0.4 and 0.6 with $\beta = 0$ to understand how the length L_s effects the size of the plug width at cross-sections χ_1 and χ_2. For $h/L_s = 0.5$, there is significant yielding of the fluids' plug region in comparison to a channel length of $h/L_s = 0.25$ as expected from fig. 5.15. The yield surfaces become much closer together and there is a clear shift of the plug region towards the lower wall of the channel with increasing amplitude y_0. There is complete yielding at χ_2 for all considered B, occurring at $y_0 = 0.3$, 0.4 and 0.5 for $B = 0.2$, 0.4 and 0.6, respectively.

At cross-section χ_1, there is always a non-zero plug width for all B, which are at least 10% smaller for $h/L_s = 0.5$ (fig. 5.35) than for $h/L_s = 0.25$ (fig. 5.34). Note also that for $h/L_s = 0.5$, there is also the formation of dead regions of fluid, neglected in the results here. The results in fig. 5.35 indicate that there is a greater amount of yielding of the plug region at both cross-sections χ_1 and χ_2, which at critical amplitudes can cause complete yielding at χ_2. The critical amplitudes become smaller as channel length h/L_s increases.

5.5.4.3 The effect of increasing the slip length on the yield surfaces

Here we consider the positions of the inner and outer yield surfaces along cross-sections χ_1 and χ_2 for different slip lengths between $\beta = 10^{-3}$ and 10^{-1} for a fixed channel length $h/L_s = 0.25$, which allows us to understand the effect of slip on the plug width. From fig. 4.7, we would expect for curved channels the plug widths would narrow slightly for larger slip lengths β.

In fig. 5.36(a), we see that at both cross-sections χ_1 and χ_2, the yield surfaces become closer together (for each amplitude y_0) with increasing slip length β. This results in the fluid at cross-section χ_2 to become fully yielded at smaller amplitudes y_0 i.e. for $\beta = 10^{-3}$ (which is more or less the same as the results for $\beta = 0$), the fluid becomes fully yielded at $y_0 = 0.9$ in comparison to $y_0 = 0.5$ for $\beta = 10^{-1}$. As for cross-section χ_1, as well as narrowing the plug width, increasing β also causes the plug region to shift closer to the bottom wall of the channel. In a way, the introduction of slip "enhances" the effect of channel amplitude y_0.

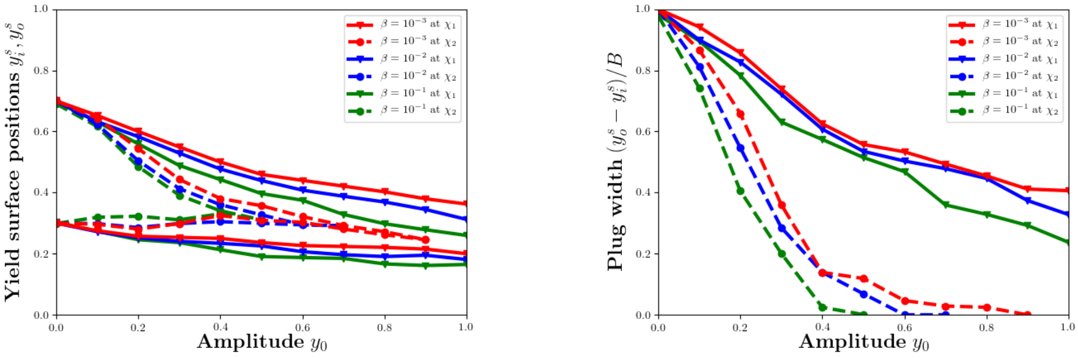

(a) (b)

Figure 5.36: (a) The yield surfaces y_i^s, y_o^s and (b) the respective plug widths $(y_o^s - y_i^s)/B$ at cross-sections χ_1 and χ_2 for $B = 0.4$, $h/L_s = 0.25$ and β between 10^{-3} and 10^{-1} as functions of channel amplitude y_0.

Fig. 5.36(b) shows the respective plug width of fluid at both cross-sections χ_1 and χ_2 for different slip lengths β. In agreement with the conclusions in fig. 5.36(a), the larger the slip length β, the narrower the plug width becomes at both cross-sections. The "amount" of yielding of the plug width remains roughly the same for all considered slip lengths, which ties into the conclusions from §4.7, that although slip lengths do induce additional yielding of the plug region, but the extent of the added yielding is minimal (for β up to 10^{-1}), although the effect is stronger in sinusoidal channels than curved channels.

5.6 Concluding remarks

We have investigated the pressure-driven flow of a Bingham fluid through a sinusoidal channel for a number of different ratios of the channel length h/L_s, amplitude y_0 and slip length β, and consider their effect on the relative plug area, speed and flow rate. Our prediction of the relative size of the plug region gives an indication of effectiveness of the foam in the sclerotherapy treatment in a two-dimensional vein-like channel.

Increasing the ratio h/L_s i.e. shortening the length of the sinusoidal region, causes the development of dead regions at the top wall for large amplitudes y_0. The size of the dead regions increase with greater channel amplitude y_0 and Bingham number B and have been of particular interest in industrial applications [Roustaei, 2016; Roustaei and Frigaard, 2013] such as the process of cleaning pipes of whey protein deposits [Christian and Fryer, 2006] or toothpaste [Cole et al., 2010]. Our findings find that at a channel amplitude of $y_0 = 1.0$, channel length $h/L_s = 0.5$ and $B = 0.6$, the width of the dead region can span up to 20% of the channel width at χ_1, which would increase further for larger B and y_0. This effect is undesirable for foam sclerotherapy.

The fluid in sinusoidal shaped veins are affected more by wall slip than for a curved channel (from chap. 4), with the amount of additional yielding of the plug region becoming greater at smaller amplitudes y_0 with increasing slip length β. Wall slip in a sinusoidal channel would decrease the efficiency of the foam within sclerotherapy due to the additional yielding of the foam within the vein. Although we acknowledge the negative effect of additional yielding caused by the wall slip, large channel amplitudes y_0 and lengths h/L_s are a much greater factors for additional yielding and the results show the necessity of straightening the vein in any way possible before treatment. The effect of wall slip becomes less of a factor as the veins become straighter (see chap. 3).

We have seen that increasing the channel amplitude increases both the speed and the flow rate of the fluid within the sinusoidal region. Increasing the channel length h/L_s and amplitudes y_0 causes the minimum perpendicular distance between the top and bottom wall to decreases by up to 40% for $h/L_s = 0.5$ and $y_0 = 1$. For the same parameters, the arc length L_s^{arc} of the sinusoidal region more than doubles. The results from the numerical simulations suggest that for $h/L_s = 0.5$ and $y_0 = 1$, the maximum speed doubles and the flow rate has increased by 25% (fig. 5.26). This suggests that shaping a pipe as a sinusoidal wave can induce larger flow rates of flows of Bingham fluids without increasing the driving pressure-gradient (but increasing the inlet pressure is required), which could be a benefit in industrial applications. But this in turn, will cause the fluid to mostly yield.

In agreement with the results found in chap. 4, flows of yield-stress fluids are sensitive to channel curvature and wall slip, which decreases the size of the plug regions. Therefore, for the purposes of using foam in sclerotherapy, it is advised to keep the vein as straight as possible during treatment. Also, it is beneficial to have a large Bingham number (i.e. yield-stress), as a greater amount of plug remains in the sinusoidal region for large B (see figs. 5.8-5.11). We characterise the foam's yield stress in the next chapter, to associate a value of B for different foams used in sclerotherapy.

6 The piston effect

6.1 Introduction

In this chapter, we characterize the yield-stress of the foam used in sclerotherapy treatment using experimental results from Carugo et al. [2016]. This chapter is based on Roberts et al. [2020], which was written for a clinical audience.

In chap. 1.3.3, we discussed process involved in the sclerotherapy treatment. The effectiveness of the treatment is determined by the ability of the foam to displace the stagnant blood within the vein and to deliver the scloresent to the vein walls, without mixing with blood, which deactivates the sclerosent.

In chapter 3, we considered a flow of Bingham fluid straight two-dimensional vein, representing a flow of foam through a straight vein. This allowed us to gain some preliminary conclusions about the effectiveness of sclerotherapy through straight veins both analytically and numerically. The finite element simulations are much simpler in two dimensions as it allows us consider simplified theory and isolates some phenomena (such as drainage) [Cox et al., 2004]. We now work in three dimensions, which provides quantitative but simplified information, by considering a vein to be a straight cylinder with parallel walls (tortuosity can be introduced as in chaps. 4 and 5, but it does not change our argument) through which foam flows from some upstream injection point.

How should we characterize a foam so as to begin to optimize this process? The efficacy will depend upon the sclerosant chemistry, the properties of the foam itself, such as the bubble size, and on the properties of the vein into which the foam is to be delivered. For example, large veins might require a foam with slightly different properties to those required for small spider veins. In very small spider veins (telangiectasias, dilated interdermal venules < 1 mm), liquid sclerosants are considered to be as effective as foam at displacing blood [Zimmet, 2003]. The choice of gas, which we do not consider here, also affects surfactant transport within the foam [Peterson and Goldman, 2001].

Carugo et al. [2016] generated polidocanol foams in several different ways to compare the resulting bubble-size distribution and foam lifetime. The commercial product Varithena® (PEM) was compared in this evalulation to typical physician-compounded foams (PCFs) produced using both the Tessari method and the double syringe system (DSS). These two methods mix a syringe of gas with a syringe partly filled with the liquid sclerosant by passing the two fluids back and forth repeatedly between the two syringes. In the DSS the syringes are joined by a simple straight connector while in the Tessari method the straight connector is replaced by a three-way valve which convolutes the path of the fluids. Despite the similarities between the methods, data suggests that the DSS method produces a foam with a narrower bubble size distribution that is preferable for sclerotherapy [Wollmann, 2010].

Typically, the liquid fraction of a PCF is high, between 0.2 and 0.25. Such foams have low yield stress and are likely to suffer from gravity override (see chap. 1.4.4), in which the foam floats above the blood in a vein rather than displacing it. To effect their comparison, Carugo et al. [2016] produced foams with different methods but with a liquid fraction consistent with PEM, $\phi_l \approx 0.125$.

Our goal is to characterize the properties of foams used for sclerotherapy with the aim of improving the effectiveness and reproducibility of the process. In §6.2 we describe our characterisation, in particular how the yield stress depends on bubble size and on any polydispersity in bubble size. In chap. 6.3 (as we did for the two-dimensional case in chap. 3), we show how the yield stress affects the shape of the displacement front within a vein, and draw conclusions about how this affects the efficacy of sclerotherapy in §6.5. In §6.4, the results of chaps. 4.7 and 5 are generalised to suggest the effects on PEM and PCFs of more tortuous vein geometries.

6.2 Characterisation of bubble size distributions

In chap. 1.4.2.3, we gave the relationship between the foams' liquid fraction and yield stress. The yield stress τ_0 can be empirically estimated by the approximation [Princen and Kiss, 1989] in eq. (1.4), which suggests that τ_0 depends quadratically on the liquid fraction ϕ_l and linearly on the Laplace pressure [Cohen-Addad et al., 2013]. Here we use the estimation to approximate the yield stress of each foam and to investigate the role of the bubble polydispersity on the yield stress by considering the arithmetic and volume-weighted mean of the bubble radii.

The mean bubble size R is an average over the foam, i.e. the sum of the bubble radii divided by the number of bubbles. Instead of this unweighted mean, Princen and Kiss [1989] found that the Sauter mean radius, R_{32}, is the most appropriate average bubble size for predicting the rheological properties of foams. The Sauter mean radius approximates the average bubble size based on the ratio of volume to surface area. Since in slow flows the response of a foam to deformation is dominated by the elasticity of the bubble interfaces, it should perhaps be no surprise the Sauter mean radius is a better measure of foam response. Indeed, Rouyer et al. [2005] state that their rheological data collapses on to a master curve *only* if the Sauter mean radius is used to scale the yield stress. The clear corollary is that bubble size polydispersity *does* affect the foam yield stress. We argue that it therefore influences the process of foam sclerotherapy.

In particular, the Sauter mean radius is sensitive to the presence of any large bubbles, recognising that a long tail in the bubble size distribution has a significant effect on foam response. It is for this reason that a narrow bubble size distribution is more appropriate for sclerotherapy.

In a foam of N_b bubbles with different radii, the mean radius is $R = \langle R_b \rangle = \frac{1}{N_b} \sum R_b$. The Sauter mean radius, on the other hand, is proportional to the ratio of bubble volume

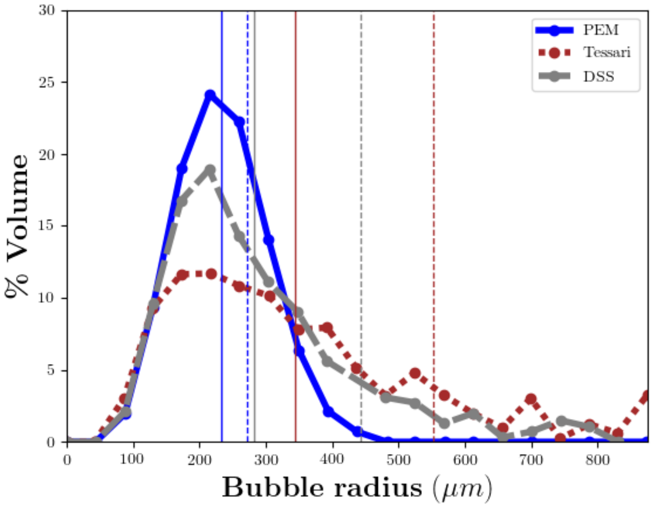

Figure 6.1: The bubble distribution for the PEM, Tessari and DSS samples produced by Carugo et al. [2016]. The measurements are recorded 115s after foam preparation in foams of the same liquid fraction. Solid vertical lines denote the mean bubble size (R) and dotted lines denote the Sauter mean radius (R_{32}).

to surface area, $R_{32} = \langle R_b^3 \rangle / \langle R_b^2 \rangle$. The Sauter mean radius can be up to about 20% greater than the mean radius in a disordered polydisperse foam [Cantat et al., 2013; Feitosa and Durian, 2008].

We calculate R_{32} for the data from Carugo et al. [2016] to determine the effect on the expected value of the yield stress of the way in which polydispersity is calculated. Figure 6.1 shows the bubble distributions of the three foams. For both the Tessari and DSS foams, there are several large bubbles with bubble radius greater than $500\mu m$; these are not present in the PEM foam. These large bubbles have a significant effect on the value of the Sauter mean radius of the foam, increasing it by 60% and 56% for the Tessari and DSS foams, respectively, over the usual mean, as shown in Table 1.

This increase in the effective average bubble radius leads (cf. eq. (1.4) with $R = R_{32}$) to a significant decrease in the predicted yield-stress of the foam. Assuming that the surface tension of all three foams are similar, about $\gamma = 30 \times 10^{-3} N/m$, allows us to calculate a value for the yield stress, as shown in Table 1.

Foam type	R (μm)	R_{32} (μm)	p	τ_0 (Pa)	B
PEM	233	272	0.168	3.04	4.48
Tessari	343	553	0.610	1.50	2.20
DSS	283	443	0.566	1.87	2.76

Table 1: Measurements extracted from the data for PEM, Tessari and DSS foams from Carugo et al. [2016]: the mean and Sauter mean bubble size, the predicted value of the yield stress τ_0 (eq. (1.4)), polydispersity (eq. (6.1)) and the Bingham number B (eq. (6.2)) using the Sauter mean radius. Using R instead of R_{32} to calculate τ_0 gives greater values but in the narrower range $2.4 - 3.6$Pa.

The table shows that the predicted yield stress of a foam depends strongly on the way in which the mean bubble size is calculated. Replacing the standard mean with the Sauter mean can reduce the predicted yield stress by up to one third. Since a high yield stress is important for sclerotherapy, this finding suggests that the efficacy of polydisperse foams may have been overestimated in the past [Carugo et al., 2016].

A measure of polydispersity p was suggested by Kraynik et al. [2004], based on the values of R_{32} and R for a foam:

$$p = \frac{R_{32}}{R} - 1. \tag{6.1}$$

p is dimensionless and non-negative. It is equal to zero when the foam is monodisperse. The measurements of R and R_{32} in tab. 1 allow us to derive polydispersity values p for each foam. The value of p for PEM ($p = 0.168$) is smaller than the values for Tessari ($p = 0.610$) and DSS ($p = 0.566$) foam, indicating that PEM is much more monodisperse in comparison to both PCFs.

We now turn to the consequences of the differences in both the mean radius R_{32} and yield stress τ_0 for the degree to which the foam can effectively displace blood from a varicose vein.

6.3 Characterisation of foams in veins: the piston effect

Having analysed foam properties, we now consider the effects of vein size and injection speed. The Bingham number, B, is a dimensionless measure of the importance of a fluid's yield stress relative to the viscous stresses induced in the fluid by the flow. As we describe below, it is advantageous to use B in place of τ_0 to represent the "piston" effect of a foam in a vein, i.e. how good it is at displacing fluid (blood) rather than mixing with it.

We consider a straight cylindrical vein of diameter D and assume that fluid flows through it due to a difference in pressure between the injection site and the next (working) valve some distance along the vein. The pressure gradient G in the vein is the difference in pressure divided by this distance. It is dictated largely by, on the one hand, the force that can be used to depress the syringe without destroying the foam and, on the other, the need to deliver the foam before it starts to disintegrate. This disintegration occurs through diffusion-driven coarsening, in which the bubbles lose their gas to the surroundings [Cantat et al., 2013]. The rate at which this coarsening occurs is determined by the solubility of the gas used to make the foam [Peterson and Goldman, 2001]: faster for carbon dioxide, slower for nitrogen, with oxygen presumably somewhere in between depending on the physiological environment.

The Stokes equations for the slow flow of a yield stress ("Bingham") fluid in a cylindrical vein [Bird et al., 1983] provide the distribution of the axial fluid velocity across the vein which can approximate the flow profile of foam within a cylindrical vein. We present examples of these velocity profiles in figure 6.2 cf. chapter 3 which represent flow profiles of foam with different yield-stresses in cylindrical veins. As for the previous chapters, we assume a zero slip length $\beta = 0$ such that the no-slip boundary condition is satisfied on the vein walls [Baker and Wayland, 1974; Sousa et al., 2011].

In clinical delivery, 5ml of foam is injected in about 75 seconds. This corresponds to a flow rate Q of roughly $6.7 \times 10^{-8}\text{m}^3/\text{s}$. In a cylindrical vein of area A_v the average velocity

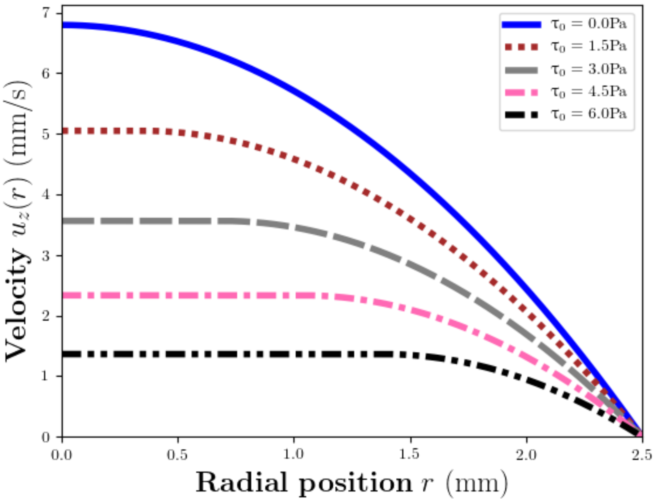

Figure 6.2: Examples of the velocity profile for flow along a cylindrical vein under a fixed pressure gradient G for different values of the yield stress τ_0.

U and flow rate Q of a Bingham fluid depend on the applied pressure gradient G, the yield stress τ_0, the foam viscosity μ and vein size D: $U = \frac{4}{\mu \pi D^2}\left(\frac{1}{2}\tau_0(r_0^2 - \frac{D^2}{4}) + \frac{1}{6}G(\frac{D^3}{8} - r_0^3)\right)$ and $Q = A_v U$, where $r_0 = 2\tau_0/G$ denotes the radial position of the yield surface. The velocities and flow rates reduce in proportion to the yield stress [Bird et al., 1983]. Using the values of τ_0 in Table 1, we can suggest the velocity profiles for each foam used in sclerotherapy. We plot the curves for different yield stresses in figure 6.2, which suggests that the average foam velocity for $\tau_0 \approx 3$ is as low as a half of the value in the absence of yield stress.

The effective viscosity of the foam is orders of magnitude greater than the viscosity of the sclerosant solution forming the liquid phase of the foam [Gopal and Durian, 1999], roughly $\mu = 1$ Pa s. The expressions for U and Q above then allow us to estimate the pressure gradient in a vein of diameter 5mm to be $G \approx 8.7 \times 10^3$ Pa/m and the average velocity $U \approx 3.4$ mm/s.

Using r to represent radial position in the vein, we note that there is an interface at $r = r_0$ which separates the plug region in the centre of the vein, with constant velocity, from the yielded region close to the walls. It is this plug region that is effective in displacing blood. Its size is directly proportional to the Bingham number defined below. A smaller pressure gradient G (and hence a slower flow), or a fluid with high yield stress τ_0, will have a wide plug of foam pushing down the vein. Thus optimisation of B is necessary.

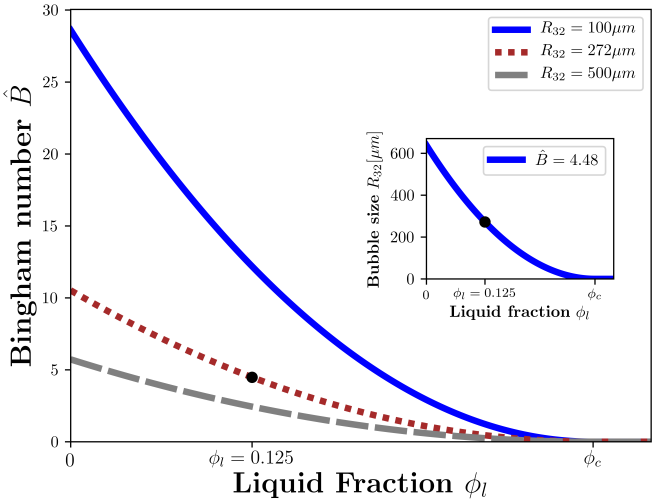

Figure 6.3: Representative values of the Bingham number $\hat{B}$, showing the strong dependence on the liquid fraction of the foam and the bubble size. Lines are shown for three values of the Sauter mean bubble radius for a vein with diameter 5mm, fluid speed $U = 3.4$ mm/s, viscosity $\mu = 1$ Pa s and interfacial tension $\gamma = 30 \times 10^{-3}$N/m. The values for PEM are shown with a black dot. The inset shows the relationship between the bubble size R_{32} and the liquid fraction ϕ_l that will result in the same value of the Bingham number $\hat{B}$.

The Bingham number depends not only on the foam properties, but also on the flow itself. For a flow of Bingham fluid through a cylinder, we write

$$\hat{B} = \tau_0 \frac{D}{\mu U} = 0.5 \frac{\gamma D}{\mu R_{32} U} \left(\phi_c - \phi_l\right)^2 , \tag{6.2}$$

using eq. (1.4), which is equivalent to writing $\hat{B}$ as the ratio of yield stress to wall stress. This relationship is shown in figure 6.3 for different values of the bubble size. The definition of the Bingham number $\hat{B}$ in eq. (6.2) differs from the previous definition in chaps. 1-5 as it is defined for a three-dimensional cylinder, whereas previously we have considered only the two-dimensional cases.

We can now use eq. (6.2) and the yield-stress values in Table 1 to find the respective values of the Bingham number for PEM, Tessari and DSS foams. As the Bingham number is also dependent on the flow properties, we assume a fixed fluid speed $U = 3.4$ mm/s. This allows us to determine the values for the Bingham number shown in tab. 1. The data shows that the Bingham number of the PEM foam is twice the value of the Bingham number for the Tessari foam and 62% greater than for the DSS foam.

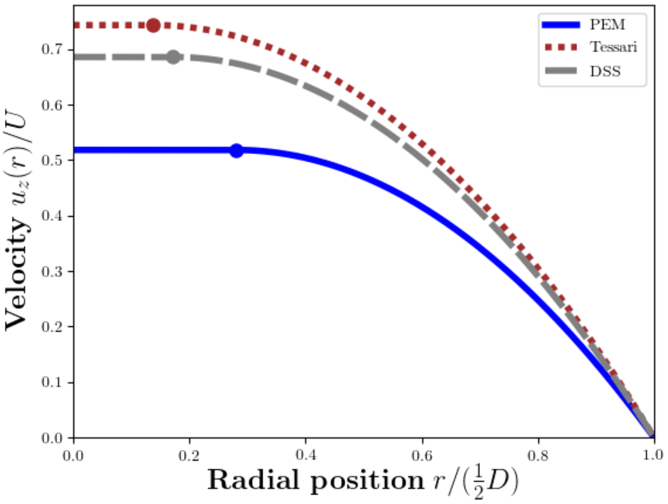

Figure 6.4: Predicted velocity profiles for PEM, Tessari and DSS foams flowing through veins with diameter 5mm due to a pressure-gradient $G = 8.7 \times 10^3$ Pa/m. Velocities are normalised by the scale U and the dots indicate the position of the yield surface.

In practice, G is set by the rate at which the surgeon injects the foam, estimated in §6.3. Figure 6.4 shows predicted velocity profiles in a cylindrical vein for each of the measured foams, with the yield surface r_0 equal to the ratio of the Bingham number and the non-dimensional pressure gradient $r_0 = 2\hat{B}/G_n$, where $G_n = GD^2/(4\mu U)$. Note how the width of the plug region is smaller for foams made with the Tessari method compared to the PEMs. Hence (for a fixed pressure gradient G_n), the difference in Bingham number is clearly correlated with a significant difference in the extent of the plug regions for the PEM and physician compounded foams.

The plug region at the centre of the channel is the effective region for the displacement of blood. For a cylindrical vein, we can measure the volume of the plug region. The relative volume of plug fluid V_{rel} is the proportion of the cross-section of the vein that is in a plug flow. Therefore, V_{rel} is a measure of plug volume V_p, equal to $2\pi r_o^2$, to the vein volume $V_t = 2\pi(1/2)^2$, and thus is equal to the square of the yield surface position i.e. $V_{rel} = 16\hat{B}^2/G_n^2$. For a fixed pressure gradient G_n, as the Bingham number $\hat{B}$ of PEM is twice the value of Tessari foam and 62% greater than the DSS foam, the relative volume V_{rel} for PEM is four and two and a half times greater than Tessari and DSS foam, respectively.

A wider plug region results from reducing the driving pressure gradient G_n (exerted by the surgeon) or increasing the Bingham number B (i.e. by increasing the yield-stress τ_0). As PEM has the largest yield-stress τ_0, reducing the pressure gradient G_n has the greatest effect on increasing the relative volume V_{rel} for each foam. For each foam, reducing the pressure-gradient G_n by 25% increases the relative volume by an additional 33% with the plug volume V_p for PEM remaining four and two and a half times larger than Tessari and DSS foam, respectively. In principle, injecting PCFs at smaller pressure gradients G_n can produce flows with large V_{rel}, although applying lower pressure gradients could lead to additional problems such as getting the foam out of the syringe.

For a fixed non-dimensional pressure gradient $G_n \approx 1.3 \times 10^4$ (with $G = 8.7 \times 10^3$Pa/m), reducing the liquid fraction of the foam by 25% (i.e from $\phi_l = 0.125$ to $\phi_l \approx 0.094$) increases the relative volume V_{rel} by 65%, which is true for all three foams. Reducing the mean radius R_{32} by 25% has an even greater effect as it causes the relative volume to increase by 77% (for all three foams), meaning that for PEM, over 20% of the vein volume consists of rigid plug flow. This implies that achieving very small improvements in the foam properties i.e. reducing liquid fraction, bubble size or polydispersity, is a more efficient way of increasing the relative plug volume V_{rel} than reducing the pressure gradient G set by the surgeon.

6.4 Discussion of the simulation results in tortuous geometries

Here, we use the results from the two-dimensional finite element simulations of a pressure-driven Bingham fluid through a straight channel connected to an annulus (chap. 4.7) and a sinusoidal channel (chap. 5) to discuss their implications for foams used in sclerotherapy.

We relate the conclusions from chaps. 4.7 and 5 and suggest the implications for three-dimensional veins. The results of the two-dimensional case, presented in chapters 1-5 of this thesis can be generalized into the 3D case, allowing us to advise possible factors that improve foam sclerotherapy to practitioners, with the goal of extending the simulations into three-dimensions in the future.

In chaps. 4.7 and 5, we considered the quantity A_{rel}, denoting the relative plug area, as a measure of the displacing capability of the foam i.e. its effectiveness of foam in sclerotherapy. A large relative plug area A_{rel} indicated that a greater "fraction" of plug area was lost due to the channel geometry (i.e. increasing channel curvature κ or amplitude y_0) or the effects of wall slip, which is counterproductive for the purpose of sclerotherapy.

In the channel geometry consisting of a straight channel connected to a curved channel of the same width (fig. 4.19), considered in chap. 4.7, the foam flows in an analytical-predictable profile providing that it is far enough away from the join (at least a distance of $2.5h$ or an angle of $\pi/8$), with a transition region where topological changes are likely to occur (T1s).

The yielding of the plug region occurs near (and at) the join of both straight and curved channels, with the length of the transitioning region of yielded fluid increasing for channels of greater curvature κ and fluid with larger Bingham numbers $\hat{B}$. Measuring the extent of yielding as the quantity A_{rel} shows that PEM loses less of its' relative plug area in comparison to Tessari and DSS foams for each non-zero curvature κ. This suggests that PEM provides a more effective sclerotherapy treatment in curved veins in comparison to PCFs as less of the plug area is lost.

As PEM has the largest yield-stress τ_0 of all three foams (hence a larger Bingham number B), it also has the widest plug width in these regions away from the join. Additionally (using the results in §4.7), it has an added advantage that its transition region between straight and curved channels is shorter in comparison to both PCFs, meaning that for PEM the plug region is reformed over a shorter distance. This is true for both considered slip lengths $\beta = 0.0$ and 0.1, that in addition to straight and curved veins, PEM performs better than PCFs in a vein which moves from being straight to curved.

For the sinusoidal channel of the same geometry of fig. 5.3, which consists of two straight channel sections separated by a sinusoidal section described by eq. (5.1), increasing the amplitude of the sinusoidal region y_0 (and slip length β) causes more of the plug region to become yielded, this increasing the quantity A_{rel}.

For both slip lengths $\beta = 0$ and 0.1, a foam such as PEM with larger B retains more of its relative plug area A_{rel} in comparison to the PCFs, thus indicating that PCFs are more susceptible to yielding in tortuous veins whereas PEM retains more of its plug region for each non-zero amplitude y_0. The existence of wall-slip is counterproductive for the use of foam in sclerotherapy and the negative effects i.e. reducing the plug areas, are amplified for foams with smaller yield stresses such as PCFs.

6.5 Concluding remarks

We have described a way to characterise the properties of foams used for sclerotherapy and to evaluate their effectiveness by introducing a framework to predict their yield stress and flow profiles. We compared the effectiveness of a PEM and PCFs by considering the Sauter mean of their bubble size distributions [Carugo et al., 2016].

The Sauter mean R_{32} is more greatly affected than the usual mean by the presence of large bubbles, which in turn affects a foam's yield stress. Given R_{32}, we estimate the value of the yield stress τ_0 for different foam liquid fractions ϕ_l. Our approximation of τ_0 allows us to estimate the shape of the displacement front of foam within a straight vein for a given flow rate and vein diameter. We use the value of τ_0 to define the Bingham number B (eq. (6.2)) as a dimensionless measure of the ability of a foam to displace blood.

Our calculations suggest that an optimal foam should have yield stress close to $\tau_0 = 3$ Pa (eq. (1.4)) and hence sclerotherapy treatments should aim for a Bingham number $B \approx 4.48$ for a vein of diameter $D \approx 5$mm, in addition to a narrow bubble size distribution. In larger veins, slightly larger bubbles will result in this same value of B and *vice versa*.

The steepness of the curves in figure 6.3 shows that such a value of B may be difficult to obtain. A foam with high liquid fraction, for example 0.25, typical of PCFs, would need tiny bubbles (of order tens of microns) to be effective at displacing blood. Such bubble sizes are not possible to obtain with e.g. the Tessari method [Tessari, 2000]. On the other hand, a dry (low liquid fraction) foam, such as could be obtained by leaving a foam to drain before injection, would have bubbles that are approaching the width of the vein, and would therefore be ineffective.

We considered the implications of the numerical simulations results of tortuous channel geometries in chaps. 4.7 and 5 for each of the foams used in sclerotherapy. Increasing the channel curvature (and amplitude) causes "additional" yielding of the plug region which decreases the effectiveness of foam in sclerotherapy. The results of the 2D simulations suggest that transitioning length for the plug region to reform is smaller for PEM in comparison to both Tessari and DSS foams, allowing it to regain its plug region over less distance. The existence of wall slip between the vein wall and foam increases the amount of yielding, measured by A_{rel} although not significantly, causing an adverse effect on the foams performance in sclerotherapy. This adverse effect decreases for foams with larger Bingham numbers B such as PEM.

Finally, we note that the affected vein should be kept as straight as possible during treatment: vein curvature induces additional stresses within the foam, leading to a greater degree of yielding and therefore reducing the size of the plug [Roberts and Cox, 2020]. In turn, this leads to a less effective displacement of blood and a greater chance of polidocanol deactivation due to mixing.

7 Conclusions

In order to investigate the effectiveness of foam in sclerotherapy, we consider the flow of foam, characterised as a yield stress fluid, through two-dimensional vein-like geometries, presenting both the analytical and numerical results for a pressure-driven Bingham fluid flowing through straight, curved and sinusoidal channels. This allow us to relate the results for an effective foam for sclerotherapy treatment. In chap. 1, we assume that the flow of a foam in a vein is slow and steady, allowing us to use the Stokes equations. We also assume that the apparent viscosity of the foams' plug region was large (at least 5 times the value of the liquid sclerocent [Martinsson and Sichen, 2016]) such that the interface between the foam and blood was stable, allowing us to consider the flow of a Bingham fluid. We link the effectiveness of foam in sclerotherapy to the size of the Bingham number as the size of the fluids plug region is proportional to B (see §6.3). The method behind the numerical simulations was outlined in chap. 2, where the Stokes equations were solved in weak form along with the regularised Papanstasiou model [Papanastasiou, 1987].

In chapters 3 and 4 we derived the analytical velocity profiles for a pressure-driven Bingham fluid in both straight and curved channel geometries with a Navier slip boundary condition. These profiles were the basis for the validation of the numerical methods. The flow profile in the straight channel case is well-known and has been previously given by Bird et al. [1983] for $\beta = 0$ (the no-slip case) and Ferrás et al. [2012] for non-zero slip length β. To the best of our knowledge, the analytical profile for the annulus case is novel - see Roberts and Cox [2020] for $\beta = 0$ and the Navier slip case in chap. 4.3.

For a pressure-driven Bingham fluid in a curved channel, the analysis shows that the performance of foam in sclerotherapy, which is quantified by measuring the size of the plug area, becomes poorer as the curvature κ of the channel increases, particularly with increasing slip length β. This is due to the narrowing of the plug due to the channel curvature, which causes the stress to become larger at the inner wall of the channel, where the pressure gradient is largest. The analysis allows us to determine the pressure-gradient above which fluid flows in a curved channel, and we derived the corresponding critical Bingham number at which the flow becomes stationary, which is written in terms of channel curvature κ (eq. (4.27)).

Wall-slip in a curved channel allows the maximum of stress (magnitude) and velocity at the channel walls to occur either at the inner wall ($r = \frac{1}{\kappa}$) or the outer wall ($r = \frac{1}{\kappa} + 1$), depending on the choices of Bingham number B, channel curvature κ and slip length β.

Having validated the numerical methods, we simulated the flow of a Bingham fluid in two complex geometries: a straight channel connected to an annular region (§4.7) and a sinusoidal channel (§5). For the former, the "transition" length for the Bingham fluid to settle to the predicted flow profiles following the change in channel curvature κ increases with decreasing Bingham number B and increasing annulus curvature κ.

For the sinusoidal channel, we varied the amplitude of the sinusoidal walls y_0 to measure the deviation of the channel from the straight channel case and measured the area of unyielded fluid. Increasing the amplitude y_0 causes the relative plug area A_{rel}, which measures the amount of the plug area lost due to increasing the channel curvature, to increase, suggesting that any vein tortuosity decreases the effectiveness of foam in sclerotherapy significantly. This suggests that for the purpose of sclerotherapy we require a foam with a large yield-stress and as straight a vein as possible during treatment.

A foam with large yield-stress (and thus a large Bingham number) will provide the most effective displacement of blood in straight, curved and sinusoidal channels due to the large plug region, but if the yield-stress is too large the foam could be too difficult to push out of the syringe. A foam with a large yield-stress will take the smallest length of vein to reform a wide plug region beyond a bend in the vein and less of the plug area becomes yielded due to channel curvature/amplitude in comparison to foams with a smaller yield-stress.

Within a sinusoidal vein, the maximum velocity and flow rate both increase with increasing amplitude y_0. One reason for the increasing flow rate is that the channel becomes narrower at larger amplitudes y_0, causing the fluid velocity to increase and the plug region to shrink.

In any industrial application where it would be beneficial to (nearly) completely yield a Bingham fluid could do so by using a sinusoidal pipe network. Another advantage of this would be that the flow rate of the fluid increases within the sinusoidal region without any large changes to the implemented pressure difference. Although, one should be careful of the pipe geometry as making the length of the sinusoidal region too short could lead to the formation of dead regions of fluid, which could lead to pockets of fluid remaining in the pipe.

Additionally for industrial applications, integrating the stress over a given length of curved pipe would allow one to examine the force that the fluid exerts on the pipe wall and approximate the amount of wear on a section of pipe. Producing a pipe which allows the fluid to slip would increase the velocity of the fluid and decrease the wear on the pipe. If the slip length is small, the wear is expected to be greatest on the inner wall of the curved pipe.

In chapter 6, the yield stress of foams used in sclerotherapy were calculated using the empirical estimate by Princen and Kiss [1989], using the values of the foam liquid fraction ϕ_l, average bubble size R and surface tension γ. We estimate the yield stress for three different foams used in sclerotherapy (polidocanol endovenous microfoam (PEM), Tessari and DSS foam) using the bubble size distributions from Carugo et al. [2016]. To derive the estimate for the yield stress, we used a volume-weighted mean R_{32}, to find the average of the bubble radii. Increases in R_{32} lead to a smaller estimated yield-stress. PEM has the largest yield stress of all three foams due to its small average bubble size R_{32}, thus it has the largest plug region.

Recall that the size of the plug region for a flow of foam through a cylindrical vein not only depends on the foam properties (i.e the Bingham number), but also on the characteristics of the flow (i.e. the pressure gradient). So in addition to a large yield-stress τ_0 (eq. (1.4)), the effectiveness of foam in sclerotherapy is enhanced if the injection of foam is as slow as possible i.e. reducing the driving pressure-gradient which increases the size of the plug region.

7.1 Future work

We have developed models and simulation of yield-stress fluids. We have focused on four different two-dimensional channel geometries and consider the pressure-driven flow of a Bingham fluid with a Navier slip condition.

We made several assumptions to simplify the problem of modelling sclerotherapy. We neglect any elasticity of the vein walls, which would allow the vein to contract and expand in response to the injected foam. The expansion of the vein could influence the performance of foam in sclerotherapy, with wider diameters leading to reduced flow velocities and thus a larger plug width. Elasticity of the vein wall has been extensively examined for the purposes of modelling [Pedrizzetti et al., 2002; Sokolis, 2013]. Li [2018] suggests that the vein walls remain fixed for stresses under a certain “threshold” and above it would expand. By coupling the foam (modelled by a Bingham fluid) and the structure (modelled by parametrised curves), as well as assuring a continuity of stress at the vein walls [Janela et al., 2010], we could in practice adapt the boundary of the mesh between iterations to incorporate the effects of vein elasticity. This can be done in FreeFem++ [Hecht, 2020a] for both 2D and 3D meshes, using the “movemesh” function.

More tortuous vein geometries could lead to regions of vein which are left untreated by the sclerosant within the foam, allowing the vein to recannalise after treatment i.e. not successfully destroying the veins endothelial lining and after which the flow within the vein is restored. This was suggested as a reason of the poor performance of a (Tessari) foam in sclerotherapy [Rasmussen et al., 2011; Van der Velden et al., 2015].

We also assumed (in chap. 1.4.4) that it was sufficient to only consider a single flow of Bingham fluid rather than a displacement of a Newtonian fluid (i.e. blood) by a Bingham fluid (foam). The reasoning behind this simplification was that the interface between foam and blood is expected to be stable, as the effective viscosity of the foam is much larger than the effective viscosity of the blood. A stable interface between foam and blood would provide an effective displacement of blood, with the effectiveness of the displacement based on the size of the unyielded plug region (hence the Bingham number) of the displacing fluid [Obernauer et al., 2000], with mixing only occurring close to the wall in the yielded regions (which experience large stresses).

In a damaged vein, the width of the vein can vary from one turn to another, which could enhance opportunities for both foam and blood to mix, thus deactivating the sclerocent (polidocanol). If that is the case, future work could explore how the tortuosity of the vein and apparent viscosity of the foam (and blood) affects the displacement. Extending our results to two-dimensional (or even 3D) flows of a Newtonian fluid being displaced by a Bingham fluid would allow us to suggest more effective sclerotherapy treatments.

Why would sclerotherapy need to cover more than one section of vein between valves at a time? It is unclear how many valves need to become dysfunctional before the vein becomes varicose but it could be several as the vein becomes tortuous and warped by the unbalance of pressure causing the vein to expand. For PEM, it is recommended that 5ml (5×10^{-6}m^3) of the foam is injected in a single treatment. For a vein of diameter 5mm and a 2.5cm length of vein between the valves, the section has volume $\approx 5 \times 10^{-7}$m^3, an order of magnitude less than the foam volume, suggesting that multiple sections are treated during sclerotherapy and valves should be considered in future work.

In this thesis, we concentrated on a length of vein situated between two valves, but one should consider how the valves affect the sclerotherapy treatment, in particular, their ef-

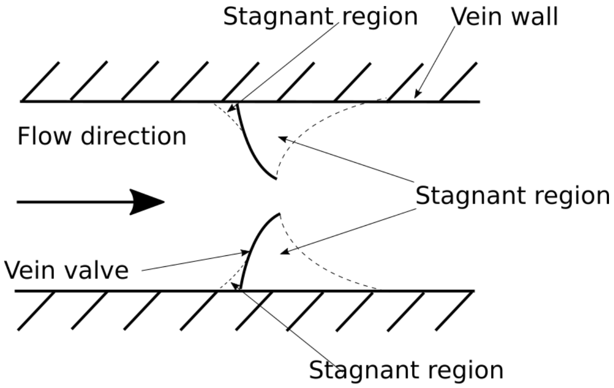

Figure 7.1: An illustration of the vein valves and their possible influence on the flow of foam in a vein. The dashed lines are sketched yield surface positions, suggesting a much larger region of plug fluid located behind the vein.

fect on the displacing capability of the foam. As the vein valves take a half-moon shape [Fernández-Colino and Jockenhoevel, 2020], the foam is funnelled past the cusps of the valve [Lurie et al., 2003]. Therefore, one would expect the foams' velocity to increase and the foam to become fully yielded at the inlet of the valve [Abdali et al., 1992]. The valves themselves could have regions of stagnant fluid which become attached to the front and back of them (defined with respect to flow direction) as suggested in fig. 7.1. As Hewitt et al. [2016] suggested for elliptical contractions, the amount of stagnant fluid on each side of the valve could depend on its inclination and on the Bingham number of the foam. We expect larger regions of stagnant fluid becoming trapped behind the valve due to its curvature and the appearance of slow moving vortices of blood trapped behind the valve Hajati et al. [2020], which for the yield-stress fluid indicate locations of stationary fluid regions (chap. 5). The stagnant region behind the valve could take a similar form to the stagnant regions seen in entry flows through abrupt expansions [Abdali et al., 1992; Mitsoulis and Huilgol, 2004]. We also expect these stagnant regions to grow with increasing Bingham number as more of the fluid becomes plugged up in the regions of low stress that appear around the valve [Denn and Bonn, 2011; Mitsoulis and Huilgol, 2004]. Would this hinder or enhance the performance of the foam in sclerotherapy? Several authors have explored flows of Bingham fluid in constricted or narrowing channels [Abdali et al., 1992; Denn and Bonn, 2011] but in the future it would be interesting to see how the existence of valves in a tortuous channel geometry affects the size of the plug regions and thus the effectiveness of foam in sclerotherapy.

By considering the foam as a collection of bubbles, not as a continuum, we could consider the effects of both drainage (i.e. changes in local liquid fraction due to gravity) and the transport of surfactant within the foam [Zaccagnino et al., 2018] on its displacing capability. The effects of drainage (due to gravity) could mean that the foams yield-stress is lower in regions where the local liquid fraction is higher. In sclerotherapy, this could lead to mixing between foam and blood in regions where the local liquid fraction is larger, leading to an ineffective treatment.

Other effects that could be incorporated into the simulation could be bubble rupture and the effects of foam polydispersity on the displacement of blood. Cantat and Delannay [2003] suggested that above a critical velocity, large bubbles within the foam move faster than the mean flow, meaning that for a polydisperse foam in sclerotherapy, larger bubbles could be moving faster than smaller bubbles in a vein. What would the implications of this be on the sclerotherapy process? Does this cause the degradation of foams' plug region as bubbles are moving at different velocities? In addition to this, could bubble rupture be induced as the flow passes the valves of the veins? Incorporating such complex systems might require the use of the software "Surface Evolver" [Brakke, 1992], used by many researchers that model foam. This would allow us to gain better understanding on how the foam dynamics effects its capability of displacing blood.

In this thesis, we also considered the effect of wall-slip on the sclerotherapy treatment. In chaps. 3-5 we set an upperbound for the slip length as $\beta = 0.1$, which is 10% of the considered channel width. For $\beta = 0.1$, we noticed that the error in the simulation data ϵ increases by 24% from the no-slip case, which implies that a non-zero slip length increases the discrepancy between the analytical profiles and numerical prediction. This suggests that implementing the Navier slip boundary condition causes larger inaccuracies in within the numerical simulation when the slip length becomes large. Karapetsas and Mitsoulis [2013] have experienced inaccuracies (and overestimations in pressure) with implementing larger slip lengths. The problem might be overcome by implementing adaptive meshes but should be addressed if we wish to explore flows of Bingham fluid with larger slip lengths.

For a slip length $\beta = 10$, does the Reynolds number Re become large enough that the Stokes equations are no longer valid approximations for the flow? The analytical results (eq. (3.20)) show that the non-dimensionalised maximum velocity a 2D straight channel is of order $\frac{1}{2}\beta(1-B)$, when β is large. If $\beta = 10$, we can approximate the dimensional value of the maximum velocity U_{max} (using eq. (2.4)) for a foam with apparent viscosity $\mu = 1$Pa s, vein diameter (channel width) $h = 5$mm and is driven by pressure gradient $G = 8.7 \times 10^3$Pa/m, then the maximum velocity $U_{max} \approx 2.7$cm/s. By assuming that the foam has a density of $\rho = 125$ kg/m^3 [McDaniel and Holt, 2000] (assuming a liquid fraction $\phi_l = 0.125$), then the Reynolds number Re (eq. (2.3)) is equal to 0.052. This suggests that for slip lengths of $\beta = 10$ or smaller, the Stokes equations remain valid and inertia can be neglected.

Since the simulation becomes less accurate when implementing wall-slip, should we consider other more accurate numerical methods for future work? Although the simple, effective and fast nature of the regularised viscosity models in finite element method simulations, Muravleva et al. [2010a] suggest that the Augmented Lagrangian Method (ALM) yields superior results. The ALM is better at capturing the shape of the plug regions [Huilgol and You, 2005; Saramito and Roquet, 2001], which is essential for determining the quantity A_{rel} (eq. (5.4)), our measure of the displacing capability of the foam. This should be the main aim for future improvements to the finite element simulations described here, as to develop a simulation using the (adaptive [Saramito and Roquet, 2001]) ALM would allow us to compare the results for both regularised and Augmented Lagrangian Methods and quantify any differences in the predicted plug areas.

The ALM is more computationally expensive (ten times the time required for regularised models [Dimakopoulos et al., 2013]). The regularised models provide a good idea of the size (and location) of the plug regions in different vein-like geometries (even if they are slightly overestimated quantities as Huilgol and You [2005] suggested).

We would like to develop simulations of more complex tortuous three-dimensional vein geometries, similar to geometries seen in Bottaro et al. [2019], for example. This would allow us to consider the effect of the foam's yield-stress on its displacing capabilities in more "realistic" vein models. The results in this thesis imply that the greater the tortuosity of the vein, the poorer the treatment, particularly for PCFs. We could also trace the regions of the vein walls which are not in contact with foam, i.e. regions that remain untreated, to gain some understanding of how the vein fails to collapse after sclerotherapy and how to prevent unsuccessful treatments. Two-dimensional experiments could be compared with the results in this thesis to further validate our findings. For example for a flow of foam in 2D sinusoidal channel, one could measure the velocity and the locations of T1 transformations, which could indicate the location of yielded regions of flow.

The work presented in this thesis could be extend into three-dimensional finite element simulations. As expected, the numerical simulations in 3D will be much slower than the 2D simulations presented in this thesis. Franci and Zhang [2018] suggest that differences between the yield surface positions for 2D and 3D simulations of Bingham fluids increase for larger yield stresses τ_0, with 3D simulations producing the more accurate predictions [Wang et al., 2016]. Irrespective of this, the 2D simulation results provide important insights into the flow of foam in tortuous veins, such as the flow profiles and size of the plug regions, which we can relate to the sclerotherapy process.

Developing 3D analytical solutions for a Bingham fluid in a cylindrical annulus would be beneficial in order to validate the numerical simulations in 3D, much like the 2D case in chapter 4. One could use the approach of both Norouzi et al. [2015] (although it has some errors in the derivation) and Norouzi et al. [2018], who developed series solutions for the flow of a Bingham fluid in a curved duct and an Oldroyd-B fluid (which is described by the Oldroyd-B constitutive model [Oldroyd, 1950] used to describe viscoelastic fluids) in a curved pipe, respectively, to develop the analytical velocity profile in 3D. The added complexity of the derivation comes from the non-linearity of the Bingham constitutive equations for non-unidirectional flows.

Lastly, one should ask whether the Bingham model that we used to model a foam in sclerotherapy is a good model for modelling foam? The Bingham model was chosen due to it's simplicity for modelling purposes as it has the simplest constitutive equation for a yield-stress fluid. A foam has a very complex rheology and their maybe other models more suited to approximate foam flow. Sheng [2013] states that "Owing to the complexity of foam rheology, there are different opinions regarding whether foams are Newtonian or non-Newtonian, shear thinning or shear-thickening", making the choice of a specific model a difficult one. The Hershel-Bulkley model, discussed in chap. 2, has been used by many to model foam [Gao et al., 2016; Saramito, 2009] and is suggested to be a more realistic model in comparison to the Bingham model. Therefore, future work could be to reproduce some of the results in chaps. 3-6 by using the Hershel-Bulkley model, which could allow us to provide a more accurate representation of foam flow in sclerotherapy.

A Appendix

A.1 Derivation of the yield surface position using the Lambert W Function

The Lambert-W function [Corless et al., 1996] is used to solve various equations involving logarithms (and exponentials). The applications of the function range from statistical mechanics, engineering of thin films and quantum chemistry [Hayes, 2005]. It was further used in the research of the motion of projectiles under air resistance [Packel and Yuen, 2004]. The anonymous reviewer from the curved channel paper suggested that the yield surfaces can be found analytically in terms of this function. Below, we outline the derivation of the yield surfaces root in a curved channel. Recall that we have an equation of the form (eq. (4.22)):

$$A_1 \ln(r_i) + A_2 r_i^2 + A_3 = 0$$

Divide both sides by A_2 (and relabel $\tilde{A}_1 = A_1/A_2$ and $\tilde{A}_3 = A_3/A_2$ to simplify notation):

$$\tilde{A}_1 \ln(r_i) + r_i^2 + \tilde{A}_3 = 0$$

We rearrange to get:

$$\ln(r_i^2) = -2(r_i^2 + \tilde{A}_3)/\tilde{A}_1$$

If we take a natural exponential of each side we get:

$$r_i^2 = \exp\left(-2(r_i^2 + \tilde{A}_3)/\tilde{A}_1\right) = \exp\left(-2r_i^2/\tilde{A}_1\right)\exp\left(-2\tilde{A}_3/\tilde{A}_1\right)$$

By multiplying each side by $2/\tilde{A}_1$ we have:

$$\underbrace{2r_i^2/\tilde{A}_1}_{\text{w}}\underbrace{\exp\left(2r_i^2/\tilde{A}_1\right)}_{\text{exp(w)}} = \underbrace{2\exp\left(-2\tilde{A}_3/\tilde{A}_1\right)/\tilde{A}_1}_{\text{z}}$$

Therefore we have an equation of the form $w\exp(w) = z$. By letting $w = W(z)$, the equation becomes

$$W(z)\exp(W(z)) = z \implies w = W(w\exp(w)).$$

This allows us to substitute $w = 2r_i^2/\tilde{A}_1$ back into the equation with $w = W(z)$

$$2r_i^2/\tilde{A}_1 = W\left(2\exp\left(-2\tilde{A}_3/\tilde{A}_1\right)/\tilde{A}_1\right).$$

Finally rearranging the above allows us to derive an expression for the yield surface in terms of the Lambert W Function:

$$r_i = \sqrt{\tilde{A}_1 W\left(-1, 2\exp\left(-2\tilde{A}_3/\tilde{A}_1\right)/\tilde{A}_1\right)/2} \tag{A.1}$$

We choose the $k = -1$ branch of the Lambert W Function as the value of z is negative. A factor of a half can be absorbed into the constants as done in chap. 4. One finds the outer yield surface using the relationship seen in eq. (4.12). We use “Python” [Oliphant, 2007] to find the values of both yield surfaces r_i and r_o, which is easily done by importing the Lambert W function from “*scipy.special*” [Scipy.org, 2020]. Alternatively, one could use “*fsolve*” (a root finder) to find the roots of eq. (4.21).

A.2 The minimum distance between the top and bottom wall in a sinusoidal channel

For a sinusoidal channel, we claim that the minimum (perpendicular) distance from the bottom and top wall becomes smaller than the channel width h as the amplitude y_0 and channel length h/L_s is increased. The walls of the channel is described by a sinusoidal function of the form $W(x)$ in eq. (5.1). The walls are separated by a constant vertical distance of h i.e. the upper wall is described by $y = W(x) + h$.

By focusing on the non-negative values of x between 0 and $L_s/2$, we first of all derive the slope of the sinusoidal wall by finding the derivative of $W(x)$:

$$W'(x) = \frac{\pi y_0}{L_s} \sin\left(\frac{2\pi}{L_s}\left(x - \frac{L_s}{2}\right)\right). \tag{A.2}$$

The slope perpendicular to the sinusoidal curve is equal to the negative of the reciprocal of the derivative of $W'(x)$:

$$m = -\frac{1}{W'(x)} = -\frac{L_s}{\pi y_0 \sin\left(\frac{2\pi}{L_s}\left(x - \frac{L_s}{2}\right)\right)}$$

The equation of a line perpendicular to the curve for an arbitrary point on the bottom wall (x_b, y_b). Than we have:

$$y - y_b = m(x - x_b). \tag{A.3}$$

We desire to find the minimum perpendicular distance from (x_b, y_b) to the top wall at point (x_t, y_t) for $|x_b| \leq L_s/2$. To find the coordinates (x_t, y_t) on the top wall, we find the roots of eq. (A.3). Both y_t and y_b can be written in terms of x_t, x_b and $W(x)$, therefore eq. (A.3) is written in the form:

$$\frac{1}{2}y_0\left(1 - \cos\left(\frac{2\pi}{L_s}\left(x_t - \frac{L_s}{2}\right)\right)\right) + h = \frac{1}{2}y_0\left(1 - \cos\left(\frac{2\pi}{L_s}\left(x_b - \frac{L_s}{2}\right)\right)\right) + m\left(x_t - x_b\right). \tag{A.4}$$

Here we fix a channel width of $h = 1$. For each x_b on the bottom wall between 0 and $L_s/2$, we find the root of eq. (A.4) to identify the position (x_t, y_t) on the top wall that is perpendicular the bottom wall at (x_b, y_b). We therefore calculate the distance between each coordinates (x, y) and (x_b, y_b) for each x_b in fig. A.1 using:

$$d(x_b) = \sqrt{(y_t - y_b)^2 + (x_t - x_b)^2}.$$

Using the formulae here allows us to calculate the minimum distance between each wall for each amplitude y_0 and channel length h/L_s as identified in fig. 5.6. We see from fig. A.1 that increasing both amplitude y_0 and channel length $h/L_s = 0.5$ decreases the minimum perpendicular distance between the channel walls. We identify that for the largest

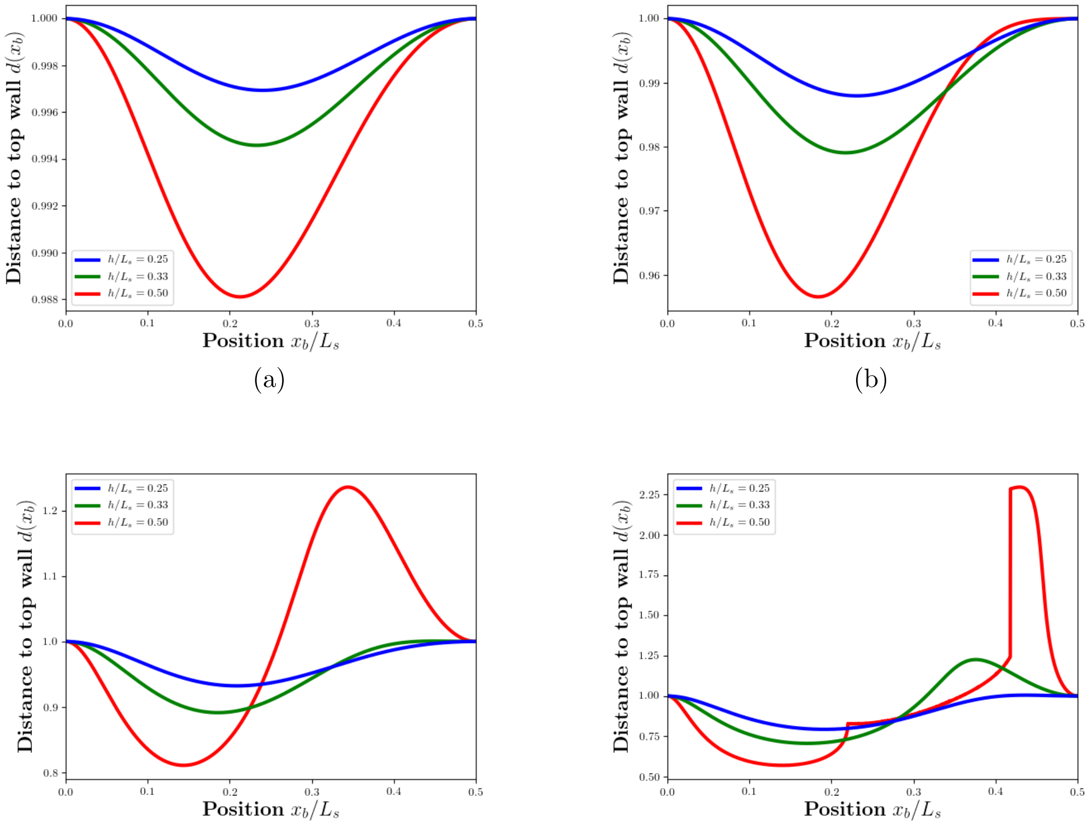

(a) (b)

(c) (d)

Figure A.1: The perpendicular distance between the top and bottom walls $d(x_b)$, where (x_b, y_b) are points on the bottom wall and (x_t, y_t) are identified as the position on the top wall perpendicular to the bottom wall for different amplitudes: (a) $y_0 = 0.1$, (b) $y_0 = 0.2$, (c) $y_0 = 0.5$ and (d) $y_0 = 1.0$.

considered amplitude $y_0 = 1$ and channel length $h/L_s = 0.5$, the minimum distance becomes $d_{min} \approx 0.57$.

For an amplitude of $y_0 = 0.2$ (fig. A.1(b)) and $h/L_s = 0.5$, we can approximate the average channel width across the sinusoidal region is around 0.98. Increasing the amplitude further causes the perpendicular distance between the top and bottom wall to become larger than one for larger values of x_b, depending on channel length h/L_s and amplitude y_0. For these values of x_b, the point perpendicular to the bottom wall falls outside the the sinusoidal region i.e. $x_t > L_s/2$ and for the large amplitudes, this causes difficulty in finding the point (x_t, y_t). The result of this causes the unfortunate red curve seen in fig. A.1(d).

The results in fig. A.2 show that by restricting the position of x_t to be within the sinusoidal region i.e. $x_t \leq L_s/2$ implies that we can only find a point on the top wall (x_t, y_t) perpendicular to the bottom wall (x_b, y_b) for x_b/L_s between 0 and 0.2 (for $y_0 = 1$ and $h/L_s = 0.5$).

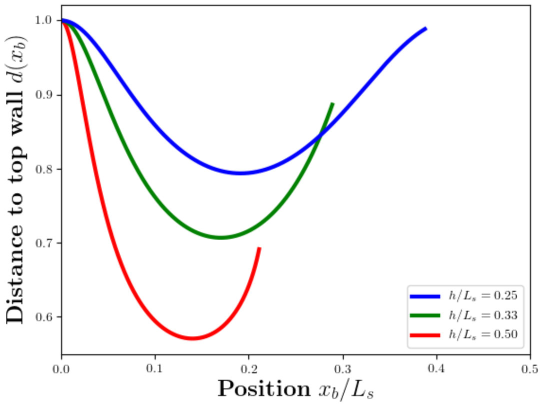

Figure A.2: For an amplitude of $y_0 = 1$, the perpendicular distance between the top and bottom walls $d(x_b)$ as a function of x_b as shown in fig. A.1(d). We now restrict the values of x_b such that the point x_t on the top wall perpendicular to the bottom wall is within the sinusoidal region i.e. $|x_t| \leq L_s/2$.

For purposes of the results in chap. 5, we focus only on the minimum distance between the top and bottom wall, which is found for x_b/L_s between 0.1 and 0.2 and do not consider values of x_t outside the sinusoidal region.

Bibliography

Abdali, S., Mitsoulis, E., and Markatos, N. (1992). Entry and exit flows of Bingham fluids. *J. Rheol.*, 36(2):389–407.

Ak, M. and Gunasekaran, S. (2000). Simulation of lubricated squeezing flow of a Herschel-Bulkley fluid under constant force. *Appl. Rheol.*, 10(6):274–279.

Aktas, S., Kalyon, D., Marín-Santibáñez, B., and Pérez-González, J. (2014). Shear viscosity and wall slip behavior of a Viscoplastic hydrogel. *J. Rheol.*, 58(2):513–535.

Almeida, J. and Raines, J. (2006). Radiofrequency ablation and laser ablation in the treatment of varicose veins. *Ann. Vasc. Surg.*, 20(4):547–552.

Almeida, J. and Raines, J. (2008). Laser ablation of cutaneous leg veins. *Persp. Vasc. Surg. Endovasc. Therapy*, 20(4):358–366.

Alos, J., Carreno, P., Lopez, J., Estadella, B., Serra-Prat, M., and Marinel-Lo, J. (2006). Efficacy and safety of sclerotherapy using polidocanol foam: a controlled clinical trial. *Eur. J. Vasc. Endovasc. Surg.*, 31(1):101–107.

Apoung Kamga, J. (2020). Stokes Equations - Implement in FreeFem++. `https://www.imo.universite-paris-saclay.fr/~apoung/mywepage/stage/2015/ExorecapStokesEn.pdf`. [Online; accessed 11-August-2020].

Ardakani, H., Mitsoulis, E., and Hatzikiriakos, S. (2011). Thixotropic flow of toothpaste through extrusion dies. *J. non-Newt. Fl. Mech.*, 166(21-22):1262–1271.

Arkilic, E., Schmidt, M., and Breuer, K. (1997). Gaseous slip flow in long microchannels. *J. of Microelectromech. S.*, 6(2):167–178.

Badeer, H. (2001). Hemodynamics for medical students. *Adv. Physio. Edu.*, 25(1):44–52.

Bai, T., Jiang, W., Chen, Y., Yan, F., Xu, Z., and Fan, Y. (2018). Effect of multiple factors on foam stability in foam sclerotherapy. *Sci. Rep.*, 8:1–7.

Baker, M. and Wayland, H. (1974). On-line volume flow rate and velocity profile measurement for blood in microvessels. *Microvasc. Res.*, 7(1):131–143.

Bakhtiyarov, S. and Siginer, D. (1996). Fluid displacement in a horizontal tube. *J. non-Newt. Fl. Mech.*, 65(1):1–15.

Balan, H., Balhoff, M., Nguyen, Q., and Rossen, W. (2011). Network modeling of gas trapping and mobility in foam enhanced oil recovery. *Energy & fuels*, 25(9):3974–3987.

Balmforth, N. and Craster, R. (1999). A consistent thin-layer theory for Bingham plastics. *J. non-Newt. Fl. Mech.*, 84(1):65–81.

Barnes, H. (1995). A review of the slip (wall depletion) of polymer solutions, emulsions and particle suspensions in Viscometers: its cause, character, and cure. *J. non-Newt. Fl. Mech.*, 56(3):221–251.

Barnes, H., Hutton, J., and Walters, K. (1989). *An introduction to Rheology*, volume 3. Elsevier.

Barrett, J., Allen, B., Ockelford, A., and Goldman, M. (2004). Microfoam ultrasound-guided sclerotherapy of varicose veins in 100 legs. *Dermatol. Surg.*, 30(1):6–12.

Bartholomew, J., King, T., Sahgal, A., and Vidimos, A. (2005). Varicose veins: Newer, better treatments available. *Cleve. Clin. J. Med.*, 72(4):312–328.

Batchelor, G. (2000). *An Introduction to Fluid Dynamics.* Cambridge University press.

Beale, R. and Gough, M. (2005). Treatment options for primary varicose veins—a review. *Eur. J. Vasc. Endovasc. Surg.*, 30(1):83–95.

Beckitt, T., Elstone, A., and Ashley, S. (2011). Air versus physiological gas for ultrasound guided foam sclerotherapy treatment of varicose veins. *Eur. J. Vasc. Endovasc. Surg.*, 42:115–119.

Bennett, L. (1967). Red cell slip at a wail in vitro. *Sci.*, 155(3769):1554–1556.

Bercovier, M. (1980). Approximation of Bingham's variational inequalities by a penalty function for the incompressibility constraint. *Numer. Funct. Anal. and Opt.*, 2(5):361–373.

Bercovier, M. and Engelman, M. (1979). A Finite Element for the numerical solution of Viscous incompressible flows. *J. Comput. Phys.*, 30(2):181–201.

Bercovier, M. and Engelman, M. (1980). A finite-element method for incompressible non-Newtonian flows. *J. Comput. Phys.*, 36(3):313–326.

Berta, M., Wiklund, J., Kotzé, R., and Stading, M. (2016). Correlation between in-line measurements of tomato ketchup shear viscosity and extensional viscosity. *J. Food Eng.*, 173:8–14.

Beverly, C. and Tanner, R. (1989). Numerical analysis of extrudate swell in viscoelastic materials with yield stress. *J. Rheol.*, 33(6):989–1009.

Biemans, A., Kockaert, M., Akkersdijk, G., van den Bos, R., de Maeseneer, M., Cuypers, P., Stijnen, T., Neumann, M., and Nijsten, T. (2013). Comparing endovenous laser ablation, foam sclerotherapy, and conventional surgery for great saphenous varicose veins. *J. Vasc. Surg.*, 58(3):727–734.

Bingham, E. (1922). *Fluidity and plasticity*, volume 2. McGraw-Hill, New York.

Bingham, E. and Roepke, R. (1944). The Rheology of the blood. III. *J. Gen. Physiol.*, 28(1):79–93.

Bird, R. and Carreau, P. (1968). A nonlinear Viscoelastic model for polymer solutions and melts—i. *Chem. Eng. Sci.*, 23(5):427–434.

Bird, R., Dai, G., and Yarusso, B. (1983). The rheology and flow of viscoplastic materials. *Rev. Chem. Eng.*, 1:1–70.

Bizzarri, G., Di Federico, V., and Cintoli, S. (2002). Stokes flow between sinusoidal walls. *Trans. Eng. Sci.*, 36.

Blackery, J. and Mitsoulis, E. (1997). Creeping motion of a sphere in tubes filled with a Bingham plastic material. *J. non-Newt. Fl. Mech.*, 70:59–77.

Bone, C. (1999). Endoluminal treatment of varicose veins with a diode laser. A preliminary study. *Rev. Vasc. Pathol.*, pages 35–46.

BostonScientific.com (2020a). Peripheral vasculature - average vessel diameter. `https://www.bostonscientific.com/content/dam/bostonscientific/pi/portfolio-group/embolization/Vessel%20Diameter%20Wall%20Chart%20(PI-324504-AA).pdf`. [Online; accessed 04-August-2020].

BostonScientific.com (2020b). Varithena - Clinical trials. `https://www.varithena.com/en-us-hcp/about-varithena/efficacy/clinical-trials.html`. [Online; accessed 06-August-2020].

BostonScientific.com (2020c). Varithena - How treatment works. `https://www.varithena.com/en-us/treatment/how-treatement-works.html`. [Online; accessed 06-August-2020].

Bottaro, E., Paterson, J., Zhang, X., Hill, M., Patel, V., Jones, S., Lewis, A., Millar, T., and Carugo, D. (2019). Physical Vein Models to quantify the flow performance of sclerosing foams. *Front. Bioeng. Biotech.*, 7:109.

Bradbury, A., Bate, G., Pang, K., Darvall, K., and Adam, D. (2010). Ultrasound-guided foam sclerotherapy is a safe and clinically effective treatment for superficial venous reflux. *J. Vasc. Surg.*, 52(4):939–945.

Brakke, K. (1992). The surface evolver. *Exp. Math.*, 1(2):141–165.

British Vein Institute (2021). Foam Sclerotherapy - BVI. `https://www.bvi.uk.com/treatments/foam-sclerotherapy/`. [Online; accessed 31-March-2021].

Brunn, P. (1975). The velocity slip of polar fluids. *Rheol. Acta*, 14(12):1039–1054.

Brunn, P. and Abu-Jdayil, B. (2007). Axial annular flow of plastic fluids: Dead zones and plug-free flow. *Rheol. acta*, 46(4):449–454.

Burgos, G., Alexandrou, A., and Entov, V. (1999). On the determination of yield surfaces in Herschel–Bulkley fluids. *J. Rheol.*, 43(3):463–483.

Burns, J. and Parkes, T. (1967). Peristaltic motion. *J. Fluid Mech.*, 29(4):731–743.

Bush, R., Derrick, M., and Manjoney, D. (2008). Major neurological events following foam sclerotherapy. *Phlebology*, 23(4):189–192.

Buxton, G. and Clarke, N. (2006). Computational phlebology: the simulation of a vein valve. *J. Bio. Phys.*, 32(6):507–521.

Caggiati, A. (2013). The venous valves of the lower limbs. *Phlebolymphology*, 20(2):87–95.

Calvert, J. and Nezhati, K. (1987). Bubble size effects in foams. *Int. J. Heat Fluid Fl.*, 8(2):102–106.

Cantat, I., Cohen-Addad, S., Elias, F.and Graner, F., Höhler, R., Pitois, O., Rouyer, F., and Saint-Jalmes, A. (2013). *Foams: structure and dynamics*. OUP Oxford.

Cantat, I. and Delannay, R. (2003). Dynamical transition induced by large bubbles in two-dimensional foam flows. *Phys. Rev. E*, 67(3):031501.

Carugo, D., Ankrett, D., O'Byrne, V., Wright, D., Lewis, A., Hill, M., and Zhang, X. (2015). The role of clinically-relevant parameters on the cohesiveness of sclerosing foams in a biomimetic vein model. *J. Mater. Sci.: Mater. Med.*, 26(11):258.

Carugo, D., Ankrett, D., Zhao, X., Zhang, X., Hill, M., O'Byrne, V., Hoad, J., Arif, M., Wright, D., and Lewis, A. (2016). Benefits of polidocanol endovenous microfoam (Varithena®) compared with physician-compounded foams. *Phlebology*, 31(4):283–295.

Casson, N. (1959). A flow equation for the pigment oil suspension of the printing ink type. *Rheol. Disperse Syst.*, pages 84–102.

Chaturani, P. and Samy, R. (1986). Pulsatile flow of Casson's fluid through stenosed arteries with applications to blood flow. *Biorheol.*, 23(5):499–511.

Chatzimina, M., Georgiou, G., Argyropaidas, I., Mitsoulis, E., and Huilgol, R. (2005). Cessation of Couette and Poiseuille flows of a Bingham plastic and finite stopping times. *J. non-Newt. Fl. Mech.*, 129(3):117–127.

Chen, W., Zhang, R., and Koplik, J. (2014). Velocity slip on curved surfaces. *Phys. Rev. E*, 89(2):023005.

Chen, Y. and Zhu, K. (2008). Couette–Poiseuille flow of Bingham fluids between two porous parallel plates with slip conditions. *J. non-Newt. Fl. Mech.*, 153(1):1–11.

Chow, K. and Mak, C. (2006). A simple model for the two dimensional blood flow in the collapse of veins. *J. Math. Bio.*, 52(6):733–744.

Christian, G. and Fryer, P. (2006). The effect of pulsing cleaning chemicals on the cleaning of whey protein deposits. *Food Bioprod. Process.*, 84(4):320–328.

Chu, W. (1996). Slip flow over rough wavy wall. *J. Appl. Math. Mech.*, 76(6):363–364.

Chu, W. (1999a). Flow in a microtube with corrugated walls. *Mech. Res. Commun.*, 26(4):457–462.

Chu, Z. (1999b). Flow in an annulus with corrugated walls. *Mech. Res. Commun.*, 26(2):167–170.

Chu, Z. (2000). Slip flow in an annulus with corrugated walls. *J. Phys. D Appl. Phys.*, 33(6):627.

Clarke, H., Smith, S., Vasdekis, S., Hobbs, J., and Nicolaides, A. (1989). Role of venous elasticity in the development of varicose veins. *British J. Surg.*, 76(6):577–580.

Cohen-Addad, S., Hoballah, H., and Höhler, R. (1998). Viscoelastic response of a coarsening foam. *Phys. Rev. E*, 57(6):6897.

Cohen-Addad, S., Höhler, R., and Pitois, O. (2013). Flow in foams and flowing foams. *Ann. Rev. Fluid Mech.*, 45:241–267.

Cole, P., Asteriadou, K., Robbins, P., Owen, E., Montague, G., and Fryer, P. (2010). Comparison of cleaning of toothpaste from surfaces and pilot scale pipework. *Food Bioprod. Process.*, 88(4):392–400.

Coleridge Smith, P. (2009). Rigidity percolation in particle-laden foams. *Phlebologie*, 24:62–72.

Corless, R., Gonnet, G., Hare, D., Jeffrey, D., and Knuth, D. (1996). On the Lambert-W function. *Adv. Comput. Math.*, 5(1):329–359.

Cox, S., Weaire, D., and Glazier, J. (2004). The rheology of two-dimensional foams. *Rheol. acta*, 43(5):442–448.

Cox, S. and Whittick, E. (2006). Shear modulus of two-dimensional foams: The effect of area dispersity and disorder. *Eur. Phys. J. E*, 21(1):49–56.

Critchley, G., Handa, A., Maw, A., Harvey, A., Harvey, M., and Corbett, C. (1997). Complications of varicose vein surgery. *Ann. Roy. Coll. Surg.*, 79(2):105.

Damianou, Y. and Georgiou, G. (2014). Viscoplastic Poiseuille flow in a rectangular duct with wall slip. *J. non-Newt. Fl. Mech.*, 214:88–105.

Damianou, Y., Georgiou, G., and Moulitsas, I. (2013). Combined effects of compressibility and slip in flows of a Herschel–Bulkley fluid. *J. non-Newt. Fl. Mech.*, 193:89–102.

Daubert, C., Tkachuk, J., and Truong, V. (1998). Quantitative measurement of food spreadability using the vane method. *J. Texture Stud.*, 29(4):427–435.

De Gorter, J. (2020). Patient advice on foam sclerotherapy. `https://www.bassclerotherapy.com/information-on-leg-vein-treatment/patient-advice-on-foam-sclerotherapy/`. [Online; accessed 14-August-2020].

Dean, W. (1928). Fluid motion in a curved channel. *P. Roy. Soc. A-Math. Phy. Sci.*, 121(787):402–420.

Debrégeas, G., Tabuteau, H., and di Meglio, J. (2001). Deformation and flow of a two-dimensional foam under continuous shear. *Phys. Rev. Lett.*, 87:178305.

Deng, M., Li, X., Liang, H., Caswell, B., and Karniadakis, G. (2012). Simulation and modelling of slip flow over surfaces grafted with polymer brushes and glycocalyx fibres. *J. Fluid Mech.*, 711.

Denn, M. (2001). Extrusion instabilities and wall slip. *Annu. Rev. Fluid Mech.*, 33(1):265–287.

Denn, M. and Bonn, D. (2011). Issues in the flow of yield-stress liquids. *Rheol. Acta*, 50(4):307–315.

Dent, J. and Lang, T. (1983). A biviscous modified Bingham model of snow avalanche motion. *Ann. Glaciol.*, 4:42–46.

Dimakopoulos, Y., Makrigiorgos, G., Georgiou, G., and Tsamopoulos, J. (2018). The PAL (penalized augmented lagrangian) method for computing Viscoplastic flows: A new fast converging scheme. *J. non-Newt. Fl. Mech.*, 256:23–41.

Dimakopoulos, Y., Pavlidis, M., and Tsamopoulos, J. (2013). Steady bubble rise in Herschel–Bulkley fluids and comparison of predictions via the Augmented Lagrangian Method with those via the Papanastasiou model. *J. non-Newt. Fl. Mech.*, 200:34–51.

Dlugogorski, B., Kennedy, E., Schaefer, T., and Vitali, J. (2002). What properties matter in fire-fighting foams? In *Proceeding of 2nd NRIFD symposium, Tokyo*, pages 57–78.

Dollet, B., Elias, F., Quilliet, C., Raufaste, C., Aubouy, M., and Graner, F. (2005). Two-dimensional flow of foam around an obstacle: Force measurements. *Phys. Rev. E*, 71:031403.

Dragoni, M., Bonafede, M., and Boschi, E. (1986). Downslope flow models of a Bingham liquid: implications for lava flows. *J. Volcanol. Geoth. Res.*, 30(3-4):305–325.

Drenckhan, W., Hutzler, S., and Weaire, D. (2005). Foam physics: the simplest example of soft condensed matter. In *AIP Conference Proceedings*, volume 748, pages 22–28. American Institute of Physics.

Ebert, W. and Sparrow, E. M. (1965). Slip flow in rectangular and annular ducts. *J. Basic Eng.*, 87(4):1018–1024.

Eckmann, D. (2009). Polidocanol for endovenous microfoam sclerosant therapy. *Expert opinion on investigational drugs*, 18(12):1919–1927.

Eckmann, D. and Kobayashi, S. (2006). Regarding "stroke after varicose vein foam injection sclerotherapy". *J. Vasc. Surg.*, 44(1):225.

Einzel, D., Panzer, P., and Liu, M. (1990). Boundary condition for fluid flow: Curved or rough surfaces. *Phys. Rev. Lett.*, 64(19):2269.

Ellahi, R., Hayat, T., Mahomed, F., and Zeeshan, A. (2010). Exact solutions for flows of an Oldroyd 8-constant fluid with nonlinear slip conditions. *Commun. Nonlinear Sci.*, 15(2):322–330.

Ellwood, K., Georgiou, G., Papanastasiou, T., and Wilkes, J. (1990). Laminar jets of Bingham-plastic liquids. *J. Rheol.*, 34(6):787–812.

Evans, D. and Sheehan, M. (2002). Don't be fobbed off: The substance of beer foam—a review. *J. Am. Soc. Brewing Chem.*, 60(2):47–57.

Faber, J., Chilian, W., Deindl, E., van Royen, N., and Simons, M. (2014). A brief etymology of the collateral circulation. *Arterioscler. Thromb. Vasc. Biol.*, 34(9):1854–1859.

Faisal, A., Bisdom, K., Zhumabek, B., Zadeh, A., Rossen, W., et al. (2009). Injectivity and gravity segregation in WAG and SWAG enhanced oil recovery. In *SPE Annual Technical Conference and Exhibition*. Society of Petroleum Engineers.

Fall, A., Bertrand, F., Ovarlez, G., and Bonn, D. (2012). Shear thickening of cornstarch suspensions. *J. Rheol.*, 56(3):575–591.

Fan, Y., Tanner, R., and Phan-Thien, N. (2001). Fully developed Viscous and Viscoelastic flows in curved pipes. *J. Fluid Mech.*, 440:327–357.

Fang, C. and Li, Y. (2018). Fully Discrete Finite Element Methods for two-dimensional Bingham flows. *Math. Prob. Eng.*, 2018.

Farajzadeh, R., Andrianov, A., Krastev, R., Hirasaki, G., and Rossen, W. (2012). Foam-oil interaction in porous media: implications for foam assisted enhanced oil recovery. *Adv. Colloid. Interfac.*, 183:1–13.

Feitosa, K. and Durian, D. (2008). Gas and liquid transport in steady-state aqueous foam. *Euro. Phys. J. E*, 26:309–316.

Fernández-Colino, A. and Jockenhoevel, S. (2020). Advances in engineering venous valves: The pursuit of a definite solution for chronic venous disease. *Tissue Eng. Part B Rev.*

Ferrás, L., Nóbrega, J., and Pinho, F. (2012). Analytical solutions for Newtonian and inelastic non-Newtonian flows with wall slip. *J. non-Newt. Fl. Mech.*, 175:76–88.

Franci, A. and Zhang, X. (2018). 3D numerical simulation of free-surface Bingham fluids interacting with structures using the PFEM. *J. Non-Newt. Fl. Mech.*, 259:1–15.

Frigaard, I. (2019). Simple yield stress fluids. *Curr. Opin. Colloid Interface Sci.*, 43:80–93.

Frigaard, I., Howison, S., and Sobey, I. (1994). On the stability of Poiseuille flow of a Bingham fluid. *J. Fluid Mech.*, 263:133–150.

Frigaard, I. and Nouar, C. (2005). On the usage of viscosity regularisation methods for Viscoplastic fluid flow computation. *J. non-Newt. Fl. Mech.*, 127(1):1–26.

Frigaard, I., Paso, K., and de Souza Mendes, P. (2017). Bingham's model in the oil and gas industry. *Rheol. Acta*, 56(3):259–282.

Frullini, A. and Cavezzi, A. (2002). Sclerosing foam in the treatment of varicose veins and telangiectases: history and analysis of safety and complications. *Dermatol. Surg.*, 28(1):11–15.

Gabe, I., Gault, J., Ross, J., Mason, D., Mills, C., Schillingford, J., and Braunwald, E. (1969). Measurement of instantaneous blood flow velocity and pressure in conscious man with a catheter-tip velocity probe. *Circ. Res.*, 40(5):603–614.

Galanopoulos, G. and Lambidis, C. (2012). Minimally invasive treatment of varicose veins: Endovenous laser ablation (EVLA). *Int. J. Surg.*, 10(3):134–139.

Gao, H., Zhang, M., Xia, J., Song, B., and Wang, Y. (2016). Time and surfactant types dependent model of foams based on the Herschel–Bulkley model. *Colloids Surf. A: Physicochem. Eng. Asp.*, 509:203–213.

Gardiner, B., Dlugogorski, B., Jameson, G., and Chhabra, R. (1998). Yield stress of firefighting foams. In *Proc., Halon Options Technical Working Conference, Albuquerque, New Mexico*, pages 12–14.

George, H. and Qureshi, F. (2013). Newton's law of Viscosity, Newtonian and Non-Newtonian fluids. *Ency. Tribology*, pages 2416–2420.

Gibson, K. and Kabnick, L. (2017). A multicenter, randomized, placebo-controlled study to evaluate the efficacy and safety of Varithena®(polidocanol endovenous microfoam 1%) for symptomatic, visible varicose veins with saphenofemoral junction incompetence. *Phlebology*, 32(3):185–193.

Gibson, R. and Cook, A. (1974). The stability of curved channel flow. *Quart. J. Mech. Appl. Math.*, 27(2):149–160.

Glowinski, R. (1980). *Numerical methods for nonlinear variational problems.* Tata Institute of Fundamental Research.

Glowinski, R. (2003). Finite Element Methods for incompressible Viscous flow. *Handb. Numer. Anal.*, 9:3–1176.

Glowinski, R. and Pironneau, O. (1978). On numerical methods for the Stokes problem. *Math. Comput. Sci. Publications of Rennes*, 1(S4):1–29.

Gopal, A. and Durian, D. (1999). Shear-induced "melting" of an aqueous foam. *J. Coll. Int. Sci.*, 213(1):169–178.

Gottlob, R., May, R., and Geleff, S. (1986). Venous valves: Morphology, function, radiology, surgery. *Int. J. Cardio.*, 1(1):227.

Gray, H. (1918). *Gray's anatomy: 20th edition.* Arcturus Publishing.

Green, A., Littlejohn, K., Hooley, P., and Cox, P. (2013). Formation and stability of food foams and aerated emulsions: Hydrophobins as novel functional ingredients. *Curr. Opin. Colloid Interface Sci.*, 18(4):292–301.

Guex, J. (1993). Microsclerotherapy. In *Sem. Dermat.*, volume 12, pages 129–134.

Hager, E. (2020). Varicose veins - Society of Vascular Surgery. `https://vascular.org/patient-resources/vascular-conditions/varicose-veins`. [Online; accessed 3-August-2020].

Hajati, Z., Moghanlou, F., Vajdi, M., Razavi, S., and Matin, S. (2020). Fluid-structure interaction of blood flow around a vein valve. *Bioimpacts*, 10(3):169–175.

Hamel-Desnos, C., Desnos, P., Wollmann, J., Ouvry, P., Mako, S., and Allaert, F. (2003). Evaluation of the efficacy of polidocanol in the form of foam compared with liquid form in sclerotherapy of the greater saphenous vein: initial results. *Dermatol. Surg.*, 29(12):1170–1175.

Hanks, R. et al. (1967). On the flow of Bingham Plastic slurries in pipes and between parallel plates. *Soc. Pet. Eng. J.*, 7(04):342–346.

Hatzikiriakos, S. (2012). Wall slip of molten polymers. *Prog. Pol. Sci.*, 37(4):624–643.

Hayes, B. (2005). Why W? on the Lambert W function, a candidate for a new elementary function in Mathematics. *Am. Sci.*, 93(2):104–108.

Hecht, F. (1998). BAMG: bidimensional anisotropic mesh generator. *User Guide. INRIA, Rocquencourt*, 17.

Hecht, F. (2012). New developments in FreeFem++. *J. Numer. Math.*, 20(3-4):251–266.

Hecht, F. (2020a). Elasticity - FreeFem++. `https://doc.freefem.org/models/elasticity.html`. [Online; accessed 28-October-2020].

Hecht, F. (2020b). Finite element - FreeFem++. `https://doc.freefem.org/documentation/finite-element.html`. [Online; accessed 07-Jan-2020].

Hecht, F. (2020c). Mesh generation - FreeFem++. `https://doc.freefem.org/documentation/mesh-generation.html`. [Online; accessed 29-May-2020].

Hecht, F. (2020d). Navier-Stokes - FreeFem++. `https://doc.freefem.org/models/navier-stokes-equations.html#equation-eqn-vfstokes`. [Online; accessed 11-August-2020].

Hecht, F. (2020e). Poisson tutorial - FreeFem++. `https://doc.freefem.org/tutorials/poisson.html`. [Online; accessed 11-August-2020].

Hecht, F. (2020f). Quadrature formula - FreeFem++. `https://doc.freefem.org/references/quadrature-formulae.html`. [Online; accessed 05-May-2020].

Hemmat, M. and Borhan, A. (1995). Creeping flow through sinusoidally constricted capillaries. *Phys. Fluids*, 7(9):2111–2121.

Hemphill, T., Campos, W., and Pilehvari, A. (1993). Yield-power law model more accurately predicts mud rheology. *Oil Gas J.*, 91(34).

Herschel, W. and Bulkley, R. (1926). Measurement of consistency as applied to rubber-benzene solutions. *Am. Soc. Test Proc*, 26(2):621–633.

Hewitt, D., Daneshi, M., Balmforth, N., and Martinez, D. (2016). Obstructed and channelized viscoplastic flow in a Hele-Shaw cell. *J. Fluid Mech.*, 790:173–204.

Higdon, J. (1985). Stokes flow in arbitrary two-dimensional domains: shear flow over ridges and cavities. *J. Fluid Mech.*, 159:195–226.

Hild, P., Ionescu, I., Lachand-Robert, T., and Roşca, I. (2002). The blocking of an inhomogeneous Bingham fluid. Applications to landslides. *ESAIM-Math. Model. Num.*, 36(6):1013–1026.

Homans, J. (1928). Thrombophlebitis of the lower extremities. *Ann. Surg.*, 87(5):641.

Huilgol, R. and You, Z. (2005). Application of the Augmented Lagrangian Method to steady pipe flows of Bingham, Casson and Herschel–Bulkley fluids. *J. non-Newt. Fl. Mech.*, 128(2-3):126–143.

Huo, Y. and Kassab, G. (2006). Pulsatile blood flow in the entire coronary arterial tree: theory and experiment. *Am. J. Physiol.-Heart C.*, 291(3):H1074–H1087.

Hussain, A., Amin, A., Vincent-Bonnieu, S., Farajzadeh, R., Andrianov, A., Hamid, P., and Rossen, W. (2017). Effect of oil on gravity segregation in sag foam flooding. In *IOR 2017-19th European Symposium on Improved Oil Recovery*, volume 1, pages 1–16. European Association of Geoscientists & Engineers.

Hutzler, S., Weaire, D., and Bolton, F. (1995). The effects of Plateau borders in the two-dimensional soap froth III. further results. *Philos. Mag. B*, 71(3):277–289.

Hutzler, S., Weaire, D., Saugey, A., Cox, S., and Peron, N. (2005). The physics of foam drainage. In *Proceedings of MIT European Detergents Conference, Wurzburg*, pages 191–206. Citeseer.

Jaeger, H. and Nagel, S. (1992). Physics of the granular state. *Science*, 255(5051):1523–1531.

Janela, J., Moura, A., and Sequeira, A. (2010). A 3D non-Newtonian fluid–structure interaction model for blood flow in arteries. *J. Comput. Appl. Math.*, 234(9):2783–2791.

Jeong, S. (2013). Determining the viscosity and yield surface of marine sediments using modified Bingham models. *Geosci. J.*, 17(3):241–247.

Johnston, B., Johnston, P., Corney, S., and Kilpatrick, D. (2004). Non-Newtonian blood flow in human right coronary arteries: steady state simulations. *J. Biomech.*, 37(5):709–720.

Joshi, Y. and Denn, M. (2003). Planar contraction flow with a slip boundary condition. *J. non-Newt. Fl. Mech.*, 114(2-3):185–195.

Kakkos, S., Bountouroglou, D., Azzam, M., Kalodiki, E., Daskalopoulos, M., and Geroulakos, G. (2006). Effectiveness and safety of ultrasound-guided foam sclerotherapy for recurrent varicose veins: immediate results. *J. Endovasc. Therapy*, 13(3):357–364.

Kalyon, D. and Malik, M. (2012). Axial laminar flow of Viscoplastic fluids in a concentric annulus subject to wall slip. *Rheol. acta*, 51(9):805–820.

Kang, T., Kim, C., and Hong, K. (2012). Rheological behavior of concentrated silica suspension and its application to soft armor. *J. Appl. Polym. Sci.*, 124(2):1534–1541.

Kaoullas, G. and Georgiou, G. (2013). Newtonian Poiseuille flows with slip and non-zero slip yield stress. *J. non-Newt. Fl. Mech.*, 197:24–30.

Karapetsas, G. and Mitsoulis, E. (2013). Some experiences with the slip boundary condition in Viscous and Viscoelastic flows. *J. non-Newt. Fl. Mech.*, 198:96–108.

Khan, S., Schnepper, C., and Armstrong, R. (1988). Foam rheology: III. Measurement of shear flow properties. *J. Rheol.*, 32(1):69–92.

Klabunde, R. (2013). Normal and abnormal blood pressure (physiology, pathophysiology and treatment). *Amazon Kindle Book*, pages 102–117.

Kokini, J. and Dickie, A. (1982). A model of food spreadability from Fluid Mechanics. *J. Texture Stud.*, 13(2):211–227.

Kraynik, A. (1983). Foam drainage. Technical report, Sandia National Labs., Albuquerque, NM (USA).

Kraynik, A. and Hansen, M. (1987). Foam rheology: a model of viscous phenomena. *J. Rheol.*, 31(2):175–205.

Kraynik, A., Reinelt, D., and van Swol, F. (2004). Structure of random foam. *Phys. Rev. Lett.*, 93(20):208301.

Kruglyakov, P., Karakashev, S., Nguyen, A., and Vilkova, N. (2008). Foam drainage. *Curr. Opin. Colloid Interface Sci.*, 13(3):163–170.

Ku, D. (1997). Blood flow in arteries. *Annu. Rev. Fluid Mech.*, 29(1):399–434.

Laird, W. (1957). Slurry and suspension transport-basic flow studies on Bingham plastic fluids. *J. Ind. Eng. Chem.*, 49(1):138–141.

Lamb, H. (1993). *Hydrodynamics*, volume 6. Cambridge university press, Cambridge.

Langevin, D. (2017). Aqueous foams and foam films stabilised by surfactants. Gravity-free studies. *Mech. Rep.*, 345(1):47–55.

Larson, R., Hostetler, R., and Edwards, B. (2006). *Calculus*. Houghton Mifflin Boston.

Lattimer, C., Azzam, M., Kalodiki, E., Shawish, E., Trueman, P., and Geroulakos, G. (2012). Cost and effectiveness of laser with phlebectomies compared with foam sclerotherapy in superficial venous insufficiency. Early results of a randomised controlled trial. *Eur. J. Vasc. Endovasc. Surg.*, 43(5):594–600.

Lauga, E., Brenner, M., and Stone, H. (2005). Handbook of Experimental Fluid Dynamics. *chap. Microfluidics: The No-Slip Boundary Condition. Springer.*

Lauga, E. and Stone, H. (2003). Effective slip in pressure-driven Stokes flow. *J. Fluid Mech.*, 489:55–77.

Laun, H., Rady, M., and Hassager, O. (1999). Analytical solutions for squeeze flow with partial wall slip. *J. non-Newt. Fl. Mech.*, 81(1-2):1–15.

Lawaetz, M., Serup, J., Lawaetz, B., Bjoern, L., Blemings, A., Eklof, B., and Rasmussen, L. (2017). Comparison of endovenous ablation techniques, foam sclerotherapy and surgical stripping for great saphenous varicose veins. extended 5-year follow-up of a rct. *Int. Angiol.*, 36(3):281–288.

Lee, A., Evans, C., Allan, P., Ruckley, C., and Fowkes, F. (2003). Lifestyle factors and the risk of varicose veins: Edinburgh vein study. *J. Clin. Epidemiol.*, 56(2):171–179.

Lee, D. and Schachter, B. (1980). Two algorithms for constructing a Delaunay triangulation. *Int. J. Comput. Inf. Sci.*, 9(3):219–242.

Li, R., Yan, W., Liu, S., Hirasaki, G., Miller, C., et al. (2010). Foam mobility control for surfactant Enhanced Oil recovery. *SPE J.*, 15(04):928–942.

Li, W. (2018). Biomechanical property and modelling of venous wall. *Prog. Biophys. Mol. Biol.*, 133:56–75.

Lighthill, M. and Rosenhead, L. (1963). Laminar boundary layers. *Clarendon Press, Oxford.*

Lipscomb, G. and Denn, M. (1984). Flow of Bingham fluids in complex geometries. *J. non-Newt. Fl. Mech.*, 14:337–346.

Lurie, F., Kistner, R., Eklof, B., and Kessler, D. (2003). Mechanism of venous valve closure and role of the valve in circulation: A new concept. *J. Vasc. Surg.*, 38(5):955–961.

Malevich, A., Mityushev, V., and Adler, P. (2006). Stokes flow through a channel with wavy walls. *Acta Mech.*, 182(3-4):151–182.

Marsden, G., Perry, M., Bradbury, A., Hickey, N., Kelley, K., Trender, H., Wonderling, D., and Davies, A. (2015). A cost-effectiveness analysis of surgery, endothermal ablation, ultrasound-guided foam sclerotherapy and compression stockings for symptomatic varicose veins. *Eur. J. Vasc. Endovasc. Surg.*, 50(6):794–801.

Martinsson, J. and Sichen, D. (2016). Study on apparent viscosity of foam and droplet movement using a cold model. *Steel Res. Int.*, 87(6):712–719.

Mason, T., Bibette, J., and Weitz, D. (1996). Yielding and flow of monodisperse emulsions. *J. Colloid Interface Sci.*, 179(2):439–448.

Matthews, M. and Hill, J. (2007). Newtonian flow with nonlinear Navier boundary condition. *Acta Mech.*, 191(3-4):195–217.

Matthews, M. and Hill, J. (2008). Nanofluidics and the Navier boundary condition. *Int. J. Nanotechnol.*, 5(2-3):218–242.

Maxwell, J. (1878). III. On stresses in rarefied gases arising from inequalities of temperature. *P. Roy. Soc. London*, 27(185-189):304–308.

McBirney, A. and Murase, T. (1984). Rheological properties of magmas. *Annu. Rev. Earth Planet Sci.*, 12(1):337–357.

McDaniel, J. and Holt, R. (2000). Measurement of aqueous foam rheology by acoustic levitation. *Phys. Rev. E*, 61(3):R2204.

Meeker, S., Bonnecaze, R., and Cloitre, M. (2004). Slip and flow in pastes of soft particles: Direct observation and rheology. *J. Rheol.*, 48(6):1295–1320.

Merrill, E., Cheng, C., and Pelletier, G. (1969). Yield stress of normal human blood as a function of endogenous fibrinogen. *J. Appl. Physiol.*, 26(1):1–3.

Min, R. and Khilnani, N. (2005). Endovenous laser ablation of varicose veins. *J. Cardiovasc. Surg.*, 46(4):395.

Min, R. and Navarro, L. (2000). Transcatheter duplex ultrasound-guided sclerotherapy for treatment of greater saphenous vein reflux: Preliminary report. *Dermat. Surg.*, 26(5):410–414.

Misra, J. and Shit, G. (2007). Role of slip velocity in blood flow through stenosed arteries: a non-Newtonian model. *J. Mech. Med. Biol.*, 7(3):337–353.

Mitsoulis, E., Abdali, S., and Markatos, N. (1993). Flow simulation of Herschel-Bulkley fluids through extrusion dies. *Canadian J. Chem. Eng.*, 71(1):147–160.

Mitsoulis, E. and Huilgol, R. (2004). Entry flows of bingham plastics in expansions. *J. non-Newt. Fl. Mech.*, 122(1-3):45–54.

Mitsoulis, E. and Zisis, T. (2001). Flow of Bingham plastics in a lid-driven square cavity. *J. non-Newt. Fl. Mech.*, 101(1-3):173–180.

Mittra, T. and Prasad, S. (1974). Interaction of peristaltic motion with Poiseuille flow. *Bull. Math. Biol.*, 36:127–141.

Molnár, G., Nemes, A., Kékesi, V., Monos, E., and Nádasy, G. (2010). Maintained geometry, elasticity and contractility of human saphenous vein segments stored in a complex tissue culture medium. *Eur. J. Vasc. Endovasc. Surg.*, 40(1):88–93.

Moore, H., Gohel, M., and Davies, A. (2011). Number and location of venous valves within the popliteal and femoral veins–a review of the literature. *J. Anat.*, 219(4):439–443.

Morse, P. and Feshbach, H. (1954). Methods of theoretical physics. *Am. J. Phys.*, 22(6):410–413.

Moyers-Gonzalez, M. and Frigaard, I. (2004). Numerical solution of duct flows of multiple Viscoplastic fluids. *J. non-Newt. Fl. Mech.*, 122(1-3):227–241.

Munavalli, G. and Weiss, R. (2007). Complications of sclerotherapy. In *Seminars in Cutan. Med. Surg.*, volume 26, pages 22–28.

Munson, B., Rangwalla, A., and Mann III, J. (1985). Low Reynolds number circular Couette flow past a wavy wall. *Phys. Fluids*, 28(9):2679–2686.

Muravleva, L. (2015). Squeeze plane flow of viscoplastic Bingham material. *J. non-Newt. Fl. Mech.*, 220:148–161.

Muravleva, L., Muravleva, E., Georgiou, G., and Mitsoulis, E. (2010a). Numerical simulations of cessation flows of a Bingham plastic with the Augmented Lagrangian Method. *J. non-Newt. Fl. Mech.*, 165(9-10):544–550.

Muravleva, L., Muravleva, E., Georgiou, G., and Mitsoulis, E. (2010b). Unsteady circular Couette flow of a Bingham plastic with the Augmented Lagrangian Method. *Rheol. Acta*, 49:1197–1206.

Myers, T. (1957). Results and technique of stripping operation for varicose veins. *J. Am. Med. Assoc.*, 163(2):87–92.

Nael, R. and Rathbun, S. (2009). Treatment of varicose veins. *Curr. Treat. Options Cardiovasc. Med.*, 11(2):91–103.

Nastasa, V., Samaras, K., Ampatzidis, C., Karapantsios, T., Trelles, M., Moreno-Moraga, J., Smarandache, A., and Pascu, M. (2015). Properties of polidocanol foam in view of its use in sclerotherapy. *Int. J. Pharm.*, 478:588–596.

Navier, C. (1823). On the laws of movement of fluids. *Mem. Acad. Sci. Inst. Fr.*, 6:389–440.

Nesbitt, C., Bedenis, R., Bhattacharya, V., and Stansby, G. (2014). Endovenous ablation (radiofrequency and laser) and foam sclerotherapy versus open surgery for great saphenous vein varices. *Cochrane Database Syst. Rev.*, 30(7).

Neto, C., Evans, D., Bonaccurso, E., Butt, H., and Craig, V. (2005). Boundary slip in Newtonian liquids: a review of experimental studies. *Rep. Prog. Phys.*, 68(12):2859.

Newton, I. (1728). Mathematical principles of natural philosophy. *London*, 1.

NHS (2020). Varicose Vein Complications - NHS. `https://www.nhs.uk/conditions/varicose-veins/complications/`. [Online; accessed 22-January-2020].

Nirmalkar, N. and Chhabra, R. (2014). Momentum and heat transfer from a heated circular cylinder in Bingham Plastic fluids. *Int. J. Heat Mass Transf.*, 70:564–577.

Noda, N., Nakano, M., Matsuura, H., Nemoto, T., and Koide, K. (2006). Numerical analysis of blood flow in vessels. In *First International Conference on Innovative Computing, Information and Control-Volume I (ICICIC'06)*, volume 3, pages 545–546. IEEE.

Norouzi, M., Davoodi, M., Bég, O., and Shamshuddin, M. (2018). Theoretical study of Oldroyd-B Visco-elastic fluid flow through curved pipes with slip effects in polymer flow processing. *Int. J. Appl. Comput. Math.*, 4(4):108.

Norouzi, M., Vamerzani, B., Davoodi, M., Biglari, N., and Shahmardan, M. (2015). An exact analytical solution for creeping Dean flow of Bingham plastics through curved rectangular ducts. *Rheol. Acta*, 54:391–402.

Obernauer, S., Drazer, G., and Rosen, M. (2000). Stable–unstable crossover in non-Newtonian radial Hele–Shaw flow. *Physica A*, 283(1-2):187–192.

O'Donovan, E. and Tanner, R. (1984). Numerical study of the Bingham squeeze film problem. *J. non-Newt. Fl. Mech.*, 15(1):75–83.

Oldroyd, J. (1950). On the formulation of rheological equations of state. *P. Roy. Soc. A-Math. Phy.*, 200(1063):523–541.

Oliphant, T. (2007). Python for scientific computing. *Comput. Sci. Eng.*, 9(3):10–20.

Otomo, H., Fan, H., Hazlett, R., Li, Y., Staroselsky, I., Zhang, R., and Chen, H. (2015). Simulation of residual oil displacement in a sinusoidal channel with the Lattice Boltzmann method. *Mech. Rep.*, 343(10-11):559–570.

Ouvry, P., Allaert, F., Desnos, P., and Hamel-Desnos, C. (2008). Efficacy of polidocanol foam versus liquid in sclerotherapy of the great saphenous vein: a multicentre randomised controlled trial with a 2-year follow-up. *Eur. J. Vasc. Endovasc. Surg.*, 36(3):366–370.

Packel, E. and Yuen, D. (2004). Projectile motion with resistance and the Lambert W function. *Coll. Math. J.*, 35(5):337–350.

Papanastasiou, T. (1987). Flows of materials with yield. *J. Rheol.*, 31(5):385–404.

Pascal, H. (1986). Stability of a moving interface in porous medium for non-Newtonian displacing fluids and its applications in oil displacement mechanism. *Acta Mech.*, 58(1-2):81–91.

Patel, K., Patel, A., Chaudhary, H., and Sen, D. (2014). Cease fire: An emergency practice in domestic as well as in profession. *Res. J. Sci. Tech.*, 6(3):133–142.

Pedley, T., Batchelor, G., Moffat, H., and Worster, M. (2000). Blood flow in arteries and veins. *Per. Fluid Dynam.*, pages 105–158.

Pedrizzetti, G., Zovatto, L., Domenichini, F., and Tortoriello, A. (2002). Pulsatile flow inside moderately elastic arteries, its modelling and effects of elasticity. *Comput. Methods. Biomech. Biomed. Eng.*, 5(3):219–231.

Pelc, L., Pelc, N., Rayhill, S., Castro, L., Glover, G., Herfkens, R., Miller, D., and Jeffrey, R. (1992). Arterial and venous blood flow: noninvasive quantitation with mr imaging. *Radiology*, 185(3):809–812.

Perrin, M. (2011). History of venous surgery. *Phlebolymphology*, 18(4):167–173.

Peterson, J. and Goldman, M. (2001). An investigation into the influence of various gases and concentrations of sclerosants on foam stability. *Dermatologic surgery*, 37:12–17.

Petkova, S., Hossain, A., Naser, J., and Palombo, E. (2003). Cfd modelling of blood flow in portal vein hypertension with and without thrombosis. In *Third International Conference on CFD in the Minerals and Process Industries CSIRO, Melborne, Australia*, pages 10–12.

Philippou, M., Kountouriotis, Z., and Georgiou, G. (2016). Viscoplastic flow development in tubes and channels with wall slip. *J. non-Newt. Fl. Mech.*, 234:69–81.

Picart, C., Piau, J., Galliard, H., and Carpentier, P. (1998). Human blood shear yield stress and its hematocrit dependence. *J. Rheol.*, 42(1):1–12.

Pit, R., Hervet, H., and Leger, L. (2000). Direct experimental evidence of slip in hexadecane: solid interfaces. *Phys. Rev. Lett.*, 85(5):980.

Pontrelli, G., Halliday, I., Spencer, T., Care, C., König, C., Collins, M., et al. (2011). Near wall hemodynamics: Modelling the glycocalyx and the endothelial surface. *Comput. Method. Biomec.*, 18(04):351–361.

Potente, H., Timmermann, K., and Kurte-Jardin, M. (2006). Description of the pressure/throughput behavior of a single-screw plasticating unit in consideration of wall slippage effects for non-Newtonian material and 1-D flow. *Int. Polym. Proc.*, 21(3):272–282.

Pozrikidis, C. et al. (1992). *Boundary integral and singularity methods for linearized viscous flow.* Cambridge University Press.

Princen, H. and Kiss, A. (1986). Rheology of foams and highly concentrated emulsions: III. Static shear modulus. *J. Coll. Int. Sci.*, 112(2):427–437.

Princen, H. and Kiss, A. (1989). Rheology of foams and highly concentrated emulsions: IV. An experimental study of the shear viscosity and yield stress of concentrated emulsions. *J. Coll. Int. Sci.*, 128(1):176–187.

Pu, W., Wei, P., Sun, L., and Wang, S. (2017). Stability, CO2 sensitivity, oil tolerance and displacement efficiency of polymer enhanced foam. *RSC Adv.*, 7(11):6251–6258.

Quanyu, W., Xiaojie, L., Lingjiao, P., Weige, T., and Chunqi, Q. (2017). Simulation analysis of blood flow in arteries of the human arm. *Biomed. Eng.: Appl. Basis Commun.*, 29(04):1750031.

Rabe, E., Pannier-Fischer, F., Gerlach, H., Breu, F., Guggenbichler, S., and Zabel, M. (2004). Guidelines for Sclerotherapy of Varicose veins. *Dermatol. Surg.*, 30(5):687–693.

Radiological Society of North America (RSNA) (2020). Laser Ablation - Radiologyinfo.org. `https://www.radiologyinfo.org/en/info.cfm?pg=varicoseabl`. [Online; accessed 22-January-2020].

Rao, J. and Goldman, M. (2005). Stability of foam in sclerotherapy: Differences between Sodium Tetradecyl Sulfate and polidocanol and the type of connector used in the Double-Syringe System technique. *Dermatol. Surg.*, 31(1):19–22.

Rasmussen, L., Bjoern, L., Lawaetz, M., Blemings, A., Lawaetz, B., and Eklof, B. (2007). Randomized trial comparing endovenous laser ablation of the great saphenous vein with high ligation and stripping in patients with varicose veins: short-term results. *J. Vasc. Surg.*, 46(2):308–315.

Rasmussen, L., Lawaetz, M., Bjoern, L., Vennits, B., Blemings, A., and Eklof, B. (2011). Randomized clinical trial comparing endovenous laser ablation, radiofrequency ablation, foam sclerotherapy and surgical stripping for great saphenous varicose veins. *British J. Surg.*, 98(8):1079–1087.

Rass, K., Frings, N., Glowacki, P., Hamsch, C., Vogt, T., Tilgen, W., et al. (2012). Comparable effectiveness of endovenous laser ablation and high ligation with stripping of the great saphenous vein: two-year results of a randomized clinical trial (RELACS study). *Arch. Dermat.*, 148(1):49–58.

Reddy, J. and Srikanth, D. (2015). The polar fluid model for blood flow through a tapered artery with overlapping stenosis: effects of catheter and velocity slip. *Appl. Bionics. Biomech.*, 2015.

Reusken, A. (2020). Numerical Methods for the Navier-Stokes equations - RWTH Aachen University. `https://pdfs.semanticscholar.org/5be5/b336940aad897afb6eb8f90d1d406170ea34.pdf`. [Online; accessed 12-August-2020].

Rieger, F. and Šesták, J. (1973). Creeping flow of Newtonian fluids in curved rectangular channels. *Appl. Sci. Res.*, 28:89–106.

Roberts, J. and Thomas, J. (1993). Mixed and Hybrid Methods, Handbook of Numerical Anaysis, vol. II. *Handb. Numer. Anal.*, 183:184.

Roberts, T. and Cox, S. (2020). An analytic velocity profile for pressure-driven flow of a Bingham fluid in a curved channel. *J. non-Newt. Fl. Mech.*, page 104278.

Roberts, T., Cox, S., Lewis, A., and Jones, S. (2020). Characterisation and optimisation of foams for varicose vein sclerotherapy. *arXiv preprint arXiv:2005.01458.*

Roquet, N., Michel, R., and Saramito, P. (2000). Errors estimate for a Viscoplastic fluid by using Pk finite elements and adaptive meshes. *Rep. Acad. Sci*, 331(7):563–568.

Roquet, N. and Saramito, P. (2003). An adaptive Finite Element Method for Bingham fluid flows around a cylinder. *Comput. Methods in Appl. Mech. Eng.*, 192(31-32):3317–3341.

Roquet, N. and Saramito, P. (2008). An adaptive Finite Element Method for Viscoplastic flows in a square pipe with stick–slip at the wall. *J. non-Newt. Fl. Mech.*, 155(3):101–115.

Rosenson, R., Mccormick, A., and Uretz, E. (1996). Distribution of blood viscosity values and biochemical correlates in healthy adults. *Clin. Chem.*, 42(8):1189–1195.

Rossen, W. (1996). Foams in enhanced oil recovery. *Foams: theory, measurements and applications*, 57:413–464.

Rossen, W. and Van Duijn, C. (2004). Gravity segregation in steady-state horizontal flow in homogeneous reservoirs. *J. Pet. Sci. Eng.*, 43(1-2):99–111.

Roustaei, A. (2014). Bingham fluid - FreeFem++. `https://www.um.es/freefem/ff++/pmwiki.php?n=Main.Bingham`. [Online; accessed 11-June-2020].

Roustaei, A. (2016). *Yield stress fluid flows in uneven geometries: applications to the oil & gas industry.* PhD thesis, University of British Columbia.

Roustaei, A. and Frigaard, I. (2013). The occurrence of fouling layers in the flow of a yield stress fluid along a wavy-walled channel. *J. non-Newt. Fl. Mech.*, 198:109–124.

Rouyer, F., Cohen-Addad, S., and Höhler, R. (2005). Is the yield stress of aqueous foam a well-defined quantity? *Coll. Surf. A*, 263:111–116.

Saint-Jalmes, A. and Durian, D. (1999). Vanishing elasticity for wet foams: Equivalence with emulsions and role of polydispersity. *J. Rheol.*, 43:1411–1422.

Sampson, S. (2020). All you need to know about varicose vein pain - Medical news today. `https://www.medicalnewstoday.com/articles/320359`. [Online; accessed 04-August-2020].

Sandri, J., Barros, F., Pontes, S., Jacques, C., and Salles-Cunha, S. (1999). Diameter-reflux relationship in perforating veins of patients with varicose veins. *J. Vasc. Surg.*, 30(5):867–875.

Saramito, P. (2009). A new elastoviscoplastic model based on the Herschel–Bulkley viscoplastic model. *J. Non-Newt. Fl. Mech.*, 158(1-3):154–161.

Saramito, P. and Roquet, N. (2001). An adaptive Finite Element Method for Viscoplastic fluid flows in pipes. *Comput. Meth. Appl. Mech. Eng.*, 190(40-41):5391–5412.

Scipy.org (2020). Lambert W Function - Python. `https://docs.scipy.org/doc/scipy-0.14.0/reference/generated/scipy.special.lambertw.html`. [Online; accessed 04-June-2020].

Sharifahmadian, A. (2015). *Numerical models for submerged breakwaters: Coastal hydrodynamics and morphodynamics*. Butterworth-Heinemann.

Sheng, J. (2013). Foams and their applications in enhancing oil recovery. In *Enhanced Oil Recovery Field Case Studies*, pages 251–280. Elsevier.

Singh, G. (2009). Short introduction to Finite Element Method. *Norwegian Uni. Sci. Tech.*

Sinha, A., Shit, G., and Kundu, P. (2013). Slip effects on pulsatile flow of blood through a stenosed arterial segment under periodic body acceleration. *ISRN Bio. Eng.*, 2013.

Smeplass, S. (1993). Applicability of the Bingham model to high strength concrete. *Spec. Concr.*, page 136.

Smyrnaios, D. and Tsamopoulos, J. (2001). Squeeze flow of Bingham plastics. *J. non-Newt. Fl. Mech.*, 100(1-3):165–189.

Sokolis, D. (2013). Experimental investigation and constitutive modeling of the 3D histomechanical properties of vein tissue. *Biomech. Model. Mechanobiol.*, 12(3):431–451.

Song, S., Yang, X., Xin, F., and Lu, T. (2018). Modeling of surface roughness effects on Stokes flow in circular pipes. *Phys. Fluids*, 30(2):023604.

Sousa, L., Castro, C., Antonio, C., and Chaves, R. (2011). Computational techniques and validation of blood flow simulation. *WSEAS Trans. Biol. Biomed.*, 8(4):145–155.

Spedding, P., Bénard, E., and McNally, G. (2004). Fluid flow through 90 degree bends. *Dev. Chem. Eng. Min. Process.*, 12:107–128.

Spivack, D., Kelly, P., Gaughan, J., and van Bemmelen, P. (2012). Mapping of superficial extremity veins: normal diameters and trends in a vascular patient-population. *Ultrasound Med. Biol.*, 38(2):190–194.

Srivastava, N. (2014). The Casson fluid model for blood flow through an inclined tapered artery of an accelerated body in the presence of magnetic field. *Int. J. Biomed. Eng. Tech.*, 15(3):198–210.

Star, P., Connor, D., and Parsi, K. (2018). Novel developments in foam sclerotherapy: Focus on Varithena®(polidocanol endovenous microfoam) in the management of varicose veins. *Phlebology*, 33(3):150–162.

Stoltz, J. and Lucius, M. (1981). Viscoelasticity and thixotropy of human blood. *Biorheol.*, 18(3-6):453–473.

Strauss, W. (2007). *Partial differential equations: An introduction.* John Wiley & Sons.

Sumetc, P. (2017). *Modelling the Endothelial Glycocalyx Layer.* PhD thesis, ResearchSpace@ Auckland.

Sun, A. and Gunasekaran, S. (2009). Yield stress in foods: measurements and applications. *Int. J. Food Prop.*, 12(1):70–101.

Tanner, R. and Milthorpe, J. (1983). Numerical simulation of the flow of fluids with yield stress. *Numer. Meth. Lami. Turb. Flow*, pages 680–690.

Taylor, A. and Wilson, S. (1997). Conduit flow of an incompressible, yield-stress fluid. *J. Rheol.*, 41:93–102.

Taylor, C., Hughes, T., and Zarins, C. (1998). Finite element modeling of blood flow in arteries. *Comput. Meth. Appl. Mech. Eng.*, 158(1-2):155–196.

Tessari, L. (2000). New technique for obtaining sclero-foam. *Phlebologie*, 53:129.

Thomasset, S., Butt, Z., Liptrot, S., Fairbrother, B., and Makhdoomi, K. (2010). Ultrasound guided foam sclerotherapy: factors associated with outcomes and complications. *Eur. J. Vasc. Endovasc. Surg.*, 40(3):389–392.

Thompson, P. and Troian, S. (1997). A general boundary condition for liquid flow at solid surfaces. *Nature*, 389(6649):360–362.

Thompson, R., Sica, L., and de Souza Mendes, P. (2018). The Yield Stress tensor. *J. non-Newt. Fl. Mech.*, 261:211–219.

Thurston, G. (1972). Viscoelasticity of human blood. *Biophys. J.*, 12(9):1205–1217.

Tibbs, K., Baras, F., and Garcia, A. (1997). Anomalous flow profile due to the curvature effect on slip length. *Phys. Rev. E*, 56(2):2282.

Todd III, K., Wright, D., and Group, V.-. I. (2014). The VANISH-2 study: A randomized, blinded, multicenter study to evaluate the efficacy and safety of polidocanol endovenous microfoam 0.5% and 1.0% compared with placebo for the treatment of saphenofemoral junction incompetence. *Phlebology*, 29(9):608–618.

Tokpavi, D., Magnin, A., and Jay, P. (2008). Very slow flow of Bingham Viscoplastic fluid around a circular cylinder. *J. non-Newt. Fl. Mech.*, 154(1):65–76.

Treskatis, T., Moyers-González, M., and Price, C. (2016). An accelerated dual proximal gradient method for applications in viscoplasticity. *J. non-Newt. Fl. Mech.*, 238:115–130.

Tretheway, D. and Meinhart, C. (2002). Apparent fluid slip at hydrophobic microchannel walls. *Phys. Fluids*, 14(3):L9–L12.

Tropea, C. and Yarin, A. (2007). *Springer handbook of experimental fluid mechanics*. Springer Science & Business Media.

van den Bremer, J. and Moll, F. (2010). Historical overview of varicose vein surgery. *Annals Vasc. Surg.*, 24(3):426–432.

Van der Velden, S., Biemans, A., De Maeseneer, M., Kockaert, M., Cuypers, P., Hollestein, L., Neumann, H., Nijsten, T., and Van Den Bos, R. (2015). Five-year results of a randomized clinical trial of conventional surgery, endovenous laser ablation and ultrasound-guided foam sclerotherapy in patients with great saphenous varicose veins. *British J. Surg.*, 102(10):1184–1194.

Van Der Vleuten, C., Kater, A., Wijnen, M., Kool, L., and Rovers, M. (2014). Effectiveness of sclerotherapy, surgery, and laser therapy in patients with venous malformations: a systematic review. *Cardiovasc. Interv. Radiol.*, 37(4):977–989.

Varela López, F. and Rosen, M. (2002). Rheological effects in roll coating of paints. *Lat. Am. Appl. Res.*, 32(3):247–252.

Venermo, M., Saarinen, J., Eskelinen, E., Vähäaho, S., Saarinen, E., Railo, M., Uurto, I., Salenius, J., Albäck, A., Collaborators, F. V. S., et al. (2016). Randomized clinical trial comparing surgery, endovenous laser ablation and ultrasound-guided foam sclerotherapy for the treatment of great saphenous varicose veins. *British J. Surg.*, 103(11):1438–1444.

Venkatesan, J. and Ganesan, S. (2015). On the Navier-slip boundary condition for computations of impinging droplets. In *2015 IEEE 22nd International Conference on High Performance Computing Workshops*, pages 2–11. IEEE.

Venkatesan, J., Sankar, D., Hemalatha, K., and Yatim, Y. (2013). Mathematical analysis of Casson fluid model for blood rheology in stenosed narrow arteries. *J. Appl. Math.*, 2013.

Verbist, G., Weaire, D., and Kraynik, A. (1996). The foam drainage equation. *J. Phys.: Cond. Matt.*, 8(21):3715.

Vlachopoulos, C., O'Rourke, M., and Nichols, W. (2011). *McDonald's blood flow in arteries: theoretical, experimental and clinical principles*. CRC press.

Vvali, M. and Ra, E. (2002). Changes of elastic and collagen fibers in varicose veins. *Int. Angi.*, 21:337–43.

Walawender, W., Chen, T., and Cala, D. (1975). An approximate Casson fluid model for tube flow of blood. *Biorheol.*, 12(2):111–119.

Walsh, D., Downing, S., Ahmed, S., and Wallace, R. (1987). Valvular obstruction of blood flow through saphenous veins. *J. Surg. Res.*, 42(1):39–42.

Walsh, S. and Saar, M. (2008). Magma yield stress and permeability: Insights from multiphase percolation theory. *J. Volcanol. Geoth. Res.*, 177(4):1011–1019.

Walton, I. and Bittleston, S. (1991). The axial flow of a Bingham plastic in a narrow eccentric annulus. *J. Fl. Mech.*, 222:39–60.

Wang, W., Chen, G., Han, Z., Zhou, S., Zhang, H., and Jing, P. (2016). 3D numerical simulation of debris-flow motion using SPH method incorporating non-Newtonian fluid behavior. *Nat. Hazards*, 81(3):1981–1998.

Wang, Y. (1997). Comment on Conduit flow of an incompressible, Yield-Stress fluid. *J. Rheol.*, 41:1387–1391.

Weaire, D., Cox, S., and Brakke, K. (2005). Liquid Foams - Precursors for Solid Foams. *Cellular Ceramics: Structure, Manufacturing, Properties and Applications, P. Colombo and M. Scheffler (eds)*, pages 18–28.

Weaire, D. and Hutzler, S. (2001). *The physics of foams.* Oxford University Press.

Weaire, D., Hutzler, S., Cox, S., Kern, N., Alonso, M., and Drenckhan, W. (2002). The fluid dynamics of Foams. *J. Phys.: Condens. Matter*, 15(1):S65.

Wexler, L., Bergel, D., Gabe, I., Makin, G., and Mills, C. (1968). Velocity of blood flow in normal human venae cavae. *Circ. Res.*, 23(3):349–359.

White, E., Chellamuthu, M., and Rothstein, J. (2010). Extensional rheology of a shear-thickening cornstarch and water suspension. *Rheol. acta*, 49(2):119–129.

Wofsey, M. (2007). Focus: The little bubbles that could. *Physics*, 19:16.

Wollmann, J. (2004). The history of sclerosing foams. *Dermatol. Surg.*, 30(5):694–703.

Wollmann, J. (2010). Sclerosant foams: stabilities, physical properties and rheological behavior. *Phlebologie*, 39:208–217.

Wu, Y. (1990). Theoretical studies of non-Newtonian and Newtonian fluid flow through porous media. Technical report, Lawrence Berkeley Lab., CA (USA).

Wu, Y., Pruess, K., and Witherspoon, P. (1991). Displacement of a Newtonian fluid by a non-Newtonian fluid in a porous medium. *Transp. Porous Media*, 6(2):115–142.

Yang, S.-P. and Zhu, K.-Q. (2006). Analytical solutions for squeeze flow of Bingham fluid with Navier slip condition. *J. non-Newt. Fl. Mech.*, 138(2-3):173–180.

Yeow, Y., Leong, Y., and Khan, A. (2006). Non-Newtonian flow in parallel-disk Viscometers in the presence of wall slip. *J. non-Newt. Fl. Mech.*, 139(1-2):85–92.

Yortsos, Y., Huang, A., et al. (1986). Linear-stability analysis of immiscible displacement: Part 1-simple basic flow profiles. *SPE Reserv. Eng.*, 1(04):378–390.

Yoshimura, A., Prud'homme, R., Princen, H., and Kiss, A. (1987). A comparison of techniques for measuring yield stresses. *J. Rheol.*, 31(8):699–710.

Yue, Y., Smith, B., Batty, C., Zheng, C., and Grinspun, E. (2015). Continuum foam: A material point method for shear-dependent flows. *ACM Trans. Graph.*, 34(5):1–20.

Zaccagnino, F., Audebert, A., and Cox, S. (2018). Simulation of surfactant transport during the rheological relaxation of two-dimensional dry foams. *Phys. Rev. E*, 98(2):022801.

Zampogna, G., Magnaudet, J., and Bottaro, A. (2019). Generalized slip condition over rough surfaces. *J. Fluid Mech.*, 858:407–436.

Zengeni, B. (2016). *Bingham yield stress and Bingham plastic viscosity of homogeneous non-Newtonian slurries.* PhD thesis, Cape Peninsula University of Technology.

Zervides, C., Narracott, A., Lawford, P., and Hose, D. (2008). The role of venous valves in pressure shielding. *Biomed. Eng. Online*, 7(1):8.

Zienkiewicz, O. and Heinrich, J. (1979). A unified treatment of steady-state shallow water and two-dimensional Navier-Stokes equations—finite element penalty function approach. *Comput. Meth. Appl. Mech. Eng.*, 17:673–698.

Zimmet, S. (2003). Sclerotherapy treatment of telangiectasias and varicose veins. *Tech. Vasc. Interv. radiol.*, 6:116–120.

Zisis, T. and Mitsoulis, E. (2002). Viscoplastic flow around a cylinder kept between parallel plates. *J. non-Newt. Fl. Mech.*, 105(1):1–20.